Enhancing engine oil performance using nanoparticles and bio-lubricants as additives

Sunil Jayantha Hettiarachchi

http://orcid.org/0000-0002-0489-270X

A thesis submitted in partial fulfillment of the requirements of London South Bank University for the degree of Doctor of Philosophy

July 2022

Abstract

Contributions to the growing environmental concerns by internal combustion engines (ICEs) is the impetus of this research. Therefore, the tribological behavior of lubricants formulated with nano/mineral, nano/bio, and bio/mineral combinations were investigated for the improvements to ICE performance by reducing friction, wear, fuel consumption and exhaust emissions. Mineral-based multigrade engine oil (15W40) was chosen as the reference oil to govern the research. Coconut oil (CCO) was chosen with 15W40 as bio and mineral-base stocks respectively for sample formulations. Graphene (G), Al_2O_3, TiO_2, Al_2O_3/G, TiO_2/G and TiO_2/reduced graphene oxide (r-GO) were utilized as nano-additives to blend with both mineral and bio-based formulations. Identity of the selected nanomaterials were confirmed using X-ray powder diffraction (XRD), transmission electron microscopy (TEM), X-ray photoelectron spectroscopy (XPS), Fourier transform infrared (FT-IR) and Raman analyses. Identified substandard of CCO were improved and characterized using differential scanning calorimetry (DSC), pour point, titration, viscometry, simultaneous thermal analysis (STA), rheometric and FT-IR analyses. Factors influencing the dispersion stability of nano/mineral and nano/bio formulations were investigated, and optical absorbance and stability observation tests were used to optimize the performance, with the results presented and discussed.

Friction tests were performed using a linear reciprocating tribometer in 3 Phases to analyze the effect of formulated lubricants at elevated temperatures using piston ring and cylinder liner segments of an ICE as test specimens. Wear scars of test specimens were analyzed using scanning electron microscopy (SEM), energy dispersive X-ray spectroscopy (EDX) and 3D non-contact optical profilometry to investigate morphologies, elemental deposition, and surface texture of wear surfaces respectively. Specific fuel consumption and exhaust emissions were tested using a dynamometer test-rig and an exhaust analyzer. Industrial generator was utilized for used engine oil sample analysis.

The results revealed that, the method and time of agitation, particle concentration with adding of nanocomposites of metal oxides and graphene with oxygen functional groups (r-GO) have improved the dispersion stability of the formulations. In-addition reduction of coefficient of friction by 28%, specific fuel consumption by 8% and reduction of CO, SO_2 and NO_x emissions with S, P, and Zn elements were the optimum enhancements recorded by the sample S35 during the research. Sample S35 is a nano/bio lubricant containing formulated CCO with nanocomposite Al_2O_3/G as nano-additives, which is a new contribution to the knowledge of nano/bio-lubricant formulation.

Acknowledgement

First, I wish to declare my sincere gratitude towards my supervisors; Associate professor, Dr Suela Kellici (London South Bank University, UK), and Senior lecturer, Dr James Bowen (The Open University, UK), for their continuous support and guidance provided throughout the project. Their subject expertise coupled with encouragement extended, specifically during challenging times is hard to quantify.

I am thankful to all the peers at Nano2D Lab and Analytical Facilities at the School of Engineering, LSBU and acknowledge the technical support and experimental facilities at the Open University, UK.

Many thanks to Vishal Panchal and Stephen Lewandowski at Bruker (Coventry, UK) for their expert assistance with Profilometry measurements. Also, the support extended by the collaboration of Ducom Instruments and BMS College of Engineering, both in Bangalore (India) for LRT tests is worth mentioning.

It is highly appreciated the assistance tendered by the Head of Departments, their academics and technical staff of Mechanical Engineering and Polymer and Chemical Engineering Divisions, of the Institute of Technology, University of Moratuwa (Sri Lanka) for various physicochemical property analyses on coconut oil during Covid-19 pandemic. Besides, acknowledge the analytical services provided by the Industrial Technical Institute (Sri Lanka) during the pandemic.

CONTENTS

Table of contents

List of tables

List of figures

Nomenclature

μ - Coefficient of friction

E - Elastic modules

G - Nondimensional material parameter

h - Film thickness

H - Nondimensional film parameter

K - Nondimensional contact parameter

P - Pressure

R - Radius

T - Temperature

U - Nondimensional speed parameter

u - Velocity

V - Volume

w - Contact load

W - Nondimensional load parameter

α - Pressure viscosity coefficient

η - Dynamic viscosity

σ - Density

τ - Shear stress

υ - Kinematic viscosity

Al - Aluminum

Al_2O_3 - Aluminum oxide

AlO(OH)- Boehmite

Cd - Cadmium

CO - Carbon monoxide

CO_2 - Carbon dioxide

CO_x - Oxides of carbon

Cr - Chromium

Cu - Copper

CuO - Copper oxide

Fe - Iron

G - Graphene

GO - Graphene oxide

H - Hydrogen

H_2O_2 - Hydrogen peroxide

H_2SO_4 - Sulfuric acid

$KMnO_4$ - Potassium permanganate

Mo - Molybdenum

N_2 - Nitrogen

$NaNO_3$ - Sodium nitrate

NaOH - Sodium hydroxide

Ni - Nickel

NO - Nitric oxide

NO_2 - Nitrogen dioxide

NO_x - Oxides of nitrogen

O - Oxygen

P - Phosphorus

Pb - Lead

r-GO - Reduced graphene oxide

S - Sulphur

S_a - Area roughness (linear)

Si - Silicon

SO_2 - Sulphur dioxide

SO_x - Oxides of sulphur

S_q - Area roughness (rms)

TiO_2 - Titanium dioxide

Zn - Zinc

Abbreviations

15W40	- Multigrade formulated mineral-based engine lubricant
2D	- 2 dimensional
3D	- 3 dimensional
AFM	- Atomic force microscopy
AO	- Antioxidant
ASTM	- American Society for Testing and Material
ATC.EU	- Technical Committee of Petroleum Additive Manufactures in Europe
AW	- Anti-wear
BDC	- Bottom Dead Centre
BET	- Brunauer-Emmett-Teller
BL	- Boundary lubrication
BU	- Bottom up
CCC	- Copyright Clearance Centre
CCO	- Coconut oil
CHFS	- Continuous hydrothermal flow synthesis
CI	- Compression ignition
CLS	- Cylinder liner segment
COF	- Coefficient of friction
CVD	- Chemical vapor deposition
DI	- Deionized
DSC	- Differential scanning calorimetry
EDX	- Energy dispersive X-ray spectroscopy
EHL	- Elastohydrodynamic lubrication
EP	- Extreme pressure
FA	- Fatty acid
FCO	- Formulated coconut oil
FF	- Frictional Force
FM	- Friction modifier

FP - Flash point

FTDC - Fired top dead Centre

FT-IR - Fourier transform infrared spectroscopy

ICE - Internal combustion engine

LIF - Laser induced fluorescence

LRT - Linear reciprocating tribometer

MDPI - Multidisciplinary Digital Publishing Institute

ML - Mixed lubrication

OA - Oleic acid

PAH - Polynuclear aromatic hydrocarbon

PEG - Polyethylene glycol

PMMA = Polymethylmethacrylate

PP - Pour point

PPD - Pour point depressant

PRP - Piston ring pack

PRS - Piston ring segment

PVD - Physical vapor deposition

SAE - Society of Automobile Engineers

SAED - Selected area electron diffraction

SAGE - SAGE publications

SCF - Super critical fluid

SEM - Scanning electron microscopy

SF - Sunflower oil

SI - Spark ignition

SP - Styrenated phenol

SPC - Specific fuel consumption

SSA - Specific surface area

STA - Simultaneous thermal analysis

TAN - Total acid number

TBN	- Total base number
TD	- Top down
TDC	- Top Dead Centre
TEM	- Transmission electron microscopy
TMP	- Trimethylolpropane
UV-vis	- Ultraviolet visible spectrophotometry
vdW	- van der Waals
VI	- Viscosity index
VM	- Viscosity modifier
WSD	- Wear scar dimeter
XPS	- X-ray photoelectron spectroscopy
XRD	- X-ray powder diffraction
ZDDP	- Zincdialkyldithiophosphate

1. Chapter 1: Introduction

1.1 Overview

It is a known fact that the internal combustion engines (ICEs), especially diesel-driven engines are the foremost power generators for all purposes including transport, marine or industries worldwide for the foreseeable future, causing environmental pollution, in-addition to depletion of fossil fuel reserves. Because the production of automobiles was 92 million worldwide in 2019, of which 91% were with ICEs (9% electric vehicles).[1] In 2018 world released 33 gigatons (Gt) of CO_2 to the environment, noted International Energy Agency (2019). From this total CO_2 emissions 24% was from global transport sector, which is an increase of 0.6% compared to the previous year statistics. [2, 3] In Europe, out of total CO_2 emissions released, approximately 30% is from transport sector. of which 72% is from road transport segment (including cars, light and heavy trucks, buses, 2 and 3 wheelers), with reference to a report published by the European Parliament.[4] Thus, reduction of emissions and improvement of fuel consumption of an ICE by reducing friction and wear with enhance lubrication is the focus of this research.

ICE is a heat engine, which converts chemical energy via a thermal or combustion process to mechanical or kinetic energy with approximate thermal efficiency of 20 – 30% for gasoline and diesel engines respectively.[5] This is because of energy losses through heat/sound and frictional dissipations.[5, 6, 7] With reference to Ali, et al.,[8, 9] it is estimated that 17-19% of power generated by an engine will be lost through friction, perhaps a piston ring assembly and cylinder liner interface will account for 40-50% of frictional power losses within an ICE. This was confirmed by Jia, et al.,[10] as illustrated in Figure 1.1.

Therefore, researchers are continually searching for new technologies to enhance ICE lubrication. Nonetheless, contemporary diesel engine lubricants are constituted with 3 different packages; base stock, performance package and viscosity modifiers with approximate compositions of 78%, 12%, and 10%, respectively.[11] Because the contemporary commercial lubricants required to keep the engine clean while preventing soot, sludge formation, with oxidative and thermal stability. In addition, needs reduction of friction and wear losses with controlled exhaust emissions.[11] Besides, in 2018 world consumed 36.4

million metric tons of lubricants of which, 50% been used as engine lubricants.[12] From that 50%, one third of engine oil was lost during engine running for many reasons, thus 65 to 68% was end up as waste crank case oil.[13] Waste crankcase oil is highly hazardous with many toxic materials including metals and heavy metals; Pb, Zn, Cu, Cr, Ni, Cd, Mo, and polynuclear aromatic hydrocarbons (PAH), which are known to be carcinogenic and mutagenic, for example; benzo(α)pyrene. Thus, waste crank case oil is dangerous to health, the environment and is hardly biodegradable.[13] Therefore, a significant environmental concern, require specific disposal processes.[13] Presently, using as an auxiliary fuel, asphalt, or bitumen production for road constructions etc., albeit, bulk quantities still disposed in landfills, causing severe impact to live organisms.[13]

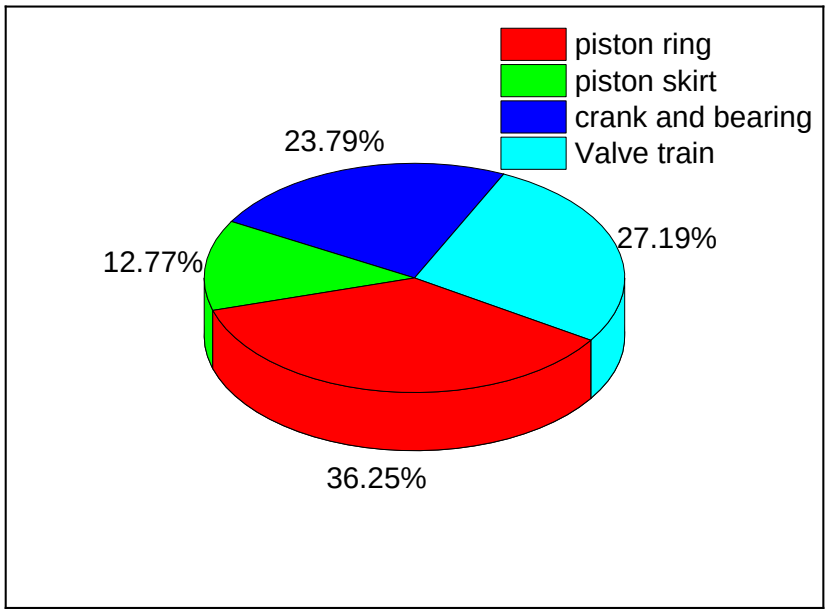

Figure 1. 1, Frictional losses within an internal combustion engine[10]

In the latest research, nanoparticles are considered to be a promising solution to improve the efficiency of ICE lubrication because of their ultrafine size, allowing them to infiltrate between asperity contacts of the surfaces in relative motion. This scale-dependent behavior,[9, 14] gives an added advantage to roll between sliding surfaces in addition to the ability to create boundary layer, because of their adhesion and cohesion properties; under Fired Top Dead Centre (FTDC) condition when combustion occurs,[15] this behavior will help to elevate the lubricant characteristics. However, agglomeration and sedimentation of nanoparticles within mineral base oil over extended period of storage time has been reported by many

researchers.[8, 9, 17] It is the barrier to overcome the appreciation of nanoparticles as engine lubricant additives to enhance ICE performance in addition to the commercial constrains.

Furthermore, according to the United Kingdom Lubricant Association, annual global lubricant consumption is approximately 40 million metric tons, [12, 16] of which 90% could be substituted with bio-based lubricants.[16] Bio-lubricants are a combination of triglycerides and fatty acids, viably available around the globe with various qualities according to the geographical location. Examples include palm oil, corn oil, coconut oil, cotton seed oil, rapeseed oil, sunflower oil, safflower oil, olive oil and many more. In-addition to their lubricity capabilities, bio-lubricants are biodegradable. Biodegrading is an ecological process; breakdown of organic elements by microorganisms with the presence of oxygen, nitrogen, and minerals.[17, 19] Along with low toxicity, high viscosity index (VI), low oxidation and are obtained from renewable sources. However, bio-lubricants, also typically exhibit high pour point; the lowest temperature at which a fluid (lubricant) loses its free-flowing qualities, thus wax formation at low temperatures and poor oxidative stability are possible negative characteristics, which needs to be improved for the application of ICE lubrication.[17, 18, 19]

1.2 The Research Aim

In view of the above, solutions to the contemporary ICE lubrication are a fundamental requisite, thus the aim of this research is to investigate the tribological behavior of various lubricants on ICE components. Particular emphasis will be placed on the piston ring cylinder liner interface, where the use of nanoparticles as engine oil additives with mineral and bio-based sample formulations will be compared with the performance of a conventional mineral-based lubricant. The ambition is to identify the optimal engine oil formulation which reduces friction and wear, hence, to improve fuel economy with reduced emissions. It therefore follows that optimizing the ICE performance, saves energy and reduces the depletion of fossil fuels and mineral reserves for a stable and sustainable environment.

1.3 Objectives

The objectives of this research are as follows.

1) Identify the factors which influence the homogenous suspension of nanoparticles within mineral and bio base stocks.
2) Produce stable, homogeneous blends of nanoparticles and mineral and bio-based lubricants with storage time before nanoparticle agglomeration and sedimentation.
3) Investigate the tribological effects on ICE components to enhance engine performance by reducing friction and wear with the application of sample lubricant formulations containing mineral and bio base-stocks blended with different nanomaterials as additives in various concentrations.
4) Suggest an optimal lubricant formulation for use in an ICE.

1.4 Methodology in brief

Inspiration is to develop an engine lubricant to enhance its performance to save energy with extended component life. Hence, different kinds of lubricant samples were blended using mineral oil and coconut oil as base stocks with various nanoparticles in different weight concentrations as additives. There are three groups of blends: a) mineral oil with nanoparticles, b) mineral oil with coconut oil and c) coconut oil with nanoparticles. Initially all the blends were tested for friction force (FF) and coefficient of friction (COF) using linear reciprocating tribometer (LRT) test rig with piston ring and cylinder liner pieces as test samples. The design is to simulate real time ICE operation, which is very challenging to achieve. From the Phase-1 LRT tests, the best additive concentration from each nanoparticle group either with mineral or bio-base stock to reduce friction was selected for Phase-II LRT tests. Phase-II LRT tests were done with two variables; 1) varying load and 2) varying velocity at a constant (elevated) temperature (140 °C) to study the tribological behavior of selected blends under extreme pressure (EP) and temperature conditions. Thereafter, all the wear scars of test specimens; cylinder liner and piston ring segments were tested with SEM, EDX, and 3D noncontact profilometry for wear scar analysis and compared with unused piston ring and cylinder liner surfaces without tribometer tests. In-addition, physicochemical properties of all selected blends were tested and evaluated to study the lubricant life and required other qualities. Simultaneously, UV-vis spectrophotometry was performed on

selected sample blends for a period of five weeks, starting from 0 hours to 72 hours in 24-hour intervals and at weekly intervals up to 5 weeks to study the stability of selected lubricant samples over shelf life/ storage time.

Further screening was done after Phase-II LRT tests to select sample blends, which could withstand the harsh operating conditions similar to an ICE. The selected samples were blended again with formulated coconut oil (FCO) and tested under Phase-III test protocol. Samples with enhanced tribological performance were selected then and utilized to run a real industrial engine for a period of standard one oil change recommended by the manufacture. In this case it is 100 hours to evaluate the fuel consumption and exhaust emissions followed by used oil sample monitoring tests to observe the physicochemical properties, remaining lubricant life, hazardous substance, or particle content for recommendations for final formulation.

Besides, with the development of the project, nanoparticles were synthesized and characterized with Fourier-transform infrared spectroscopy (FT-IR), Raman analyses, transmission electron microscopy (TEM), x-ray powder diffraction (XRD), and x-ray photoelectron spectroscopy (XPS) for verification and to understand the characteristics of selected nanomaterials.

Moreover, many pour point depressants (PPD) were added in different weight concentrations to improve pour cold flow behavior of coconut oil and the results were analyzed via differential scanning calorimetry (DSC) and conventional ASTM D97-96A tests. Thereafter, the combination of coconut oil with best PPD concentration was added with various weight concentrations of dissimilar antioxidants, viscosity modifiers, and alkalinity improvers to enhance required characteristics of coconut oil, followed by physicochemical property analyses for appraisal.

This is an outline of experimental methodology which is elaborated within Chapter 3 in detail.

1.5 Layout of the thesis

Henceforward, the following Chapters will establish the reminder of this thesis followed by the references with Chapter 8, containing evidence incorporated within the report and if necessary, appendices containing other pertinent details of the study.

Chapter 2 – Literature review: This Chapter is split into 3 sections; thus, Section 1 is exploring basic operation of ICE with underpinning engineering hypothesis effecting the lubrication. Specifically, the piston ring cylinder liner interface during reciprocating strokes with three lubricating regimes called boundary, mixed and elastohydrodynamic lubrication. The required minimum lubricant film thickness to keep sliding asperities apart and the characteristics of lubricant effecting the minimum film thickness. In addition, reviews the contemporary engine lubricants for their functionalities, constituents, and thus other effects to the environment.

Section 2 is scrutinizing properties, characteristics and functionalities of nanoparticles while reviewing previous research for the application of nanoparticles as lubricant additives.

Section 3 elucidates structures, thus physicochemical properties of bio-lubricants, especially the lubricating behavior of coconut oil, advantages, and disadvantages, therefore, reviewing literature for a remedy to improve observed substandard of coconut oil as a lubricant.

Chapter 3 – Research methodology: All the tests and experiments involved with this study are elaborated in detail as outlined in Section 1.5.

Chapter 4 – Material characterization: The exploration and discussion of test results begins with this Chapter. There are two segments in part I. In the first segment the data observed through various experiments for nanoparticle characterization are scrutinized. The next segment is for the improvement of observed substandard of coconut oil thus findings from proposed experiments are presented and discussed. In-addition, the results observed through the experiments performed for the absorbance, thus colloidal stability of sample blends are presented, which are with mineral oil and coconut oil base stocks having various nanoparticles as additives.

Chapter 5 – Tribological analysis on formulated nano/bio lubricants: Findings from all friction tests, and wear scar analyses of test specimens of sample blends are presented in this Chapter.

Chapter 6 – Field performance tests: This Chapter elucidates the field test observations on selected blends after laboratory friction tests. Here the improvements achieved on fuel consumption, exhaust emissions, wear metal and hazardous material observed through

sample monitoring tests are examined, including physicochemical property analysis to investigate lubricant life.

Chapter 7 – Conclusions and future works: This chapter concludes the thesis by summarizing observations and discussions presented in chapters 4, 5 and 6 along with suggestions regarding how to formulate the most desirable engine lubricant. Furthermore, future works and published papers arising from this work are presented herein.

2. Chapter 2: Literature review

2.1 Principles of internal combustion Engine (ICE) operation

ICEs are heat engines that transfer chemical energy via a combustion process to mechanical or kinetic energy. There are numerous applications of ICEs which are generally used to enhance the quality of human life. There are four main categories of ICEs in use, which differs on the ignition process and duty cycle or power cycle of the engine, such as spark ignition (SI) or compression ignition (CI) according to the fuel used, and the power cycle; two-stroke or four-stroke configurations. However, the most used are four stroke gasoline or SI engines for passenger cars and four stroke diesel or CI engines for heavy transport and industrial purposes. There are numerous components within an ICE, including, piston with rings, cylinder liner or cylinder block, crank shaft, connecting rods, flywheel, cam shaft, inlet and exhaust valves, fuel injector (for diesel engines and spark plug in case of gasoline engines) and cylinder head. The piston and rings assembly is the fundamental constituent, which makes the critical link with the crank shaft to convert thermal energy to mechanical energy (Figure 2.1a).

In a standard configuration, the piston assembly, which reciprocates back and forth (up and down depending on the orientation of the piston assembly) inside the cylinder bore is connected to the crank shaft via a connecting rod. This assembly creates a cranking mechanism whereby the crank revolves around its axis. This displacement of the piston from the top to the bottom of the cylinder bore or liner is called a stroke. The stroke length is equivalent to a half turn or 180° rotation of the crank shaft. Both top and bottom displacement ends of a cylinder bore of an ICE where piston terminates its reciprocating motion (i.e., the stroke) are known as Top Dead Centre (TDC) and Bottom Dead Centre (BDC) respectively, as illustrated in Figure 2.1b. Therefore, during a four-stroke cycle, the piston assembly needs to travel up and down (or back and forth) twice, inside the bore for one power cycle, causing the crank shaft or engine to rotate two revolutions or 720° during the same time slot. The thrust created after the fuel ignition forces the piston assembly downward, thus causing the crank shaft to rotate with the flywheel, which is fitted to one end of the crank shaft (mostly rear end). With the rotation, the flywheel will absorb any excess energy created during power strokes by the fuel combustion thrust as a moment of inertia or torque to keep flywheel/engine

rotating during other three strokes to continue piston assembly sliding for uninterrupted engine running, thus continuous kinetic energy supply for desired end application.

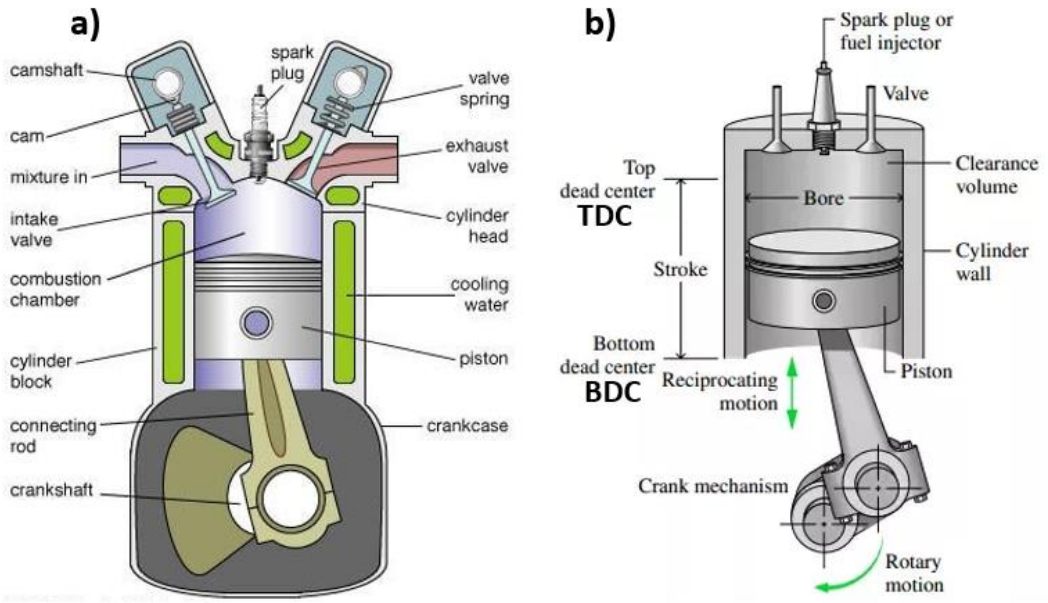

Figure 2. 1, Typical schematic illustration of an ICE, a) basic components b) TDC and BDC where piston terminates its reciprocating stroke.[20, 21]

Figure 2.2 exemplifies the four strokes of a diesel engine, which are named as 1) suction or intake, 2) compression, 3) power or expansion 4) exhaust. Their functions are as follows:

1) **Suction stroke:** Is the beginning of a power cycle where piston assembly starts sliding downward from TDC with the inlet valve open. This allows air to flow in the cylinder bore, until the piston reaches BDC, where suction stroke terminates with air filled cylinder bore.

2) **Compression stroke:** When piston reaches BDC, ending the suction stroke, it begins return stroke upward with both inlet and exhaust valves closed. Thus, compressing the air trapped inside the bore until piston arrives at TDC, while achieving desired pressure. Referring to the combined gas law (Eq. 2.1), it is obvious that the highly pressurized air will reach higher pressures and temperatures, enabling injected atomized high temperature diesel molecules to ignite spontaneously at the end of the compression stroke.

The combined gas law: $$\frac{P_1V_1}{T_1} = \frac{P_2V_2}{T_2} = K \qquad (2.1)$$

Where P_1, V_1 and T_1 represent the initial pressure, volume, and temperature, and P_2, V_2, and T_2 are for the new or final pressure, volume, and temperature respectively. K is a constant.

3) **Power stroke:** The thrust propagated with the impulsive ignition of diesel fuel at the end of the compression stroke forces the piston down. Although, before it reaches BDC, the exhaust valve start opening and is kept it fully open when piston reaches at BDC causing exhaust blowdown due to pressure drop inside the cylinder.

4) **Exhaust stroke:** At the end of the power stroke the piston returns to TDC with the exhaust valve open causing exhaust gases to exhale. Some exhaust gases may remain and mix with the next air intake. To prevent this mix of gases the inlet valve will open before the piston reaches the TDC and the exhaust valve will close after the TDC. This valve overlapping process will allow some of the intake air to push those remaining exhaust fumes out of the combustion chamber.

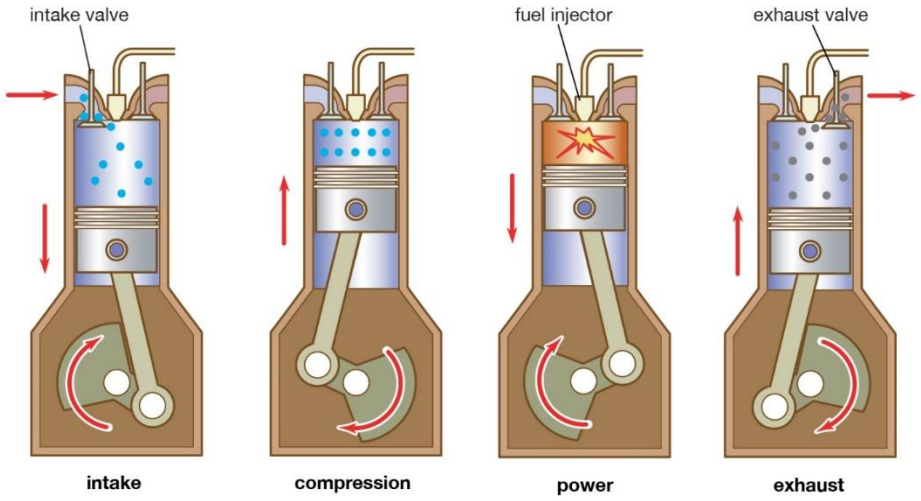

Figure 2. 2, Typical sequence of the operation in a power cycle of a four-stroke diesel engine[2] [2]

The valve and fuel timing within a power cycle or 720° of crank rotation plays the fundamental role for the four-stroke functioning, which will vary with the engine design according to the manufacturers. Nevertheless, it is obvious that the piston ring pack (PRP) has a crucial role in preventing gas leaks from combustion chamber to crank case throughout all four strokes while sliding.[5-7] This is to achieve the designed gas compression ratio or gas pressure inside the combustion chamber at the end of the compression stroke for an enhanced combustion process, leading for maximum thermal efficiency, thus for efficient engine performance. Also, this sealing of combustion chamber by PRP will prevent excessive lubricant from passing into combustion chamber through this path. Hence, this minimizes engine oil consumption, deterring excessive hazardous emissions including particulates,

NO_x, greenhouse gases and other air pollutants.[23, 24,25] And as a secondary role of PRP to transfer heat absorbed by the piston during fuel combustion while sliding. This is via the lubricant film between PRP and cylinder wall through to the engine coolant.[24] Thus, reducing friction by decreasing temperature of the combustion chamber and associated elements.[5] All above functionalities of PRP will be appreciated by tightly conforming into their grooves situated in the top of the piston (piston crown) and to the cylinder wall as illustrated in Figure 2.3, which will generate high friction between piston ring and cylinder wall. Thus, require a lubricant with minimum film thickness capable of reducing friction under all lubrication regimes, along with ability to transfer heat generated during combustion.[25] In this case piston ring contact face profile considerably affects the entrainment of lubricants to the piston ring cylinder liner interface.[25] Besides, piston skirt; the bottom part below the ring grooves is vital for transmitting transvers forces to the cylinder wall, also through lubricant film in between. Presumably, the complex piston secondary moment because of the forces acting on piston during strokes, clearance between piston skirt and cylinder wall thus tilting of piston from wrist pin axis may have caused the transfer of transverse forces, in-addition to the twisting of piston rings in the ring groove (Fig. 2.3). Considering this ring twist or piston secondary moment, Morris et al.,[23] suggested for center shift of compression ring's face profile as illustrated in Figure 2.4, which will affect to inlet wedge effect thus increase of lubricant entrainment leading to augmentation of lubricant film thickness, load carrying capacity, subsequently alter the counter face asperity interactions and boundary friction.[23]

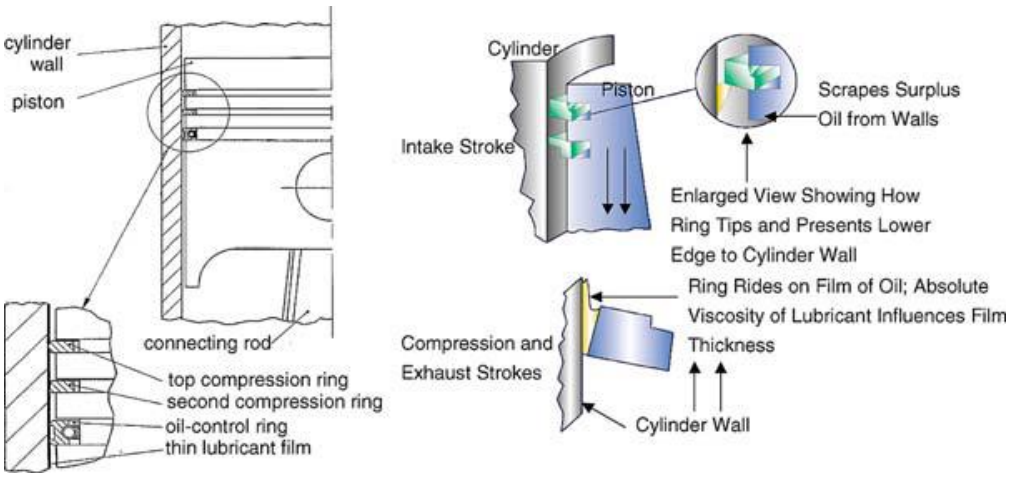

Figure 2. 3, Functions of a piston ring assembly of an ICE,[5]

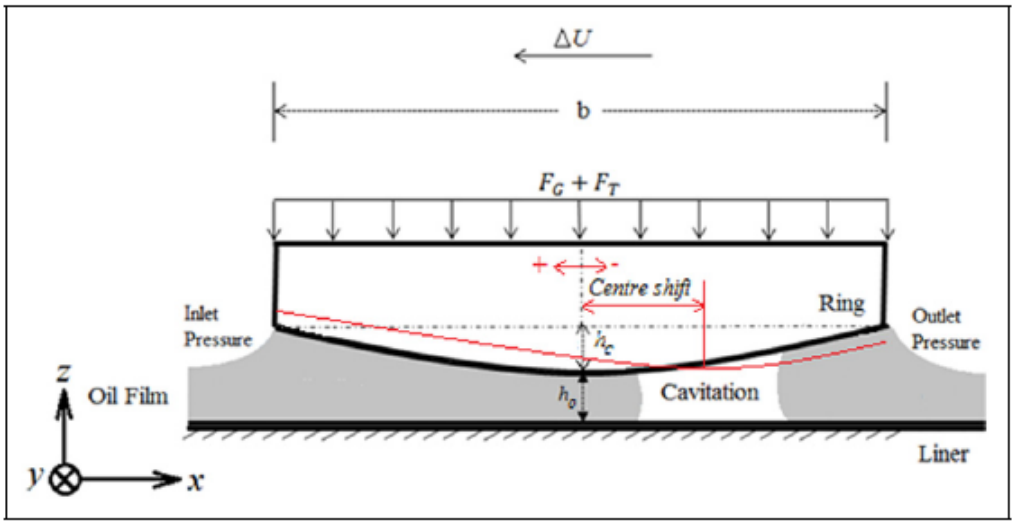

Figure 2. 4, Profile of a piston ring running surface, illustrating the increase of lubricant entrainment because of the center shift of ring's face profile.[23]

2.1.1 Tribology within an ICE

History of tribology goes back to the era of Pharaoh's of Egypt, where traces of animal oil were found in wheel hubs presumably used for lubrication.[26, 27] There are numerous mechanical parts or assemblies within an ICE; pistons with rings, cylinder liners, connecting rods, crank shaft, cam shafts, gear terrains, valve mechanisms, bearings, pulleys are a few to mention (Fig. 2.1), which need lubrication to reduce friction and wear, for a longer component life to save energy, all will contribute to the sustainability of the environment. Nevertheless, piston ring and cylinder liner mechanism are the fundamental contributors to friction and wear within an engine with 40-50% of total frictional losses,[8, 9, 10] where the lubrication is most needed. When a piston functioning inside a cylinder bore (with its reciprocating motion from TDC to BDC), it requires a lubrication film or a fluid layer to separate sliding surfaces throughout its stroke length with the necessary load carrying capacity to reduce friction, and wear, thus, protect the surfaces in their relative motion. However, the sliding motion (linear velocity) of a piston ring assembly is not unique. There is a decelerating towards zero velocity at the TDC and BDC, thus causing different lubricating regimes (see Section 2.1.3) during one stroke. These regimes are classified as boundary lubrication (BL), mixed lubrication (ML) and elastohydrodynamic lubrication (EHL) regimes. The zero sliding velocity will create boundary or mixed lubrication at TDC or BDC. In contrast, EHL will occur during mid-stroke region where the maximum sliding

velocity occurs during the stroke. Therefore, all depend on the qualities of the surfaces in relative motion including surface roughness, and surface hardness, i.e., the deformability of surface asperities. In addition, rheological properties of the lubricant should be suitable for maintaining a separation of the asperities of piston ring cylinder liner interface to enhance engine performance under fired condition with varying high temperatures, high pressures and load capacities or operating condition.[27,28]

2.1.2 Physiochemical properties of a lubricant

In addition to density, the resistance to flow is the principal characteristic of a lubricant and is determined by its dynamic viscosity. Also, the kinematic viscosity (which incorporates density), viscosity index (VI), total base number (TBN), total acid number (TAN), pour point (PP), flash point (FP), oxidation resistance, shear stability, and thermal conductivity, all are essential properties of a lubricant.[28, 29] Most of these properties will be temperature dependent, and in some cases pressure-dependent also. These characteristics will be briefly defined below with reference to their significance within a lubricant.

According to Newton's viscosity law, the shear stress between laminarly flowing fluid layers is proportional to the velocity gradients between the two layers (Figure; 2.5).

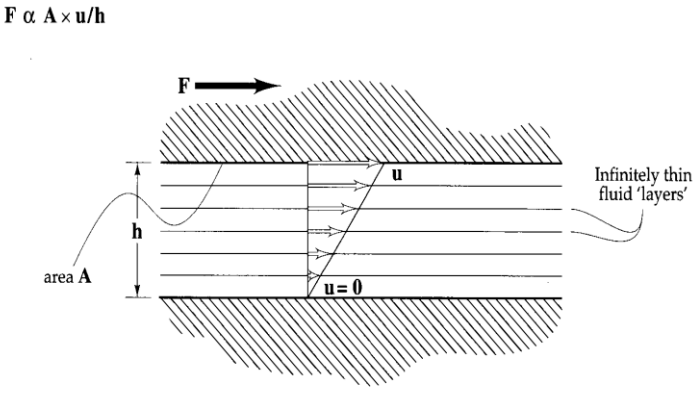

Figure 2. 5, Typical illustration of fluid layers separating two surfaces at proximity.[28]

Therefore, shear stress; $\boldsymbol{\tau} = \frac{\boldsymbol{F}}{\boldsymbol{A}} = \boldsymbol{\eta}\left(\frac{\boldsymbol{u}}{\boldsymbol{h}}\right)$ (2.2)

Where $\boldsymbol{\eta}$ - dynamic viscosity, $\boldsymbol{\tau}$ - shear stress, $\frac{\boldsymbol{u}}{\boldsymbol{h}}$ - velocity gradient between two layers in relative motion, $\boldsymbol{h}$ – thickness of fluid layer, $\boldsymbol{u}$ – velocity of fluid layer

Ratio of dynamic viscosity to fluid density is defined as the kinematic viscosity.

i.e., kinematic viscosity; $\boldsymbol{\upsilon} = \frac{\boldsymbol{\eta}}{\boldsymbol{\rho}}$ (2.3)

Where, $\boldsymbol{\rho}$ = fluid density

VI is defined as the fluid's resistance to viscosity variation with the change of fluid temperature. Thus, this is a vital parameter with an engine oil to have higher VI lubricants in order to gain less viscosity variation within ICE operation. VI is a comparison of kinematic viscosity of the oil of interest with two reference oils having 0 and 100 VI at 37.8 $^{\circ}$C and have the same kinematic viscosity at 98.9 $^{\circ}$C. Hence VI is an empirical value without units.[28]

TBN is the quantity of alkaline substance in oil; a measure of potassium hydroxide (KOH) milligrams required to neutralize alkalinity of one gram of oil. Likewise, **TAN** is the quantity of KOH milligrams required to neutralize acidity of one gram of oil. Both TAN and TBN are commonly termed as **Neutralization number** is a deciding factor and for determining the oil life or oil change interval.

PP is the lowest temperature, at which the lubricant loses its free flow characteristics. Cold flow is also an extremely significant parameter for an automobile lubricant, which needs to be functioned in varying temperatures, extreme cold to very worm ambient conditions worldwide. Vapor igniting temperature of a lubricant is defined as **FP,** thus**,** is very important stricture from the safety perspective to have a higher FP than operating temperature of an ICE.

Oxidation is a sequence of complex reactions because of molecule breakdown or rearrangement, which varies with the elemental integration of a lubricant causing sludge, soot, varnish, or emulsion formation and depositing on engine components, besides oxidation causing formation of acidic compounds hence corrosion leading to surface damage or excessive wear of components.

Shear stability is a key attribute, a measure of resistance to change in viscosity of a fluid under mechanical stress or shear. The reduction of viscosity under mechanical stress or load is termed as shear thinning and the fluid is called non-Newtonian fluid. In contrast Newtonian fluids have constant viscosity with changing of shear rate.[28, 30] Moreover, it is presumed that the fluids with plain molecular structures, that are not affected by shearing action are having Newtonian behavior, examples include water, benzene, glycerol. In contrast, non-Newtonian

behavior comes with the complexity of the molecular structure of the liquid. However, non-Newtonian behavior, which affects for shear thinning and shear thickening because of microscale structural changes; phase separation or disentanglement of molecular chains are widely regarded.[27, 28, 30] Pseudoplasticity and thixotropy, which refer to a decrease in viscosity with increased stress and the duration of stress have been used to reduce viscosity respectively.[28]

Thermal conductivity is directly associated with the temperature variance, affected by the polarity and hydrogen bonding of the molecules.[28] This is an important characteristic of a lubricant to transfer the heat generated between surfaces in relative motion to reduce friction. Also, the temperature and pressure dependence of fluid viscosity is very important in engine lubrication. Fluid viscosity increases with increasing operating pressures. In contrast fluid viscosity falls with increasing operating temperatures.

There are several assumptions for viscosity-temperature relationship, albeit, Reynolds, Slotte, Walther and Vogel equations are the commonly used among many. Besides, Vogel's equation is regarded as the most accurate for engineering calculations. One of the widely used American Standard for Testing and Materials (ASTM) chart for viscosity temperature relationship is based on Walther's equation.[28]

Vogel's equation; $\boldsymbol{\eta = ae^{b/(T-c)}}$ (2.4)

Walther's equation; $\boldsymbol{(v + a) = bd^{1/T^c}}$ (2.5)

Where, $\boldsymbol{a}$, $\boldsymbol{b}$, $\boldsymbol{c}$ and $\boldsymbol{d}$ are constants and $\boldsymbol{T}$ - absolute temperature.[28]

Lubricant viscosity is increasing with the increase of operating pressure and this effect is larger than the one obtained by changing operating temperature. Increasing viscosity with operating pressure will help to create thicker lubricant film and to separate asperities of surfaces in relative motion, nevertheless, high viscosity will increase the shear stress between fluid layers, increasing viscose drag, influencing more friction and heat generation between sliding surfaces. There are many assumptions in the literature for viscosity pressure relationships, some are good for specific fluids and not accurate for others. For instance, Barus equation is widely used for viscosity pressure relationship at moderate pressures close to atmospheric, albeit proved to be erotic at high pressures above 0.5 GPa.[28] The maximum

pressure inside a combustion chamber of an ICE may reach 500 bars maximum,[31, 32] thus well below the margin given above.

Barus equation: $\boldsymbol{\eta_p = \eta_o\, e^{\alpha P}}$ (2.6)

Where $\boldsymbol{\eta_p}$ **-** Viscosity at pressure P, $\boldsymbol{\eta_o}$ – Viscosity at atmospheric pressure, $\boldsymbol{\alpha}$ **-** Pressure–Viscosity coefficient and, ***P*** **-** Pressure of interest.

Shear stability of a lubricant is depending on the flow behavior or rheological behavior (change of viscosity) of that fluid under mechanical stress or shear, as discussed under the subheading "Shear stability" (page 14).

2.1.3 Lubrication regimes

With regards to the mode of lubrication, three distinct situations can be perceived with increasing loads on contacting surfaces, which are called lubrication regimes. Namely, elastohydrodynamic, boundary and mixed lubrication regimes.[27] Typical asperity contacts during these lubrication regimes are illustrated in Figure 2.6. Elastohydrodynamic lubrication (EHL) could occur because of high pressure and temperature generation during sliding of the piston within the duty cycle of an engine. Here the properties of lubricant play a vital role in creating fluid layer with required minimum film thickness to keep the asperities apart (Fig, 2.6c). Maximum EHL will take place with maximum sliding velocity if the load is constant, thus decreases towards TDC and BDC with the piston stroke where the velocity is absolute zero. This area is called boundary lubrication (BL) regime, where no hydrodynamic pressure to separate asperities (Fig. 2.6a). At this juncture the lubricant additives will portray an imperative role to create BL film with their adhesion and cohesion abilities to avoid asperities in contact. Maximum EHL befalls with the maximum sliding velocity and decreases with decreasing velocity towards TDC or BDC. Mixed lubrication (ML) happens with the decreasing velocity when piston reaching at TDC or BDC with mixed results, because the generated lubricating film thickness may be inadequate to separate surfaces completely (Fig. 2.6b).

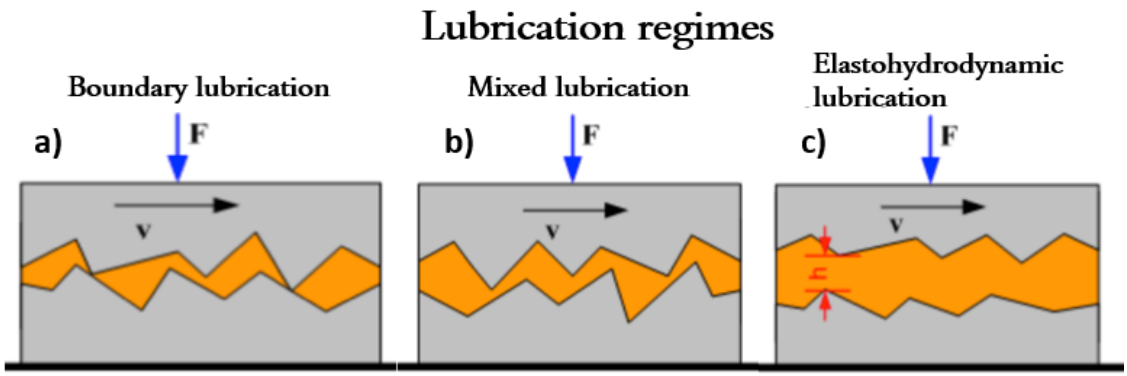

Figure 2. 6, Typical illustration of lubrication regimes, a) asperities contacting, b) asperities not in contact, c) asperities deformation due to fluid pressure.[33]

2.1.3.1 Elastohydrodynamic lubrication (EHL)

Increase of viscosity and elastic deformation of surfaces under extreme pressure and hydrodynamics plays fundamental roles within the EHL mechanism. Therefore, ambient viscosity, operating temperature and pressure, pressure viscosity coefficient, thermal conductivity, surface tension, surface contact area, flash and surface conjunction temperature, reduced radius, contact load, Young's modulus, lubricant film thickness, surface hardness, surface roughness, reciprocating surface velocity, all are essential factors effecting this lubrication regime.[34, 35] Beauchamp Tower and Osborne Reynolds are the champions who pioneered the scientific understanding of hydrodynamic lubrication, albeit Grubin and Ertel[35] are the first to publish realistic approximation for EHL film thickness calculation. The ability of lubricant viscosity to create a film layer thick enough to separate the asperities apart of both surfaces in proximity, which are with relative motion, to reduce the friction and wear under these elevated temperature and pressure conditions (*ca* 80 – 100 °C and *ca* 1.5 – 2.5 MPa with instantaneous temperature ≈ 500 °C and instantaneous pressure up to ≈ 50 MPa during the instant of ignition/combustion) with elastic deformation is crucial in this lubrication system. (Also, the operating temperature and pressure will vary with the design factors like aspiration; natural, supercharge, turbocharge, after/inter cool and likes.)[5, 6, 23, 30]

Leeuwen,[36] compared 11 equations for lubrication film thickness calculation from literature and highlighted the importance of pressure viscosity coefficient (α) of the subject

fluid. According to the Leeuwen's analysis, most suitable approximation formula for central film thickness in EHL circular contacts is from Chittenden, et al.,[36] with close results from Hamrock, Higginson, and Dowson formulas for all type of contacts; inclusive of central, linear or elliptical contact surfaces. Solving Reynolds equation mathematically and adapting power formulas is the standard methodology for examining characteristics of EHL lubrication to ascertain numerous parameters within the system. Reynolds one dimensional equation; the origin of the EHL film thickness (Eq. 2.7) and widely used Hamrock and Dowson formula for all types of contact (Eq. 2.8) are as follows.[27, 35, 36]

$$\frac{dp}{dx} = 6u\eta\left(\frac{h-\hat{h}}{h^3}\right) \tag{2.7}$$

Where; p - Hydrodynamic pressure, u – Entraining surface velocity, η - Lubricant viscosity, h - Film thickness, $\hat{h}$ - Film thickness where the pressure gradient is zero and x - Distance in the direction of motion.

$$\frac{h_0}{R_r} = 3.63\left(\frac{u\eta_0}{E_c R_r}\right)^{0.67}(\alpha E_c)^{0.53}\left(\frac{W}{E_c R_r}\right)^{-0.067}(1-0.61e^{-0.73K}) \tag{2.8}$$

Where, h_0 – minimum film thickness, R_r – Reduced radius, E_c – Reduced elastic modulus, W – Contact load and α, η_o, and u are defined by the equations (2.6) and (2.7).

u, is defined as;[27, 35]

$$u = \left(\frac{u_A+u_B}{2}\right) \tag{2.9}$$

where the subscripts A and B denote the surfaces in relative motion, thus u_A and u_B represent the velocities of surfaces A and B respectively. However, in cylinder liner and piston ring mechanism within an ICE, piston ring reciprocates, and cylinder liner remains station. In such a situation $u = \frac{u_A}{2}$, where u_A refers to the sliding velocity of the piston ring.

E_c, is defined as;[35]

$$\frac{1}{E_c} = \frac{1}{2}\left(\frac{1-v_A^2}{E_A} + \frac{1-v_B^2}{E_B}\right) \tag{2.10}$$

Where v_A and v_B are the Poisson's ratio of the surfaces A and B in relative motion and E_A and E_B are the elastic modulus of the same surfaces A and B respectively.[27, 35]

The definition of reduced radius $\boldsymbol{R_r}$ will vary with the geometry of the contact area of the surfaces in contact. Assuming that, the piston ring running surface is having a convex profile, the geometry of the contact area of a piston ring and cylinder liner mechanism of an ICE will be elliptical, similar to a geometry of a convex and concave surfaces in contact as illustrated in Figure 2.7.

In that case $\boldsymbol{R_r}$ could be defined as;[35]

$$\frac{\mathbf{1}}{\boldsymbol{R_r}} = \frac{\mathbf{1}}{\boldsymbol{R_x}} + \frac{\mathbf{1}}{\boldsymbol{Ry}} = \frac{\mathbf{1}}{\boldsymbol{R_{ax}}} - \frac{\mathbf{1}}{\boldsymbol{R_{bx}}} + \frac{\mathbf{1}}{\boldsymbol{R_{ay}}} - \frac{\mathbf{1}}{\boldsymbol{R_{by}}} \tag{2.11}$$

Where:

$\boldsymbol{R_x}$ – Reduced radius of the curvature in x direction

$\boldsymbol{R_y}$ – Reduced radius of the curvature in y direction

$\boldsymbol{R_{ax}}$ – Radius of curvature of body 'A' in the x direction

$\boldsymbol{R_{ay}}$ – Radius of curvature of 'A' in the y direction

$\boldsymbol{R_{bx}}$ – Radius of curvature of body 'B' in the x direction

$\boldsymbol{R_{by}}$ – Radius of curvature of body 'B' in the y direction

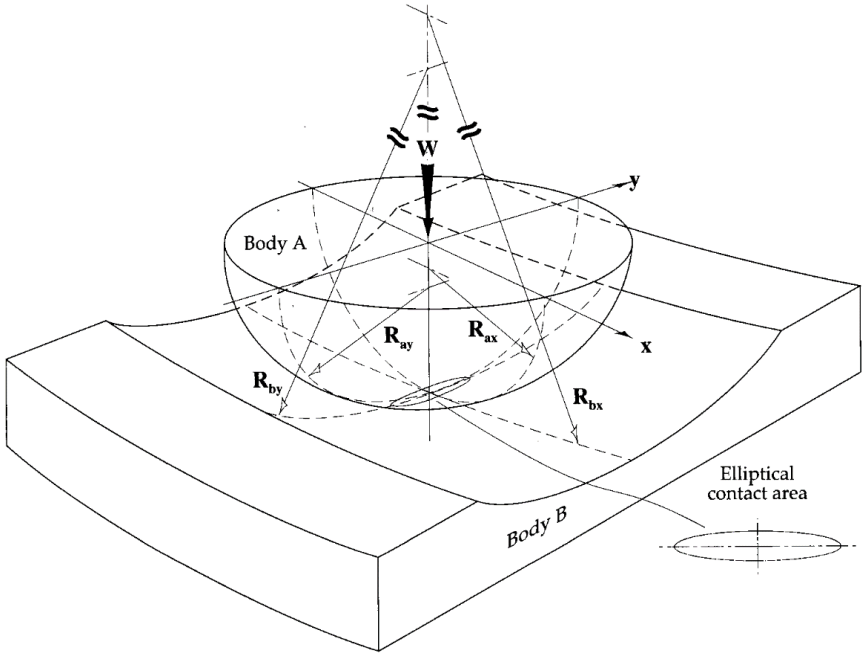

Figure 2. 7, Typical geometry of two bodies in contact with a convex and concave surface.[35]

In this research, friction (tribometer) experiments were performed using piston ring and cylinder liner segments as test specimens. Thus, with cylinder liner, piston ring mechanism,

piston ring and cylinder liner diameters should be equal or almost equal to prevent compression leaks to the crank case for optimum engine performance. Also, for the X direction, cylinder liner is having straight line similar to plane surface, hence $\boldsymbol{R_{bx} = \infty}$,

Therefore, $\boldsymbol{R_r = R_{ax}}$ (2.12)

From the Equation 2.12, the reduced radius $\boldsymbol{R_r}$ is approximately equal to the outer curvature of the piston ring running profile, which could be measured through optical profilometry if required for necessary calculations.

Besides, the Equation 2.8 can be subdivided in four dimensionless groups such as, speed, material, load, and contact parameters thus, could be simplified with non-dimensional parameters for easy reference as follows:

$$\boldsymbol{H = 3.63\, U^{0.67} G^{0.53}\, W^{-0.067}\, K} \quad (2.13)$$

Where dimensionless film parameter $\boldsymbol{H = \frac{h_0}{R_r}}$

dimensionless speed parameter $\boldsymbol{U = \left(\frac{U\eta_0}{E_c R_r}\right)}$

dimensionless material parameter $\boldsymbol{G = (\alpha E_c)}$

dimensionless load parameter $\boldsymbol{W = \left(\frac{W}{E_c R_r}\right)}$

dimensionless contact parameter $\boldsymbol{K = (1 - 0.61 e^{-0.73K})}$

From the Equation 2.13 it is evident that the speed, material and contact parameters have higher effect on film parameter, than the load parameter "$\boldsymbol{W}$", which does not have a strong impact on film thickness with the term "$\boldsymbol{W^{-0.067}}$" (Eq. 2.13). Relative motion of adjacent surfaces, which induces fluid pressure, initiates EHL film between surfaces in motion, thus with the increase of speed increases the fluid pressure with maximum fluid film in between to keep the loaded surfaces apart.[37] Figure 2.8, indicates the typical changes of fluid viscosity at EHL, showing swift escalation with the entry of lubricant to the contact, trailed by steep deterioration of viscosity levels at the exit. To compensate this viscosity slump, constriction is formed at the exit where minimum film thickness ($\boldsymbol{h_0}$) is found, which is very important for asperity separation and lubrication, otherwise central film thickness ($\boldsymbol{h_c}$) will maintain the interaction of opposing surfaces. This sharp pressure disparities at the entry and exit of contacts along the asperities strongly depends on the pressure viscosity characteristics of the

subject lubricant. In-addition, all parameters; ***U***, ***G***, ***W*** and ***K*** are correlated with each other. For example, the elastic modulus E_c is present in three parameters; speed, material and load, thus all physicochemical properties, characteristics of lubricant and surfaces in relative motion are vital for creation of lubrication film to inhibit asperity interactions.[37, 38]

Nevertheless, pressure-viscosity coefficient (α) which defines the relationship between variation of viscosity with changing pressure (Eq. 2.6) is the most important characteristics within this EHL film thickness calculation among other parameters,[36] which could be tested or calculated with the use of available test procedures or approximations.[38] There will be many diversities of blended lubricants involved with this project, thus α will vary with each sample lubricant and will be unknown, because sample lubricants will be custom made for the research. Thus, measuring lubrication film thickness with available technology is one solution to overcome the situation.

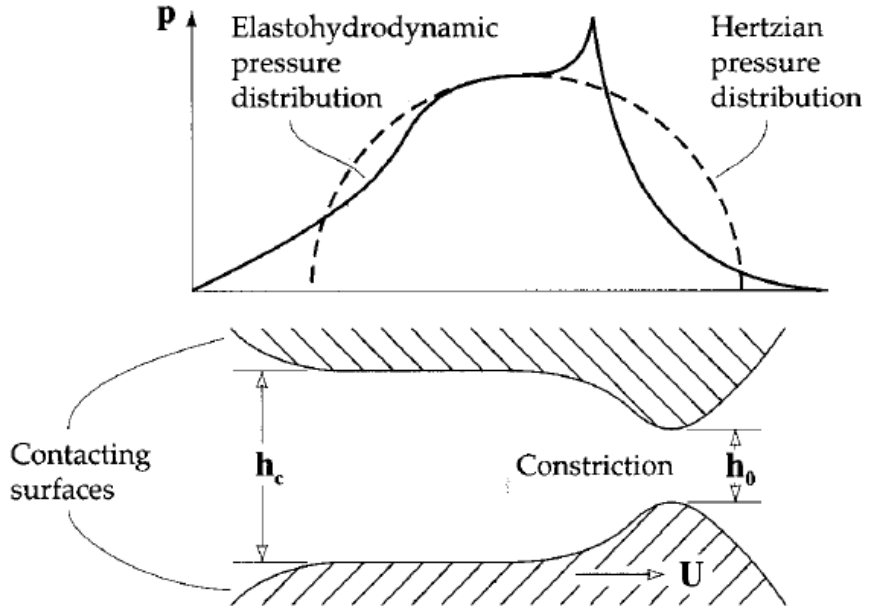

Figure 2. 8, Typical pressure distribution at EHL films[35]

2.1.3.2 Boundary lubrication (BL)

At the TDC in a fired engine, the lubrication of piston ring, cylinder liner interface is extremely complex with increased temperature, pressure, and load conditions where the fuel combustion occurs. With the oil starving due to the action of oil scraping ring and almost zero sliding velocity at TDC will create no lubricating film condition, resulting in no

separation between asperity contacts causing a scuffing state where lubrication is most needed under boundary lubrication.[39] This is an important challenge to overcome by modern-day engine lubrication.

The situation, where lubricants with additives having adhesive and cohesive properties play a major role to keep asperities apart to reduce friction, consequently for a lower COF. Material with high hardness and lower shear stress are required for a lower COF.[20] Because, in general terms, COF **"μ"** is defined as the proportion between frictional force **"F"** and applied load **"W"**, i.e.:

$$\mu = \frac{F}{W},$$

whereas $F = A_t \tau$

Where: F – frictional force (N), A_t – true contact area (m^2), τ – effective shear stress (Pa), and $W = A_t P_y$, thus, yield the approximation,

$$\mu = \frac{\tau}{P_y} \qquad (2.14)$$

where; P_y for plastic flow stress of the material; correlated to the indention hardness ($P_y \approx 3\sigma_y$'; σ_y is for the yield strength of the material [Pa]).[15, 27]

Except for special cases, hardness of a material (in this case P_y) is always proportional to the shear stress (τ), thus material with high hardness and low shear stress is an incompatible situation. Though, the lubricant's ability to create a thin layer with low shear stress on a sliding hard surface is the requirement at BL to reduce friction.[15] However, it is evident that the complex hydrocarbon structures of lubricants comprising linear molecules with polarity are more effective in forming protective layer. This will be achieved by aligning of polar heads of functional groups attached to the lubricant molecule structure on the opposing contacting surfaces, because of their attraction to the surfaces and repulsion at the other end of the molecule to keep asperities apart, for example carboxyl group (-COOH) of a fatty acid to attract substrate, while alkyl group (-R) to repel at the other end as illustrated in Figure 2.9, the mechanism which is known as boundary or adsorption lubrication.[15, 27] This boundary layer formation could be achieved by adding a surfactant if the lubricant molecules are constitute with inadequate functional groups.

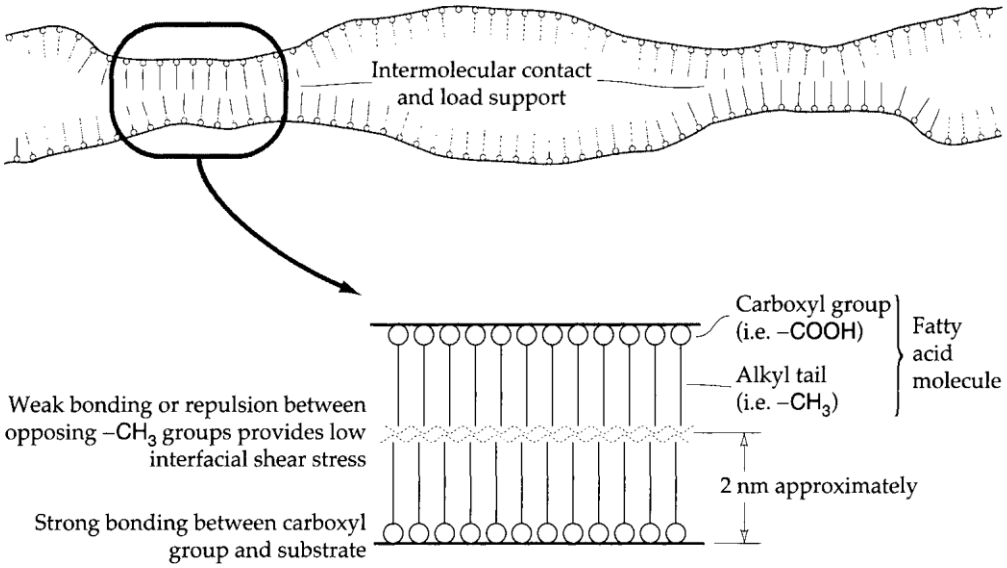

Figure 2. 9, Typical illustration of fatty acid polar molecules as adsorbed to create low friction mono molecular lubricant layer.[15]

Besides, linear molecular structure of a lubricant will enhance proper stacking on the substrate and longer chain length will induce combined intensity of feeble bonds between neighboring molecules to boost durability of the film as illustrated in Figure 2.10.[15]

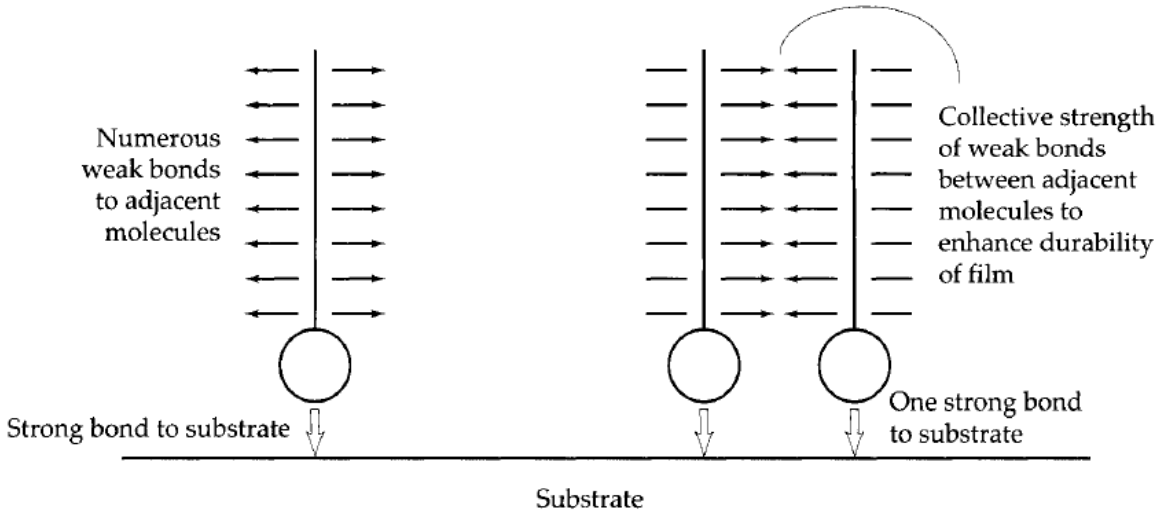

Figure 2. 10, Attraction between closely packed linear FA molecules to strengthen bonding between monolayer adsorbed and substrate,[15]

The adsorption, which is attributed to the additives of the lubricant can be divided into two fundamental categories such as “physisorption” and “chemisorption” because of their adsorption characteristics. Physisorption or physical adsorption that occurs at ambient or low temperatures due to the van der Waals forces, dispersion, or other low energy mechanisms.[15] However, adsorbate may attract or repulse from substrate with the increase of temperature (which depends on the constituents of lubricant and mating metal surfaces)[15], without any permanent alteration due to the weak molecular bonding between substrate and adsorbate.

In contrast, chemisorption or chemical adsorption will create stronger irreversible molecular bonding between substrate and adsorbate than physisorption, under high temperature and pressure conditions and depends on the additives and molecular structure of the lubricant (Figure 2.11).[15, 27]

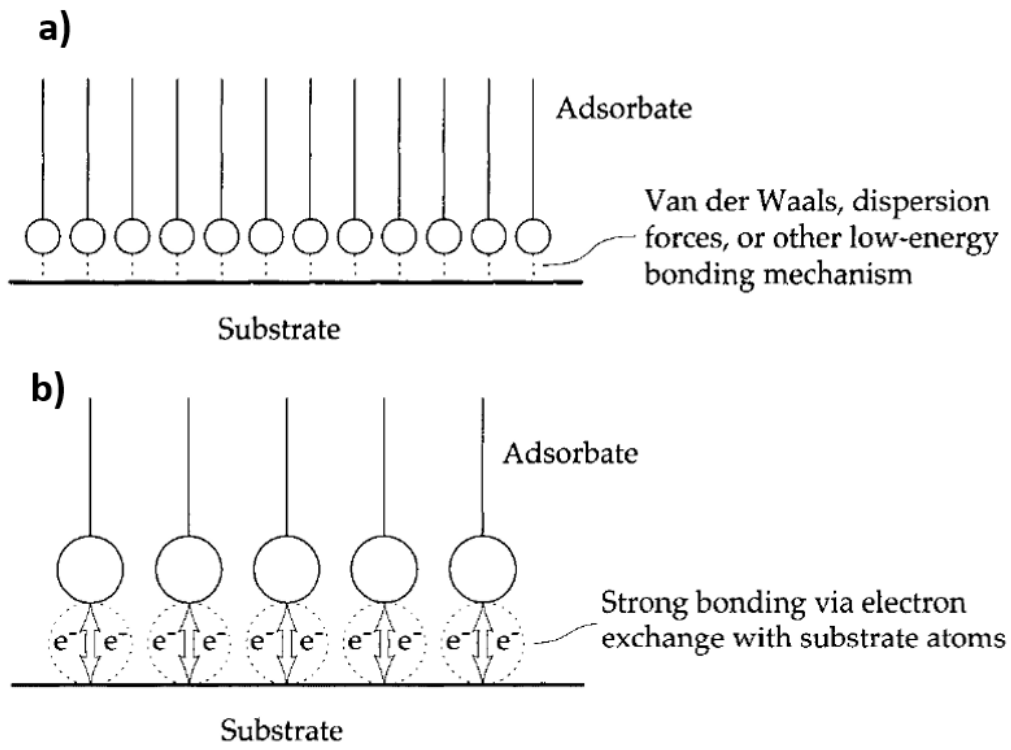

Figure 2.11, Schematic illustration of a) physisorption, b) chemisorption mechanisms for BL[15]

Apart from adsorption there are many mechanisms in BL such as surface localized viscosity improvement, formation of amorphous films, metal oxide or glass layer or nascent sacrificial layers, which depends on the operating environment like, load, speed, operating pressure and temperature. In-addition, properties of material such as surface hardness, surface roughness and rheological and physicochemical properties of the lubricant. BL or

"boundary and extreme pressure (EP) lubrication" as traditionally termed is a complex phenomenon, which Table 2.1 summarizes the application of different lubrication mechanisms with varying pressure and temperature.[15, 39]

Regardless of the practical importance of BL and associate mechanisms, the knowledge of these mechanisms is lacking the excellence and accuracy it requires with reference to present literature, thus needs improvement. In addition, from Table 2.1 and from the literature, it is obvious that, the temperature of sliding surfaces has an effect on all lubrication mechanisms, which is a sum of ambient temperature, steady state frictional heating and transient frictional temperature.[15]. Principal impetus for rising of transient frictional temperature is the asperity collisions at the interface, which leads to a sudden increase of friction at the location with the support of increased load and sliding velocity.[15] The situation when a lubricant fails to create a viable mechanism to reduce friction and lower the interface temperature (which is termed as critical temperature in literature) could lead to scuffing state or component seizer.[39] However, this elevated temperature will facilitate chemisorption bonding, or any other nascent film or process mentioned above instead of physisorption layer, depending on the properties of the additives and the base stock of a lubricant. Albeit, continuous removal and generation of adsorbed layers, certainly will reduce friction and increase wear.

Additives containing inorganic elements like sulfur, chlorine and phosphorus have been proved to be capable of forming sulfides, chlorides and phosphates by reacting with metal (iron) surfaces. The adhesion of these sacrificial films on both asperities will create the basis of BL or EP lubrication by minimizing the impact caused by passing asperity peak collisions. If the concentrations of metal chlorides, sulfides and phosphates are unbalanced, erosion and excessive wear may occur. In-addition, byproducts of these substances (emissions and waste crank case oil) are hazardous and toxic, thus numerous legislative restrictions are in place to minimize the usage of additives containing sulfur, chlorine and phosphorous elements. In addition, atmospheric oxygen and water vapor react with sliding metal surfaces under EP and extreme temperature conditions to form metal oxide layers. The resultant effect will suppress metal to metal contact bypassing asperity contacts, thus minimizing friction.

Table 2. 1, Lubrication mechanisms for different EP - BL situations[15, 40]

Temperature	Load	Lubrication mechanisms
Low	Low	Improvement of viscosity near contacting surfaces, not specific to lubricant
	High	Formation of physisorption film to cover surfaces in contact to minimize friction.
High	Medium	Creation of irretrievable soap films and other viscous substances by chemical reaction among lubricant additives and metal surfaces on worn surface.
		Enhancement of viscosity by lubricant additive and base-stock for localized surfaces.
		Formation of amorphous layers via reaction between additives and substrate metal surface.
	High	Reactions of lubricant additives on metal surface.
		Creation of sacrificial films of inorganic material, impeding metallic contact and acute wear on eroded surfaces.

Nevertheless, excessive oxidation may lead to a catastrophic situation with the formation of emulsion and acidic compounds thus resulting in more wear than anticipated. High temperature has a detrimental effect on this lubrication regime; thus, it is required to keep under control to avoid reaching critical temperature to minimize friction and wear. Therefore, transferring the generated heat from combustion and friction by sliding asperity contacts is recommended.[15, 39] Heat transfer from piston ring to coolant via lubrication film and cylinder wall by conduction and to carry away by lubricant itself to the oil cooler through convection are the possible routes, thus, the lubricant's ability to transfer heat via convection and conduction to engine coolant will be an added advantage to reduce friction and wear under these BL and EP situation.[15, 27, 40]

Mixed lubrication (ML) is the transitional region between both EHL and BL regimes. Thus, hydrodynamic pressure and layer formation is required in ML regime to support the asperity load, which are elaborated under the Sections 2.1.3.1 and 2.1.3.2.

2.1.3.3 The Measurement of lubricant-film thickness

From Equation 2.13 it is evident that the film thickness depends on the material, velocity, load and contact parameters thus it is affected by the properties of the lubricant and material

of the surfaces in relative motion. With the development of technology there are many test procedures available to measure the film thickness. The electrical inductance method was the earliest recorded technique applied, followed by eddy current and capacitance procedures. Measuring capacitance between two non-contacting metallic surfaces (for example piston ring and cylinder liner interface) separated by a relative permittivity (dielectric) of a media (lubricant film) is the technique utilized in the capacitance methodology with some success. Another method used is the laser induced fluorescence (LIF) and it is the latest methodology in development.

Dwyer-Joyce,[41-43] and Green,[44] utilized the reflection of ultrasonic pulse to measure the lubricant film thickness separated by opposing surfaces in motion. Here the amplitude of reflected incident pulse, which is depending on the stiffness of the separating film, generated by a piezoelectric sensor, and promulgated through cylinder liner wall, was measured as an impedance to calculate the reflection coefficient.[45] The piezoelectric sensor was attached to outer wall of the cylinder liner, which was used to both emit and collect ultrasonic pulses. The reflection coefficient was expressed as the acoustic impedance mismatch between two materials in contact.[41-45]

Green,[44] in his experiment used three types of ultrasonic transducers; element and contact transducers to measure an area equivalent to a circle with 7 mm diameter and focusing transducer for an area equivalent to a circle with 0.65 mm diameter. This experiment was used to analyze film thickness characteristics of a cylinder liner piston ring mechanism having bore and stroke measurements of 96 mm × 64 mm respectively. The test results reveled that the minimum film thickness of 9.4 μm and 16.5 μm at TDC and BDC respectively.[44]

Within the lubrication of piston ring cylinder liner interface, the variation of layer separation (film thickness) will affect in changing the capacitance of two infinite parallel conducting surfaces. Thus, was the hypothesis utilized to measure film thickness when utilizing capacitance mode.[46, 47]

Nevertheless, Dhar, et al.,[47] who studied the lubricating film thickness characteristics using capacitance probe, highlighted that the LIF method should be utilized for more accurate film thickness measurements.

When measuring film thickness utilizing LIF method, combination of laser induced fluorescence and fiber optics have been used to appraise the ratio of the incident excitation intensity with emitted fluorescence intensity, which is proportional to the optical path length.[48, 49] A typical schematic of the optical structure is illustrated in Figure 2.12. In this process energy will be provided by a laser beam in the form of incident photons to begin the excitation (Fig. 2.12-1). Exited photons will be expanded and refocused the objective to give electro-photonic imaging (epi) illumination (Fig. 2.12-2, 4). A dichroic mirror (wavelength selective beam splitter) will be utilized to direct the laser beam towards the lubricant film through excitation filter (Fig. 2.12-5b, 5c). The lubricant will be doped with a combination of laser dyes; Pyrromethene 567 or Rhodamine 640 or similar for LIF measurements[47,49-51]. Fluorescence emitted from dye molecules after energy absorption will be observed through magnifying lens and emission filter (Fig. 2.12-5a, 6), and fluorescence intensity images will be captured utilizing an electron multiplying, charged-coupled device (EMCCD) camera or photo-multiplying tube (MPT) for film thickness analysis (Fig. 2.12-7). Because the intensity of the fluorescence is related to the thickness of the oil film.[48]

However, Fowell,[49] noted that the influences on fluorescence from quenching, temperature, viscosity have an effect on the measurements.

Obert, et al.,[50] who studied the lubricant film thickness within the piston ring cylinder liner interface determined with LIF methodology, implemented the sheet of light technique to excite only the area to be analyzed, which could eliminate the influence of scattered light from outside the contact area. Nevertheless, he measured a film thickness for an area of 0.8 mm × 3 mm, out of a complete lubricated area with cylinder liner having 83 mm bore (however, stroke length was not specified to calculate the total area).[50]

It was found that Green,[44] utilized ultrasonic pulse technique to measure the film thickness of a circular area equivalent to 154 mm^2 as the maximum, out of 19,310 mm^2 of total lubricated area, which indicates, that he measured only 0.8% of lubricated area for his approximations. Likewise, Obert,[50] utilized LIF technique to measure an area of 2.4 mm^2 out of 14,347 mm^2, thus measured 0.02% of total lubricated area for his assumptions. Obert, et al.,[50] managed to measure oil film thicknesses less than 0.05 μm and assumed that the sufficient oil supply to the contact area is a critical requirement to prevent scuffing on contact surfaces. Moreover, there are eight assumptions within the famous scientist Osborne

Reynolds equation for hydrodynamic lubrication.[34] The scenarios, which exposes the accuracy of approximations within the tribology. In film thickness calculation or measurement, all the relevant parameters are surface roughness, temperature, pressure, lubricant entrain velocity, load carrying capacity, all are changing, thus predicting with the values representative of 0.8% or 0.02% area needs serious consideration. Therefore, this research is suggesting comparing, analyzed lubricant characteristics such as COF, FF, wear scar patterns, morphologies, exhaust emissions, used oil contaminants and many with the analytical results of the selected reference oil; formulated mineral oil 15W40.

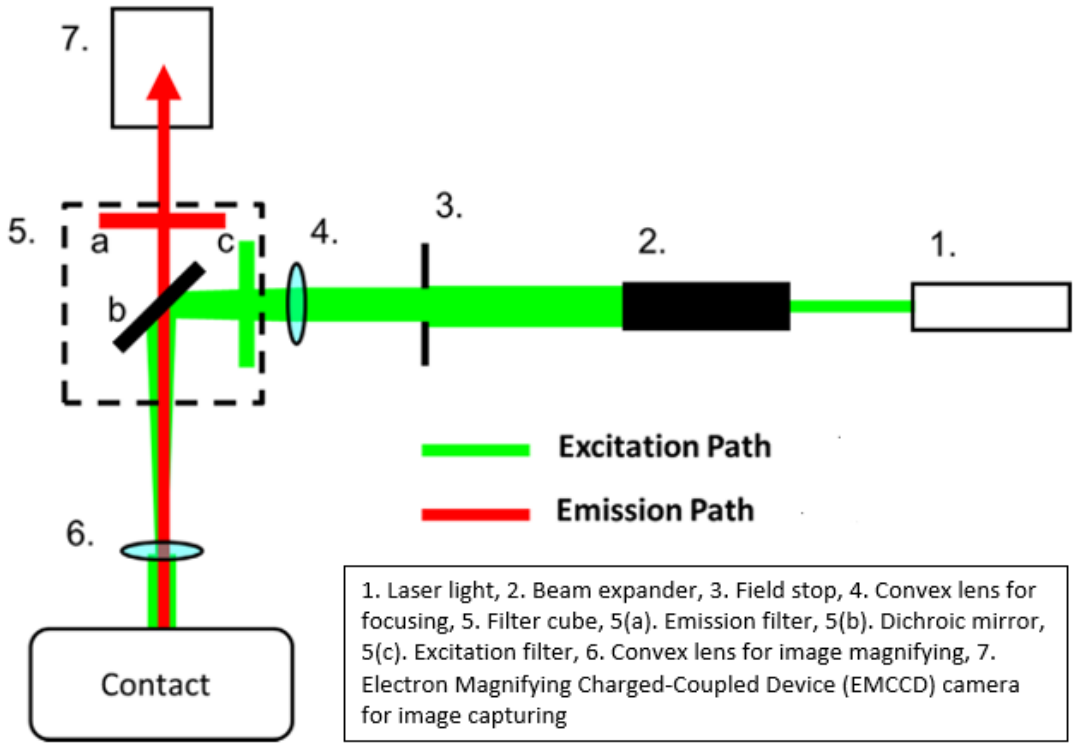

Figure 2.12, Schematic of an optical setup for LIF method utilized for film thickness measurement[49].

2.1.4 Surface roughness

Surface roughness is an essential characteristic within tribology, which affects the load carrying capacity of a lubricant at asperities, thus influences the minimum film thickness required to enhance lubrication.[32, 55] There are many descriptors of surface roughness, including 2D descriptors, such as the linear profile parameters, represented by R_a for the mean vertical height deviation and R_q or R_{rms} for root mean square deviation. 3D descriptors

such as the area profile parameters are represented by S_a and S_q symbols for 3D linear and 3D rms deviations respectively. Besides R_a or R_q (R_{rms}) are widely used,[32, 52] such as;

R_t or $R_{(P-V)}$ – Peak to valley roughness (vertical height from highest asperity to lowest valley)

R_p – Distance from highest asperity to the mean height

R_z – Average of the distance from the five highest points to five lowest points

The R_a and R_q or R_{rms} are defined as follows:[32]

$$R_a = \frac{1}{L}\int_0^L (|z|dx) \tag{2.15}$$

$$\sigma = R_{rms} = R_q = \left(\frac{1}{L}\int_0^L \left(|z^2|dx\right)\right)^{1/2} \tag{2.16}$$

where z – height of the profile, L – length of the profile as illustrated in Figure 2.13. Therefore, combined surface roughness (R_{qc}) for the surfaces in relative motion could be defined as,[32]

$$R_{qc} = \left[\left(R_{q1}\right)^2 + \left(R_{q2}\right)^2\right]^{1/2} \tag{2.17}$$

where subscripts q_1 and q_2 refers to the rms values of surface 1 and 2.

This composite surface roughness (R_{qc}) in relation to the minimum film thickness is termed as lambda ratio (λ), which is affecting to define the lubrication regimes. Besides, Vrcek, et al.,[53] observed that, the λ and wear are affecting the micro-pitting on EHL surfaces.[53] Also, Kumar and Rao[54] noted that the load carrying capacity and squeeze time increases with the increasing surface roughness.[54] Nevertheless, these linear parameters, R_a, R_q will not characterize the topography of a surface adequately with lateral information such as; slopes, shapes or size of asperity summit curvatures or their spacing or regularity, albeit, only the height variations from valley to peak or surface mean to summit of a surface will be described. Although, area roughness parameters S_a and S_q will give more significant values for engineering calculations or applications. Therefore, an area defined in the same linear surface roughness evaluation manner, could be utilized to determine the 3D values; S_a and S_q of a surface.[32, 56, 57]

There are many techniques developed over the years to measure surface topographies, which could be classified into two broad categories such as contact, and none contact methods. In contact methods, a stylus or measuring arm with mild load will absorb the surface variation while moving on traveling line of the surface.[58]

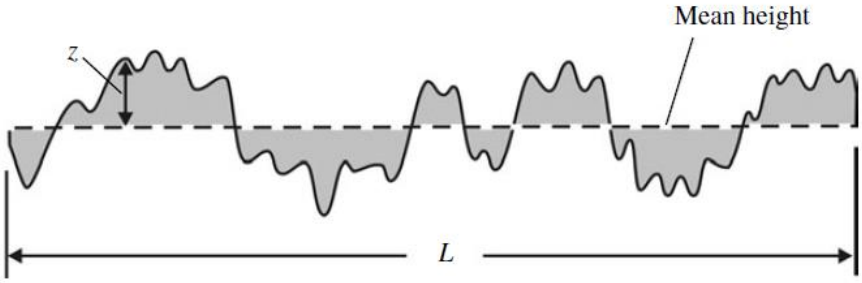

Figure 2. 13, Typical single profile trace in x direction[32]

Also, with the non-contact methods, optical interference, scattering, capacitance or scanning microscopy will be utilized to evaluate surface roughness of an area with more specific topographical details. Atomic force microscopy (AFM) is proved to be regarded as the choice for measuring surface roughness at the finest scale. However, in this experiment the surface roughness of test specimens is not suitable for atomic scale roughness quantification, thus non-contact 3D optical profilometer (Figure 2.14) will be utilized to analysis the surface texture of the test specimens before and after the tests.[32, 52, 56, 57, 58]

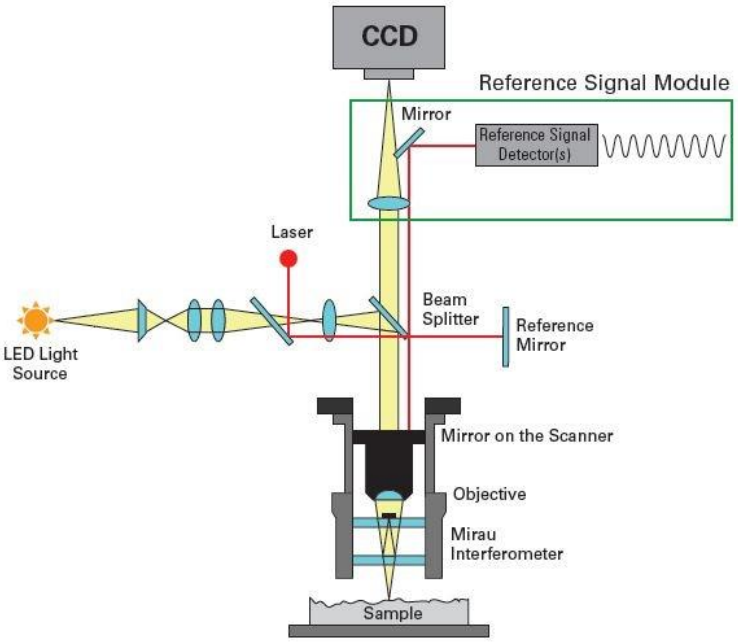

Figure 2. 14, Typical illustration of a non-contact 3D optical profilometer[59]

2.1.5 Contemporary engine lubricants

Today the world uses circa forty million metric tons of lubricants annually, out of which, 50% been used as engine lubricants.[12, 16] Shell, Mobil, Total, Castrol, BP, Caltex are a few leading brands among many to provide engine lubricants worldwide. The fundamental objective of an engine oil is to reduce friction between surfaces with relative motion in proximity. However, in addition, other key functions of contemporary engine oils are to:[60]

- Prevent corrosion and excessive wear.
- Dissipate excessive heat, waste energy from combustion.
- Prevention of soot, sludge, emulsion formation.
- Reduce energy losses, improve fuel economy.
- Control emissions

Thus, constitute with three basic packages; base stock, performance package and viscosity modifiers with approximate composition of 78%, 12% and 10% respectively for diesel engine lubricants.[11] Base stocks are mineral, or petroleum based, and synthetic. Mineral base stocks are manufactured from crude oil with long and high molecular weight aliphatic and aromatic hydrocarbons containing weight percentages of 73-80% of aliphatic, 11-15% of mono-aromatic, 2-5% of di-aromatic, and 4-8% of poly-aromatic hydrocarbons with many organic elements.[13] The structures are very complex in nature with more than 30 carbon atoms in each hydrocarbon molecule. Also, 125 combinations of molecules had been revealed so far, out of which, as many as 45 different compounds have been analyzed in detail.[37] Chemical forms, sulfur content and viscosity are the fundamental characteristics, vary among different base stocks. Paraffinic, naphthenic and aromatic are the three different chemical forms as illustrated in Figure 2.15, which will affect the physicochemical properties of lubricants.[37]

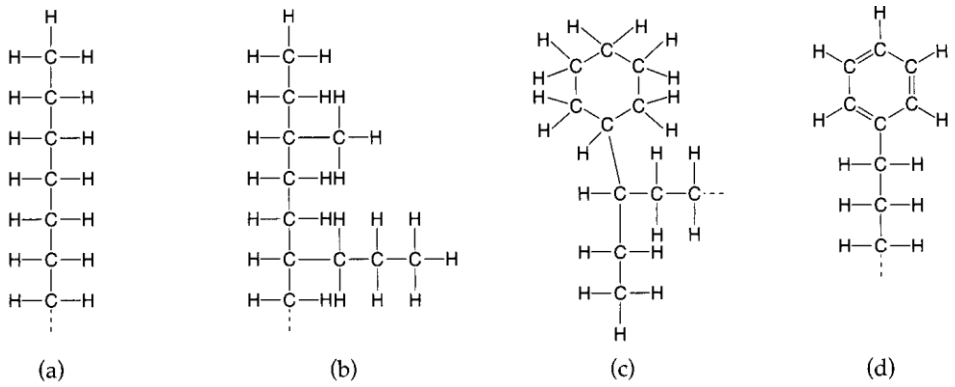

Figure 2. 15, Typical chemical structures of a mineral oil, a) straight paraffin, b) branched paraffin, c) naphthenic, d) aromatic,[37]

Synthetic base oils are artificially developed chemical compounds made from petroleum sub derives with the refinery process is called "Petroleum Cracking", which consist of branch-chained chemical structure with low molecular weight hydrocarbons to minimize viscosity variation with operating temperatures.[37]

Performance package and viscosity modifiers are complex combinations of numerous elements or functional groups to enhance engine oil functionalities. For example, olefin copolymers, acrylate polymers, styrene-diene copolymers are some compounds among many, which are using as viscosity modifiers.[11, 61, 62]

2.1.5.1 Existing engine oil additives

There are many additive packages, albeit remain highly confidential among manufactures, because of commercial constraints. The focus when formulating a lubricant is to obtain a combined enhanced performance rather than optimizing one specialized area of functionality.[60] Thus, it requires a thorough understanding to circumvent physical or chemical incompatibilities, because of observed synergistic or detrimental effects of additives on each other.[11, 62, 63] Table 2.2 summarize the functions of a modern performance package, which indicates that many additive groups have similar functionalities as well as distinctive characteristics within a lubricant. Transformation of molecule structures to others under the influence of rubbing or mechanical agitation is the phenomenon, which is termed as tribo-chemical or tribolysis.[40] It is a segment of a mechano-chemical reactions affecting the desired characteristics and performance of a lubricant. These chemical reactions

(arrangements of atoms between or within molecules) are associated with breaking and making of chemical bonds. This process is a transition of mechanical energy to chemical energy. Presumably extreme pressure and temperature conditions at mixed or boundary circumstances may provide the required energy, thus possible impetus for above reactions are summarized below as illustrated in Figure 2.16.[40]

- Heat generated because of friction due to rubbing contacts at asperity interfaces.
- Induction of chemically active transition metals because of vacant d-atomic orbitals due to lattice defects, caused by exposed nascent surfaces.
- Possibility to produce radical intermediates for further chemical reactions with the assistance of Exo – electrons emitted from rubbing surfaces.
- Initiation of chemical reactions at high pressures under static conditions because of collision of molecules due to compression of reactants.
- Closeness of functional groups because of their molecular orientation together with elevated pressure, presumed increases the probability of reactions.
- Dissociation of chemical bonds under shearing condition to influence formation of radical species

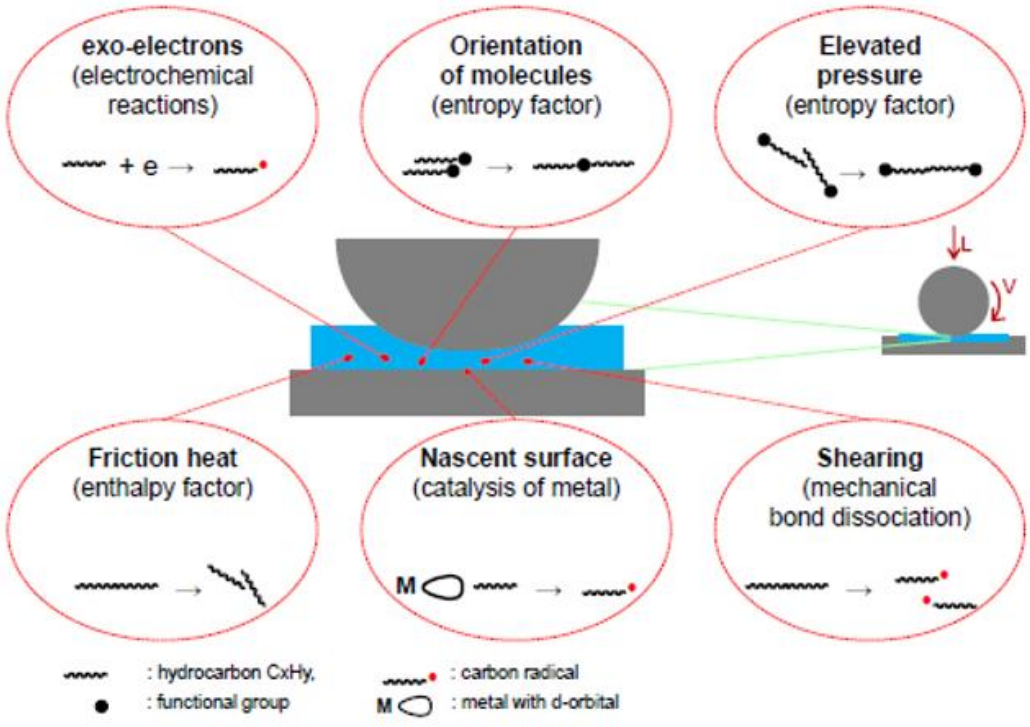

Figure 2. 16, Viable impetus for chemical reactions at tribo interface[40]

Table 2. 2, Additive groups and their functionalities within a contemporary engine lubricant[11, 61-63]

Additive	Purpose	Additive compounds
Inhibitors	Prevent or minimize oxidation, foam, corrosion, friction, and wear	ZDDPs, aromatic amines, hindered phenols, alkylphosphates, slufurized fatty acids, polysiloxanes, fatty acid derivatives.
Dispersants	Prevent sludge, soot, emulsion formation and sedimentation at low temperatures and low load conditions	Polyesters, benzylamides, polyisobutylene succinimide, succinic esters of polyol, mannich bases
Detergents	To keep the engine clean, reduce deposits, prevent oxidation	Sulfonates, phenates, salicylates, incorporated with calcium and magnesium cations
Antifoam agent	To speed up the release of gases churned into lubricants	polymethylsiloxanes, polymethylsilicones
Anti-wear agents	To form protective lubricant layer on metal surfaces	ZDDPs, dithiophosphates, phosphates, polysulfides
Antioxidants	To prevent/reduce oxidation, oil thickening, varnish or gum formation and corrosion	ZDDPs, sulfur and phosphorus elements, aromatic amines, hindered phenols, copper and molybdenum organic compounds
Friction modifiers	To develop low shearing fluid layer to avoid asperity contacts	ZDDPs, sulfurized fats and esters, amides of fatty acids, polyol esters of fatty acids (glyceryl monooleate), molybdenum dithiocarbamate, molybdenum dithiophosphate
Viscosity modifiers	To make lubricant less sensitive to temperature variations	Acrylate polymers, olefin polymers, olefin copolymers, hydrogenated styrene butadiene copolymers,
Pour point depressants	To lower the lowest temperature at which lubricant could pour or to improve cold flow properties	Polyalkylacrylate, polyalkylmethacrylate, alkyl aromatic polymers

Zincdialkyldithеophosphates (ZDDPs) are the most successful additive in the history of present lubricant additives for the last 90 years.[63, 64] Today ZDDPs are proven to be additives with multifunctional capabilities as a corrosion inhibitor, dispersant, detergent and most prominently as an anti-wear agent,[62] albeit initially utilized as an antioxidant. Perhaps, these functionalities of ZDDPs are critically dependent on four different reactions such as, 1) ligand exchange, 2) reaction with peroxides/peroxy-radicals, 3) thermal degradation via O/S exchange, and 4) adsorption at metal surfaces.[64]

There are many additives in a typical finished engine lubricant with different chemical compounds in addition to ZDDPs (Table. 2.2).[11, 37, 61, 62] Colloidal stability of additives in base-stock is essential for optimum performance. Most of the additive molecules are constituted by small active hydrophilic group;[62] a polar head and non-polar long chain tail with different solubilities, thus incline to exist colloidally as inverse micelles.[11] Besides, these polar heads interact with metal substrates to create adsorption or chemisorption layer to prevent asperity contact of cylinder liner piston ring interface of an ICE, while nonpolar long chain tail remain soluble in the fluid (Fig. 2.9).[11, 37]

Formation of a boundary film, which will affect the friction under extreme pressure (EP) at BL or ML condition because of adhesion and cohesion properties of the additives.[67] Also, this functionality, which generates low shear film of the adsorbate on the surface of adsorbent is the hypothesis for anti-wear mechanism.[40] In addition, antioxidation is directly correlated to minimize wear through corrosion prevention and to improve lubricant life by inhibiting oil thickening via impeding sludge, soot or emulsion formation within a lubricant.[42] ZDDPs are the leading antioxidants in use,[64] albeit there are many other compounds in use to inhibit oxidation, which are having the capability to act as free radical traps or peroxide decomposers to interrupt chain propagation steps of oxidation.[11, 62]

There are three reaction stages to reduce oxidation reported in literature; 1) initiation, 2) propagation and 3) termination, leading to oxidation, as illustrated below;[11, 62]

Initiation: $RH \longrightarrow R^{\bullet} + H^{\bullet}$

Propagation: $R^{\bullet} + O_2 \longrightarrow ROO^{\bullet}$

$ROO^{\bullet} + RH \longrightarrow ROOH + R^{\bullet}$

$ROOH \longrightarrow RO^{\bullet} + OH^{\bullet}$

$RO^{\bullet} + RH \longrightarrow ROH + R^{\bullet}$

$$HO^{\bullet} + RH \longrightarrow R^{\bullet} + H_2O$$

Termination:

$$R^{\bullet} + ROO^{\bullet} \longrightarrow ROOR$$

$$R^{\bullet} + R^{\bullet} \longrightarrow RR$$

Where, **RH** – Hydrocarbon, **R** – Radical, **R•** – Free radical, **H•** – Hydrogen ion, **ROO•** Peroxide radical, **ROOH** – Organic acid and **ROOR** – Organic peroxide. Figure 2.17 illustrates the sequence of reactions by hindered alkyl phenols to trap free radicals to intercept propagation progression.

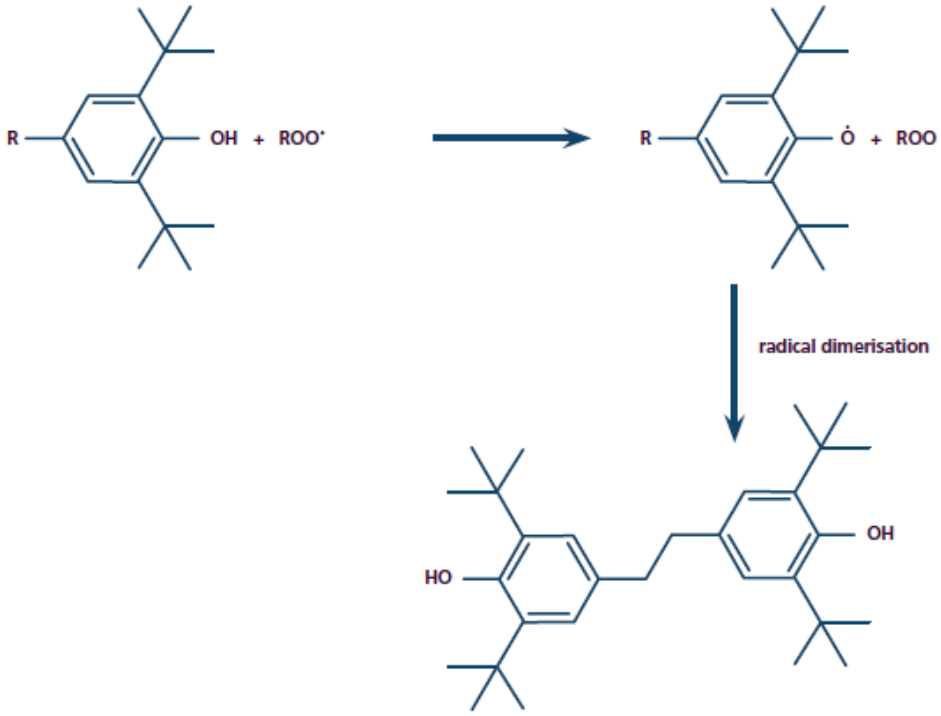

Figure 2. 17, Reaction path of hindered phenols for radical trapping[11]

Detergents, over-based detergents, and dispersants have similar functionalities to prevent soot sludge or deposits formation within a lubricant. This is in addition to keep engine surfaces clean. All are having polar substrate to form micelles to trap deposit precursors, thus, to keep in solution in the fluid avoiding settlement of deposits in the engine, albeit with different chemical structures and effects as listed in Table 2.3.

Silicon polymers such as polydimethylsiloxanes are widely used defoamers to prevent air entrainment or foam creation within an engine, because of high velocity modern engines with

extreme operating temperatures. The mechanism to rupture air or foam bubbles more frequently is by weakening their walls because of the low interfacial tension of the constituents of these additives.[11, 40, 62]

Table 2. 3, Summary of functional groups and their molecular structures of dispersants, detergents, and over-based detergents of existing engine oils[11, 61, 62]

	Detergent	Over-based Detergent	Dispersant
constituents	Polar substrate + metal oxide/hydroxide	Polar substrate + metal oxide/hydroxide + additional metal base	Nonmetallic (ash-less) polar substrate
Polar head	Active acidic group	Active acidic group	Oxygen or nitrogen moieties
Tail	Oleophilic hydrocarbon chain	Oleophilic hydrocarbon chain	Oleophilic hydrocarbon chain (longer than detergents)
Micelle's capacity	0 - 20 nm precursor particles	0 - 20 nm precursor particles	0 - 50 nm precursor particles
Ability	Can attract and hold deposit particles	more micelles than detergents	Can hold 10 times more deposit particles than detergent. Can stabilize large particles by charge repulsion

Viscosity modifiers (VM) are VI improvers, which make lubricant's viscosity less sensitive to operating temperature variations. Polymers with high molecular weights greater than or equal to critical mass (M_c) will develop large entangled chains, which are very effective as additives due to their coil expanding capability with increasing temperatures as presented in Figure 2.18a.[40, 68] This is the widely attributed mechanism caused by globule to random coil transition, which depends on the attractive or repulsive interactions between polymer chain segments and solvent molecules.[51] However, from another development it is observed that the increase of molecular weight will increase friction thus wear under boundary conditions.[68] Polymethylmethacrylate (PMMA) proved to be an affective additive to increase VI[69, 70] because of its thermal coil expansion behavior, which is significantly dependent on the monomer composition of the polymer. [11, 37, 40, 69, 70]

Pour point depressants (PPD)s used are typically branched hydrocarbons to inhibit the development of interlocking wax crystal structures at low temperatures because of interaction between alkyl branches with base stock molecules.[11, 62] This broadly regarded phenomenon, which Figure 2.18b illustrates will prevent wax formation within lubricant and allow the fluid to flow freely at low temperatures, thus increasing the operating parameters, albeit reaction mechanism are not fully understood yet.[11, 40] PMMA is a leading additive for both VM and PPD, also a polymer with macro molecules with reference to the molecular mass of the base oil molecule. However, as a PPD and as a WM, PMMA has to function actively throughout the operating range of an engine lubricating oil, albeit functions are dissimilar from inhibiting crystal formation at cloud point to augmenting intrinsic viscosity with increasing temperature.

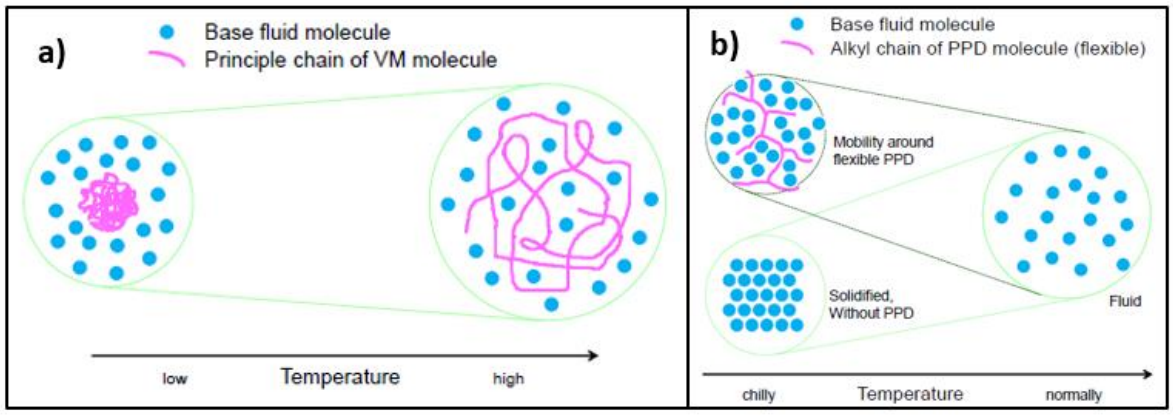

Figure 2. 18, Presumed lubrication mechanisms for a) viscosity modifiers, b) pour point depressants[11, 51]

2.2 Nanoparticulate as additives in lubricants

Dealing with numerous structures of elements with dimensions of the order of a billionth of a meter ($m10^{-9}$) is termed as **"Nanotechnology"**, which realizes the capabilities of different matters to exhibit dissimilar properties based on their shape and size.[71] Nanoparticles are the finest form of material evolved with numerous innovative products having one structural dimension less than 100 nm with large surface area to volume ratio, including reduced surface imperfections, spatial confinement, large fraction of surface atoms, thus high surface energy. In-addition, these ultra-fine particles could be categorized into various kinds according to their physical and chemical properties, shape, size, morphologies

and material, such as carbon-based, ceramic, metal, semiconductor, polymeric and lipid-based nanoparticles.

Top down and bottom-up are two different approaches for synthesis of nanomaterials. Breaking down macro scale material into nano scale elements is termed as top-down method, which could be achieved through either mechanical-based or chemical-based routes.[71, 72] Micromechanical cleavage, ball milling, chemical exfoliation, and lithography are a few approaches among many in top-down route.[72] For example, synthesis of nano-magnetite with average particle size of 20 – 50 nm and zeta potential of +42 mV, was achieved via wet ball milling.[73] Also, the chemical exfoliation is very attractive because of high yield gained. There are many routes under this process, however, Hummer's method is widely used among researchers to synthesis graphene (G) from graphite because of less reaction time and low energy consumption.[74] In this method synthesis of graphene oxide (GO) is achieved via oxidizing bulk graphite powder with the reaction between graphite and a mixture of concentrated H_2SO_4, $KMnO_4$ and $NaNO_3$, followed by exfoliation.[74] And thereafter chemical or thermal reduction to obtain reduced graphene oxide (r-GO) or chemically converted graphene (CCG).[74] Nevertheless, deficiency of surface morphologies proved to be the fundamental challenge with this approach.[72]

In contrast, bottom-up approach or molecular nanotechnology is to develop nanoscale structures with required functionalities to suit the application via chemical processes by forming molecular clusters from atomic level.[72] Chemical vapor deposition (CVD), sol-gel, hydro/solvothermal, molecular/atomic condensation, inverse-micelle, laser pyrolysis, plasma or flame spraying are a few among many methods, selection of which is based on the available precursors.[72, 74] Moreover, these methodologies offer solution-based approach for the best course for scaled-up 2D material processing with tailored functionalization.[74] For example, Uthman, et al.,[75] elaborated the broadly adopted batch and continuous hydrothermal flow synthesis (CHFS) route with precursor-product progression to yield nanoparticles with different qualities like surface area, size, and morphologies to suit desired application.

In-addition, synthesizing hybrid nanomaterials via various means is a popular technic to produce nanocomposites with tailored properties to meet anticipated functionalities. Also, thermal annealing and doping are other popular technics to produce nanocomposite materials.[76]

Nanoparticles are a promising technology to reduce friction, and wear, hence enhance ICE performance as an additive to engine lubricants. This is because of their ultrafine size to infiltrate through asperities, adhesion, and cohesion qualities to create boundary film at TDC under oil starving with high temperature and EP conditions. Also, their molecular structures to create rolling effect during EHL regimes; nano-bearing, instead of sliding between moving metal surfaces to reduce friction further in engines.[8, 9, 14] Nanoparticles are applied in various researches as additives in engine lubricants.[77, 78, 79]

Hsu,[79] highlighted the importance of creating a nanoscale, non-volatile, antioxidant, thermal decomposition resistant, self-repairing, monolayer with adhesion and cohesion qualities to protect rubbing asperities under high temperature and pressure conditions.[79] Xiao, and Liu,[80] have done a comprehensive review on selected two-dimensional (2D) nanomaterials as lubricant additives, because of their unique molecular structures; high within layer and low inter layer shear strengths, adhesion and stiction properties. They have selected nanoparticles from (1) Graphene family, (2) Transition metal dichalcogenides (TMDCs); MXene nanoflowers, layers, belts (3) Other nanomaterials; yttrium oxide (Y_2O_3), alpha zirconium phosphate (α–ZrP), nano boron nitride (n–BN) etc., in their review and emphasized the tribological performance of 2D nanomaterials as lubricant additives to separate the contacts with extreme load carrying capacity. Another review by Zhang, et al.,[81] elaborated the excellent tribological potentials of layered 2D nanoparticles like; graphene, hexagonal BN and MoS_2, because of their extraordinary structural, chemical, thermal, mechanical, and electrical characteristics to reduce friction as summarized in Figure 2.19.[81] Their performance in atomically thin solid-state lubricant to reduce coefficient of friction below 0.01 is termed as "structural superlubricity".[81] The mechanism reviewed was interlayer sliding of 2D materials, which depends on the weak layer interface interaction coupled with distinctive crystalline alignment of sliding atomic layers of 2D surfaces.[81] Besides, the influence of electro-phonon coupling, in-plane strain, chemical modification and functionalization revealed to be significant in interlayer interaction.[81]

Despite of able advantages of nanomaterials, there exists current challenges including poor dispersion and solubility because of π- π interactions for 2D materials. A study by Singh, et al.,[82] exposed the tribological enhancements by various nanoparticles involving different mechanisms like, rolling, mending, polishing and protective layer formation (Figure 2.20). However, revealed the importance of optimum particle concentration to enhance dispersion

stability of nano-additives in base-stocks to avoid agglomeration, and sedimentation, which leads to minimize friction and wear of the subject nano-lubricant. Hence, solutions proposed are surface modification either by chemical modification; nucleation or alkylation or utilizing other techniques; exfoliation with focused solar electromagnetic radiation or simple mixing and stirring method as a remedy.[80]

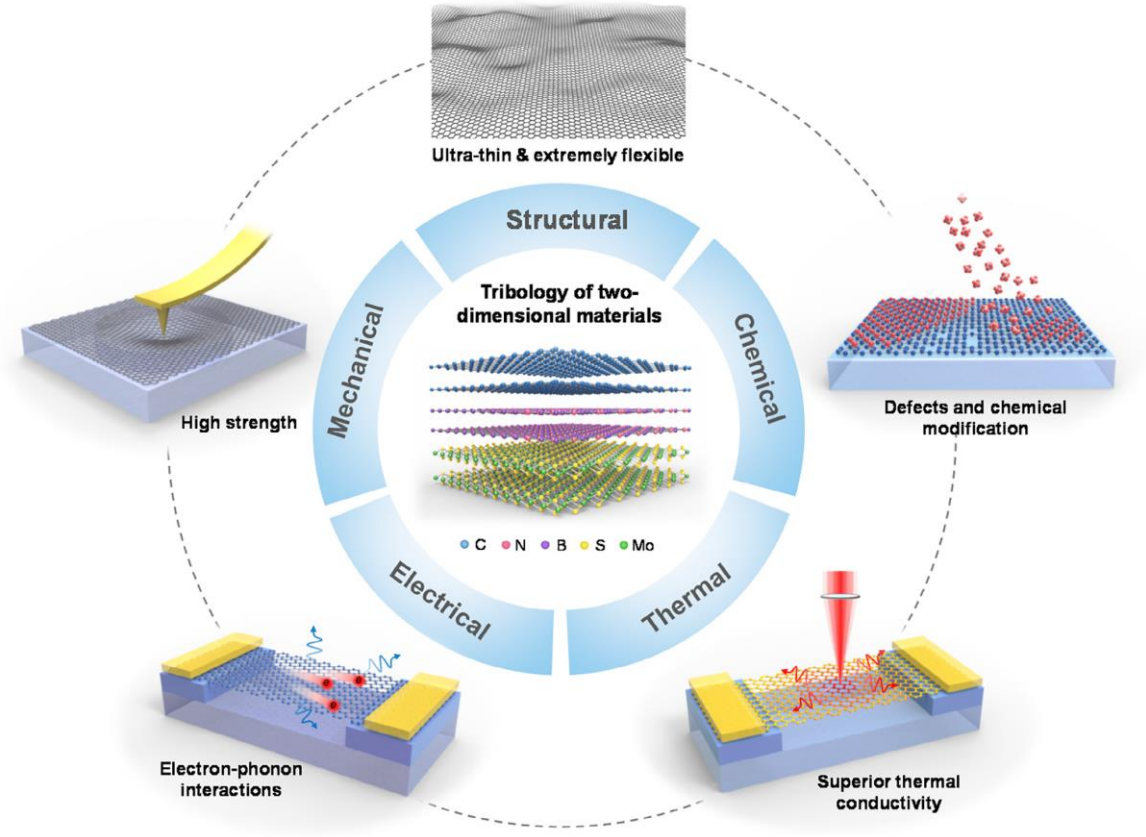

Figure 2. 19, Overview of structural, mechanical, electrical, thermal, and chemical properties of 2D materials that are relevant to tribological performance.[81]

In another development, superlubricity of nanomaterials from all ranges; 0D, 1D, 2D and 3D were reviewed by Zahi and Zhou[78] and highlighted the superlubricity capabilities of TMDs and graphene layers in 2D scale, especially the MoS_2 and graphene nanoflakes for vigorous superlubric forms at both nanoscale and macroscale. (Kellici et al.,[77] emphasized the importance of green process engineering (GPE) for the future industrial success by utilizing innovative supercritical fluids (SCF), or CHFS techniques for chemical processing of nanomaterials synthesis).

Many types of nanoparticles have been used as additives to lubricants and have shown different percentages of enhancements to the tribological performances. The findings are summarized in Table 2.4, which provides the insight for the potential of nanoparticles as lubricant additives to enhance tribological performances of mechanical components with extensive operating conditions.

Gulzar,[83] noted that, it is imperative to examine and understand the tribo-mechanisms engrossed with nano-lubricants for ICE lubrication. There are several mechanisms suggested in literature as illustrated in Figure 2.20, with the aid of contemporary surface analyses techniques, albeit need further elucidation. The mechanisms proposed are: i) formation of a protective boundary film, ii) sliding to rolling (ball bearing) effect, iii) mending effect and iv) polishing effect etc., which could be categorized in to two main streams such as: 1) direct effect of nanoparticles including ball bearing and protective layer formation and 2) surface enhancement or secondary effect of nanoparticles by mending/repairing and polishing/smoothing of sliding surfaces. The mechanisms reviewed through literature for different research are summarized in Table 2.5, However, it is still a challenge to characterize effective mechanisms associated with specific nano-lubrication, which depends on the properties; morphology, particle size and surface hardness of nano-additives in use.[83, 84]

From literature, it is evident that nanomaterials from graphene family and TiO_2 had been involved with many tribological experiments showing enhanced results.[9, 84, 86, 87, 88, 89] Moreover, nano-Al_2O_3 had performed good results as a lubricant additive and is widely available,[9] thus selected nano-particulates of interest for this investigation are Al_2O_3, TiO_2, and graphene (G). In-addition, TiO_2/r-GO, TiO_2/G, and Al_2O_3/G nanocomposites are selected as a novelty, because there is not any evidence in literature of using these combinations as nano-additives in ICE lubricants before. Besides, nanoparticles of graphene, TiO_2, and Al_2O_3 are selected to synthesize above nanocomposites, because of their enhanced performance in ICE lubrication, as reported in the literature. [9, 84, 86, 87, 88, 89] Thus amalgamation of these materials may help to develop nanocomposites with integrated attributes of principle materials, not only to improve tribological performance, but also to enhance other essential lubricant characteristics to improve the gaps, for example, dispersion, oxidative, shear, and thermal stability.

Table 2.4, A review of tribological performances by nanoparticles as additives in engine lubricants

		Nano-lubricant					Test conditions				Reduction	
								Speed				
Year	Ref.	Nano material	Grain size (nm)	concentration (wt. %)	Base oil	Tribo meter	Load (N)	(m s^{-1})	(rpm)	Temp °C	COF %	WR/ MWD %
2012	85	α-Fe_2O_3 /GO	15-30 L 3-5 D	0.5	Paraffin oil	Ball on Disc	19.6	3.412	N/A		Improvements reported	
2015	14	CuO	11		5W20	Pin on Disc		N/A	N/A		Improvements reported	
2016	9	Al_2O_3.	08-Dec	0.25	5W30	LRT	120	0.5	N/A	100	45	21
		TiO_2	10	0.25	5W30	LRT	120	0.5	N/A	100	50	29
2016	86	TiO_2	Oct-25	0.3	10W30	Pin on Disc	59	1	N/A		34.5	40
2016	87	TiO_2-BN-MRG		0.15	Paraffin oil	Four ball	392	N/A	1200	75	25.4	50.88
		BN-MRG		0.15	Paraffin oil	Four ball	392	N/A	1200	75	20.37	33.15
2015	88	Sc-Au/GO	04-Oct	0.1	PAO6	Ball on Disc	10	0.1	N/A	RT	33.6	72.8
2018	89	G (2D)	03-Oct	0.4	5W30	LRT	216	0.258	N/A		29 - 35	22-29
2019	84	GNS/MoS_2 -NFs	200 - 300	0.02	Dibutyl phthalate	Four ball	392	N/A	1200		42.8	16.9
		GNS/MoS_2 -NPs	200 - 300	0.02	Dibutyl phthalate	Four ball	392	N/A	1200		37.6	11.9

Legend: *LRT – Linear Reciprocating Tribometer, 5W20, 5W30 and 10W30 – Engine lubricants with different viscosity grades, COF – Coefficient of friction, WR – Wear rate, MWD – Mean wear diameter, RT – Room temperature*

Table 2. 5, A review of lubrication mechanisms correlated with different nanomaterials as additives in engine lubricants.

		Nano lubricant					
Year	Ref	Nano-material	Particle size (nm)	Base oil	Additive function	Mechanisms	Surface analysis technique
2012	85	α-Fe_2O_3/GO	15-30 L 3-5 D	Paraffin oil	FM, AW	Rolling/Tribo film	SEM, Optical micrograph
2014	90	Al_2O_3	78		FM, AW	Rolling/Tribo film	SEM, EDS
2015	14	CuO	11	5W20/PAO	FM, AW	Rolling/Tribo film	
2015	88	Sc-Au/GO	4 - 10	PAO6	FM, AW	Mending/Tribo film	SEM, XPS, Raman, Optical Profilometry
2015	91	Cu/GO	5 - 10	Paraffin oil	FM, AW	Rolling/Tribo film	SEM, XPS
2016	9	Al_2O_3	8 - 12	5W30	FM, AW	Mending/Tribo film/rolling	FE-SEM/EDS, XPS, 3D optical profilometry
		TiO_2	10			Rolling/Tribo film	
2016	86	TiO_2	10 - 25	10W30	FM, AW	Rolling/Tribo film	
2016	87	TiO_2-BN-MRG		Paraffin oil	FM, AW	Tribo film/Tribo sintering	SEM, AFM, XPS
		BN-MRG					
2018	89	G(2D)	3 - 10	5W30	FM, AW	Mending/Tribo film	FE-SEM/EDS, XPS, Raman, 3D surface profilometry
2018	83	CuO, MoS_2, TiO_2/SiO_2	< 100	Palm - TMP	FM, AW	Polishing/Mending / Tribo film	SEM, EDX, Raman, 3D surface profilometry
2019	84	GNS/MoS_2-NF_3	200 - 300	Dibutyl phthalate	EP, FM, AW	Mending/Tribo film	SEM, EDX, XPS, Raman
		GNS/MoS_2-NP_3					

Key: FM – Friction modifiers, AW – Anti wear, EP – Extreme Pressure

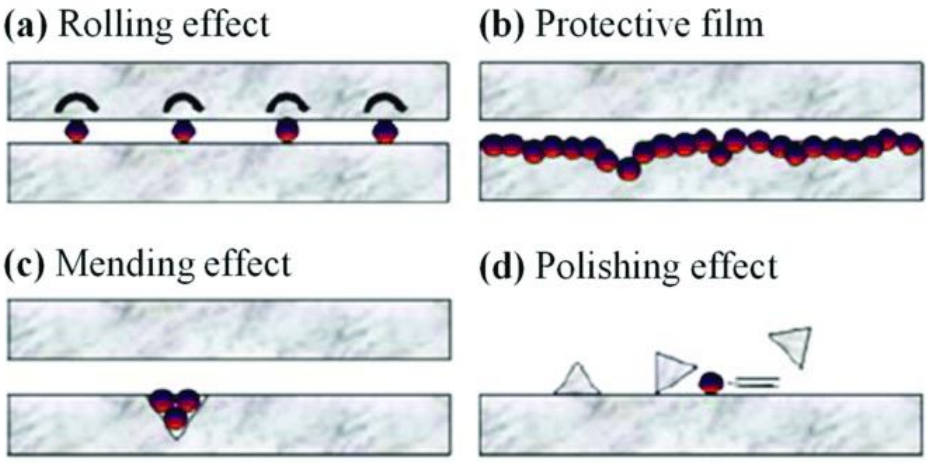

Figure 2. 20, Presumed lubrication mechanisms associated with nanoparticle additives at boundary lubrication.[92]

2.2.1 Aluminum oxide (Al_2O_3) nanoparticles

Nano Al_2O_3, is a white powder with spherical or semi spherical morphologies[9] used in many applications including; plastics, rubber, ceramics, glass, refractory products, integrated circuit boards, YAG (Yttrium, Aluminum, Garnet) laser crystals, single crystals and so on.[90] In addition to the cost-effective synthesizing processes, the material exhibits high thermal conductivity (30 W m^{-1} K^{-1}), thermal and chemical stability, high mechanical strength, high specific surface area (SSA), as well as anti-wear, adhesion and cohesion qualities to create protective layer as a lubricant additive.[8, 9, 90, 93, 94, 95] Laser ablation in deionized water, mechanical ball milling, mechanochemical, solution reduction, exploding wire, gas evaporation and decomposition are the processes in use for synthesizing nano Al_2O_3.[90, 95]

Luo, et al.,[90] studied the tribological properties of Al_2O_3 nano powders, and identified the agglomeration and poor absorption of nano-aluminum oxide additives within the blend. Thus, Al_2O_3 nanoparticles were synthesized via hydrothermal route with situ-modified surface using silane coupling in an autoclave. Aluminum isopropanol, isopropanol alcohol, polyethylene glycol (PEG), 3-glycidoxypropyltrimethoxysilane (KH-560), nitric acid and ammonia were used as precursors to obtain AlO(OH) with pH 9 when synthesizing modified Al_2O_3 nanoparticles.[90] Figure 2.21 illustrates the formulation path for modified nano Al_2O_3, for stable, homogeneous blend with improved tribological performance. From the test results it is revealed that the COF and wear scare diameter (WSD) of worn surface was reduced by 17.61% and 41.75% respectively compared to the reference oil. These results were achieved

with 0.1 wt.% concentration of nano-Al_2O_3 in base-stock. The lubrication mechanisms proposed were formation of a self-laminated protective layer on the friction interface and the change of wear behavior from sliding to rolling because of the spherical nature of Al_2O_3 nanoparticles.[9, 90] Also, a study by Liu, et al.,[96] revealed that the mixing temperature, method (ultrasonication), and period of agitation and concentration of nanoparticles/surfactants could enhance the dispersion, thus enhancing the colloidal stability of a nano-lubricant with Al_2O_3 additives.

A study by Ali, et. al,[9] emphasized the enhanced tribological performance of Al_2O_3 nanoparticles, 0.25 wt.% concentration as an additive in formulated mineral oil 5W30. In-addition to the reduction of COF and wear rate, VI was increased by 1.84% compared to the base lubricant. Tribological achievements; COF and wear rate reductions were 35% and 21% respectively. These results were attributed to the formation of a tribo-boundary film on sliding asperities and conversion of sliding to rolling lubrication, which were revealed through SEM, EDS, XRD, XPS and 3D profilometry analyses.[9]

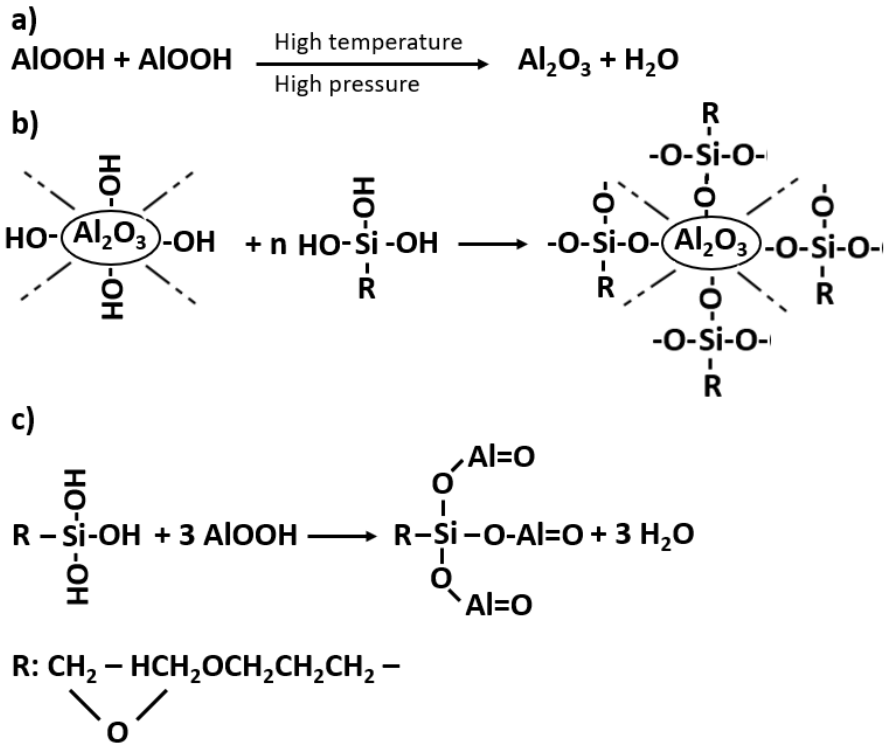

Figure 2. 21, Reaction path for nano-Al_2O_3 synthesis, a) AlOOH dehydration under high temperature and high pressure, b) modification of Al_2O_3 nanoparticles, c) dehydration condensation reaction between AlOOH and hydrolysis of KH-560,[90]

2.2.2. Titanium dioxide (TiO_2) nanoparticles

Anatase, rutile and brookite are the crystal forms of TiO_2 nanoparticles, which could be found in many nano TiO_2 structures such as; nanoparticles, nanorods, nanowires and nanotubes.[97] There has been an increase in research works available in nanoscience and nanotechnologies in the past couple of decades. TiO_2 nanoparticles are associated with many applications such as; air and water purification, pollutant or organic molecule destruction, self-cleaning windows, anti-bacterial coatings, photocatalysis, photovoltaics, photonic crystals, batteries, sensors, ultraviolet blockers, pigments are some among many.[86, 97,98] Their high surface area, surface to volume ratio (S:V), chemical stability and the low cost of production have been reported as reasons for effective application of TiO_2.[86, 98]

There are many preparation methods to synthesize TiO_2; sol-gel, sol, solvothermal/hydrothermal, electrodeposition, physical/chemical vapor deposition (PVD/CVD), metal organic CVD.[54] Kellici, et. al,[98] synthesized TiO_2 nanoparticles via CHFS route using titanium bis ammonium lactato dihydroxide (TiBALD) 50 wt.% in water as precursor with the assistance of super critical water at 400 °C and 24.1 MPa as the reaction medium. The prepared particles have the following properties; particle size of 4.9 ± 1.3 nm, lattice spacing of 0.355 nm and Brunauer-Emmett-Teller (BET) surface area of 290 $m^2 g^{-1}$. It was also found that, the particle size increased up-to 55 nm during heat treatment at 800 °C with 34.7% of anatase-rutile transition. The phenomenon was ascribed to phonon confinement effect in nanocrystals, which is vital to the increase of Raman (E_g) band in nano-TiO_2, without heat treatment.[98] In-another development, nano-TiO_2 structures with controlled phase and morphology were formulated using titanate nano tubes (TNTs) with H_2O_2 as precursors in NaOH aqueous solution via batch supercritical hydrothermal media at 400 °C.[99] Dissolution – nucleation – growth mechanism is the suggested reaction path influenced by both the supercritical temperature and NaOH aqueous pH for controlling properties of final product.[99] Chen, X.,[97] highlighted that, doping TiO_2 nanoparticles with other elements could improve the properties to suit the desired application.

There were many researches aimed to investigate the tribological enhancement of TiO_2 nanomaterials. For instance, Ali, et al., [9] reported that the 50% and 21% of reduction on friction and wear respectively by 0.25 wt.% of TiO_2, nanoparticles as an additive in 5W30 commercial lubricant. Wu, et al.,[100] studied the tribological performance of nano-TiO_2, 0.8

wt.% as an additive in water-based lubricant and observed the 49.5% and 97.8% COF and wear reduction respectively compared to dry condition (nanoparticles in solid (powder) state without any fluid base-stock). Gulzar,[83] blended palm trimethylolpropane (TMP) with nano-titanium silicate ($TiSiO_4$) - 0.75 wt% as additive and observed 68% of COF and 50% wear volume reduction.

Based on the findings from the literature nanomaterials of TiO_2 and TiO_2/r-GO were synthesized utilizing CHFS reactor with the use of deionized superheated water feed at 450 °C with 24.1 MPa and TiO_2/G nanocomposite was prepared through thermal annealing route[98] to use in this research as nano-additives.

2.2.3. Graphene (G)

Graphene is mostly a 2D flat monolayer with honeycomb lattice arrangement, consist of tightly packed sp^2 carbon atoms.[74] Also, graphene is an extraordinary material, is the core element for vast array of nano-products in all 0D, 1D, 2D and 3D forms including, quantum dots, nanoparticles, nanoflowers, nanosheets, nanotubes, fullerene, thus applicable in diverse products and applications. This is owing to its excellent physical and chemical properties because of enormous collection of allotrope forms (Figure 2.22).[74, 101, 105]

There are many routes to synthesize of graphene. Examples include mechanical exfoliation, which was recorded as the first methodology utilized to produce single layer graphene in 2004. The methods are defined as a) top down (TD) and b) bottom up (BU) approaches. For example, mechanical exfoliation, chemical exfoliation, chemical synthesis, for TD and CHFS, CVD, microwave synthesis for BU are few methods among many techniques in use correspondingly. [74, 102]

The extraordinary mechanical, electrical, optical and thermal properties of graphene such as: high SSA (2630 $m^2 g^{-1}$), Young's modulus (~ 1.0 TPa), intrinsic mobility (200,000 $cm^2 V^{-1} s^{-1}$), thermal conductivity (~ 5000 $W m^{-1} K^{-1}$), optical transmittance (~97.7%) etc., paved the way for exponential researches leading to different applications ranging from bioscience to aerospace engineering.[74, 91, 102] Nevertheless, Meng, et al.,[103] who studied the tribological properties of graphene, utilized facile chemical reduction assisted with supercritical CO_2 ($scCO_2$) to synthesis silver /graphene nanocomposites (Sc–Ag/GN). Used mineral oil 10W40

as base-stock to blend with Sc-Ag/GN as nano-additives and observed the enhancement of COF and WSD by 30.4% and 27.4% respectively, with the 0.06% ~ 0.1 wt.% concentration. Similarly, Song, W., et al.,[84] used GNS/MoS_2 nanocomposites as ICE lubricant additive and reported improvements. Song, H. J., et al.,[85] utilized α-Fe_2O_3 nanorod/graphene composites and reported tribological enhancement.

Uthman, et al.,[75] and Ali, et al.,[89] are among many to notice the hydrophobic/nonpolar nature of graphene, which affects its application as an additive in lubrication. Despite the assortment of simulating characteristics, agglomeration and sedimentation is the end result due to van der Waals attraction and π-π stacking among molecules. However, it was found that, adding polar functional groups; hydroxyl, carboxyl or hydroxy-epoxide groups will enhance the stability of graphene suspended solution with varying tribological characteristics.[104] Besides, it is obvious that graphene is likely to be used in various dissimilar engineering products with intergraded properties by combining with other capable materials/functional groups.[75, 101, 104, 105, 106] Thus, in-addition to TiO_2/r-GO (Section 2.2.2.), nanocomposites Al_2O_3/G and TiO_2/G were synthesized via thermal annealing to blend with mineral and bio base-stocks in this research.

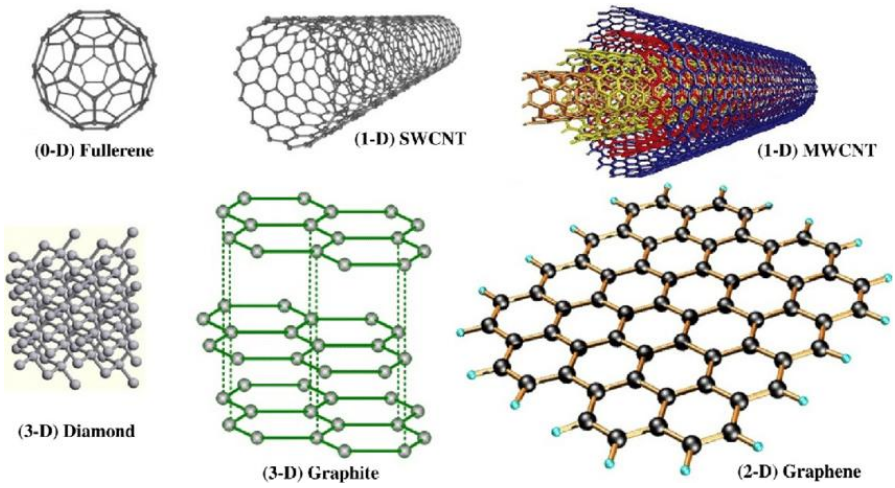

Figure 2. 22, Different forms of graphene allotropes,[105]

2.3 Bio-lubricants

Contemporary mineral-based lubricants begins with the invention of bitumen from mineral crude oil, albeit it is accepted that the humankind used bio-lubricants; fatty acids or animal fats as the mode of lubrication before inventing crude oil.[107] In contrast, modern

scientists are in pursuit for substitutes, either to replace or reduce the consumption of crude oil derivatives lubricants to mitigate escalating ecological concerns. The lubricants, which are prepared from bio-based raw materials, such as plant oil, animal fats and other ecologically friendly resources, that are renewable, biodegradable and nontoxic to human and other live organisms have been attributed to the term "bio-lubricant".[83] Bio-lubricants have been proven to have superior biodegradability, low toxicity, higher viscosity index, recyclable and renewable compared to mineral-based lubricants, thus good factors to substitute mineral-based lubricants.[17, 107] Nonetheless, one of the limitations observed for bio-lubricants are low temperature characteristics; wax formation, poor cold flow, higher pour point (PP), and low oxidative stability are the qualities in need of enhancements.[17, 19] There are numerous bio-lubricants containing plant oils or animal fats in use with reasonably identical molecular structures, commonly known as triglyceride molecules. Figure 2.23 illustrates a typical bio-lubricant (triglyceride) molecule which consists of 2 main segments: glycerol and fatty acid (FA). Glycerol segment consists of 3 linked hydroxyl groups and FA segment contains long chain saturated and unsaturated hydrocarbons with carboxyl group at one end. The hydroxyl groups of glycerol part had esterified with carboxyl group of each FA in a triglyceride molecule.[17] Syahir, et al.,[17] remarked that, there are 3 types of natural FAs found in vegetable oils such as, saturated, monounsaturated, and polyunsaturated as illustrated in Table 2.6. Nevertheless, coconut oil (CCO), is with the botanical term "*Cocos nucifera"* has been selected in this research because of the availability in the geographical region (south Asia; India, Sri Lanka). CCO is an edible oil used in many dietary products and as a cosmetic to enhance hair and skin growth for thousands of years in the region.[108]

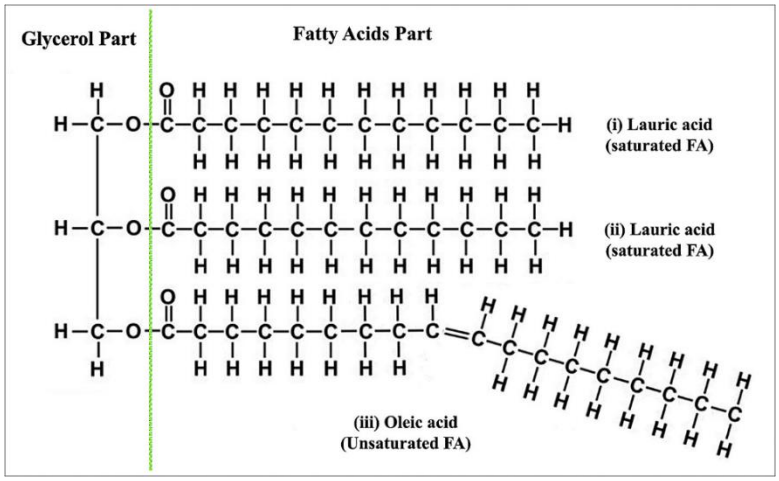

Figure 2. 23, Typical illustration of a bio-lubricant molecule[17]

2.3.1 Structure and characteristics of coconut oil

Zainal, et al.,[107] documented that long chain length, linear chain, low unsaturation, and high polarity were the key factors for a better lubricity of a lubricant for machinery lubrication. Also, noted that CCO been used as a lubricant in scooters in South India had shown improved engine pickup and mileage, generating less smoke compared to conventional lubricants.

From Table 2.6 it is observed that CCO is constituted with 83.4%, 7.8% and 8.8% of saturated FAs, unsaturated FAs, and unknown elements respectively. Constituents are C8:0-Caprylic acid 7.6%, C10:0-Capric acid 5.5%, C12:0-Lauric acid 47.7%, C14:0-Myristic acid 19.9% and C18:0-Stearic acid 2.7% for saturated FAs and monounsaturated C18:1-Oleic acid, 6.2% and polyunsaturated C18:2-Linoleic acid 1.6% (Table 2.6). Low unsaturated FA composition provides better oxidation stability, albeit less long chain molecules,[107] high PP (21-24 °C)[17, 107] are some of the drawbacks of CCO, regardless of its superiority over other qualities of conventional lubricants. CCO contains 6.2% of oleic acid with unsaturated C=C double bond, (Table 2.6) which is significant in creating branches to inhibit the progression of crystallization,[17, 107, 109] Delaying the crystallization will enhance the flow behavior at low temperatures,[40] albeit percentage may require improvement. In contrast, increase of unsaturated FA concentration will affect oxidation stability.[17, 107, 109]

Moreover, CCO constituents are FAs with carboxyl (-COOH) functional groups in its chain ends (Fig. 2.23), which are polar molecules capable of generating physisorption film with metal substrate under normal temperature because of the polarity attractions. Besides, 83.4% of CCO constituents are with linear molecular chains (C8:0-7.6%, C10:0-5.5%, C12:0-47.7%, C14:0-19.9%, C18:0-2.7%, Table 2.6), hence enable to create closely packed monolayers with weak bonds between adjoining molecules as shown in Figure 2.10, to improve the stability of the film.[15, 27] However, ICE's EP-BL environment is with elevated temperature near 100 °C. Therefore, formation of soap layers as chemisorption films is possible with viable reaction path; formation of iron or metal hydroxides using water vapor which enters with the intake air and reaction of metal hydroxide with lauric or stearate acid which are constituents of CCO.[15, 27, 51] Albeit, continuous sliding with high reciprocating velocities will affect to regenerate nascent layers, thus reduction of friction with elevated

wear is presumed, because of probable micro pitting or removal of metal molecules with incessant regeneration of soap layers on substrate.

2.3.2 Physicochemical properties and application of coconut oil

Table 2.7 summarizes the physicochemical properties of CCO. Higher PP (21~24 °C), TAN (1.99 ~ 12.8 KOH mg g^{-1}) and viscosity at 100 °C (5.5 $mm^2 s^{-1}$) are the drawbacks which need attention. Nonetheless, this situation could be improved by using additives. For example, Syahir, et al.,[17] Zainal, et al.,[107] Kumar et al.,[110] assessed procedures such as addition of additives, emulsification, and chemical modification; transesterification, epoxidation and hydrogenation to lower the PP or to improve substandard cold flow properties of coconut oil.

Babu et al.,[111] lowered the PP of CCO from 26.8 °C to -4.5 °C via alkyl esterification by extracting glycerol molecules. Albeit experienced negative tribological performance compared to untreated CCO. Therefore, supplemented tricresyl phosphate, oleic acid and ethylene vinyl acetate and observed the reduction of COF and wear by 12.8% and 2.3% respectively with further reduction of PP down to -6.9 °C.[111] Sharma et al.,[112] observed triboligical enhancement of vegetable oil via chemical modification by incorporating thiols forming thioether hydroxy vegetable oil. Bahari,[113] noted that adding 2% of ZDDP to coconut oil performed well to reduce COF and wear better than reference oil SAE 20W50.

Table 2. 6, Fatty acid composition of some common vegetable oils,[17]

	Saturated fatty acids (%)									Unsaturated fatty acids (%)									
	C8:0	C10:0	C12:0	C14:0	C16:0	C18:0	C20:0	C22:0	C24:0	C16:1	C17:1	C18:1	C18:2	C18:3	C20:1	C20:2	C22:1	C22:2	C24:1
Safflower	–	–	–	0.10	6.70	2.40	–	–	–	0.08	–	11.50	79.00	0.15	–	–	–	–	–
Grapeseed	0.01	–	0.01	0.05	6.60	2.40	–	–	–	0.08	–	14.30	74.70	0.15	0.40	–	–	–	–
Silybum marianum	–	–	0.01	0.09	7.90	4.50	2.60	–	–	0.05	0.03	20.4	63.3	0.88	0.15	–	–	–	–
Hemp	–	–	–	0.07	6.40	2.60	–	–	–	0.11	–	11.50	59.4	3.36	16.5	–	–	–	–
Sunflower	–	–	0.02	0.09	6.20	2.80	0.21	–	0.31	0.12	–	28.0	62.2	0.16	0.18	0.09	–	–	0.39
Wheat germ	–	–	0.07	–	17.40	0.70	–	–	–	0.21	–	12.70	59.7	1.20	7.91	–	–	–	–
Pumpkin seed	–	–	–	0.17	13.10	5.70	0.47	–	–	0.12	–	24.90	54.2	0.12	1.08	–	–	–	–
Sesame	–	–	–	–	9.70	6.50	0.63	0.14	–	0.11	–	41.5	40.9	0.21	0.32	–	–	–	–
Rice bran	–	–	–	0.39	20.0	2.10	–	–	–	0.19	–	42.70	33.1	0.45	1.11	0.11	–	–	0.38
Almond	–	–	0.09	0.07	6.80	2.30	0.09	–	–	0.53	–	67.2	22.8	–	0.16	–	–	–	–
Rapeseed	–	0.01	–	–	4.60	1.70	–	–	–	0.21	–	64.7	19.60	1.20	9.10	–	–	–	–
Peanut	–	–	–	0.04	7.50	2.10	1.01	–	1.66	0.07	–	71.1	18.20	–	–	–	0.12	–	–
Olive	–	–	–	–	16.50	2.30	0.43	0.15	0.06	1.80	–	66.4	16.40	1.60	0.30	–	–	0.05	–
Extra virgin olive	–	–	–	–	8.70	3.47	0.46	0.13	0.05	0.51	0.25	76.34	8.64	0.75	0.34	–	–	0.19	–
Coconut	7.60	5.50	47.70	19.90	–	2.70	–	–	–	–	–	6.20	1.60	–	–	–	–	–	–
Borage seed	–	–	–	0.06	8.75	3.46	0.22	0.30	0.11	0.29	0.07	16.52	38.47	22.97	4.05	0.35	2.23	–	2.09
Canola	–	–	–	0.06	3.75	1.87	0.64	0.35	0.27	0.21	–	62.41	20.12	8.37	1.54	0.11	–	–	0.26
Corn	–	–	–	–	10.34	2.04	0.44	0.31	0.26	–	0.05	24.23	60.38	0.99	0.28	–	–	–	0.20
Cottonseed	–	–	–	0.77	21.87	2.27	0.26	0.36	0.12	0.47	0.11	16.61	56.35	0.33	0.14	0.10	–	–	0.16
Evening-primrose	–	–	–	0.04	5.47	1.83	0.30	0.31	0.09	–	0.06	7.50	74.00	9.76	0.24	0.14	–	–	0.19
Linseed		–	–	0.05	4.81	3.03	0.20	–	0.01	–	0.12	21.42	15.18	54.24	0.40	0.39	–	–	0.10
Soybean	–	–	–	0.06	9.90	3.94	0.41	0.48	0.21	0.08	0.08	21.35	56.02	7.15	0.22	–	–	–	–
Palm	–	–	–	1.12	42.70	4.55	0.39	0.58	0.06	–	0.06	39.37	10.62	0.21	0.17	–	–	–	0.06
Palm kernel	3.43	3.23	46.14	16.17	8.65	2.27	0.15	–	0.30	–	–	16.46	2.76	–	0.17	–	–	–	0.27
Castor bean	–	–	–	–	1.30	1.20	–	–	–	–	–	89.70	7.30	0.50	–	–	–	–	–

Table 2.7, Physicochemical properties of coconut oil[17, 83, 109]

Properties	Coconut oil
Density @ 15 °C (Kgm^{-3})	0.919 ~ 0.937
Kinematic viscosity @ 40 °C (mm^2s^{-1})	24.8
Kinematic viscosity @ 100 °C (mm^2s^{-1})	5.5
Viscosity Index (VI) (-)	169
Flash point (°C)	325
Pour point (°C)	21~ 24
Total acid number (TAN) (KOH, mg g^{-1})	1.99 ~ 12.8

There are many researchers, experimented via numerous paths to enhance cold flow properties of CCO using different chemicals as encapsulated in Table 2.8, with the focus of inhibiting macro-crystallization, leading to micro-crystallization by impeding self-molecular stacking advancing to improvements on poor cold flow behavior of CCO.[114] From another development, Gulzar,[83] used CuO, MoS_2 and $TiSiO_4$ nanomaterials as additives in trimethylolpropane (TMP) originated from palm oil to study the tribological behavior of nanoparticles as additives in bio base-stocks and observed the best tribological performance from the blend consist of 0.75 wt.% of nano-$TiSiO_4$ with palm oil TMP ester. The observations were 68% and 50% reduction of COF and wear volume respectively. In addition, with long hours of real time engine tests observed that, the 17% viscosity reduction along with 30% and 16.8% increase of TAN and oxidation respectively, thus degradation of nano/bio lubricant with the usage. Abdulrahiman, et al.,[115] observed the enhancement of tribological performance by adding 0.5 wt.% of nano CuO to CCO. Abere,[92] utilized nanoparticles of Al_2O_3, SiO_2 and graphite, 0.1 wt.% with untreated rapeseed oil and formulated mineral oil SAE15W40 and observed the enhanced tribological performance with combined additives; nanoparticles and ZDDP together, conforming the nanoparticle's ability to work in synergy with ZDDP. Talib, et al.,[116] used hexagonal boron nitride in many concentrations with modified jatropha oil and observed the best COF and wear reduction of 76% and 26% respectively with the 0.55 wt.%. Jibin, et al.,[117] acknowledge the optimized COF and wear reduction performance by the combination of CCO and hybrid Ce-Zr nanoparticles, 0.62 wt.%, with improved thermo-physical properties. However, Alves et al.,[118] noted the ineptness of adding nano-additives to bio-lubricants to abate wear. ATC-

Europe,[11] Mehic[61] and Heinemann, et al.,[62] acknowledged that, PMMA and ZDDPs could be added as pour point dispersants (PPD) and antioxidant respectively, albeit those are having many functionalities such as; PMMA as a PPD and VM and ZDDP as VM, FM, AW, AO and many, as reviewed in Section 2.1.5.1.

It is obvious that there are numerous paths, adding chemicals, nano/macro particle additives could enhance functionalities of an engine lubricant. Albeit formulating an engine oil while enhancing overall performance of an ICE is the necessity, despite of optimizing particular area of functioning, which require a comprehensive awareness of synergistic or antagonistic behavior of the constituents, compounds or additives on each other (Section 2.1.5.1).

In summary, formulation of a comparative/competitive bio-lubricant using CCO as base stock requires structural tuning to impede or mitigate the identified imperfect characteristics. Thus, require in-depth understanding with following structural alterations.

- Could inhibit progression of macro crystallization by adding more unsaturated FAs to create branching utilizing C=C double bonds, allowing progression of micro crystallization leading to lower PP of CCO.
- Adding more unsaturated FAs will influence oxidation by developing free radicals.
- Formation of metal oxide layers on metal substrate at EP – BL circumstance will help to protect sliding interface by impeding metal to metal contact.
- Continuous formation of nascent layers by saponification or oxidation will precede to remove more metal particles from sliding interface, thus resulting erosion and excessive wear.

Oxidation is a series of reactions, is a challenge to abate when started, albeit if not restricted will lead to the growth of acidic substances, significant in sludge, soot and emulsion like compound formation within a lubricant.

Table 2.8, Summary of different additives used in CCO as pour point depressants (PPD) and antioxidants (AO)

Year	Ref	Coconut oil (wt.%)	Additive		PPD		AO		Blending	Improvement	
			Type	wt. %	Type	wt. %	Type	wt. %		PP (^{0}C)	OS (%)
2009	109	85	styrenated phenol	15	NIL		NIL		Magnetic stirrer	12	
		99.5			polymethyl methacrylate	0.5				18	
		50	Sunflower oil	50						18	
2018	114	80	Poly alpha olefin 4 (PAO4)	20	Ethylene co-vinyl acetate	1	2, 6 Di-tetra butyl phenol	1.5	Magnetic stirrer	12	9
2019	115	94.5	n-CuO	0.5	Ethyl cellulose	3	Butylated hydroxyl toluene	2	Magnetic stirrer	13	not effected

Key: PP – Pour point, OS – Oxidative stability, AO – Anti Oxidant

3. Chapter 3: Research Methodology

The focus of this research is to propose a lubricant formulation, which optimizes engine performance by reducing friction, wear, exhaust emissions, thus saving energy and helping the environment (Section 1.2). Therefore, to achieve the set objectives, different formulations of blended lubricants were examined according to their ability to reduce (i) friction, (ii) wear, (iii) fuel consumption, (iv) control of exhaust emissions. Comparisons were made with the tribological performance of the selected reference engine lubricant; formulated mineral-based engine oil, 15W40. Besides, different nanomaterials and a bio-lubricant were selected as additives and as a base stock correspondingly, because of their superior and ecofriendly qualities as discussed during the literature review (Sections 2.2 and 2.3). To compare tribological performance of different lubricants on engine components, numerous linear reciprocating tribometer (LRT) tests were conducted with each blended lubricant to examine friction force (FF) and coefficient of friction (COF) under different test protocols. Tests were done using real engine piston ring and cylinder liner segments, as test specimens. This is to simulate a running ICE situation. In-addition to the results of friction tests, the wear scares obtained on test specimens, and other data collected from performance tests; fuel consumption, exhaust emissions, particle content of used oil and physiochemical properties of each lubricant sample were analyzed separately for a viable conclusion.

Therefore, the whole program has been divided into four segments for easy reference as mentioned below:

1. Synthesis and characterization of nanomaterials
2. Enhancement of physicochemical properties of CCO
3. Blending and stability studies of sample lubricants
4. Performance tests

Material: Virgin coconut oil (CCO) was procured from local mills in Sri Lanka. Reference oil "15W40" (CEYPETCO/CALTEX) had the following specification, with parameter values in the range specified:

Total base number (TBN): 9.8 – 10.2 (mg KOH g^{-1})

Kinematic viscosity at 40 °C: 109 – 115 ($mm^2 s^{-1}$)

Kinematic viscosity at 100 °C: 14.1 – 15.1 ($mm^2 s^{-1}$)

Viscosity Index: 130 – 137 (unitless)

15W40 was purchased from the Ceylon petroleum cooperation (CEYPETCO), Sri Lanka and sunflower oil (SF), styrenated phenol (SP), and oleic acid (OA) were from GLORCHEM Enterprise, Sri Lanka.

Nanomaterials: Al_2O_3 and graphene were procured from XF-NANO Co., Ltd., China. All other chemicals: nano precursors, antioxidants, viscosity modifiers, were procured either from Sigma-Aldrich, UK and Fisher Scientific, UK.

3.1 Synthesis and characterization of nanomaterials

Analysis of characteristics of the material used in the experiment is an essential factor to optimize performances of the formulated lubricants. Therefore, characterization and analysis of properties of the nanomaterial to performing within a lubricant as desired within the tribological domain is vital for the success of this investigation.

In this study, Al_2O_3, TiO_2, graphene (G) and TiO_2/reduced graphene oxide (r-GO), TiO_2/G, Al_2O_3/G, nanocomposites were selected as nanomaterials of interest, with reference to the recommendations of previous researchers observed through the literature.[8, 9, 14, 79, 86, 88, 89] In-addition to Al_2O_3 and G, TiO_2 and TiO_2/r-GO nanomaterials were synthesized through the CHFS method, and Al_2O_3/G and TiO_2/G via the thermal annealing.

3.1.1 Synthesis of nano-particulates of interest

Nano TiO_2 was synthesized via CHFS route as illustrated in Figure 3.1. Aqueous solution of titanium bis ammonium lactato dihydroxide (TiBALD; Ti^{+4}), and KOH were used as precursors with deionized (DI) water as reaction media through three feed pumps namely, F1, F2 and F3 (Fig. 3.1). In detail, F1: DI water at 20 ml min^{-1}, F2: 0.2M Ti^{+4} precursor at 10 ml min^{-1} and F3: 1M KOH at 10 ml min^{-1} of concentrations and flow rates, where F2 and F3 meets at a "T" junction for premixing precursors at room temperature before entering the reactor.[75, 98] This feed met with supercritical water (fed from F1 via heater to reach at 450 °C with 24.82 MPa [3600 psi] pressure) where the reactions occur; hydrolyzation, dehydration, condensation and thermal decomposition leading to nucleation and growth. Suggested

reaction paths for formation of titanium dioxide nanoparticles are as follows:[75] (reaction 1 for hydrolysis and 2 for dehydration)

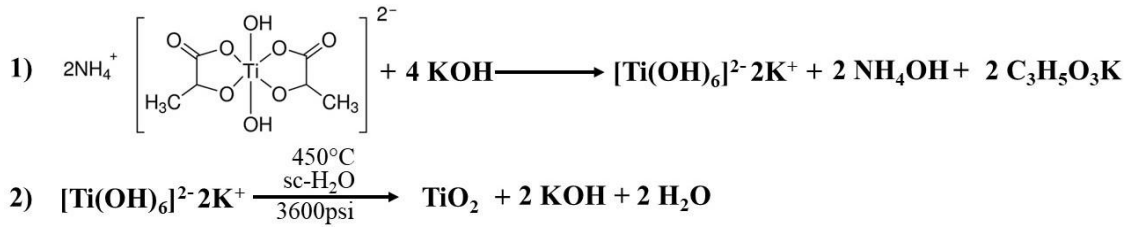

Thereafter, the aqueous suspension was collected in a collection vessel via back pressure regulator (BPR) after cooling through the cooler. The product was centrifuged for 15 minutes at 9000 rpm (using THERMO / SORVALL RC 6 PLUS centrifuge) to separate precipitate from the supernatant. Cleaning of precipitate with DI water was repeated until pH 7 was achieved. The collected wet solids were freeze-dried (ca. 24 h) and prepared for characterization.[79]

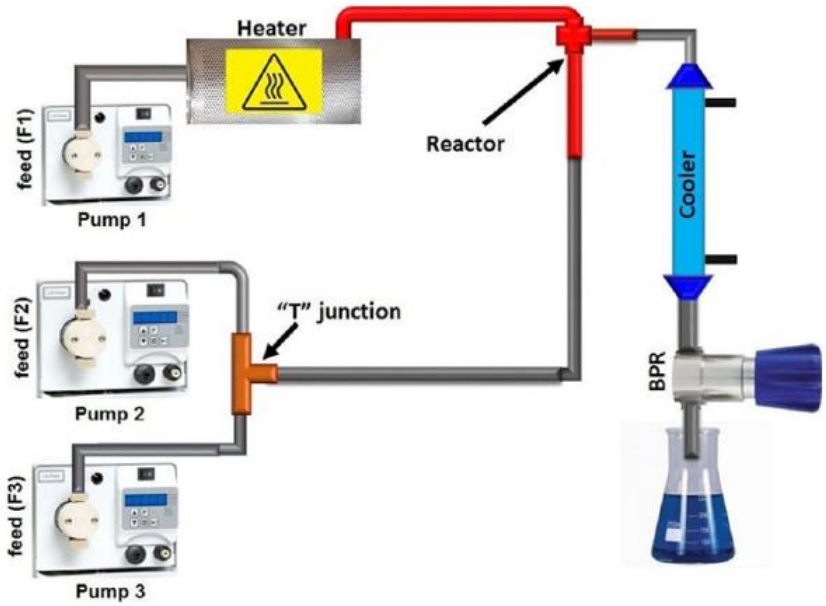

Figure 3. 1; Schematic illustration of CHFS process,[75]

Likewise, TiO_2/r-GO nanocomposite was synthesized using similar approach, albeit with different feeds, such as, F1: DI water at 20 ml. min^{-1}, F2: 0.2 M Ti^{+4} precursor at 10 ml min^{-1} and F3: 1M KOH + 0.5 mg ml^{-1} of GO at 10 ml min^{-1}.

Moreover, nanocomposites Al_2O_3/G and TiO_2/G were synthesized via traditional thermal annealing route with following sequence.[76] Initially 95.0 wt.% nanoparticles (Al_2O_3 and

TiO_2) and 5.0 wt.% of graphene were mixed manually in a beaker with 300 ml of isopropanol before sonication. Then the mixtures were sonicated for 1hour using ultrasonic mixer (KERRY - KS 200) followed by centrifuging at 8000 rpm for 3 hours (utilizing THERMO / SORVALL RC 6 PLUS centrifuge). Thereafter, the slurry was kept in an oven and annealed for another 3 hours at 280 °C (using MICROMERITICS FLOW-PREP 060), using an argon gas supply to avoid oxidation during processing. The final products were processed for characterization.

3.1.2 Characterization of nanomaterials of interest

Selected nanomaterials were characterized utilizing a variety of techniques including,

- Transmission electron microscopy (TEM)
- X-ray powder diffraction (XRD)
- Raman spectroscopy
- X-ray photoelectron spectroscopy (XPS)
- Fourier Transform Infrared spectroscopy (FT-IR)

TEM was used to observe morphological statistics in ultrafine scale, specifically for material characterization in atomic or nano scale.[119] Thus, a transmission electron microscope "JEOL-JEM-2100" at the acceleration voltage of 200 kV with magnification up to 400k was used to characterize the materials. Captured high resolution images were analyzed for particle size and lattice fringe spacing with the assistance of "ImageJ" software.

XRD is regarded as the fingerprint for material characterization and identification of polycrystalline phases.[120, 121, 122, 123]

XRD technique was used to examine the crystalline structures of nanomaterials used in this project. Diffraction patterns of nanomaterials were observed by deploying X-Ray diffractometer (Bruker D8 Advance) with "DIFFRAC.EVA" software. Experimental conditions were, Cu-Kα radiation (1.5406 Å), voltage of 40 kV, current of 40 mA, 2θ range from 5° - 80°, with three different scan rates:

i. Step size of 0.021° with scan speed of 1.0 s/step - graphene, TiO_2, Al_2O_3 and Al_2O_3/G
ii. Step size of 0.021° with scan speed of 1.2 s/step - TiO_2/G
iii. Step size of 0.010° with scan speed of 3.0 s/step - TiO_2/r-GO

Raman spectroscopy is a technique which uses inelastic scattering of a laser beam incident on test material because of the interaction between light and the chemical bonds of the material. This scattering provides comprehensive evidence on chemical structure, crystallinity, phase, polymorphs, and molecular interactions because of functional group bonds such as; C-C, C=C, N-O, C-H and likes.[124 - 128]

In this study two Raman microscope spectrophotometers (Horiba LabRam HR Evolution and Horiba LabRam 800) were utilized for the identification of nanomaterial composition required to characterize the different nanomaterials. Table 3.1 presents the different parameters applied for the different nanomaterials. Two dissimilar wavelengths; 532 and 633 nm were selected for the investigation with the availability of equipment. Because lower wavelengths will provide stronger Raman signal with high resolution imaging, however material may spoil with the high intensity of shorter wavelength laser beams.

Table 3.1, Equipment details and different test parameters applied for the Raman analyses on nanomaterials used in the research

Nanomaterial	Equipment	Laser power (mW)	Laser (nm)	Grating (gr mm^{-1})	resolution (cm^{-1})	Acquisition time (s)
Graphene	Horiba LabRam HR Solution	100	633	1800	0.35	10
TiO_2		100	633	1800	0.35	10
TiO_2/G		100	633	1800	0.35	10
TiO_2/r-GO		100	633	1200	0.35	10
Al_2O_3	Horiba LabRam 800	50	532		1.5	10
Al_2O_3/G		50	532		1.5	10

Ejection of electrons from a sample surface by absorbing energy from photons incident by an X-ray beam is the principle of **XPS**, which is also known as electron spectroscopy for chemical analysis (ESCA).[129-131] High energy Al-Kα and Mg-Kα (1000 – 1500 eV)[129, 132] are the typical sources used for this irradiation, which allow to measure the kinetic energy of photoelectrons to determine the binding energy (Be) of ejected electrons.[130, 133]

XPS is used in this experiment to observe the elemental composition and functional groups associated with the nanomaterials involved in the research. The surface chemistry was evaluated by XPS performed in an AXIS Ultra DLD (Kratos Surface Analysis) setup, using Al $K_{\alpha 1}$ (1486.74 eV) radiation produced by a monochromatized X-Ray source at operating power of 192 W (16 kV × 12 mA). The base pressure in the analysis chamber was 1.0×10^{-8} mbar. Charge compensation was reached by using a flood gun operating at 1.5 A filament current, 2.7 V charge balance, 1.0 V filament bias. High resolution core level spectra have been recorded using hybrid lens mode, 50 eV pass energy and slot aperture.

FT-IR spectroscopy is used to identify the different functional groups or molecular fingerprint of formulated coconut oil (FCO) and nanomaterial utilized in this experiment. [134-136]

The conventional region for FT-IR spectroscopy is 4,000 ~ 400 (cm^{-1}), however the span of infrared region is 12,800 ~ 10 (cm^{-1}).[134] FT-IR spectrophotometer "SHIMADZU IR-AFFINITY 1" was used in this experiment for aforesaid characterization.

3.2 Enhancement of physicochemical properties of CCO

CCO was selected as the bio-lubricant, because of its ample availability in the region. CCO is a popular edible oil with significant tribological properties coupled with substandard; poor cold flow, higher TAN and low kinematic viscosity at 100 °C, albeit not much research evidence compared to other bio-lubricants.

From Table 2.7 it was observed that the CCO has kinematic viscosity of 5.5 ($mm^2\ s^{-1}$) at 100 °C, pour point (PP) of 21 ~ 24 °C (below this temperature, the oil is not able to flow), and TAN of 1.99 ~ 12.8 (mg KOH g^{-1}).[17, 83, 109] These characteristics are the significant substandard that need improvements compared to the mineral oil (15W40). With reference to many standards TBN of diesel engine oils should be ≥ 7 (mg KOH.g^{-1})[137, 138] for unused oil. Used oil require TBN above TAN to neutralize acidity within a lubricant during its life cycle, which is a deciding factor for its service life.[60, 139, 140] Nevertheless, from the literature it was elucidated that many researchers had dissimilar approaches with numerous additives/compounds and methodologies to improve the properties of CCO. PMMA, polymer with different weights are widely used as a pour point depressant (PPD) and viscosity

modifier (VM).[11, 51, 61, 68, 69, 109] In-addition, SF, SP, and OA are few chemicals, that are also applied to improve PP of CCO.[109, 111, 114, 115] ZDDP is used as a multi-purpose additive, such as VM, anti-oxidant (AO), friction modifier (FM), anti-wear (AW), and as a dispersant in contemporary mineral-based lubricant industry.[11, 51, 61, 64] Thus, PMMA, SF and SP as PPD and ZDDP, PMMA, and KOH were mixed with CCO to enhance its properties as details given below.

3.2.1 Depression of the PP of CCO

Three different chemicals; PMMA (Mw˜15,000), SF, and SP were blended with CCO in different concentrations; 4 weight concentrations (0.25. 0.5, 0.75 and 1.0 wt.%), of PMMA and 4 volume concentrations (5, 10, 15 and 20 v/v%), of SF and SP, details are summarized in Table 3.2. All twelve mixtures were blended using an ultrasonic mixer (KERRY - KS 200) for 1 hour followed by 2 hours of further agitation using magnetic stirrer hotplate (Thermo Scientific – CIMAREC^{+}) for homogeneous solutions.

PMMA and SP were added to CCO with reference to Ajithkumar's observations,[109] and SF was added, because of low PP (-12 °C),[17, 109] and 91.14% of high unsaturated FA concentration [18:1, OA – 28.0%, 18:2, linoleic acid – 62.2% (Table 2.6)].[17]

Subsequently, all samples were analyzed utilizing the thermo-analytical technique via differential scanning calorimetry (DSC) tests using endothermic and exothermic reactions. The best concentration from each category was further tested using a pour point tester (Stenhope – Seta) following ASTM D97-96a standard procedures.

These 12 samples (Table 3.2) are for improving sub standards of CCO, thus will not carry forward after formulating CCO (with enhanced physicochemical properties), for any tribological or other related investigations

Table 3.2, Sample descriptions and compositions of chemicals used as PPD to improve the PP of CCO

		Composition				
		Base stock		PPD		
		CCO		PMMA	SF	SP
S/N	Sample no	(wt.%)	(v/v%)	(wt.%)	(v/v%)	(v/v%)
1	**PM25**	99.75	x	0.25	x	x
2	**PM50**	99.50	x	0.50	x	x
3	**PM75**	99.25	x	0.75	x	x
4	**PM100**	99.00	x	1.00	x	x
5	**SF0.5**	x	95.00	x	5.00	x
6	**SF1.0**	x	90.00	x	10.00	x
7	**SF1.5**	x	85.00	x	15.00	x
8	**SF2.0**	x	80.00	x	20.00	x
9	**SP0.5**	x	95.00	x	x	5.00
10	**SP1.0**	x	90.00	x	x	10.00
11	**SP1.5**	x	85.00	x	x	15.00
12	**SP2.0**	x	80.00	x	x	20.00

Key: CCO – coconut oil, PPD – pour point depressant, PMMA – polymethylmethacrylate, SF – sunflower oil, SP – styrenated phenol,

3.2.2 Differential scanning calorimetry (DSC) tests

The quantity of heat transferred by absorption or extraction from the sample and the reference as a function of temperature is the principle used in DSC tests. That is, the measure of the difference of heat flow between a sample and the reference, while both are at the same temperature. This is because of heat absorbance or dissipation by the sample as of phase transition from solid to liquid or liquid to solid state depending on the ongoing endothermic or exothermic process, respectively.[109, 141, 142, 143]

Figure 3.2 illustrates a typical DSC arrangement where sample and reference are placed in different pans located in a hermetic chamber. The chamber is covered/constituted with aluminum alloy to prevent radiation, for good heat conducting and to prevent external

thermal agitation. Also equipped with heat cells for heating and liquid nitrogen circulation for cooling, thermocouple with a computer for setting test parameters, data acquisition and analysis.

During this research DSC apparatus ("DISCOVERY – TA DSC 25") was utilized for the tests at first with inbuilt software ("UNIVERSAL ANALYSIS") for computer integration. In-addition, TA instrument "Q2000 DSC" was used during final stage DSC experiments.

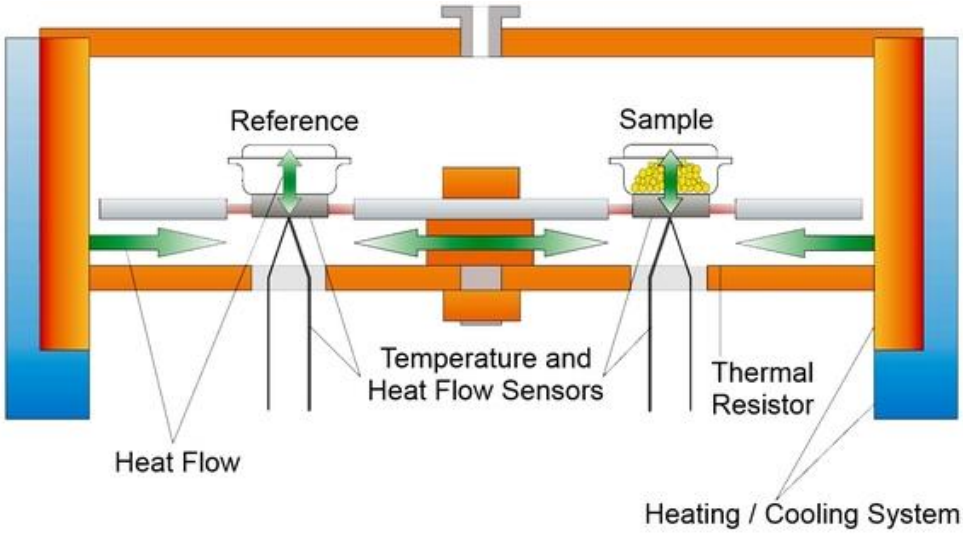

Figure 3.2, Schematic view of a typical DSC test setup,[144]

In this analysis two types of heat exchanges were studied: namely, cooling and heating experiments with the following procedure.

1. **Cooling (exothermic) tests:** Sample and reference were heated up to 50 $^{\circ}$C and kept isothermal for 10 minutes to liquify and normalize any wax-like matter present in oil, which may act as source to accelerate wax crystal formation while cooling. Then allowed to cool down at a steady rate of 10 $^{\circ}$C min^{-1}, until the sample and reference reaches -50 $^{\circ}$C, using liquid nitrogen as cooling media.

2. **Heating (endothermic) tests:** After the sample and reference reached -50 $^{\circ}$C (at the end of exothermic test), heated both at a constant rate of 10 $^{\circ}$C min^{-1}, until reaching at 50 $^{\circ}$C.

Thereafter, samples with best endothermic thermograms from each PPD additive category were tested for PP using "STANHOPE – SETA" cloud and pour point tester following ASTM D97 – 96a guidelines.

3.2.3 Improving viscosity, oxidative stability, and TBN of CCO

PMMA proved to be a good viscosity modifier,[11, 37, 51, 69, 70] thus, was added 0.5 and 1.0 wt.% concentrations to the best CCO/PPD combinations and tested kinematic viscosity at 40 and 100 °C (using "STANHOPE – SETA KN6" and "AMBICA T8006 B" capillary tube and redwood viscometers).[137, 149]

Enhancing TBN or strengthening alkalinity of a lubricant above TAN is an effective remedy to maintain the oil neutralization, which is the deciding factor for its life cycle.[139, 140] Existing diesel engine oils are using over-based detergents, like phenates, sulfonates, salicylates of barium, sodium, magnesium and calcium oxides to derive alkalinity.[145] Besides, dispersants and anti-wear agents has been used to contribute the same.[145] Also, inhibiting oxidative stability will minimize acidic substances formation.[145] ZDDP is proven to be a good additive with many functionalities, including AO, AW, FM, VM and as a dispersant and able to work in synergy with other additives.[92] Therefore, ZDDP was added in 0.5, 1.0, 1.5, 2.0, 2.5 and 3.0 wt.% concentrations as a multi-purpose additive after improving the PP of CCO. Also, hindered phenols are good for radical trapping (Figure 2.16) thus, mixed as an antioxidant in different concentrations in-addition to ZDDP.

Simultaneous thermal analyses (STA) were done via combination of TGA and DSC tests to study the thermal and oxidative stability using STA analyzer (Rheometric Scientific STA 1500) and a calorimeter (TA Instrument – Q2000 DSC). TAN and TBN were tested via titration using "METROHM TITRINO PLUS 848" analyzer following ASTM D664-18 and ASTM D 2896-21 standards respectively.[146-148]

Also, KOH, was added in 0.25, 0.5, 0.75 and 1.0 wt.% concentrations to the best CCO/PPD combination and tested for TAN and TBN following same procedure.

Furthermore, final product; formulated coconut oil (FCO) after improving aforesaid substandard, was investigated via FT-IR (SHIMADZU IR-AFFINITY1) analysis for identifying elements/functional groups associated with the structure of CCO to improve poor cold flow properties.

3.3 Blending and stability studies of sample lubricants

A total of 37 blended lubricants were used in this experiment. All the samples were created, blended in two stages (before and after formulating CCO), which are summarized in Table 3.3. According to the base-stock/additive combination, all 37 samples could be segregated into three lubricant groups as mentioned below:

I. Various weight concentrations of selected nanomaterials blended with mineral base stock; formulated 15W40 (samples S3 to S11 and S26 to S28; Table: 3.3a).

II. Bio-lubricant; CCO blended with treated mineral base stock, 15W40, in different volume concentrations (samples S12 to S16; Table: 3.3a).

III. Various weight concentrations of nanomaterials blended with CCO and FCO (sample S17 to S25 and S29 to S37; Table: 3.3a-b)

There are six varieties of nanomaterials (Al_2O_3, TiO_2, G, Al_2O_3/G, TiO_2/G and TiO_2/r-GO) used in this investigation as nano additives during sample formulation. Details of these nanomaterials are elucidated in Section 3.1. Therefore, the above three groups were further divided into 12 subcategories according to the base-stock/nanoparticle combination. Details of these 12 sample subcategories are presented with Section 3.2.2.

3.3.1 Colloidal stability and surfactants

Formulation of sample blends begins with the blending process, where the stability of dispersed colloids is critical for dependable lubrication functioning. This is because of van der Waals forces and double layer interactions associated between the contents of a solution.[83] Out of three lubricant groups mentioned above, two groups are with nanomaterials. Therefore, suspension stability of nanoparticles in the lubricant is vital for optimum tribological enhancement. There are many methods including electrostatic or steric stabilization of nanoparticles in the solution to establish surface functionalization for formulation stability. Adsorption of ionic surfactant on the nanoparticle surface is the method selected. In this project, oleic acid (OA) [cis-9-octadecenoic acid; $C_{18}H_{34}O_2$] was selected as the surfactant when blending nanoparticles, because of the high polarity resulted from strong monounsaturated fatty acid structure.[83, 94]

3.3.2 Formulation of sample blends

Sample lubricants were blended in two stages: before and after formulating of CCO. CCO was formulated to eliminate or mitigate observed substandard (Section 3.2). Thus, after the second Phase friction tests, all the selected samples with enhanced tribological performance were re-blended using FCO. Moreover, blends S32 – S37 were added to the sample list, which were formulated using FCO and newly synthesized nanocomposites; TiO_2/r-GO, TiO_2/G and Al_2O_3/G (Table 3.3b). In-addition samples S9A and S24A were included in Table 3.3b, which were blended using GO in place of G, as an additive with same compositions as of S9 and S24 with the purpose of studying dispersion stability of GO as an additive in place of graphene in both mineral and bio-based formulations.

There are three constituents for nano-lubricants: mineral/bio base stock, nano-additives, and surfactant and two constituents for mineral/bio combination. Method and time of agitation are vital factors affecting to minimize the size of nanoaggregates leading to a stable and homogeneous suspension.[83] Initially, magnetic stirrer hotplate (Thermo Scientific – CIMAREC$^+$) was used for blending for 4 hours at 1000 rpm with elevated temperature 150 °C. However, as a result of UV-vis absorbance tests it is revealed that, the nanoparticles are unstable in sample blends, thus the mixing method was changed to improve the suspension stability.

During the 2nd stage blending, ultrasonic mixer (KERRY - KS 200) was used for 2 hours for sonicating samples to improve the suspension stability followed by further 2 hours of agitation using a magnetic stirrer hotplate. Instead of nanoparticles of metal oxides and graphene (G), synthesized nanocomposites consist of graphene (G), reduced graphene oxide (r-GO) and metal oxides were utilized to combine the properties of individual nanoparticles to improve the colloidal stability of solutions in addition to tribological enhancements.

Nanoparticle concentration is also an essential feature to enhance suspension stability and tribological behavior of a lubricant.[8, 9, 14, 83] Therefore, 3 weight concentrations 0.1%, 0.25% and 0.5% were selected for the nanomaterials utilized.[8, 9, 14, 89] Likewise, volume concentrations for CCO and 15W40 combinations will be 10%, 25%, 50%, 75% and 90% (table 3.3a). Overall, there are 37 samples with 12 different subcategories (within 3 main groups) as summarized below. Furthermore, sample S38 (FCO) is included in Table 3.3b, which is the base oil for nano/bio lubricant formulations.

1) 15W40 – reference oil
2) 15W40 + OA + Al_2O_3
3) 15W40 + OA + TiO_2
4) 15W40 + OA + G
5) 15W40 + OA + TiO_2/r-GO
6) 15W40 + CCO
7) CCO + OA + Al_2O_3
8) CCO + OA + TiO_2
9) CCO + OA + G
10) CCO + OA + TiO_2/r-GO
11) FCO + OA + TiO_2/G
12) FCO + OA + Al_2O_3/G

Table 3.3a, Elemental composition of sample lubricants – stage 1 (before improving physicochemical properties of CCO)

Sample No	Base oil			Surfactant (OA)		Additives		
	Composition	Concentration		Concentration		Composition	Concentration	
		wt %	v/v %	wt %	v/v %		wt %	v/v %
S1	15W40	100.00	N/A	N/A	N/A	N/A	N/A	N/A
S2	15W40	N/A	98.00	N/A	2.00	N/A	N/A	N/A
S3	15W40	98.00	N/A	1.90	N/A	Al_2O_3	0.10	N/A
S4	15W40	98.00	N/A	1.75	N/A	Al_2O_3	0.25	N/A
S5	15W40	98.00	N/A	1.50	N/A	Al_2O_3	0.50	N/A
S6	15W40	98.00	N/A	1.90	N/A	TiO_2	0.10	N/A
S7	15W40	98.00	N/A	1.75	N/A	TiO_2	0.25	N/A
S8	15W40	98.00	N/A	1.50	N/A	TiO_2	0.50	N/A
S9	15W40	98.00	N/A	1.90	N/A	G	0.10	N/A
S10	15W40	98.00	N/A	1.75	N/A	G	0.25	N/A
S11	15W40	98.00	N/A	1.50	N/A	G	0.50	N/A
S12	15W40	N/A	90.00	N/A	N/A	CCO	N/A	10.00
S13	15W40	N/A	75.00	N/A	N/A	CCO	N/A	25.00
S14	15W40	N/A	50.00	N/A	N/A	CCO	N/A	50.00
S15	CCO	N/A	75.00	N/A	N/A	15W40	N/A	25.00
S16	CCO	N/A	90.00	N/A	N/A	15W40	N/A	10.00
S17	CCO	98.00	N/A	1.90	N/A	Al_2O_3	0.10	N/A
S18	CCO	98.00	N/A	1.75	N/A	Al_2O_3	0.25	N/A
S19	CCO	98.00	N/A	1.50	N/A	Al_2O_3	0.50	N/A
S20	CCO	98.00	N/A	1.90	N/A	TiO_2	0.10	N/A
S21	CCO	98.00	N/A	1.75	N/A	TiO_2	0.25	N/A

S22	CCO	98.00	N/A	1.50	N/A	TiO_2	0.50	N/A
S23	CCO	98.00	N/A	1.90	N/A	G	0.10	N/A
S24	CCO	98.00	N/A	1.75	N/A	G	0.25	N/A
S25	CCO	98.00	N/A	1.50	N/A	G	0.50	N/A
S26	15W40	98.00	N/A	1.90	N/A	TiO_2/r-GO	0.10	N/A
S27	15W40	98.00	N/A	1.75	N/A	TiO_2/r-GO	0.25	N/A
S28	15W40	98.00	N/A	1.50	N/A	TiO_2/r-GO	0.50	N/A
S29	CCO	98.00	N/A	1.90	N/A	TiO_2/r-GO	0.10	N/A
S30	CCO	98.00	N/A	1.75	N/A	TiO_2/r-GO	0.25	N/A
S31	CCO	98.00	N/A	1.50	N/A	TiO_2/r-GO	0.50	N/A

Table 3.3b, Elemental composition of sample lubricants – stage 2 (after improving physicochemical properties of CCO)

Sample No	**Base oil**			**Surfactant (OA)**		**Additives**		
	Composition	**Concentration**		**Concentration**		**Composition**	**Concentration**	
		wt %	**v/v %**	**wt %**	**v/v %**		**wt %**	**v/v %**
S1	15W40	100.00	N/A	N/A	N/A	N/A	N/A	N/A
S9	15W40	98.00	N/A	1.90	N/A	G	0.10	N/A
S9A	15W40	98.00	N/A	1.90	N/A	GO	0.10	N/A
S16	FCO	N/A	90.00	N/A	N/A	15W40	N/A	10.00
S24	FCO	98.00	N/A	1.75	N/A	G	0.25	N/A
S24A	FCO	98.00	N/A	1.75	N/A	GO	0.25	N/A
S29	FCO	98.00	N/A	1.90	N/A	TiO_2/r-GO	0.10	N/A
S30	FCO	98.00	N/A	1.75	N/A	TiO_2/r-GO	0.25	N/A
S31	FCO	98.00	N/A	1.50	N/A	TiO_2/r-GO	0.50	N/A
S32	FCO	98.00	N/A	1.90	N/A	TiO_2/G	0.10	N/A
S33	FCO	98.00	N/A	1.75	N/A	TiO_2/G	0.25	N/A
S34	FCO	98.00	N/A	1.50	N/A	TiO_2/G	0.50	N/A
S35	FCO	98.00	N/A	1.90	N/A	Al2O3/G	0.10	N/A
S36	FCO	98.00	N/A	1.75	N/A	Al_2O_3/G	0.25	N/A
S37	FCO	98.00	N/A	1.50	N/A	Al_2O_3/G	0.50	N/A
S38	FCO	100.00	N/A	N/A	N/A	N/A	N/A	N/A

3.3.3 Absorbance analyses of sample blends over storage time

Suspension stability of nanoparticles within the sample blends was investigated with the aid of optical absorbance spectrum using a double beam UV-vis spectrophotometer (Shimadzu – UV – 1800) having wavelength range of 190-1100 nm with 1 nm bandwidth.

In built “UV Probe” software was used to analyze the observed spectrum data. Samples were examined from 0 – 72 hours in 24-hour intervals and continued up to five weeks in weekly intervals. Furthermore, colloidal stability of G vs GO was investigated using samples S9, S9A, S24, and S24A.

3.4 Performance tests

Performance tests were divided into two sections: 1) Laboratory tests and 2) Field tests. Laboratory tests consisted of friction and wear analyses to investigate frictional force (FF), coefficient of friction (COF), morphologies, elemental deposition, and the surface texture of wear surfaces with different lubricants. Friction tests were implemented using a linear reciprocating tribometer (LRT). Wear scar analysis was performed via scanning electron microscopy (SEM), energy dispersive X-ray spectroscopy (EDX) and 3D noncontact optical profilometry. Field tests were executed using a dynamometer test rig and an industrial engine to investigate fuel consumption, exhaust emissions and for used crank case oil sample analyses respectively.

3.4.1 Linear reciprocating tribometer (LRT) tests

Friction tests were implemented in 3 Phases using an LRT test rig (DUCOM TR – 282). This is to simulate the reciprocating motion of a piston ring/cylinder liner interface of an ICE. Preprograming test protocol with real time display of COF and FF with associated waveforms as a function of prescribed experiment parameters, gaining and processing the data generated including controlling the test rig during the tests was done utilizing custom built “WINDUCOM – 2010” software. Figures 3.3 and 3.4 illustrate the various preparation and operational stages of the LRT test rig.

Initially Phase-I tests were executed on the first 31 samples (blended in stage 1, Table 3.2a) using piston ring and cylinder liner segments as test specimens, with the intension of observing tribological enhancement or reduction of COF and FF by each sample. This is to select the optimum nanoparticle concentration from the first 10 out of 12 subcategories mentioned above.

Phase-II LRT tests were performed with the 10 samples selected from Phase-I tests, which were with best nanoparticle concentration to reduce friction. This is to investigate the lubricant's tribological behavior under two variables: diverse loads and sliding velocities. A total of 16 load/velocity combinations were investigated using the same piston ring, cylinder liner segments as test specimens, to mimic real engine application.

Phase-III tests were performed with the samples blended using FCO (after improving substandard of CCO) and synthesized nanocomposites. Also with two variables, sliding velocity and load thus 25 load/velocity combinations.

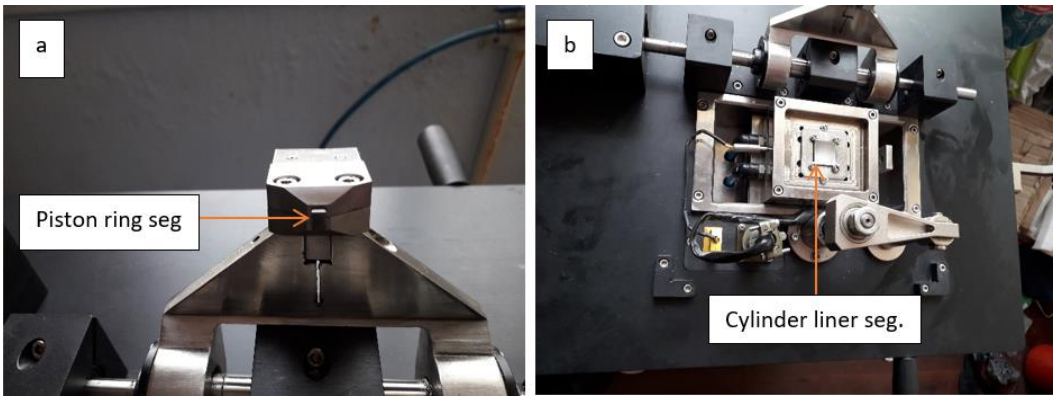

Figure 3.3, Test specimens mounted on LRT test rig, a) piston ring segment in the upper sliding arm holder, b) cylinder liner segment in the lower stationary holder.

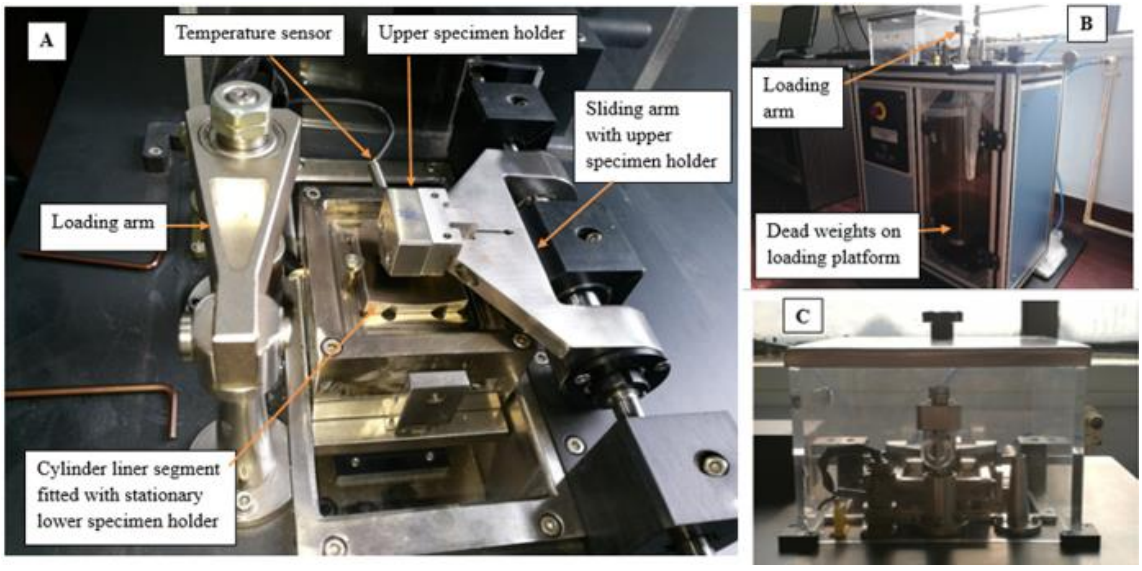

Figure 3.4, Linear reciprocating tribometer (LRT), (A) sliding arm with specimen holder, (B) dead weights with platform and loading arm, (C) test rig in action.

3.4.1.1 Design of LRT experiments

All the LRT tests in three Phases were performed as per the ASTM G181-11 standards.

Phase-I

i. All the tests were performed at 100 °C, after aligning the test specimens axially and laterally to avoid mismatch of curvatures.
ii. A constant mean reciprocating velocity of 0.40 m s^{-1} (with reference to sliding frequency of 20 Hz with 10 mm stroke) with 120 N fixed load were applied.
iii. Total test duration of 3600 seconds (1 hour).

Phase-II

Experiments were done with two variables: different mean reciprocating velocities with different loads to par with real time ICE operation. Four reciprocating velocities reference to four sliding frequency/stroke length combinations (15 Hz × 10 mm, 20 Hz × 8 mm, 30 Hz × 5 mm, and 40 Hz × 2mm) with 120, 160, 180, and 200 N loads.

The test sequence, consisting of 16 segments (velocity/load combinations) is as follows:

i. Constant load of 120 N with varying reciprocating velocities with reference to (a) 15, (b) 20, (c) 30, and (d) 40 Hz sliding frequencies.
ii. Constant load of 160 N with varying reciprocating velocities with reference to (e) 15, (f) 20, (g) 30, and (h) 40 Hz sliding frequencies.
iii. Constant load of 180 N with varying reciprocating velocities with reference to (i) 15, (j) 20, (k) 30, and (l) 40 Hz sliding frequencies.
iv. Constant load of 200 N with varying reciprocating velocities with reference to (m) 15, (n) 20, (o) 30, and (p) 40 Hz sliding frequencies.

All tests were done at 140 °C for 400 s for each segment,[31] thus, total test duration of 6400 s net (≈ 1 hour and 47 minutes). During load changing, (after completing four velocity tests under one load) 200 µl of lubricant was added to simulate oil starving condition of an ICE at TDC.

Phase-III

Test protocol is similar to Phase-II, albeit with 25 load/velocity combinations, five different loads (120, 140, 160, 180, and 200 N) with five different sliding velocities reference

to 15, 20, 30, 40, and 50 Hz of sliding frequencies. Each test was performed for 360 s at 140 °C, thus total test duration of 9000 s (2.5 hours). Also, 200 µl of lubricant was added after every 30 minutes of operation when increasing load to next stage, that is after completion of one load with five velocity combinations.

Test specimens were aligned axially and laterally to avoid mismatch of curvatures during all 3 Phases since specific contact pressures generated at the interface of the piston ring cylinder liner segments during LRT tests are inversely related to the contact areas of the specimens. Contact parameter is an effective limit along with load, speed and material parameters to develop a lubricant film, thick enough to separate rubbing asperities according to Reynold and Hammrock & Dowson predictions (Eq. 2.7 and 2.13).[27, 35-38]

3.4.1.2 Test specimens

Test specimens were fragmented from a new piston ring and a cylinder liner from a heavy-duty Perkins, model 4000 series diesel engine to confirm that the test specimens are with same hardness as real ICE engine components. Therefore, Vickers surface hardness tests were performed following ASTM E92 – 2017 guidelines. The observations are tabulated and presented in Table 3.4.

Contact area of ring segment is approximately equals to 3.8 mm × 7.75 mm = 29.45 mm^2, (Table 3.4) assuming that the ring segment was uniformly aligned on the liner segment mounted in the bottom specimen holder (Figure 3.3b), thus 120, 140, 160, 180 and 200 N test loads represents the contact pressures of 4.08, 4.75, 5.43, 6.11 and 6.79 mPa respectively. Figure 3.5 illustrates the tribo-testing geometry of test specimens, which confirms the elliptical contact area at the interface of reciprocating concave, convex surfaces in contact.[35]

Table 3.4, LRT test specimen specifications

Specimen	Material	Dimension (h x l x w) mm³	Surface finish	Hardness (MPa)	Roughness (S_q) (nm)
Piston ring	Cast steel	5.3 × 7.75 × 3.8	Chrome/Nickel plated	3364	817
Cylinder liner	Cast steel	5.1 × 20.0 × 20.0	Honed	4903	2270

Key: h – height, l – length, w – width

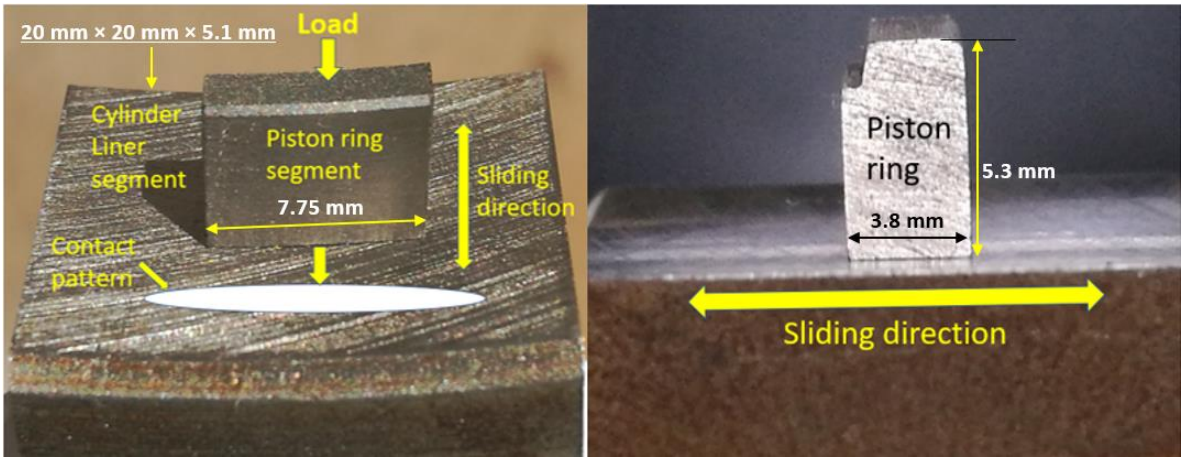

Figure 3.5, Tribo-testing geometry of test specimens

3.4.2. Wear scar analyses

After the Phase-III (final) LRT tests, the test specimens from the lubricants with enhanced tribological performance were selected for further investigation. Wear scars of these test specimens were analysed via scanning electron microscopy (SEM) and energy dispersive X-ray spectroscopy (EDX) techniques to investigate the morphologies of worn surfaces, and elemental deposition and adsorption on test specimens respectively. Thereafter the same test specimens were analysed for surface roughness of topographies utilizing 3D noncontact optical profilometry. Subsequently, all these test results were examined to propose an appropriate lubrication mechanism.

Microscope “PEMTRON PS-230” integrated with “OXFORD INSTRUMENT x-ACF” setup was utilized for SEM and EDX analyses. 3D noncontact optical profilometer (Leica DCM3D) was used to capture the surface texture of test specimen used with different lubricant formulations.

3.4.3. Analyses of rheological behavior

Rheological behavior of sample blends having improved tribological performances, (shown during final Phase LRT tests) were examined using a rheometer (Bohlin/GEMINI 2 – GEM200 – 903). Test protocol is with ramping shear rates vs temperature table ranging from 40 – 120 C°, with an increment of 20 C° steps.

3.4.4. Analyses of specific fuel consumption and exhaust emissions

Fuel consumption and exhaust emissions were examined on sample lubricants with enhanced tribological performance during Phase-III LRT tests. Dynamometer test-rig powered by Kiloskar diesel engine was utilized for the investigation as specifications presented in Table 3.5. Fuel consumption was tested for five load variations ending up with 25% overload condition to study the lubricant’s behavior under adverse conditions. Each test was performed three times to minimize errors. Exhaust emissions were analyzed using “TECHNOVATION – FEM7” exhaust gas analyzer with the interest of quantifying Carbon, Nitrogen and Sulphur oxides (CO_x, NO_x, SO_x) percentage.

Table 3.5, Dynamometer test rig specifications

Parameter	Specification
Make & Model	Kiloskar - AK 65
Rated power	4.8 KW (6.5 bhp) @ 1500 rpm
Type	Single cylinder, 4 stroke, diesel
Configuration	Naturally aspirated, water cooled

3.4.5. Used crankcase oil sample analyses

Used crank case oil samples were analyzed to compare the lubricant degradation with reference to sample S1 (conventional diesel engine oil, 15W40). Industrial generator (MEN 5500) with 5 kW capacity, powered by a diesel engine was utilized to run each lubricant sample for 100 hours as per the manufacturer's instructions. Basic specifications are presented in Table 3.6. Samples with optimum performance observed after Phase-III LRT tests were selected along with the sample S1.

Table 3.6, Specifications of diesel generator

Parameter	Specifications
Make and Model	MEN 5500
Engine model	PT186FAE
Engine type	Single cylinder, 4 stroke, diesel
Configuration	Naturally aspirated, air cooled
Bore x Stroke (mm^2)	86 x 72
Displacement (cc)	418
Compression ratio	19.5:1
Max. power (HP/rpm)	9.0/3,600
Rated power (HP/rpm)	8.6/3,600
Max. Output (KW)	5.5
Rated output (KW)	5

Collected used oil samples (after 100 hours of running) were tested for kinematic viscosity at 40 and 100 °C, VI, TBN, particle count, elemental analyses including wear metals, additives and contaminants using following equipment. In-addition, physicochemical properties of samples selected after Phase-I, LRT tests (before formulating CCO) were also tested using same apparatus.

a) Viscometers:
   - iSL V0661230 for viscosity at 40 °C
   - SPECTRO-VISC S-Flow-1200/1 for viscosity at 100 °C

b) METROHM 848; TITRINO PLUS for TAN

c) METROHM 794; BASIC TITRINO for TBN
d) METROHM 831 KF; Coulometer for moisture content
e) PARKIN ELMER – OPTIMA 8300 for elemental analysis
f) PARKIN ELMER – LR 64912C for FTIR (sulphation, oxidation, nitration, and soot content) analysis
g) ANALEX pqM – ASK-15333 for ferrous debris monitor (PQ index)
h) LAWLER - 334 for PP test
i) CANNON, ACO-8 for FP test

4. Chapter 4: Results part I – Material characterization

In this section the results of both nanomaterials and bio lubricant characterization are presented and discussed. Details of different characterization techniques, parameters, experiment protocols are described in Sections 3.1, 3,2 and 3.3.

4.1 Characterization of nanomaterials

As specified in the methodology (Section 3.1.2) TEM, XRD, Raman, FT-IR, and XPS technologies were utilized to confirm the identity of the nanomaterials and their properties.

Particle size and morphology of nanoparticles

TEM was used to investigate the morphologies and particle size of nanoparticles employed in this research. Electron microscopy and SAED (inset) images of corresponding metal oxide phase for Al_2O_3, TiO_2, Al_2O_3/G, TiO_2/r-GO, TiO_2/G are shown in Figure 4.1. These images were used to analyze the particle size, lattice fringes and d-spacing of these nanomaterials, which are vital parameters in tribological domain.[8, 9, 89, 103] The observations revealed the average particle sizes for the following metal oxide materials: Al_2O_3: 7.0 ± 0.7 nm, TiO_2: 9.0 ± 0.2 nm, Al_2O_3/G: 10.0 ± 0.3 nm, TiO_2/r-GO: 10.0 ± 0.3 nm, and TiO_2/G: 14.0 ± 0.3 nm. Particle size distributions are presented in Figure 4.2. Graphene sheets are with 319 ± 50 nm lateral dimensions (Figure 4.1f) and a lattice spacing of 0.33 ± 0.004 nm (Figure 4.3a).[150] Lattice fringe spacings of 0.37 ± 0.005 nm, 0.38 ± 0.003 nm, and 0.37 ± 0.002 nm were observed for 2D-graphene in nanocomposites of: Al_2O_3/G, TiO_2/G and TiO_2/r-GO respectively (Figure 4.3b-d). The slight increase in inter-lattice spacing of 2D-graphene may attributed to the attachment of oxygen functional groups or deposition of metal oxide nanoparticles on the edge or between graphene sheets.[151] For example, XPS analysis confirmed the change of elemental composition of TiO_2/G with increase of C 1s by 17.4%, decrease of O 1s by 15.1% and Ti 2p by 2.3% than TiO_2 (Table 4.1). The values are in ultra-

fine scale to infiltrate through asperities of piston ring cylinder liner interface, compared to the reported ICE lubrication film thicknesses, which are in macro scale (0.1 µm – 10 µm).[152]

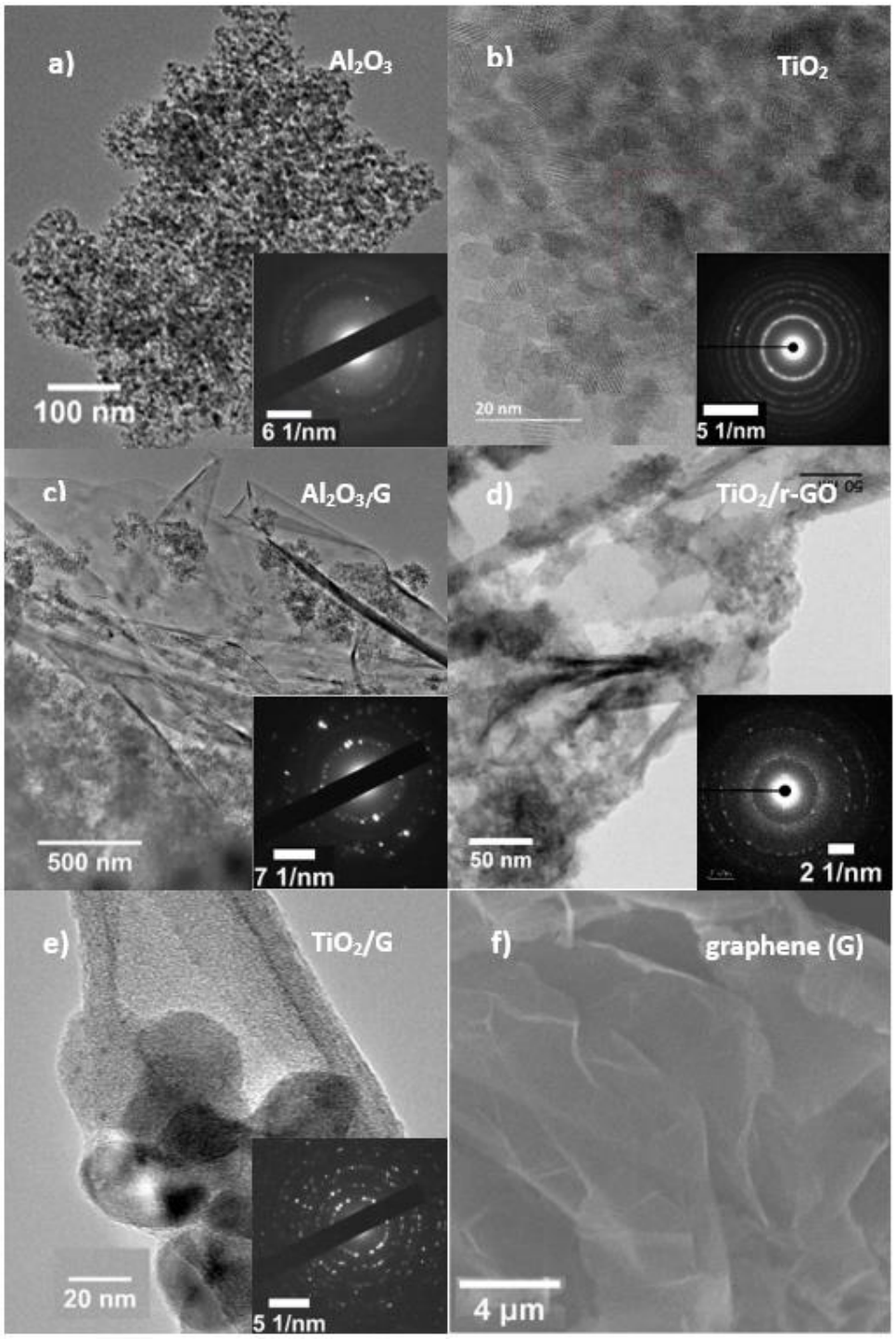

Figure 4.1, Morphologies of nanoparticles; TEM with SAED (inset) patterns for a) Al_2O_3, b) TiO_2, c) Al_2O_3/G, d) TiO_2/r-GO, e) TiO_2/G, and f) SEM image for graphene sheets (G), utilized with the project.

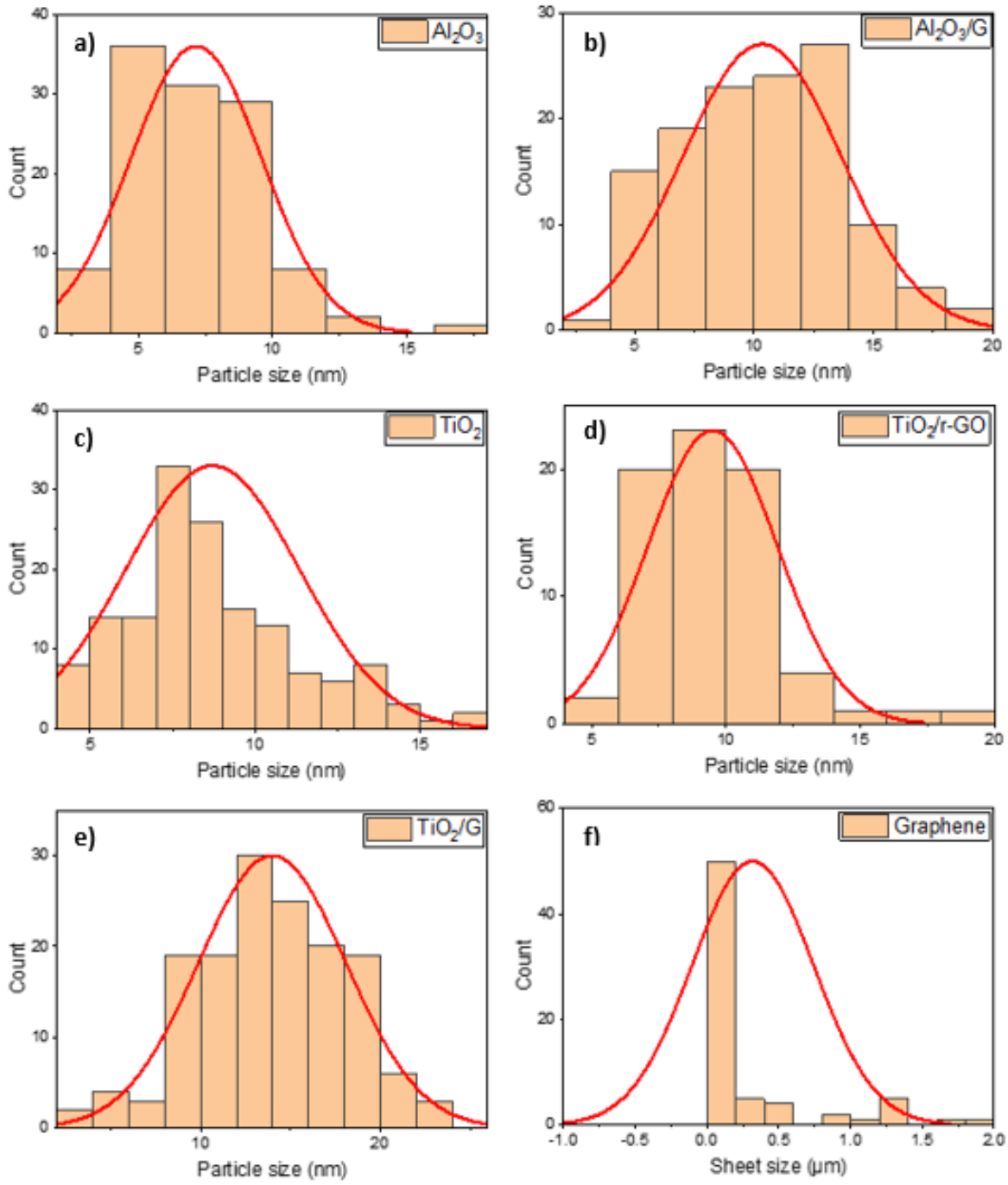

Figure 4.2, Particle size distribution for the nanomaterials used; a) Al_2O_3, b) Al_2O_3/G, c) TiO_2, d) TiO_2/r-Go, e) TiO_2/G, and f) graphene.

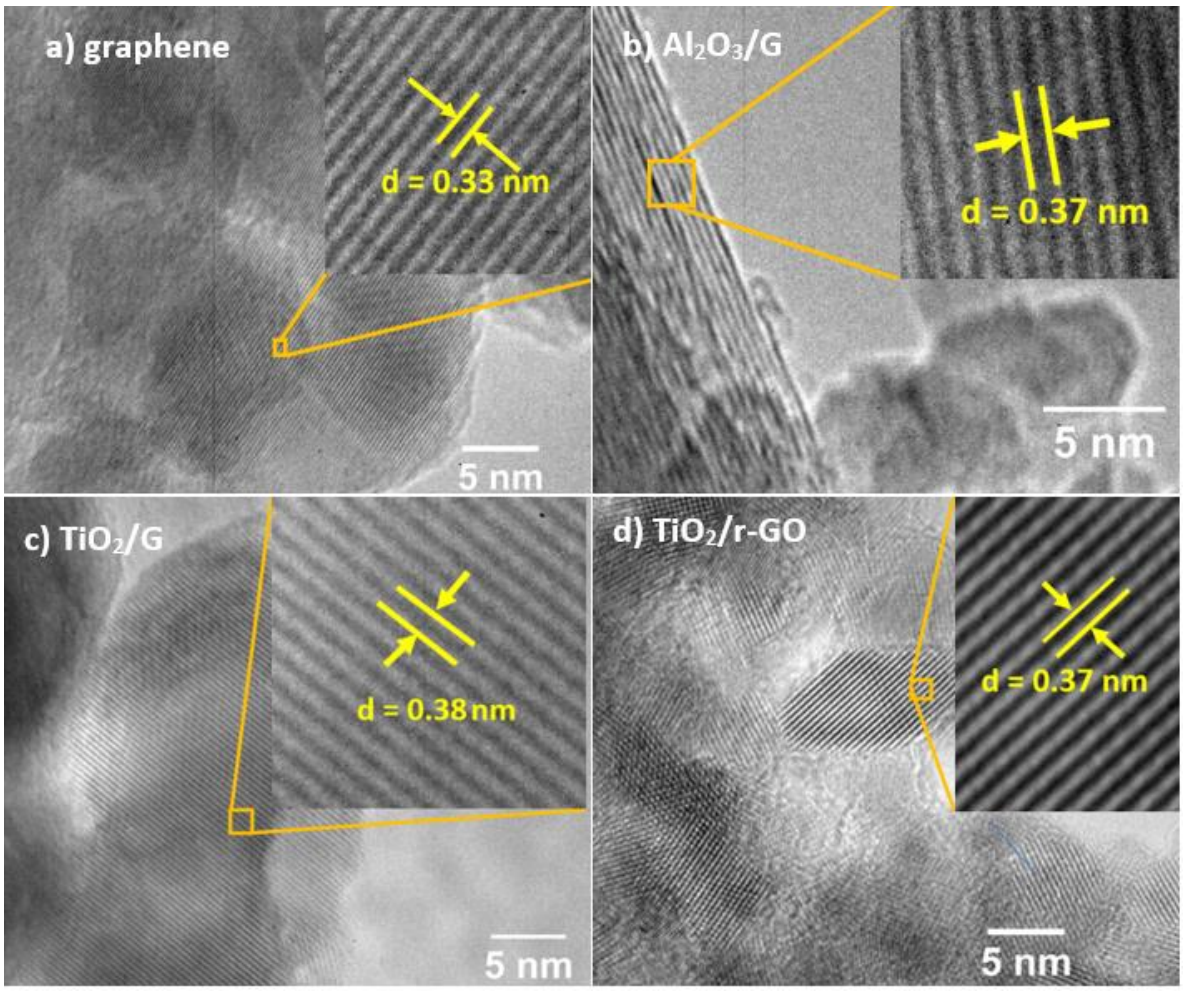

Figure 4.3, TEM images with lattice fringe spacing (inset) for 2D-graphene sheets in nanocomposites used; a) graphene (d = 0.33 nm), b) Al_2O_3/G (d = 0.37 nm), c) TiO_2/G (d = 0.38 nm), d) TiO_2/r-GO (d = 0.37 nm). Note: "d" denotes lattice fringe spacing.

XRD patterns

The XRD patterns presented in Figures 4.4 and 4.5 confirm the nanomaterials used in this study as Al_2O_3, TiO_2 metal oxides, graphene, and their nanocomposites; Al_2O_3/G, TiO_2/G and TiO_2/r-GO. For example, XRD pattern for TiO_2 (Figure 4.4a) is with (101), (103), (004), (112), (200), (105), (211), (213), (204), (116), (220), and (215) phase indices at 2θ = 25.4°, 36.9°, 37.8°, 38.4°, 48.0°, 53.8°, 55.0°, 62.4°, 62.8°, 68.5°, 70.2°, and 75.0° respectively (ICDD: 21-1272).[9, 153, 154] The strong peaks at 2θ = 25.4°, 37.8°, and 48.0° which represent the indices (101), (004), and (200) confirms that the titania is in anatase phase.[9, 153, 154] Figure 4.4b indicates that Al_2O_3 is with phase indices of (111), (220), (311),

(222), (400), (511), and (440) at 2θ = 20.08°, 32.4°, 37.4°, 39.5°, 45.7°, 60.7°, and 66.9° respectively (ICDD: 00-50-0741).[9, 155, 156] The observations, which confirms that the alumina is in gamma phase with strong peaks at (311), (400) and (440) indices.[155] Also, XRD patterns for graphene (Fig. 4.5a) reveals the corresponding diffraction peaks of (002) and (004) at 2θ = 26.1° and 54.4° respectively.[150, 157] In addition, broadened peak at 2θ = 44.3° represents the phase index (101) (ICDD: 00-041-1487). Figures 4.5b-d, confirm that, the diffraction peaks of nanocomposites; TiO_2/r-GO, TiO_2/G, and Al_2O_3/G are represent in the nanoparticle compositions associated with the syntheses of the respective nanocomposite. Moreover, broadened peaks of Al_2O_3, Al_2O_3/G, and TiO_2/r-GO suggests low crystallinity compared to TiO_2 and TiO_2/G, presumably because of smaller particle sizes compared to TiO_2, which agrees with the observed SAED patterns of metal oxide phase for those nanomaterials (Figure 4.1).[9]

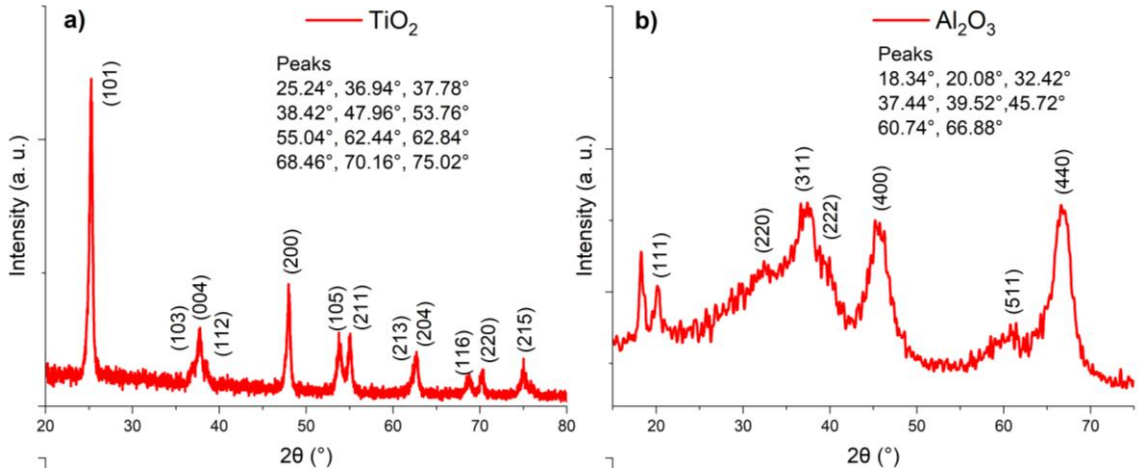

Figure 4.4, XRD patterns for nanoparticles of metal oxides used; a) TiO_2, b) Al_2O_3

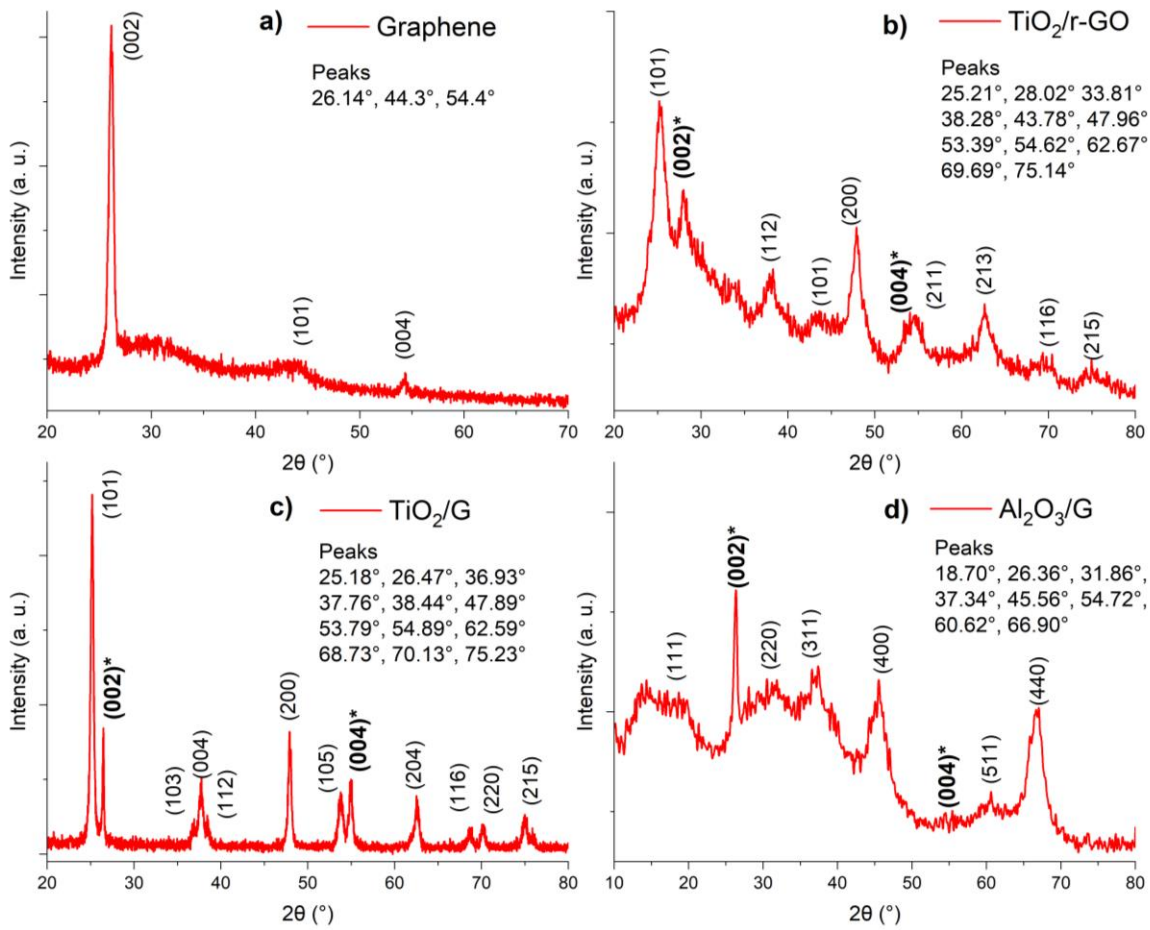

Figure 4.5, XRD patterns of graphene and nanocomposites used; a) graphene, b) TiO_2/r-GO, c) TiO_2/G, and d) Al_2O_3/G.

Raman spectroscopy

Figure 4.6. shows the observed Raman spectra for the above nanomaterials. Spectra for graphene exhibit sharp peaks at the wavenumbers of 1334.5, 1579.74 and 2686.6 cm^{-1} (Fig. 4.6a) representing Diamondoid (D), Graphitic (G), and 2D bands respectively. G band, which is at 1579.7 cm^{-1} is ascribed to the first order scattering of E_{2g} phonons vibration because of sp^2 hybridization.[151, 158-162] D band at 1334.5 cm^{-1} is simulated by in-plane scattering of the A_{1g} phonon vibration, which could be attributed to the change of atomic bond hybridization from sp^2 to sp^3 configuration. Most apparently caused by the oxidation or incorporation of oxygen functional groups leading to structural defects.[162] However, relative intensity between D and G bands i.e., $I_D/I_G = 0.21$ (Figure 4.6a), which indicates a rich sp^2 domain, minimal disorder or structural defects of the graphene sheets utilized. [158-162] 2D band at

2686.6 cm^{-1} represents double resonance enhanced A_1 phonon vibration, which may be affected by the structural imperfections.[151]

Raman peaks for TiO_2 at 142.8, 395.4, 515.9 and 637.9, cm^{-1} (Fig. 4.6b), match with the XRD observations (Fig. 4.4a), which confirms that, TiO_2 is in anatase phase.[154, 164] Anatase phase TiO_2 is a better option than rutile phase for wear prevention, because of lesser hardness of anatase phase (Mohs 5.5 – 6.0) than rutile phase (Mohs 6.0 – 6.5) titania.[97, 98] High hardness will resist deformation. Albeit elastic deformation is an essential attribute of an ICE lubrication to have ball bearing mechanism to reduce friction under EHL at piston ring cylinder liner interface.

Figure 4.6c exemplifies Raman bands for TiO_2/r-GO at 151.8, 1326.9 and 1596.9 cm^{-1}, which confirms that the assortment of TiO_2 (151.8 cm^{-1}) and r-GO (1326.9 and 1596.9 cm^{-1}) elements in the composite. Similarly, nanocomposite TiO2/G illustrates peaks at 147.1, 395.7, 514.6, and 636.3 cm^{-1} with 1337.4 and 1579.5 cm^{-1} (Figure 4.6d), indicating TiO_2 and r-GO elements within the composite.[163-164] Raman spectra for Al_2O_3 (Figure 4.6e) shows peaks ranging from 200–1200 cm^{-1}. Peaks at 240.7, 381.1, 430.6, 568.2, 713.0, 820.9, and 898.8 cm^{-1} are identical with the established data, which confirms that the material as Al_2O_3.[165-166] High intensity bands at 240 – 500 cm^{-1} range represents Al-O vibration stretching, whereas sharp intensity bands above 500 cm^{-1} signifies the stretching of hydroxyl groups. Moderate and low intensity bands appear in the same range to indicate deformation of hydroxyl groups.[165-166] Figure 4.6f shows that the Raman spectra for Al_2O_3/G is consisting with Raman bands at 455.3, 789.9, 916.8, 1086.1 cm^{-1} representing Al_2O_3. Graphene is represented by the bands at 1355.5, 1582.0, and 2727.9 cm^{-1}, confirming combination of alumina and graphene within the nanocomposite. Nevertheless, Raman peaks of Al_2O_3/G are shifted towards higher wavenumbers (Figure 4.1) indicating the increase of grain size (from 7.0 to 10.0 nm).[167-168]

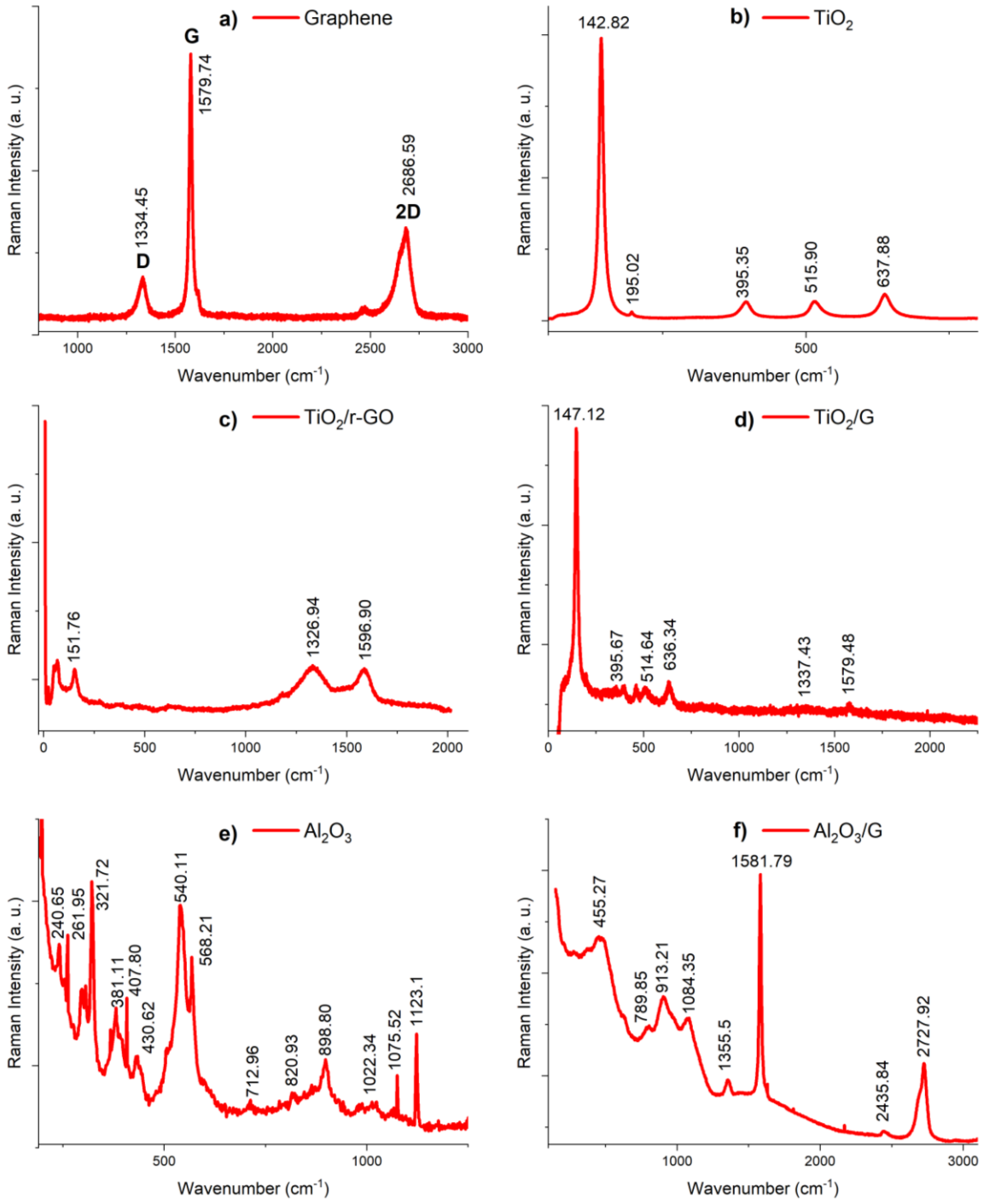

Figure 4.6, Raman intensity spectrometry graphs for the nanomaterials used; a) graphene, b) TiO_2, c) TiO_2/r-Go, d) TiO_2/G, e) Al_2O_3, and f) Al_2O_3/G.

FT-IR transmittance

Figure 4.7. displays the FTIR spectrophotometry graphs, for graphene and graphene-based metal oxide nanocomposites; TiO_2/r-GO, TiO_2/G and Al_2O_3/G used in this research.

Figure 4.7a illustrates the FTIR spectra for graphene with IR bands at 3742.5, 2312.8, 1705.5, and 1525.4 cm^{-1} indicating the attachment of variety of oxygen functionalities: hydroxyl, carboxyl, or carbonyl groups on the substrate. Most prominent O–H (R-OH or H-OH) stretching vibration could be ascribed to the IR band at 3742.5 cm^{-1}. Other bands at 2312.8, 1705.5 and 1525.4 cm^{-1} could be assigned to C=C, C=O and COO-H stretching vibrations respectively.[151, 153, 157, 160, 169]

Figure 4.7b-d presents the FTIR spectra for TiO_2/r-GO, TiO_2/G and Al_2O_3/G nanocomposites respectively. All three graphs are identical with similar stretching vibrations at approximately the same wavenumbers as illustrated with IR spectra for graphene (Figure 4.7a). Hence it is confirmed that all three nanocomposites are a combination of graphene or reduced graphene oxide with respective metal oxide accordingly. Nevertheless, Figure 4.7b, which is for the TiO_2/r-GO is with strong OH and COOH stretching vibrations at 3215.3 and 1558.5 cm^{-1} accordingly. This is an indication of higher concentration of oxygen functional groups on the r-GO substrate. This observation will lend further support to the Raman analysis, which indicates a higher I_D/I_G ratio for the TiO_2/r-GO nanocomposite (Figure 4.6c). Higher concentration of oxygen functional groups (hydroxyl, carboxyl, or carbonyl) in a suspension will lead to surface functionalization between molecular substrates of solvent and solute of solution; the characteristics, which may influence the colloidal stability of a formulation when blending with a base oil as a nano-additive to formulate a lubricant.

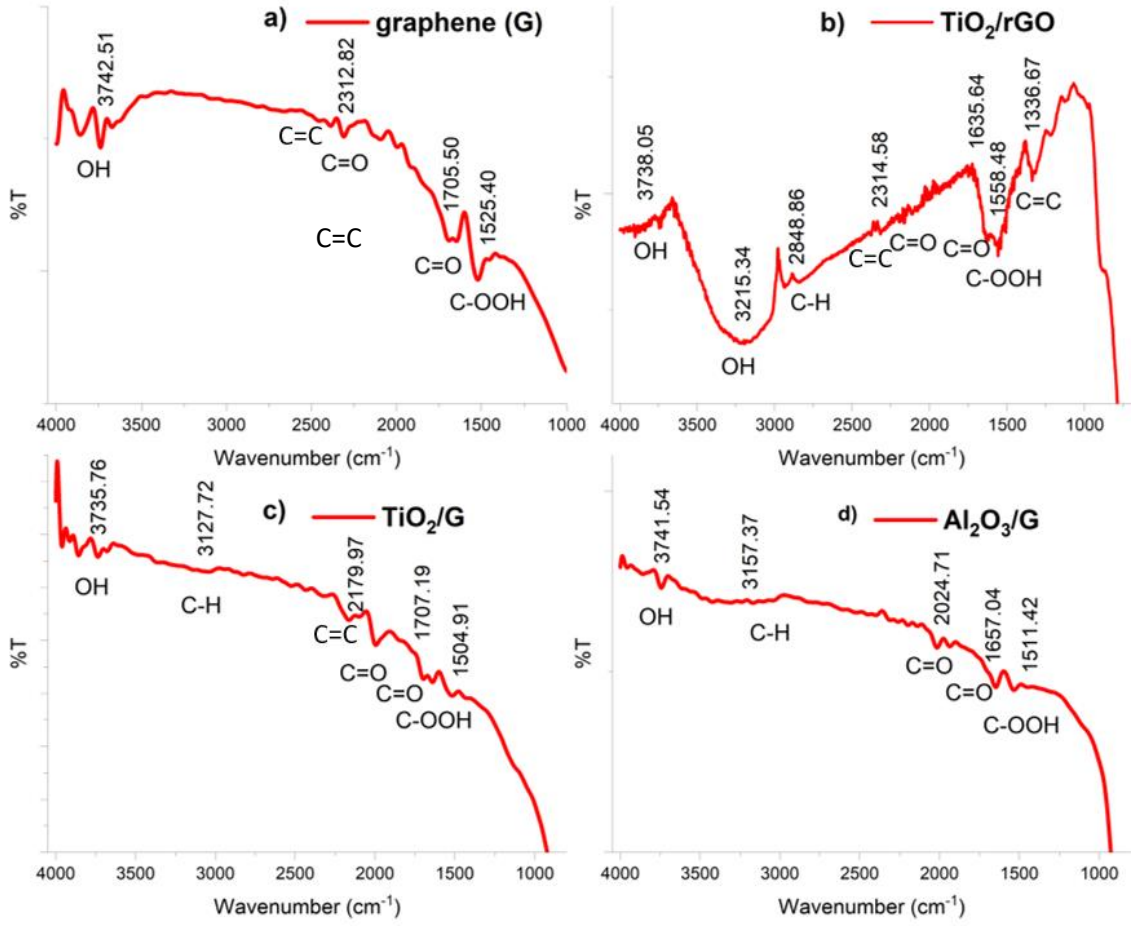

Figure 4.7, FT-IR spectrophotometry graphs for the graphene and graphene-based nanocomposites used; a) graphene, b) TiO_2/r-Go, c) TiO_2/G, and d) Al_2O_3/G.

XPS analysis

XPS analyses were performed to ascertain the elemental composition and chemical states of the nanomaterials used in the research. The observations are presented in Figures 4.8–4.11, for graphene (G), Al_2O_3, TiO_2 and TiO_2/G respectively. All the core level spectra of interest (C 1s, O 1s, Ti 2p and Al 2p) have been deconvoluted using Voigt profiles, based on the methods described by Teodorescu, et al.[170] The atomic composition has been determined by using the integral areas provided by the deconvolution procedure normed to the atomic sensitivity factors provided by Wagner, et al.[171]

Survey scan for G (Figure 4.8c) illustrates higher elemental composition of C than O with C:O ratio of 18.19:1 (C: 94.3%, O: 5.7%), which lends further reinforcement to Raman observations; rich sp^2 domain with 0.21 of low relative intensity (I_D/I_G). In-addition expanded

XPS spectra for C 1s orbital (Figure 4.8a) shows peaks at 284.55 eV, 285.04 eV, and 285.52 eV indicating three different chemical states, which could be ascribed to sp^2 C (G), C-O, (sp^3), and C=O (sp^2), respectively. In the O 1s spectra (Figure 4.8b), peaks at 531.1 eV, and 532.5 eV could be assigned to C=O (sp^2) and C-O (sp^3) correspondingly, confirming less carbonyl or oxygen functional groups with the utilized graphene.[169, 172,]

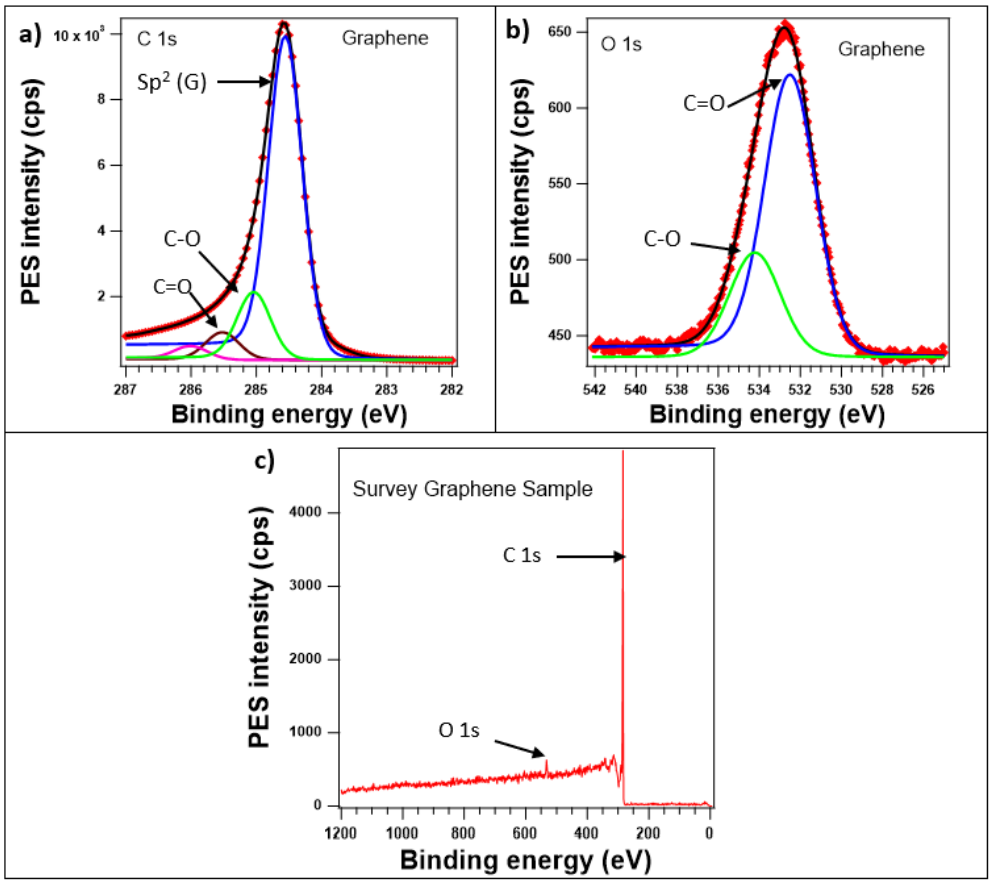

Figure 4.8, XPS spectra for graphene with high resolution of a) C 1s, b) O 1s regions and c) survey scan covering C 1s and O 1s regions

Figure 4.9(a-d) illustrates the XPS spectra for Al_2O_3 including core level details of C 1s, O 1s and Al 2p with survey scan for the same regions respectively. Peaks for C 1s at 284.55 eV, 286.1 eV, and 289.57 eV could be attributed C-C, C-O, O-C=O indicating possible adventitious carbon. O 1s band shows peaks representing Al-OH and Al-O-Al at 531.16 eV and 532.84 eV correspondingly. Also, the deconvoluted spectrum for Al 2p has two peaks at 74.93 eV and 75.66 eV, which could be ascribed to Al_2O_3 and $Al(OH)_3$ chemical states, respectively.[173, 174] The results, which shed lights on the additional diffraction peaks observed

with XRD patterns (Figure 4.4b), confirming the formation of alumina-tetrahydrate ($Al_2O_3.3H_2O$) within the Al_2O_3 nanoparticles.

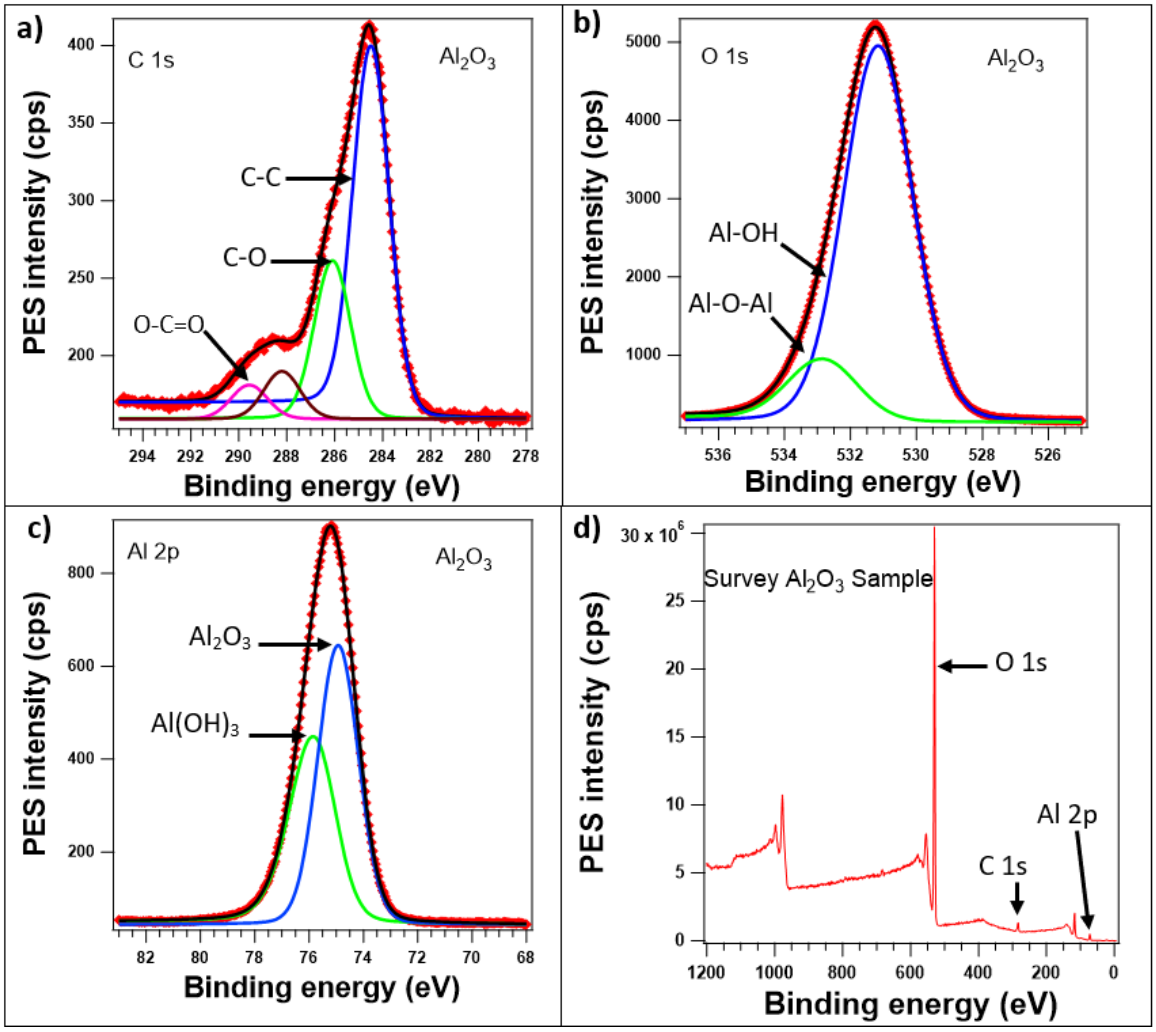

Figure 4.9, XPS spectra for Al_2O_3 nanoparticles with expanded details for a) C 1s, b) O 1s, c) Al 2p orbitals with d) survey scan for C 1s, O 1s, and Al 2p regions.

Figure 4.10 presents the overlay of survey scans for both TiO_2 and TiO_2/G. All regions: C 1s, O 1s and Ti 2p orbitals are in same position with different intensities. Table 4.1 shows the atomic concentrations of both nanomaterials, which revealed that the change in concentrations of elements in the TiO_2/G at the presence of G. This is including the increase of C 1s by 17.4% and decrease of O 1s by 15.1% and Ti 2p by 2.3% concentrations of TiO_2/G than TiO_2 nanoparticles.

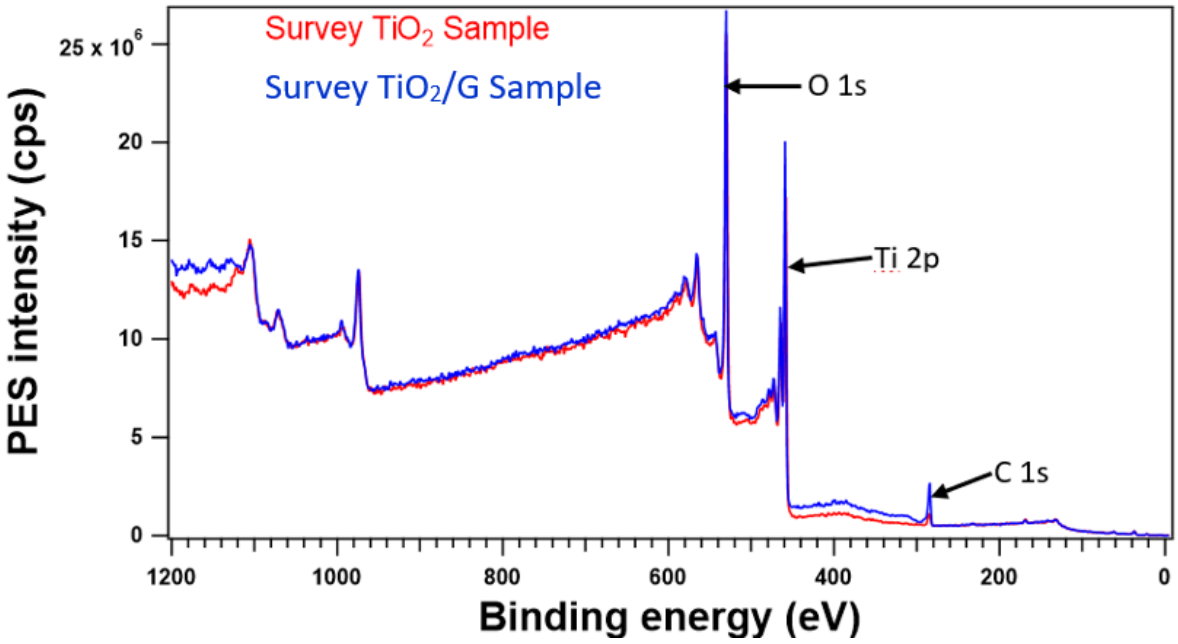

Figure 4.10, XPS survey scan spectra for both TiO_2 and TiO_2/G nanocomposites.

Table 4.1, Elemental composition of $T1O_2$ and TiO_2/G nanomaterials.

Nanomaterial	Atomic concentration (%)		
	C	O	Ti
TiO_2	11.21	61.12	27.67
TiO_2/G	28.60	46.00	25.40

Moreover, Figure 4.11(a-f) illustrates the high-resolution spectra (a-c) for TiO_2 and (d-f) for TiO_2/G respectively. Ti $2p_{3/2}$ exhibits an intense peak at 458.05 eV and Ti $2p_{1/2}$ at 463.08 with Δ=5.03 eV for TiO_2 (Figure 4.11c). Figure 4.11f exhibits that Ti $2p_{3/2}$ shows an intense peak at 459.9 eV and Ti $2p_{1/2}$ at 465.6 for TiO_2/G with a spin-orbital splitting value Δ=5.7 eV which is specific for an oxide.[175] Both components of Ti 2p, in the presence of G, have a shift of 1.2 eV towards higher binding energy (E_B).[175] Nevertheless, spectrographs indicate that, both the nanomaterials (TiO_2 and TiO_2/G) have same core level bands with similar chemical status.[153, 163]

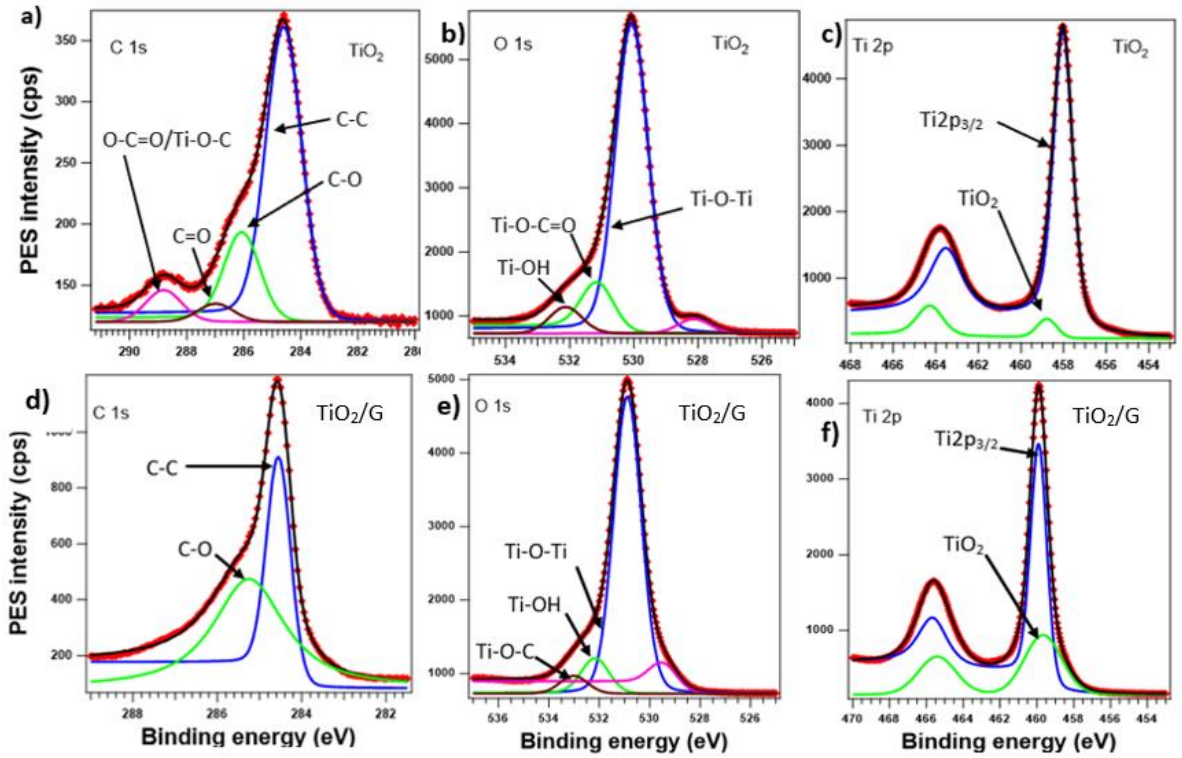

Figure 4.11, XPS high-resolution spectra for core level bands of TiO_2: a) C 1s, b) O 1s and c) Ti 2p and for TiO_2/G; d) C 1s, e) O 1s and f) Ti 2p respectively.

4.2. Enhancing physicochemical properties of coconut oil (CCO)

Test results obtained through various experiments are analyzed and disscussed in this section. All the experiments were executed according to the test protocols explained with the experiment methodology (Section 3.2.) to improve the mentioned substandard of CCO.

4.2.1. Improving poor cold flow properties of CCO

Figure 4.12 presents the DSC thermogram for the CCO, which is a study of observing the changes in enthalpy illustrating exothermic and endothermic processes with heat dissipating and absorbing characteristics of CCO. There are two exothermic peaks: Exo1 and Exo2 at 0.4 °C and -7.7 °C, with 1.9 °C and -4.7 °C onset transition temperatures respectively signifying two crystallization points. Perhaps, different crystallizing points could be attributed to different crystal phases (creating polymorphs) of complex triglyceride

molecules of CCO.[109] There is one endothermic peak: Endo1 at 22.7 °C with onset temperature at 12.2 °C, which represents the melting or de-crystallization behavior of CCO, which begins at 12.2 °C.

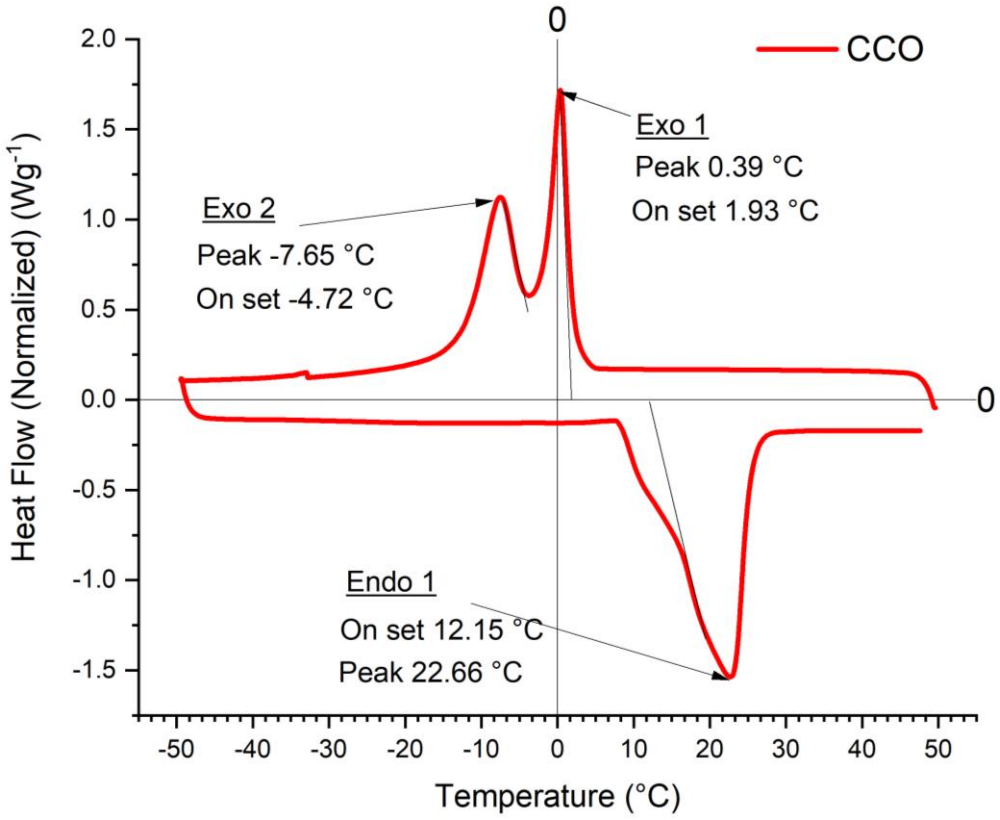

Figure 4.12, DSC thermogram of CCO; Key: Exo – exothermic, Endo – endothermic.

Figure 4.13 shows the DSC thermograms of formulations containing different concentrations of PMMA with CCO as the base stock. Detailed sample compositions and corresponding sample labels were presented in Table 3.2. From the test results it is evident that the sample PM50 has the lowest endothermic peak with onset temperature among the group at 22.7 °C and 11.5 °C respectively (Endo1, Fig 4.13b). Endothermic peak transition temperature, which represents the pour point (PP) of the fluid is almost the same for all four blends in the group similar to the CCO (Fig 4.12). Only a marginal shift of Endo1 onset temperature (from 12.2°C to 11.5 °C) was observed for all samples indicating early beginning of de-crystallization process. Similar results were observed from exothermic experiments, which indicates minimal delays in the beginning of crystallization process with reference to the monitored Exo1 and Exo2, peak and onset temperatures.

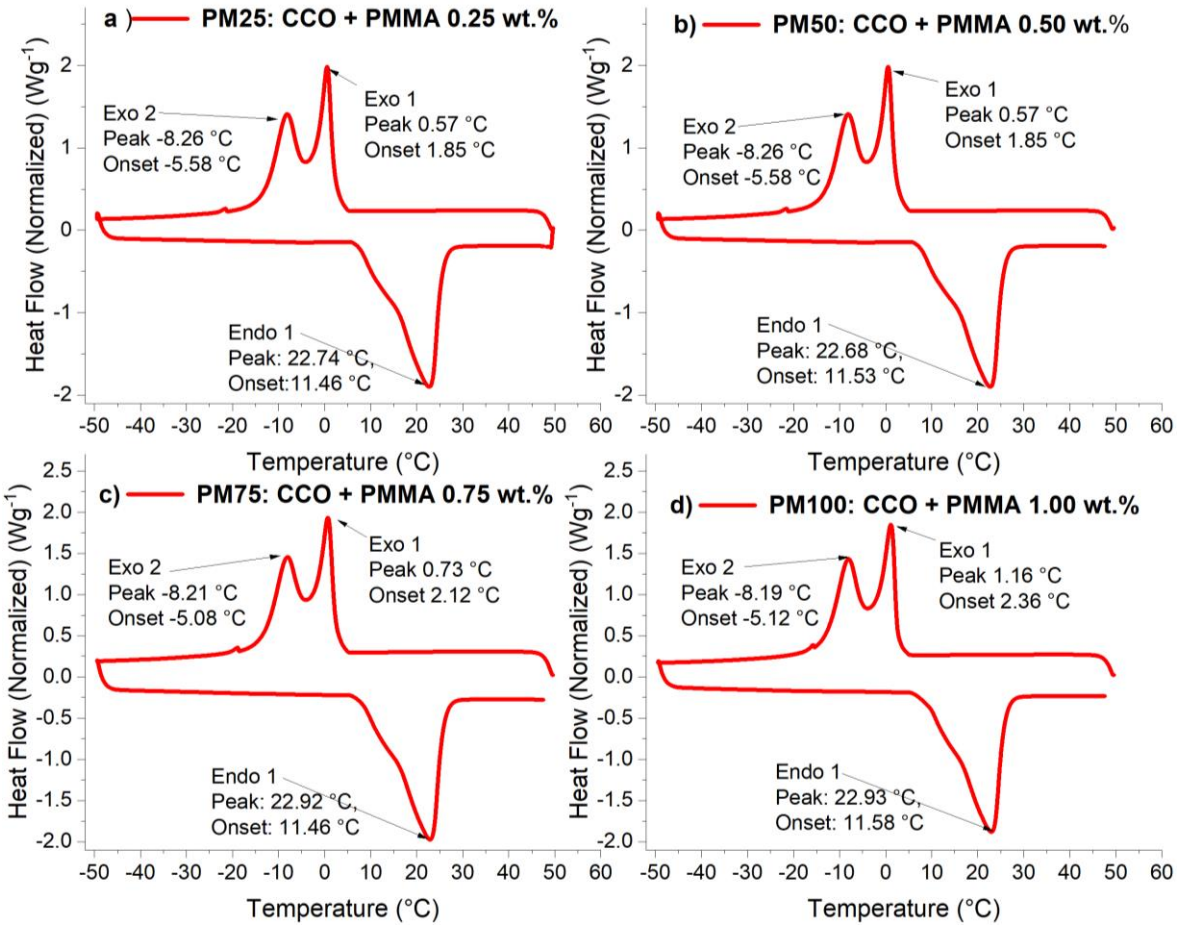

Figure 4.13, DSC thermograms for the formulations having CCO with different concentrations of PMMA; a) PM25: CCO + PMMA 0.25 wt.%, b) PM50: CCO + PMMA 0.50 wt.%, c) PM75: CCO + PMMA 0.75 wt.%, d) PM100: CCO + PMMA 1.00 wt.%,

DSC thermograms for sample blends containing different concentrations of SF with CCO are presented in Figure 4.14. Sample SF2.0 has the lowest endothermic peak and onset values at 20.9 °C and 8.4 °C, showing 1.8 °C of PP reduction with ~ 3.7 °C of advanced beginning of de-crystallization process compared to the Endo1 of CCO (Figure 4.12). From the Exo1 & Exo2 values of SF2.0 it is evident that the beginning of crystallization process has been delayed by ~1.2 °C and ~2.9 °C with lower peak values at -1.39 °C and -10.6 °C respectively compared to the Exo1 & Exo2 peak values (0.4 °C and -7.7 °C) of CCO (Figure 4.12).

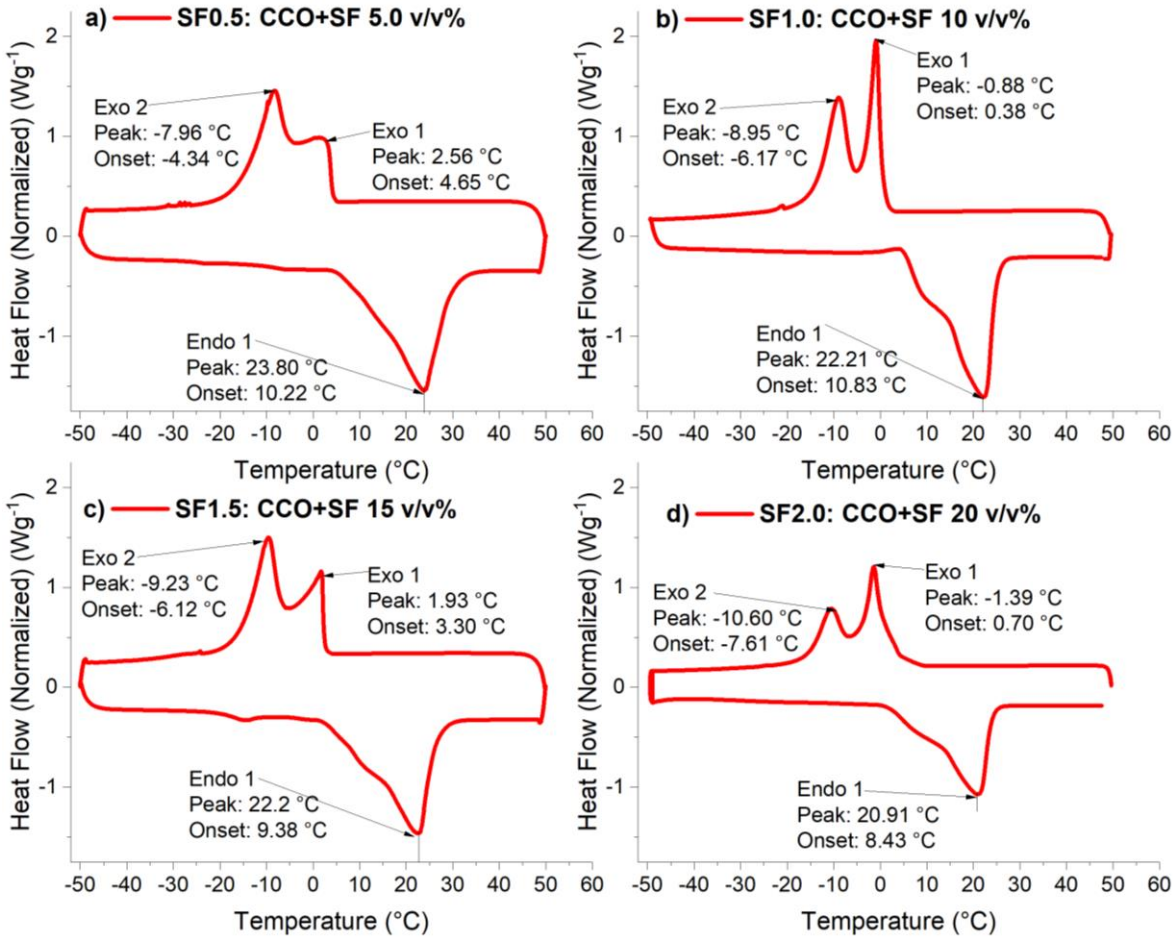

Figure 4.14, DSC thermograms for the formulations having CCO with different concentrations of SF; a) SF0.5: CCO + SF 5 v/v%, b) SF1.0: CCO + SF 10 v/v%, c) SF1.5: CCO + SF 15 v/v%, d) SF2.0: CCO + SF 20 v/v%,

From all twelve DSC samples with three different PPDs, sample SP2.0 has shown an impressive improvement on the cold flow behavior of CCO reporting ~ 5.0 °C Endo1 peak difference between CCO and SP2.0 (Figure 4.12 and 4.15d). In-addition, Endo1 onset temperature has been reduced to -1.3 °C, indicating ~ 13.5 °C early beginning of de-crystallization compared to CCO. Moreover, sample SP1.5 shows a broadened Exo2 peak at -23.9 °C. Whereas there is no Exo2 with SP2.0, instead exothermic peak appears during endothermic process with peak and onset temperatures of -4.0 °C and -11.6 °C respectively (Endo2, Figure 4.15d). This signifies the recrystallization of low melting polymorphs to high melting polymorphs [hexagonal subcell (α) – orthogonal subcell (β') – triclinic subcell (β)] before commencing the de-crystallization process.[11, 40, 109]

From the results of cooling processes of CCO and SP2.0, it is evident that the onset of Exo1 has been lowered by ~ 6.9 °C of SP2 than CCO, confirming the improvement of cold flow by starting of crystallization at a lower temperature than CCO.

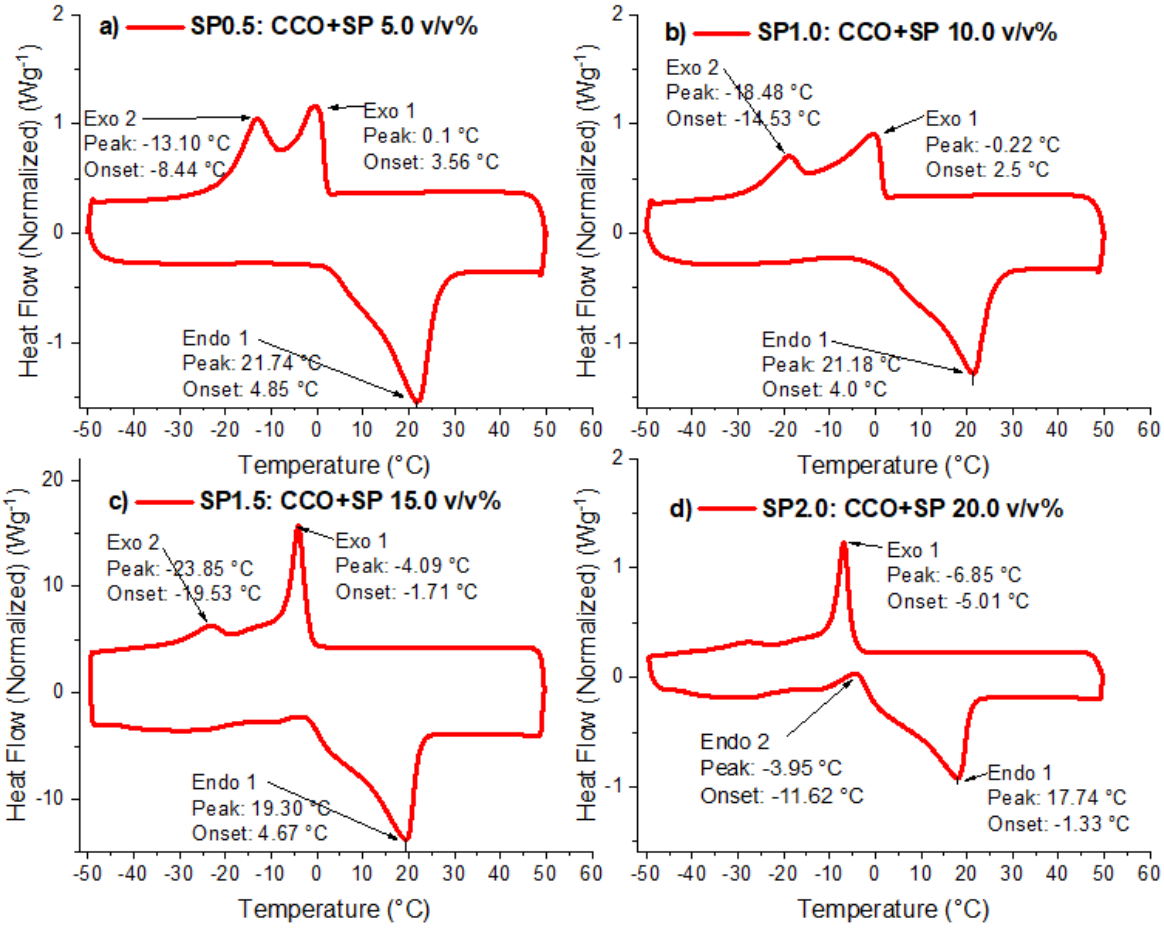

Figure 4.15, DSC thermograms for lubricant samples containing CCO with different concentrations of SP; a) SP0.5: CCO + SP 5 v/v%, b) SP1.0: CCO + SP 10 v/v%, c) SP1.5: CCO + SP 15 v/v%, d) SP2.0: CCO + SP 20 v/v%,

Figure 4.16 illustrates the DSC thermograms for sample blends having SP2.0 with two concentrations of PMMA. Sample codes and descriptions of these two formulations are presented in Table 4.2 (which are for improving physicochemical properties of CCO, hence sample codes did not continue after formulation of FCO). Both samples are without Exo1 peak during cooling process, confirming crystallizing into low melting *"α"* crystalline form.[40, 109] Both blends are with broadened exothermic peak during heating process at the range of -21.0 °C to 6.75 °C and -21.0 °C to 5.25 °C for SP2/P05 and SP2/P10 respectively,

confirming change of crystallization and de-crystallization patterns of the formulation than CCO.

Table 4.2, Sample descriptions for the formulations having SP2 with different concentrations of PMMA.

	Composition		
Sample code	**Base oil**	**Additive**	**wt. %**
SP2/P05	SP2.0	PMMA	0.5
SP2/P10	SP2.0	PMMA	1.0

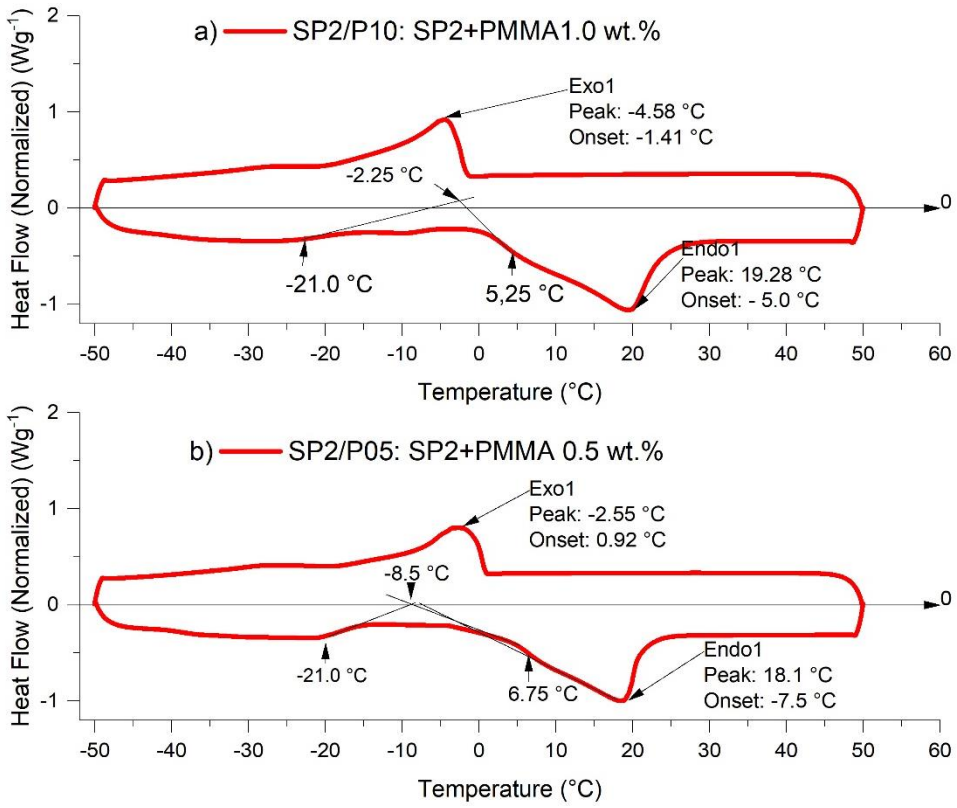

Figure 4.16, DSC thermograms for sample blends having SP2 with different concentrations of PMMA.

PP is the widely used parameter to define cold flow behavior of liquid lubricants tested in accordance with ASTM D97-96A guidelines. Albeit DSC analysis will facilitate for an in-depth understanding on the structural behavior of a fluid under different thermal conditions. The PP of the samples with best performance from each PPD group and of both

SP2/P samples were tested following ASTM D97-96A standard procedures and results are presented in Table 4.3 along with DSC – Endo1 peak and onset values for evaluation. From the test results it is evident that the SP2/P05 has the optimum cold flow behavior with PP at 6.0 °C. Reduction of PP by15 °C of CCO, albeit endothermic peak value of SP2/P05 remains at 18.1 °C. However, this improvement could be ascribed to the commencement of de-crystallization at a lower temperature (-7.5 °C – Endo1 onset) and continuing up to 18.1 °C (Endo1 peak), as the range which the formulation passes through many transition phases to gain liquid state. Thus, it is assumed that the flowing will start within the range, showing lower temperature as PP than the value of endothermic peak of the thermogram.

Table 4.3, Summary of PP and Endo1 peak and onset values during the DSC endothermic process.

Sample no	Pour point* (°C) ASTM D97-96A	DSC - Endo 1 Peak (°C)	Onset (°C)
CCO	21	22.7	12.2
PM50	21	22.7	11.5
SF2	21	20.9	8.4
SP2	15	17.7	-1.3
SP2/P05	6	18.1	-7.5
SP2/P10	9	19.3	-5.0

Measured in 3 °C intervals

Figure 4.17 illustrates the overlay of DSC thermograms for the samples CCO and SP2/P05, which clearly indicate the change in exothermic and endothermic curve patterns resulting enhancement in the low temperature flow behavior of CCO.

FTIR spectroscopy results for CCO, SP2/P05 and SP are presented in Figure 4.18, which exhibits variety of oxygen functional groups (carbonyl, carboxyl, or hydroxyl) on their molecular surface. Also, it is revealed that SP2/P05 is with additional IR bands than CCO. A broad peak (3600 cm^{-1} – 3300 cm^{-1}) could be ascribed to OH stretching (phenol or alcohol) and the peak at 1600 cm^{-1}could be C=C stretching vibration (alkene – aliphatic/aromatic). Additional bands in the range of 800 to 500 cm^{-1} could be assigned to C-H or C=C bending vibrations. The results, which could be attributed to the addition or amalgamation of functional groups of SP and PMMA to the CCO structure (since, the major constituents of CCO are saturated fatty acids: dodecanoic (Lauric) acid (47.7%) and tetra-decanoic

(myristic) acid (19.9%) (Table 2.6 and Table 4.4). Thus, the formulation SP2/P05 is improving the poor cold flow characteristics of CCO presumably by entangling or creating branches with the molecular structure, inhibiting macro-crystallization leading to micro-crystallization impeding self-molecular stacking, therefore, enhancing free flow behavior of CCO at lower temperatures (PP).[11, 40, 62-64, 109] The mechanism which aligns with the Minami's hypothesis (2017)[40] as illustrated in Figure 2.18b. Specifications of CCO constituents are tabulated in Table 4.4.

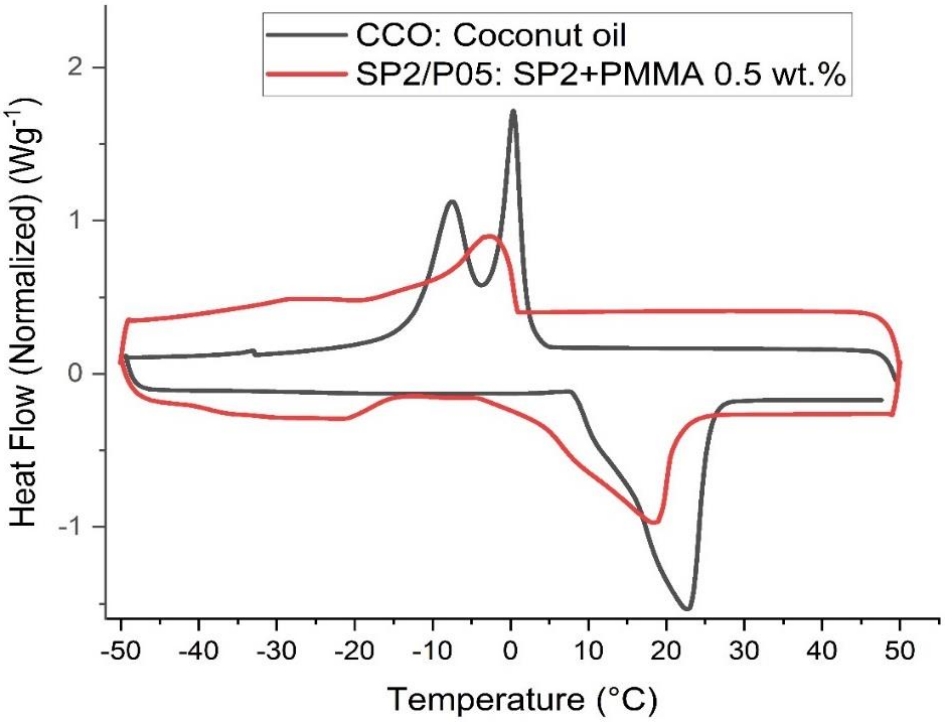

Figure 4.17, Overlay of DSC thermograms for CCO and SP2/P05

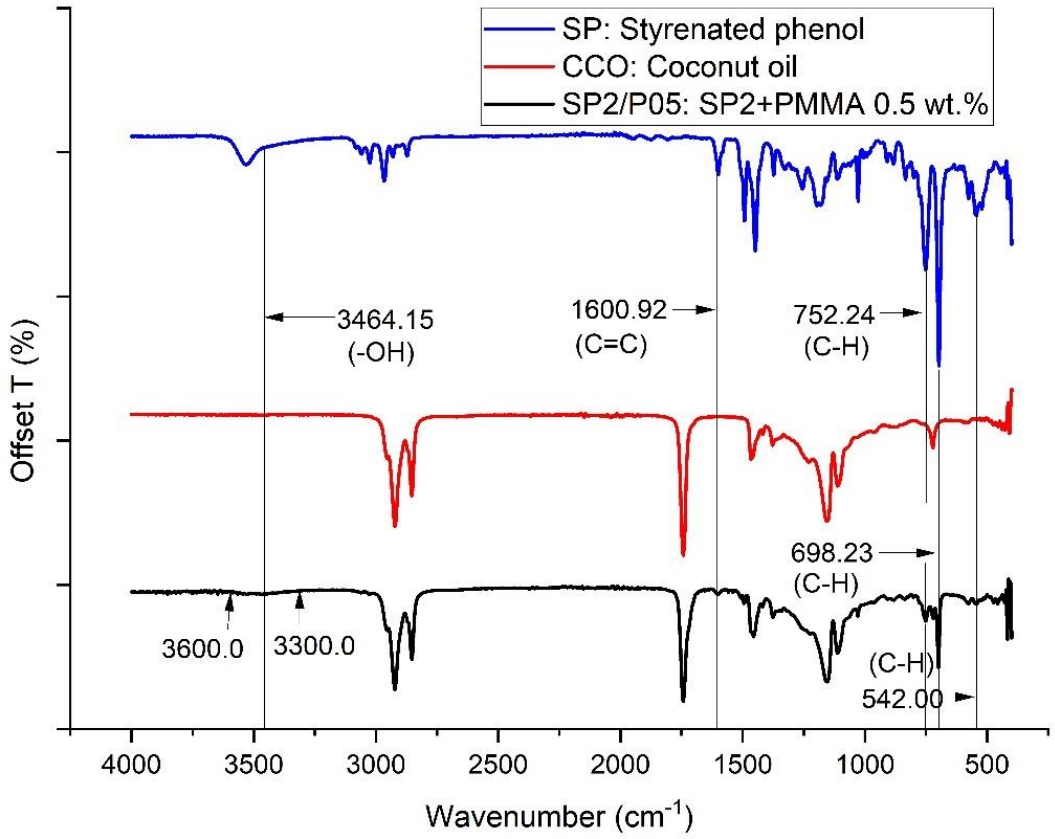

Figure 4.18, FTIR spectrometry graphs for SP2/P05, CCO and SP

Table 4.4, Specifications of CCO constituents[17, 108]

Component	UPAC name	Chain length	Molecular formula	Molar mass (g mol^{-1})	Density (g cm^{-3})	Melting point (°C)	Boiling point (°C)	Vapour pressure (Pa)	Heat capacity (J K^{-1} mol^{-1})
Caprylic acid	Octanoic acid	C8	$C_8H_{16}O_2$	144.214	0.91	16.7	239.7	0.250000	297.9
Capric acid	Decanoic acid	C10	$C_{10}H_{20}O_2$	172.268	0.893	31.6	268.7	0.048800	475.59
Lauric acid	Dodecanoic acid	C12	$C_{12}H_{24}O_2$	200.322	1.007	43.8	297.9	0.002130	404.28
Myristic acid	Tetradecanoic acid	C14	$C_{14}H_{28}O_2$	228.376	1.03	54.4	326.2	0.000187	432.01
Palmitic acid	Hexadecanoic acid	C16	$C_{16}H_{32}O_2$	256.43	0.852	62.9	352	0.000051	463.36
Stearic acid	Octadecanoic acid	C18	$C_{18}H_{36}O_2$	284.484	0.9408	69.3	361	9.5E-08	501.5
Oleic acid	(9Z)-Octadec-9-enoic acid	C18-1	$C_{18}H_{34}O_2$	282.468	0.895	13	360	0.0000019	577.9
Linoleic acid	(9Z,12Z)-Octadeca-9,12-dienoic acid	C18-2	$C_{18}H_{32}O_2$	280.452	0.9	-5	230		

4.2.2. Improving VI of formulated CCO

With reference to methodology (Section 3.2.3.) kinematic viscosity of sample formulations were tested at 40 °C and 100 °C after improving the cold flow behavior following guidelines of ASTM D445-19a. Sample SP2.0 and both SP2/P formulations (Table 4.2) were selected for this investigation. Observed viscosity values are used to evaluate the VI of formulations adhering to ASTM D2270 directives. The results are presented in Table 4.5, which confirms the ability of polymers to modify lubricant's viscosity less sensitive to varying operating temperatures. From the test results it is evident that the sample SP2/P10 is more effective in increasing VI, however the sample SP2/P05 is more successful improving cold flow behavior than SP2/P10. Nevertheless, these results confirm the ability of polymers having large, entangled chains with expanding capability to convert the solution less sensitive with increasing temperatures as proposed in Figure 2.18a.[40, 68] Also, presumed that, these functioning could be caused by globule to random coil transition depends on the attractive or repulsive interactions between solvent molecules and polymer chain segments, because of its thermal coil expansion behavior.[11, 37, 40, 69, 70]

Table 4.5, Summary of VI for formulations containing CCO with different additives compared with reference oil 15W40.

Sample	Kinematic viscosity at 40 °C ($mm^2 s^{-1}$)	Kinematic viscosity at 100 °C ($mm^2 s^{-1}$)	Viscosity Index (VI) (-)
15W40	115	15.1	137
CCO	24.8	5.5	169
SP2.0	39.4	6.4	112
SP2/P05	46.2	9.8	206
SP2/P10	43.4	11.1	260

4.2.3. Improving TBN of formulated CCO

TBN is an important parameter, which decides the life cycle of an ICE lubricant. TBN of the sample blends were tested after adding ZDDP as elucidated in Section 3.2.3. All six

ZDDP concentrations did not affect to improve the TBN. Sample descriptions and the results are presented in Table 4.6. As a summary SP2 (without ZDDP) recorded 0.23 mg KOH g^{-1} as TBN, which gradually decreased to 0.15 mg KOH g^{-1} with the addition of ZDDP. In contrast adding ZDDP had affected to increase the TAN from 0.29 to 5.1 mg KOH g^{-1}. Perhaps, this outcome could be assigned to an interaction between dithiol group of ZDDP with functional groups (carboxyl, phenol, alkyl) of CCO and SP. In view of above results three different concentrations (0.25, 0.50, and 1.0 wt.%) of KOH were added to 2 SP2/P formulations (Table 4.2), because of their cold flow improving capabilities.

TBN was tested referring to ASTM D2896-21 directives. Sample descriptions and results are summarized in Table 4.7, which indicate that, the increase of PMMA in SP2 has affected to reduce the TBN. Perhaps, could be assigned to the combination of carbonyl and hydroxyl groups of PMMA and SP respectively to create more carboxyl groups in the solution. Although, sample SP2/P05/K50 appeared with improved TBN of 4.14 mg KOH g^{-1} (Table 4.7) among other formulations. Albeit, adding 1.0 wt.% of KOH concentrations ended up with saponification. With this results formulation SP2/P05/K50 is selected as formulated coconut oil (FCO) for further investigations including blending with selected nanomaterials for rheological and tribological investigations. Comparison of achieved physicochemical properties of FCO with CCO is summarized in Table 4.8.

Table 4.6, Summary of TAN and TBN test results for the formulations containing SP2 with different concentrations of ZDDP.

Sample no	Composition	TAN (mg KOH g^{-1})	TBN (mg KOH g^{-1})
SP2	CCO + SP 20 v/v%	0.29	0.23
SP2/Z05	SP2 + ZDDP 0.50 v/v %	1.06	0.22
SP2/Z10	SP2 + ZDDP 1.00 v/v %	1.66	0.16
SP2/Z15	SP2 + ZDDP 1.50 v/v %	2.01	0.15
SP2/Z20	SP2 + ZDDP 2.00 v/v %	2.84	0.14
SP2/Z25	SP2 + ZDDP 2.50 v/v %	3.35	0.15
SP2/Z30	SP2 + ZDDP 3.00 v/v %	5.1	0.15

Table 4.7, Summary of TBN test results for the formulations containing SP2 with different concentrations of PMMA and KOH

Sample no	Composition	TBN (mg KOH g^{-1})
SP2	CCO + SP 20 v/v%	0.23
SP2/P05	SP2 + PMMA 0.5 wt.%	0.16
SP2/P05/K25	SP2/P05 + KOH 0.25 wt.%	1.74
SP2/P05/K50	SP2/P05 + KOH 0.50 wt.%	4.14
SP2/P10	SP2 + PMMA 1.0 wt.%	0.13
SP2/P10/K25	SP2/P10 + KOH 0.25 wt.%	0.86
SP2/P10/K50	SP2/P10 + KOH 0.50 wt.%	1.66

Table 4.8, Comparison of physicochemical properties of CCO vs FCO

Sample	TAN (mg KOH g^{-1})	TBN (mg KOH g^{-1})	Viscosity @ 40 °C ($mm^2 s^{-1}$)	Viscosity @ 100 °C ($mm^2 s^{-1}$)	Viscosity Index (VI) ()	Pour point* (°C)
CCO	1.94 - 12.8	****	24.8	5.5	169	21.0
FCO	0.29	4.14	46.2	9.8	206	6.0
15W40	****	9.8	109	14.1	130	-33.0

**** Measured in 3 °C intervals***

4.2.4. Analyses on thermal and oxidative stability of FCO

Thermal and oxidative stability of FCO was analyzed as explained with Section 3.2.3. with two reaction environments to differentiate oxidative and thermal degradation of sample formulations. Flow of atmospheric air and N_2 (inert gas) were the selected experimental backgrounds to superimpose the observed STA thermographs on each other. The results: difference between quantified weight loss percentages could be predicted as the percentage of oxidative degradation for the respective lubricant sample at that experiment temperature. Besides, weight loss percentage of the thermogram under N_2 environment could be assigned to thermal degradation assuming that the experiment chamber is sealed and not possible for atmospheric air (oxygen) to infiltrate through reaction media.[176, 177]

Figure 4.19 presents the STA thermograms for CCO at 100 °C and 150 °C under flowing air and flowing N_2, which indicates that CCO has 100% of oxidative stability with degradation of -0.02% at 150 °C compared to 0.23% of oxidative degradation at 100 °C. However, thermal degradation is high (3.24%) at 150 °C, compared to 0.05% of thermal degradation at 100 °C, which could be ascribed to higher saturated fatty acid concentration (~ 92.0%, Table 2.6) of CCO.[17, 107]

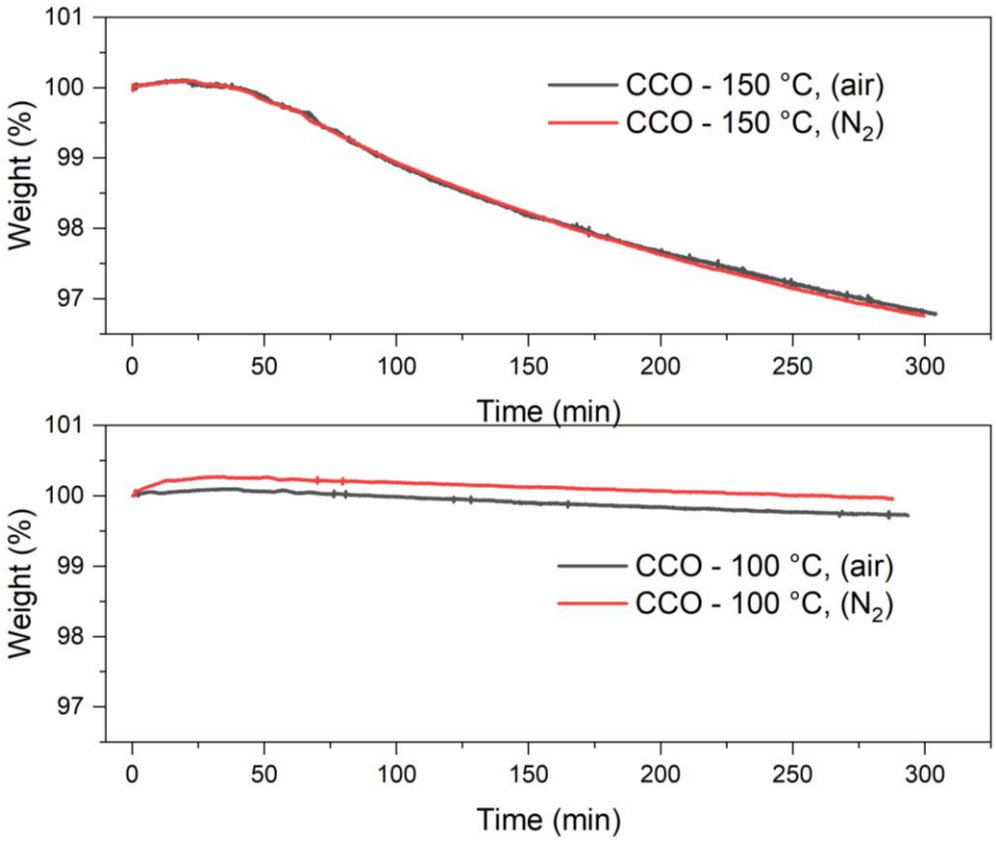

Figure 4.19, STA thermogram for CCO at 100 °C and 150 °C under atmospheric air and inert gas (N_2) environments.

Figure 4.20 illustrates the STA thermograms for sample blends SP2/P05 and SP2/P10, which illustrates that both the samples are having similar oxidative and thermal characteristics at 100 °C. Also, sample SP2/P05 shows more rapid mass loss under the N_2 flow than the air flow, indicating better oxidative stability than thermal stability at 150 °C (Figure 4.20c). Perhaps, oxygen or any functional element in air may have reacted with SP2/P05 structure under air flow at elevated temperature (150 °C) resulting improved thermal stability under air flow than the N_2 flow. If not, any structural element of SP2/P05 may have reacted with N_2 under the N_2 flow at 150 °C for this increased thermal degradation.

In contrast, sample SP2/P10 is showing less thermal degradation under the N_2 flow than the air flow at the same temperature (Figure 4.20d). In-addition SP2/P10 is with higher weight loss percentages than SP2/05 under both N_2 and air flow environments. SP2/P05 and SP2/P10 are with 0.5 wt.% and 1.0 wt.% of PMMA is the only difference among these 2 samples. Overall SP2/P05 is showing improved oxidative and thermal stability over SP2/P10, which could be ascribed to lesser PMMA concentration (0.5 wt.%) of SP2/P05. All the oxidative and thermal degradations with reference to weight loss percentages are presented in Table 4.9. Oxidative degradation is the difference between weight loss percentage under flowing air and flowing N_2, assuming that, the weight loss under flowing air is due to thermal and oxidation degradation and weight loss under N_2 is only because of thermal degradation.

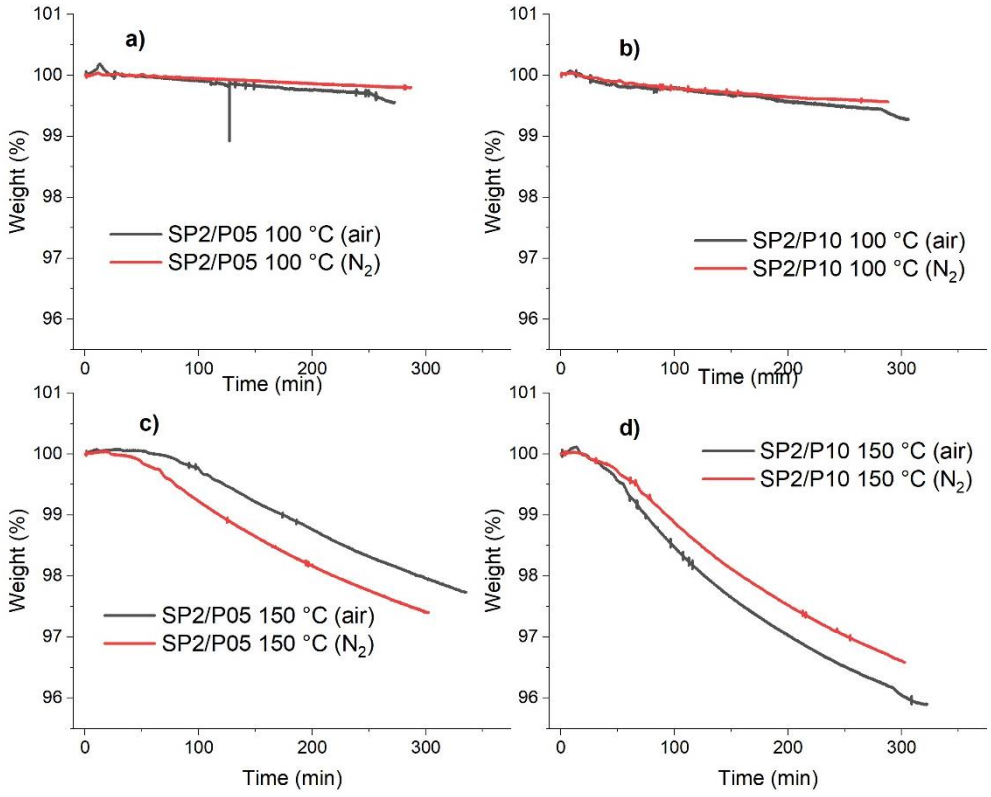

Figure 4.20, STA thermograms of SP2/PM05 and SP2/PM10, for oxidative and thermal stability under atmospheric air and N_2 environments; a) SP2/P05 at 100 °C, b) SP2/P10 100 °C, c) SP2/P05 at 150 °C, d) SP2/P10 at 150 °C

Table 4.9, Summary of oxidative and thermal stability for different formulated coconut oil samples.

	Weight loss after 5 h (%)					
	Temperature (100 °C)			Temperature (150 °C)		
Sample	**Air**	**N_2**	**Oxid%**	**Air**	**N_2**	**Oxid%**
CCO	0.28	0.05	0.23	3.22	3.24	-0.02
SP2/P05	0.45	0.20	0.25	2.26	2.60	-0.34
SP2/P10	0.73	0.43	0.30	4.10	3.42	0.68
FCO	0.45	0.20	0.25	2.26	2.60	-0.34

Key: Oxid – oxidation

Figure 4.21 presents the STA thermograms for CCO and FCO with same temperatures and backgrounds for comparison. Also Figure 4.21d shows that, the FCO is having higher mass loss under the N_2 flow than air flow, confirming higher thermal stability of FCO under the air flow. The phenomenon, which could be ascribed to reaction and amalgamation of the elements of air with FCO structure at elevated temperatures above 100 °C. Nevertheless, thermograms indicate similar characteristics for both samples, though FCO has a slight edge over CCO (Table 4.9). This slight improvement of thermal and oxidative stability of FCO than CCO could be caused by the addition of chemicals to improve other physicochemical properties like PP, VI of CCO. Specifically, to improve poor cold flow, it is necessary to create branches to CCO molecule structure or entangling CCO molecule is the mechanisms suggested. Adding branches might have created supplementary C= bonds with unsaturated polar situation in the solution is the assumption for this effect.

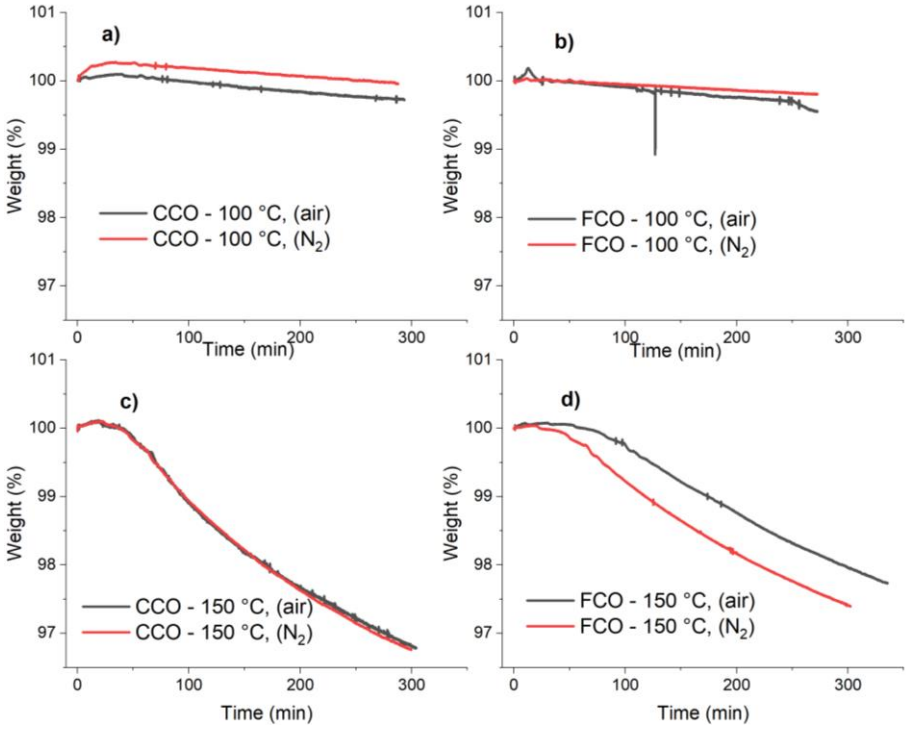

Figure 4.21, STA thermogram for weight loss analysis on CCO and FCO at 100 °C and 150 °C under dissimilar environments; a) CCO at 100 °C, b) FCO at 100 °C, c) CCO at 150 °C, d) FCO at 150 °C,

All above tests were done with the duration of 5 hours, thus long hold STA was done on FCO at 120 °C, for 31 hours. The results are presented in Figure 4.22, which revealed a 3.6% weight loss over ~30 hours of isothermal condition, before the solution became stable in terms of mass loss. FCO is a combination of CCO, SP. PMMA, and KOH. Constituents of CCO and their physical properties are presented in Table 4.4, which confirms that the boiling point of all the constituents are above 230 °C. Boiling point of SP is 256 °C, and melting points of PMMA and KOH are 150 °C, and 360 °C respectively, thus this degradation could be assigned to oxidative influence on release of volatile substances or formation of oxidation products with high molecular weight.[176] Figure 4.23 demonstrates the comparison of STA observations of octanoic acid, CCO and FCO at 100 °C under naturally aspirated environment. Octanoic acid is a constituent of CCO (7.6%, Tables 2.8, and 4.4), a saturated fatty acid with straight medium chain structural backbone having chemical formula of $C_8H_{16}O_2$. The test results indicate that the octanoic acid is having 56.9% weight loss compared to 0.28% degradation of CCO under same test conditions (Table 4.9). The combination of other constituents of CCO may have affected to control such degradation effect. Moisture content of the CCO is ~ 0.37%,[178] therefore, this long hold weight loss could

be ascribed to any interaction between other constituents of CCO. Nevertheless, this weight loss seems to terminate after 30 hours of long hold, thus preconditioning FCO by keeping at 120 °C for more than 30 hours before use could eliminate this degradation before the end application.

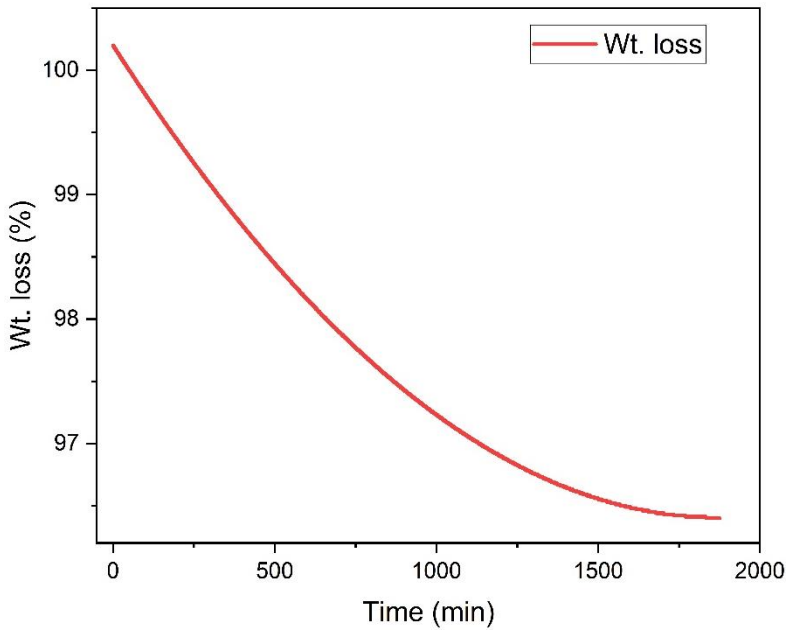

Figure 4.22, STA thermogram for FCO under naturally aspirated environment for extended hours.

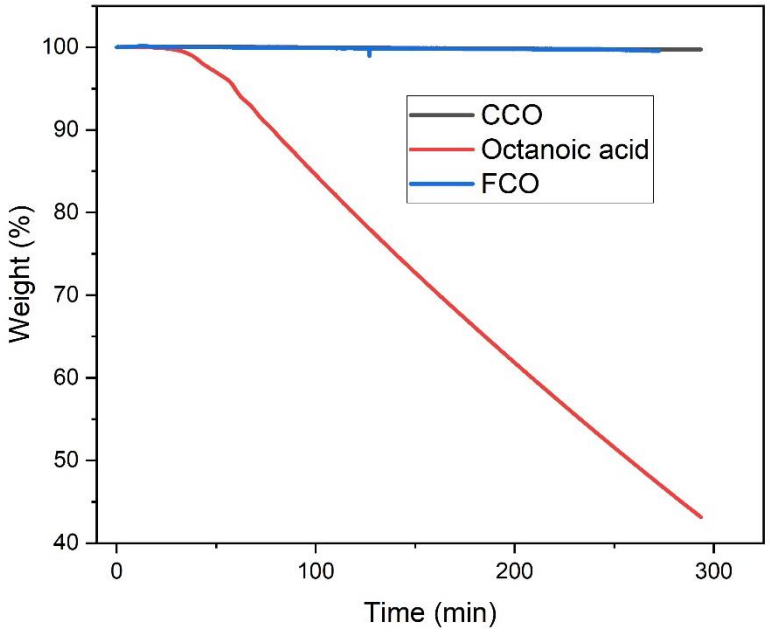

Figure 4.23, STA comparison on CCO, FCO and octanoic acid at 100 °C under naturally aspirated background.

4.3. Rheological analysis on the shear stability of sample lubricants

Viscometry tests were performed using a rheometer (Bohlin/GEMINI2 – GEM 200 – 903) to study the flow behavior of sample lubricants under ramping shear rates at elevated temperatures ranging from 40 – 120 °C (Section 3.4.3).

Test results are presented in Figures 4.24 – 4.26, for all tested samples including reference oil S1. Figure 4.24 shows better shear stability of FCO than S1. Besides, both the samples are showing similar pseudoplastic characteristics in the range of ~ 5×10^2 to 7×10^3 s^{-1} for all test temperatures except for the temperature 40 °C. In-addition, 3 different flow behaviors are visible at 3 different ranges of shear-rates: a) Sharp viscosity reduction at the range of ~ 0 to 5×10^2 s^{-1}, b) Minor viscosity reduction across the range of ~ 5×10^2 to 7×10^3 s^{-1}, and c) Shear thickening behavior after the shear-rate ~ 7×10^3 s^{-1}.

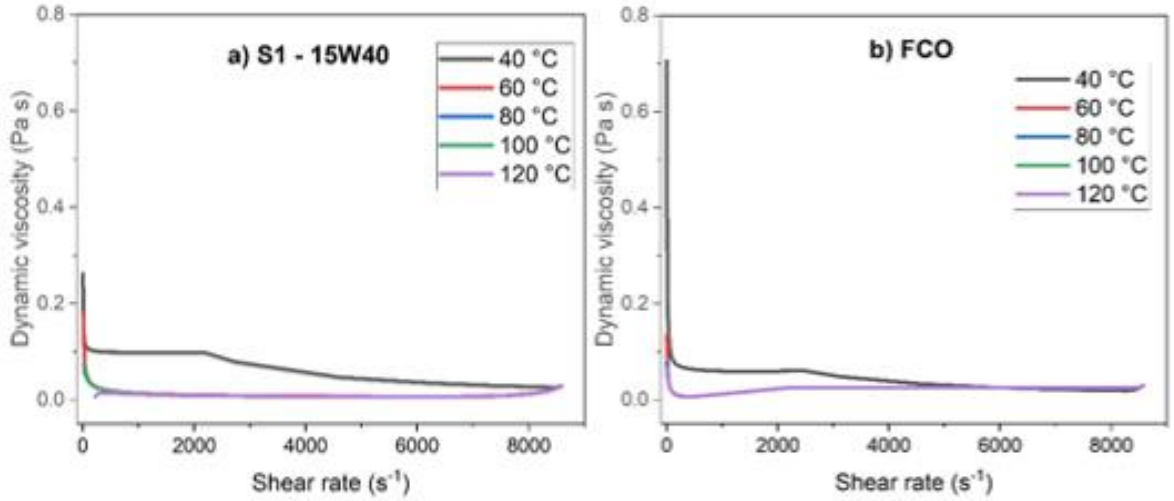

Figure 4.24, Rheometric curves in linear-linear axes for a) S1-reference oil (15W40), and b) FCO

Figure 4.25 indicates the rheological characteristics of samples containing G and GO as additives with base-stocks 15W40 and FCO respectively (samples S9, S9A, S24, S24A). From the test results it is evident that the samples S9 and S24 are having better shear stability than the samples S9A and S24A, which are having GO in place of G, as nano-additive. In addition, these 4 samples also indicate the viscosity changing behavior at similar ranges of shear-rates.

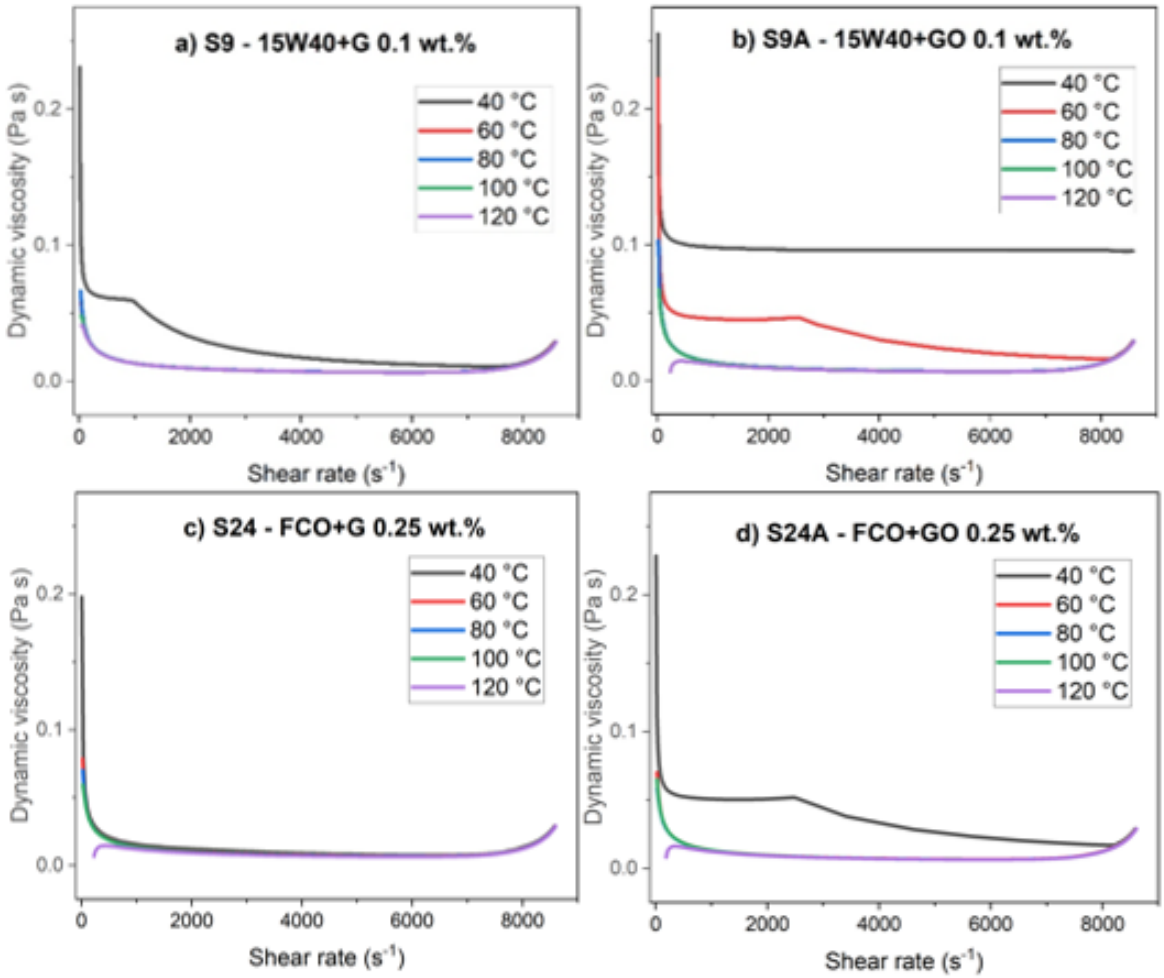

Figure 4.25, Rheometric curves of lubricant samples with G and GO as additives in linear-linear axes for; a) S9 – 15W40+G 0.1wt.%, b) S9A – 15W40+GO 0.1 wt.%, c) S24 – FCO+G 0.25 wt.%, and d) S24A – FCO+GO 0.25 wt.%.

Rheometric test results for the samples containing FCO as base stock with different nano-additives are presented in Figure 4.26. Samples S30, S32, and S35 were selected because of their improved tribological performance. From the test results it is evident that the sample S30 is having better shear stability than other 2 samples. However rheological behavior for all 3 samples appears same, identical to the test results of previous samples (Fig. 4.24 and 4.25). Nevertheless, lubricants behavior with ramping shear-rates under different elevated temperatures are not clearly visible. Therefore, plotting the results on log-log axes, instead of linear-linear axes, may reveal new insights into their flow characteristics. For example, assumed the power-law model be fit to the data, in order to analyze the flow behavior of selected sample lubricants further.

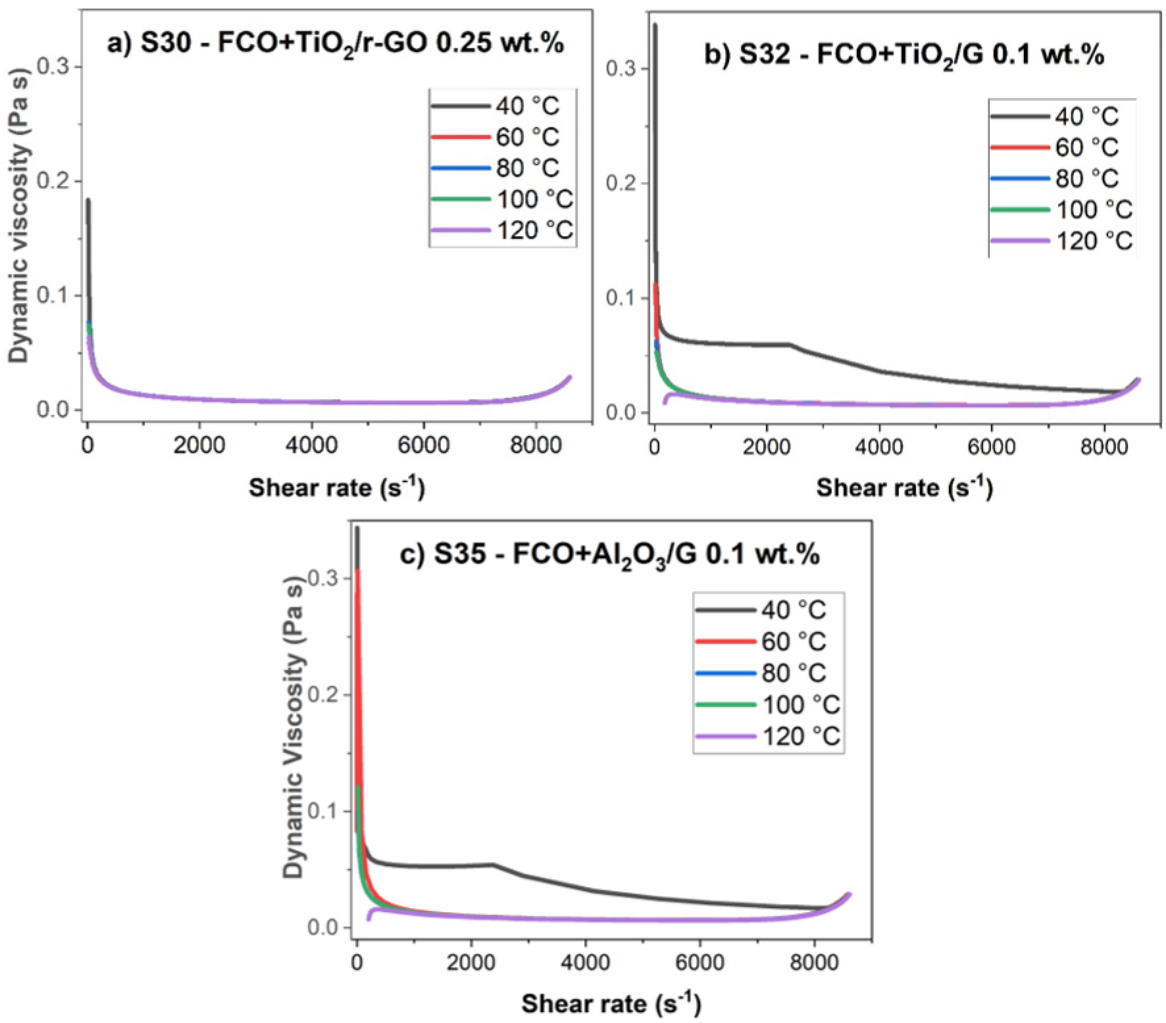

Figure 4.26, Rheometric test results of sample lubricants of FCO with different nanocomposites as additives in linear-linear axes for; a) S30 – FCO+TiO_2/r-GO 0.25 wt.%, b) S32 – FCO+TiO_2/G 0.1 wt.%, and c) S35 – FCO+ Al_2O_3/G 0.1 wt.%

Power-law (Ostwald-de Waele) prediction for sample blends

Power-law model is fitting mostly with non-Newtonian lubricants having pseudoplastic behavior or the measured data is entirely within the shear thinning regime across all the tested shear rates. Proportionality between shear stress (σ) and change of shear stress [shear rate or velocity gradient] ($\dot{\gamma}$) is defined as the shear viscosity or dynamic viscosity (η). With reference to power-law model (Eq. 4.1), above parameters are combined to predict characteristics of the subject fluid using flow curves in double logarithmic scale.[179, 180]

Power-law equations:[179, 180]

$$\boldsymbol{\sigma} = \boldsymbol{K}\dot{\gamma}^{\boldsymbol{n}} \tag{4.1}$$

$$\boldsymbol{\eta} = \frac{\boldsymbol{\sigma}}{\dot{\gamma}} = \boldsymbol{K}\dot{\gamma}^{(\boldsymbol{n}-\mathbf{1})} \tag{4.2}$$

Where: $\boldsymbol{K}$ – Flow consistency index (or dynamic viscosity when shear rate is 1 ($\log \dot{\boldsymbol{\gamma}} = 0$) with units (Pa s^n)

$\boldsymbol{n}$ – The flow behavior index (dimensionless)

Figure 4.27 presents the flow behavior of FCO under ramping shear rates in double log scale for different temperatures (40, 60, 80, 100 and 120 °C). Flow curves indicate similar characteristics for all temperatures except for the curve for 40 °C, which demonstrates higher $\boldsymbol{\eta}$ values than other temperatures for similar shear rates. The linear section of curves indicates the power-law region suggesting shear thinning behavior of the liquid, where the points A (3.57, -2.13) and B (2.10, -1.45) are marked.

Thus, gradient for the AB section (power-law region) = -0.462 = $\boldsymbol{n}$ – 1 (Eq. 4.2; power-law fitting).

∴ $\boldsymbol{n}$ = 0.538, which confirms the pseudoplasticity behavior ($\boldsymbol{n}$ < 1) of the liquid in the region of 2.0 to 3.7 log shear rates [10^2 (s^{-1}) to 7×10^3 (s^{-1})] approximately. The value of "$\boldsymbol{n}$" for other samples also confirms the shear thinning performance due to the presence of a similar power-law region, which are listed in Table 4.10. In addition, from Equation 4.2 it is observed that flow consistency index $\boldsymbol{K}$ could be defined as follows:

$$\log \boldsymbol{\eta} = \log \boldsymbol{K} + (\boldsymbol{n} - \mathbf{1}) \log \dot{\gamma} \tag{4.3}$$

$$\therefore \quad \log \boldsymbol{\eta} = \log \boldsymbol{k}, \text{ when } \dot{\boldsymbol{\gamma}} = 1, (\log \dot{\boldsymbol{\gamma}} = 0) \tag{4.4}$$

Therefore, intercept of power law gradient line at $\log \dot{\boldsymbol{\gamma}} = 0$ (value of y axis where x = 0) will give the value of $\boldsymbol{K}$.

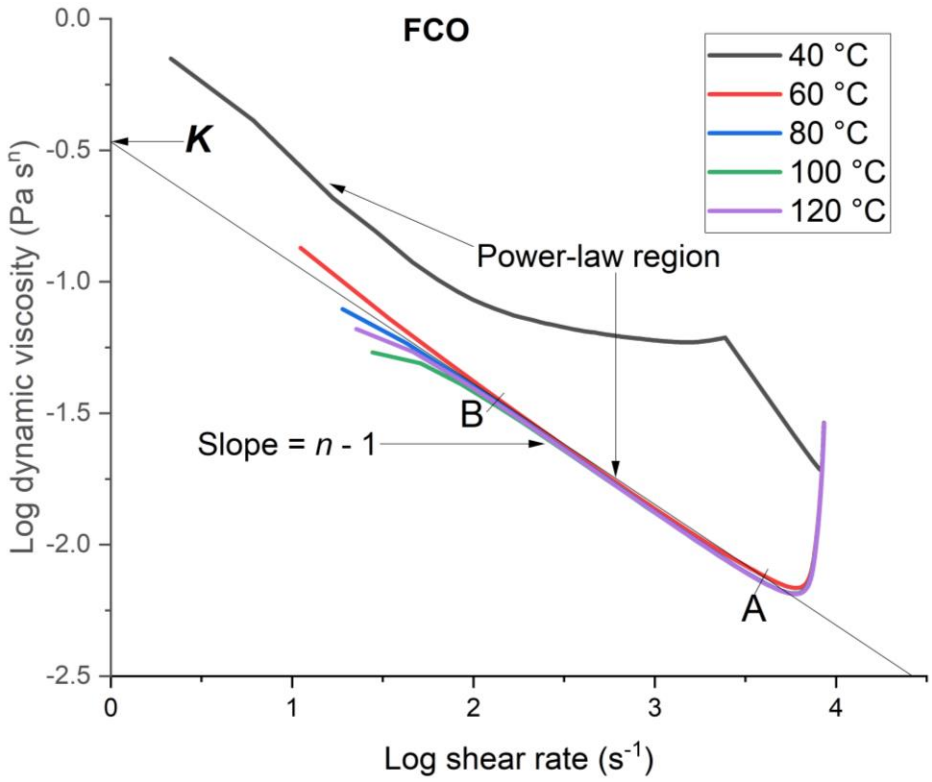

Figure 4.27, Rheometric curves of FCO in log – log axes under ramping shear rates in different temperatures (40, 60, 80, 100, and 120 °C, AB – the range of shear thinning).

Table 4.10, Calculated flow behavior index (n) for all tested sample blends

	Sample								
	FCO	**S1**	**S9**	**S9A**	**S24**	**S24A**	**S30**	**S32**	**S35**
Gradient (*n*-1)	-0.463	-0.473	-0.446	-0.461	-0.459	-0.461	-0.461	-0.457	-0.476
n	0.537	0.527	0.554	0.539	0.541	0.539	0.539	0.543	0.524

*Note: "**n**" denotes the flow behavior index*

Figures 4.28–4.30 reveal the pseudoplasticity ($n < 1$) of all tested sample blends including reference oil (15W40). Moreover, it may be the effect of solids shear thickening appears to occur at high shear rates for all samples including 15W40. This is a measurement artefact, which could be ascribed to:

a) Cooling-down of fast spinning upper cone because of air flow across to cooldown the cone spinning motor.

b) Slight material ejection from the edge of cone and plate conjunction is possible because of high spinning velocities of the cone at high shear rates.

c) Only the stationary bottom plate is equipped with heating, and cooling arrangements to control the temperature, albeit upper cone without heating and the spinning area is not enclosed. Elevated temperature of the bottom plate may cause evaporation of fluids or temperature difference between top and bottom plates may create temperature difference between fluid layers could have been influenced this effect.

From Figure 4.28 it is observed that the FCO exhibits greater shear stability than 15W40, particularly at elevated temperatures. Perhaps this effect could be attributed to the addition of PMMA as viscosity modifier during formulation of raw coconut oil (CCO). PMMA is constituted with large molecular chains having expanding capability to entangle with the solvent molecules (Section 4.2.2). The result, which improved the viscosity dependance on temperature of FCO with enhanced VI, compared to 15W40 and CCO (Table 4.8).[28, 40] Nevertheless, this pseudoplastic behavior of lubricant with ramping shear rates could be restricted to avoid viscosity reduction further by regulating the fluid temperature. Because fluid temperature is inversely proportional to the viscosity, in case if it is difficult to control the ramping high shear rates.[28]

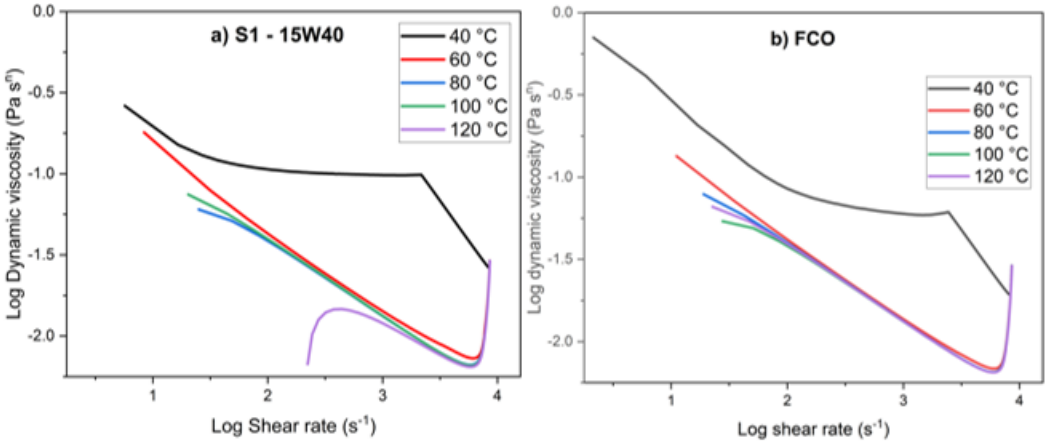

Figure 4.28, Rheometric curves in log-log axes for a) S1-reference oil (15W40), and b) FCO.

Figure 4.29(a-d) presents the non-Newtonian behavior of lubricants with graphene (G) and graphene oxide (GO) as additives for sample blends with 15W40 and FCO as base stocks. From the results it is evident that the blends with G, as additive are more stable than the blends with GO in both 15W40 and FCO base stocks.

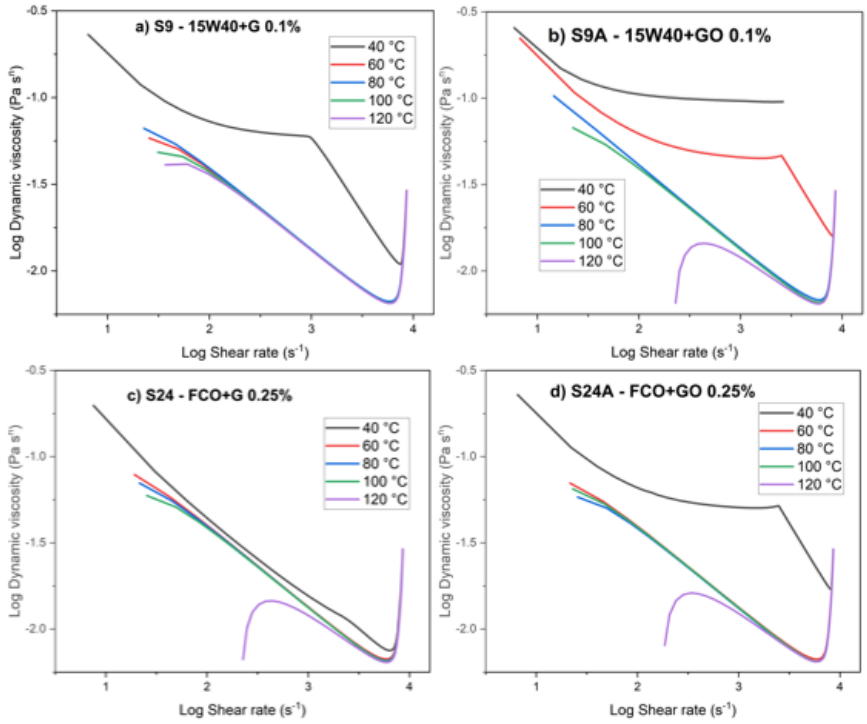

Figure 4.29, Rheometric curves for lubricant samples with G and GO as additives in log-log axes; a) S9 – 15W40+G 0.1wt.%, b) S9A – 15W40+GO 0.1 wt.%, c)S24 – FCO+G 0.25 wt.%, and d)S24A – FCO+GO 0.25 wt.%.

Figure 4.30 (a-c) illustrates the flow curves for sample lubricants blended using FCO and different nanocomposites; TiO_2/r-GO, TiO_2/G and Al_2O_3/G as base stock and additives respectively. From the outcomes it is observed that the sample S30 had shown the best shear stability among all three blends. The results suggest that TiO_2/r-GO nanoparticles are more stable than other nanocomposites used as additives under different temperatures with ramping shear rates. This may be attributed to functional groups attached to TiO_2/r-GO nanocomposite, which agrees with the results of FTIR spectra for TiO_2/r-GO. Moreover, broadened XRD peaks with scattered SAED images proposes low crystallinity or amorphous state. Thus, may have contributed to colloidal stability leading to the above rheometric observations.

Shear thickening behavior illustrated by all samples at high shear rates after the power-law region may be attributed to the testing conditions as explained above. It is hypothesized that the temperature difference between layers could have influenced this performance. If not shear thickening, most non-Newtonian fluids will reach a viscosity plateau at high shear rates according to Carreau-Yasuda and Cross model predctions.[180, 181] From the other hand shear

thickening is critical at high shear rates to maintain lubricant viscosity in real ICE operation. The remedies are as mentioned above to regulate ramping shear rate if possible. If not, to maintain the temperature of lubricant or by improving piezo-viscous behavior of the lubricant, which will increase the entrain velocity of the lubricant to separate the sliding asperities apart.[182, 183] Viscosity/pressure and viscosity/temperature relationships of a fluid are depending on the properties of elements associated with that solution.[28] In fact both parameters, shear rate and fluid entrain velocity, depend on the relative velocity of the surfaces in motion (piston ring cylinder liner interface). Thus, increasing fluid pressure and cooling lubricant temperature by external means is the solution suggested to overcome the situation.

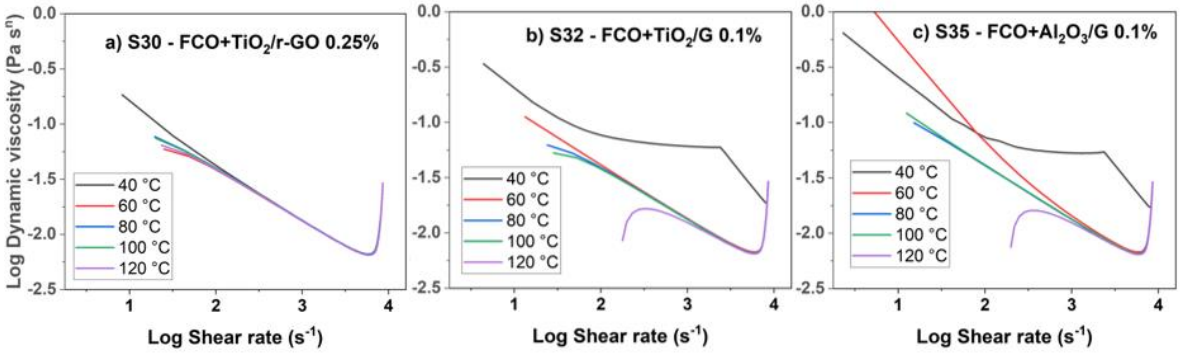

Figure 4.30, Rheometric test results for sample lubricants of FCO with different nanocomposites as additives in log-log axes; a) S30 – FCO+TiO_2/r-GO 0.25 wt.%, b) S32 – FCO+TiO_2/G 0.1 wt.%, and c) S35 – FCO+ Al_2O_3/G 0.1 wt.%

4.4. Dispersion stability of formulated nano-lubricants

Dispersion stability of formulated sample blends were studied using UV-vis spectrophotometry measurements with reference to the procedure explained via Section 3.3.3. in two stages.

1. Samples selected with optimum nanoparticle concentration to reduce friction from each group after Phase-I LRT tests, before improving the physicochemical properties of CCO.
2. Samples selected with enhanced tribological performance after phase-III, LRT tests, following improving the physicochemical properties of CCO.

Spectral absorbency test results for stage 1 are presented in Figures 4.31 and 4.32. Figure 4.31 shows the UV-vis spectra for five weeks overlay on nano-lubricants based with 15W40 (samples S3, S7, S9, and S28) and Figure 4.32 for nano-lubricants with CCO (samples S17, S20, S24 and S31). Out of both groups sample S28 indicates better dispersion with colloidal stability, which could be attributed to functional groups attached to r-GO. Because nanoparticle surface functionalization is an important factor to create repulsive or attractive forces among molecular substrates within the solution.[83, 184]

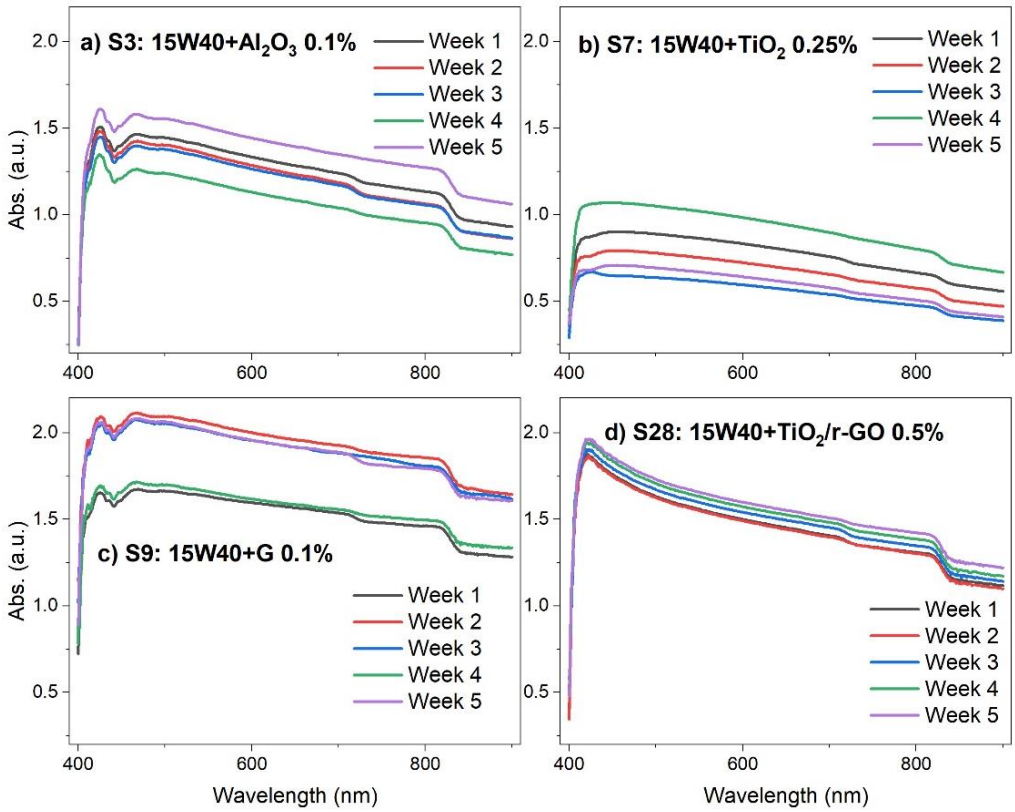

4.31, Overlayed UV-vis spectra (stage 1) for five weeks on formulated nano-lubricants having 15W40 with different Figure nanomaterials as additives with their optimum concentration to reduce friction; a) S3, b) S7, c) S9, d) S28

From CCO group sample S 31 is showing better dispersion stability with relatively poor absorbance than all other nano-lubricants (Figure 4.32), again the stability could be ascribed to r-GO group attached to TiO_2/r-GO nanocomposite. Samples with graphene in both groups show a higher degree of absorbance, which could be assigned to high specific surface area of graphene (~2630 m^2 g^{-1}),[102] albeit with inconsistent dispersion stability. Other samples:

S3, S7, S17 and S20 are also illustrating better absorbance, albeit inconsistency in colloidal stability is the concern need improvement.

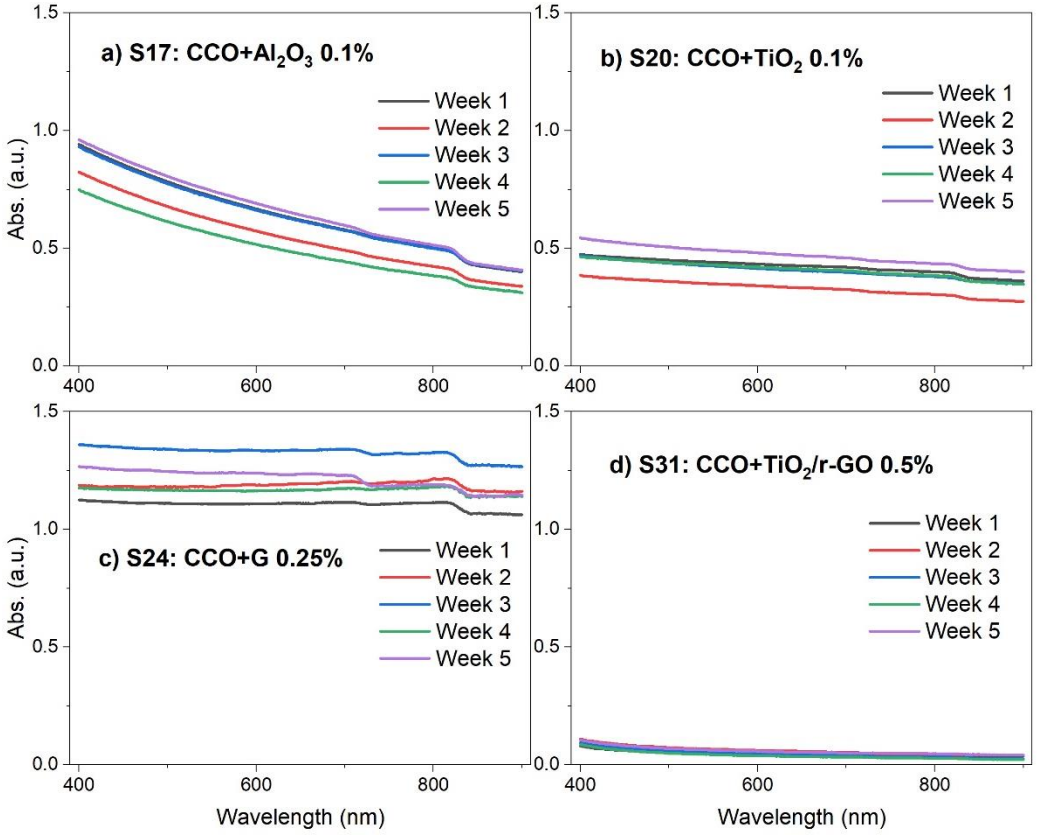

Figure 4.32, Overlayed UV-Vis. spectra (stage 1) for five weeks on CCO based nano-lubricant formulations having different nanomaterials as additives with their optimum concentration to reduce friction; a) S17, b) S20, c) S24, d) S31

Dispersion stability is a fundamental requisite of a lubricant for consistent tribological functioning. Particle size, method of agitation, duration of agitation, surface potential etc., are essential factors affecting improvement. [83, 96, 184] In view of above ultrasonic mixer was used, which uses ultrasonic waves for agitation. This is in place of magnetic stirrer to avoid coagulation, flocculation leading to agglomeration. This includes keeping nanoparticle equally dispersed in the solution, while keeping particle size as minimum as possible.[185] From the nanoparticle characterization results it is observed that graphene used in this research is with less oxygen functional groups (Raman: I_D/I_G = 0.21, XPS: C- 94.3%: O- 5.7%, Section 4.1). As illustrated in Figures 4.31 and 4.32, nanocomposite with r-GO group is showing better dispersion stability, thus blended two more samples S9A and S24A using GO instead of G, as nano additive. Sample descriptions are elucidated in Table 3.3b. In addition to

TiO_2/r-GO, TiO_2/G and Al_2O_3/G nanocomposites were synthesized and used to blend more samples to enhance overall performance of formulations, including colloidal stability by integrating qualities of individual nanoparticle to a composite element.

From Figure 4.33 it is confirmed that the sample S9A, which is with GO as nano-additive is stable than the sample with G (S9), which could be hypothesized that functional groups (C=O, -COOH, -OH) attached to GO may have been functionalized with long chain molecules of 15W40. (15W40 is a multigrade mineral oil consisting of long chain and high molecular weight hydrocarbons with more than 30 carbon atoms in each molecule).[13, 37]

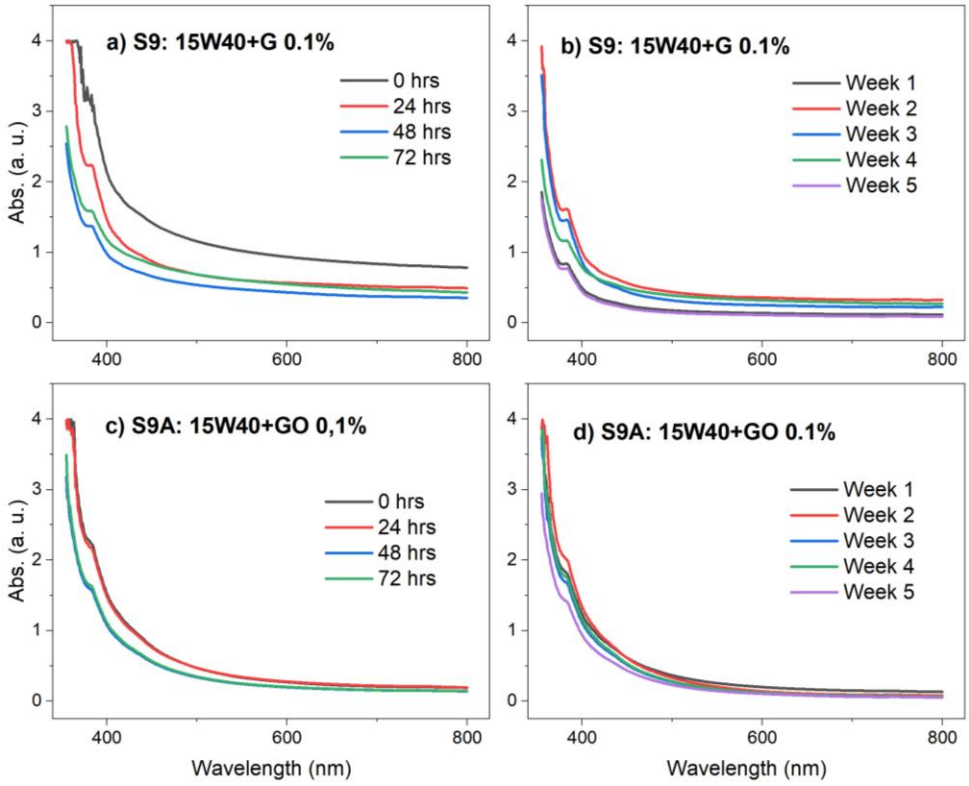

Figure 4.33, Overlayed UV-Vis spectra for samples S9 and S9A, a) & c) 0 -72 h overlay in 24 h intervals, b) & d) 5 weeks overlay in weekly intervals respectively.

Absorbency test results for samples S24 and S24A are presented in Figure 4.34, which indicates mixed results compared to the 15W40 based formulations S9 and S9A. Both the samples (S24, S24A) are shoving better absorbance with inconsistent colloidal stability, which could be assigned to dissimilar intermolecular reactions of FCO.

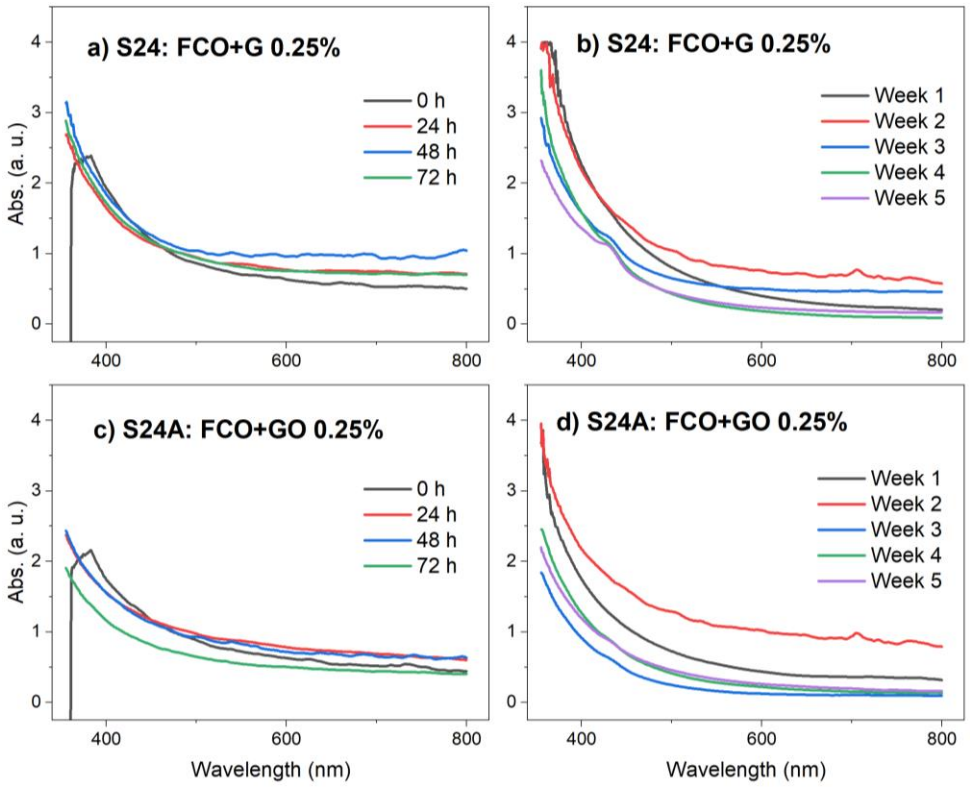

Figure 4.34, Overlayed UV-vis spectra for the samples S24 and S24A, a) & c) 0 -72 h overlay in 24 h intervals, b) & d) 5 weeks overlay in weekly intervals respectively.

Figure 4.35 indicates the variation of optical absorbance measurements of above samples with time for the period of 5 weeks based on the results of UV-vis spectrometry profiles. Sample S9 shows a sharp reduction of absorbance from 0 h – 72 h and remains stable thereafter. S9A has enhanced dispersion stability among all 4 samples, albeit minor agglomeration is evident during 0 h – 72 h period. Perhaps, solutions become stable after sedimentation of surplus quantities than soluble in a base stock.[184] Both FCO samples (S24 & S24A) are also showing early sedimentation up to 72 h, albeit stability is not consistent as 15W40 based nano-lubricants. The results further corroborated with the evidence of observation stability test results (Figure 4.36).

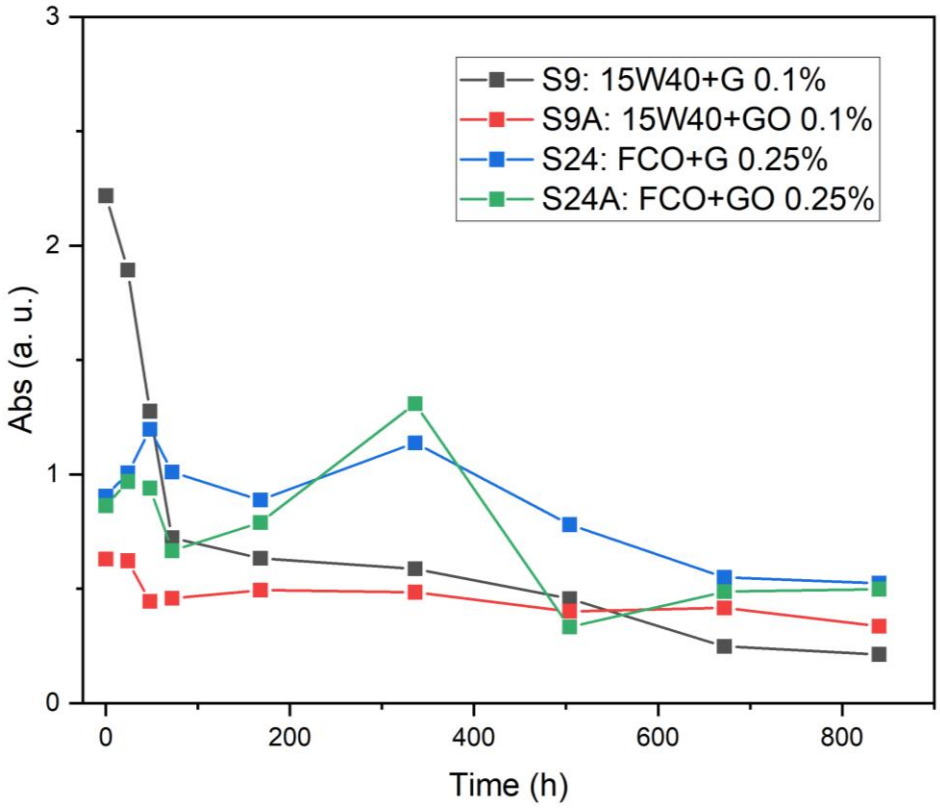

Figure 4.35, Overlayed optical absorbance vs time profiles for samples S9, S9A, S24, and S24A

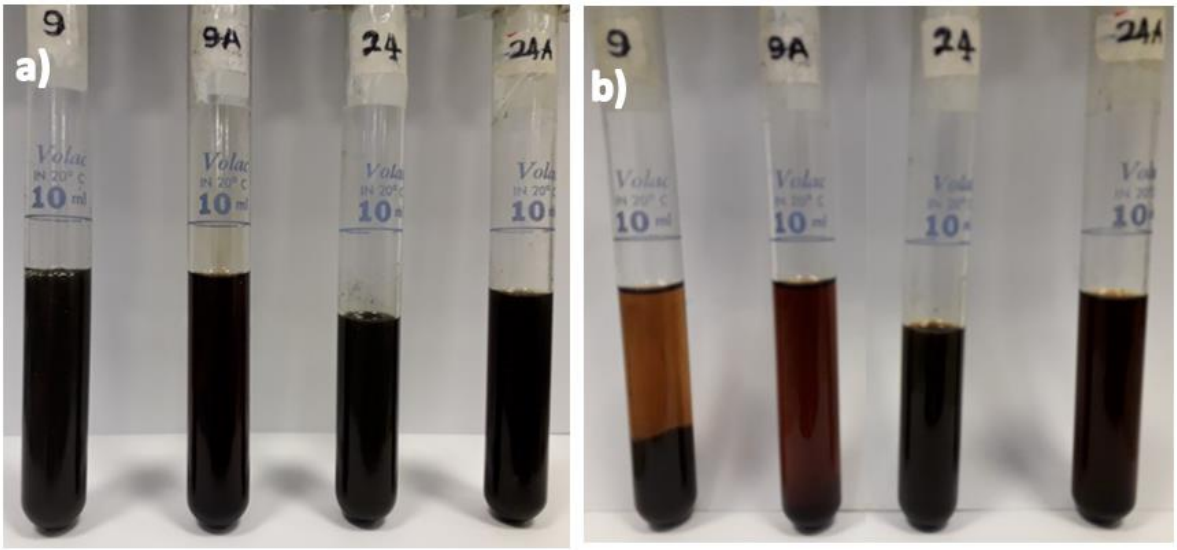

Figure 4.36, Stability observations for samples S9, S9A, S24, and S24A at a) 0 h, b) after 336 h.

Optical absorbance spectra for samples S30, S32, and S35 are presented in Figure 4.37, because of their impressive tribological performance during Phase-III LRT tests. Sample S30 consisting of TiO_2/r-GO as nano-additives shows significant colloidal stability. The results further confirm that the capability of functional groups of r-GO to keep nanoparticles dispersed within the solution. Thus, reinforcing the suggested hypothesis with previous UV-vis (Figure 4.31, 4.32) and rheometric findings (Figure 4.30).

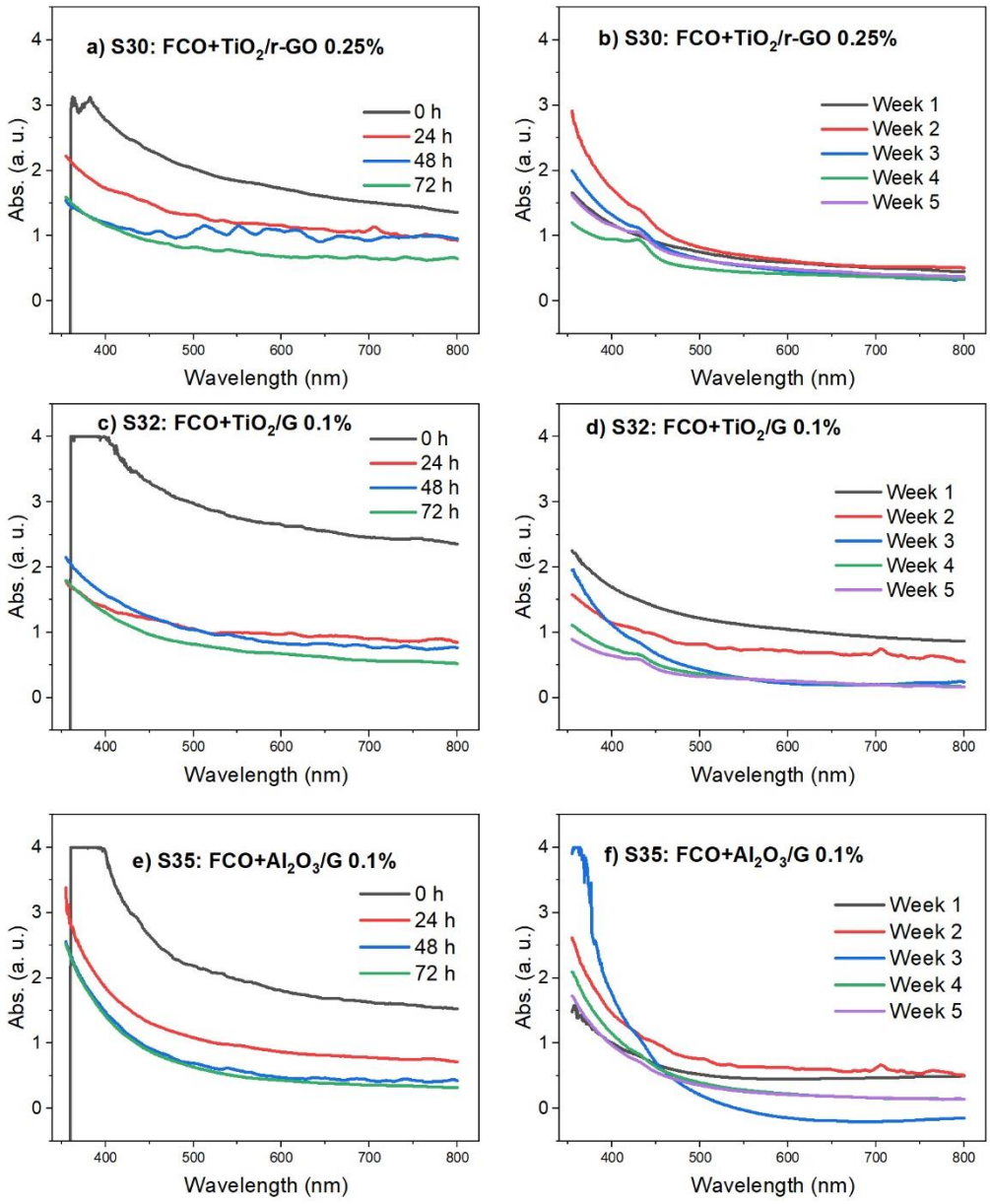

Figure 4.37, Overlayed optical absorbance spectra for samples S30, S32, and S35 from 0 – 72 h in 24 h intervals and up to 5 weeks in weekly intervals; a) & b) S30, C) & d) S32, e) & f) S35

Sample S32 is composed of TiO_2/G nano-additive, variation of G in place of r-GO exhibited poor dispersion stability, when compared to S30. Therefore, convincing the potential of r-GO for a stable and homogenous solution. Sample S35, (Al_2O_3/G nano-additives) shows better dispersion stability than S32, perhaps the amorphous nature and particle size of Al_2O_3/G (Figure 4.1) could have played a role. Moreover, all 3 samples exhibited different degrees of sedimentation during the 0 – 72 h period. Figure 4.38 shows the results of absorbance vs time analysis for these 3 blends, which confirms the minor sedimentation of S30 compared to other two blends with consistent colloidal stability thereafter, throughout the experiment range. This result is further confirmed by the results of stability observation tests presented in Figure 4.39.

In summary, the improvement in colloidal stability of formulated nano-lubricants could be ascribed to the use of surfactant, method and time of agitation, incorporation of nanoparticles to create nanocomposites with integrated qualities, particle size, morphology and surface functioning of nano-additives utilized.[83, 96, 184]

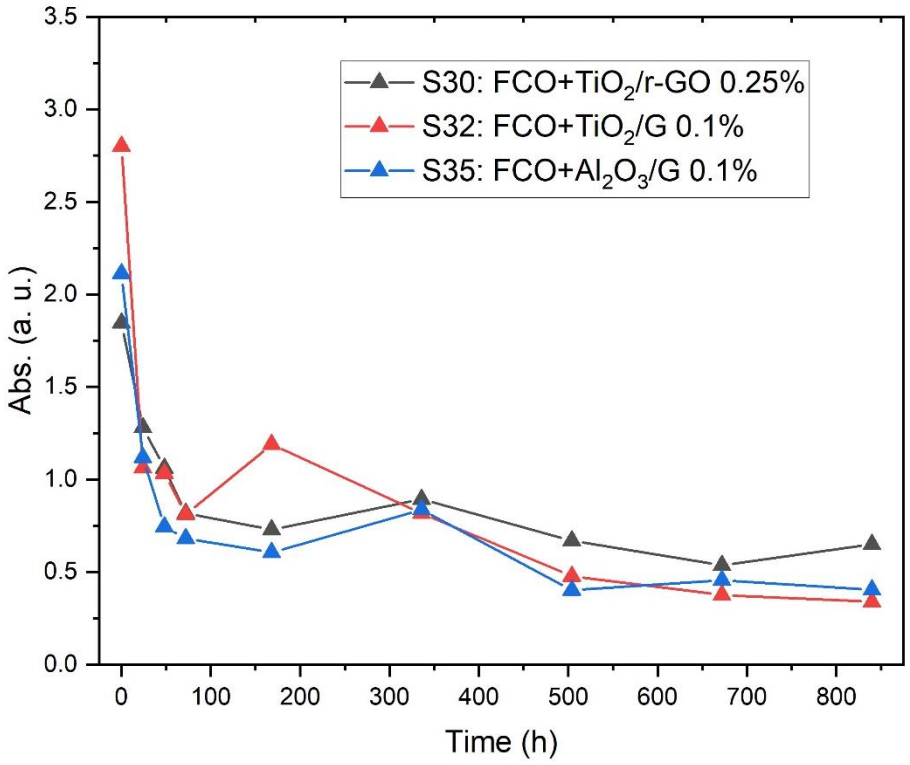

Figure 4.38, Overlayed optical absorbance vs time profiles for samples S30, S32, and S35.

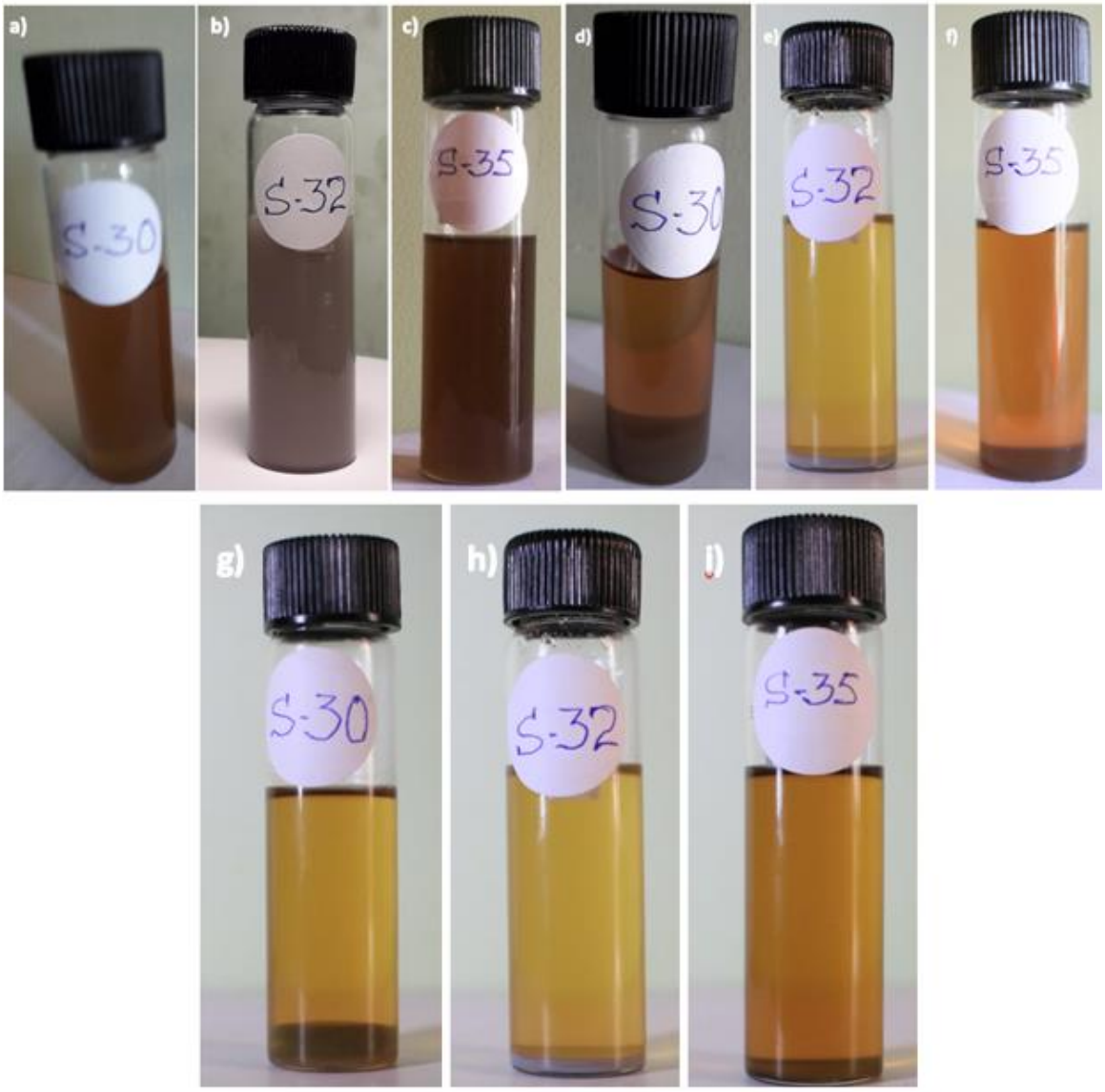

Figure 4.39, Stability observations for samples S30, S32, and S35; a-c) at 0 h, d-f) after 72 h, g-i) after 336 h.

5. Chapter 5: Results part II – Tribological analyses on formulated nano/bio lubricants

Tribological behavior of formulated sample lubricants were investigated using a tribometer and other surface characterization tools with reference to the test protocols elucidated with the experimental methodology (Sections 3.4) and the test results are presented and discussed in this section.

5.1. Analysis of coefficient of friction (COF)

As described in the methodology (Section 3.4.1) LRT test rig (DUCOM TR – 282) was utilized to investigate tribological performance of sample lubricants. Figure 5.1 illustrates the results of Phase-I LRT tests for COF vs time analysis under the test conditions of sliding frequency of 20 Hz with 120 N load at the temperature of 100 °C for selected samples. Samples S3-S25 and S26-S31 were tested on two different occasions with the same model, different machines. Therefore, S1 as the reference oil was tested with samples on both occasions. As a result, the scale of the Y axis for the layer "d" is not matching with the scale of Y axes for other layers: a-c.

Sample S7 indicates heavy vibration with Phase-I test results (Fig. 5.1a), suggesting trapping of agglomerated additive clusters between rubbing asperities. Figure 5.1d indicates an increase of FCO by sample S28 than S1 which is a combination of 15W40 and TiO_2/r-GO. Sample S31, which is constituted with CCO and TiO_2/r-GO is showing marginal decrease of COF compared to S1. Samples S3, S7, S9, S16, S17, S24, S28 and S31 were selected as the optimum concentration to reduce friction from each nanoparticle/base oil category along with S1 as reference oil (Table 3.3a).

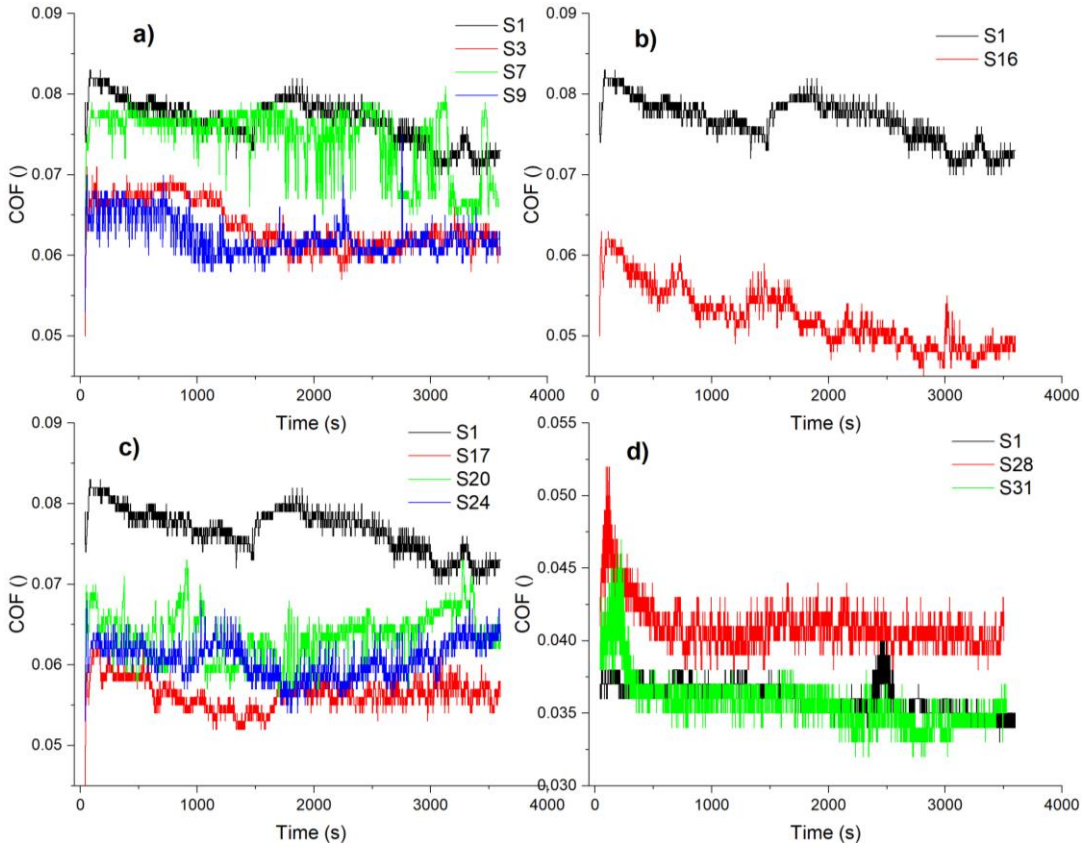

Figure 5.1, Phase-I LRT tests; COF vs time analysis with the test conditions of 20 Hz sliding frequency with 120 N load at the temperature of 100 °C for the blends with optimum concentration to reduce friction, from all sample groups, a) 15W40 with different nanoparticles, b) CCO with 15W40, c) CCO with different nanoparticles, d) TiO_2/r-GO with 15W40 and CCO. Sample S1 is included in all for groups as reference oil.

Figure 5.2a, represents the mean COF for sample blends based on mineral stock (15W40) and different nanoparticles (graphene(G), Al_2O_3, and TiO_2), in varying concentrations. The mean COF was obtained from approximately 35,000 COF readings within a test period of 3600 (s) for a sample. The standard error of the COF for all samples is in the range of 1.74×10^{-4} to 6.77×10^{-6}, thus error bars do not appear with the plotted mean COF bar charts for all lubricants (Figure 5.2). Samples S3, S7 and S9 were chosen for further investigation as the best concentration to reduce friction from respective lubricant group based on the results of the 15W40 with nanoparticles group. Similarly Figures 5.2b–d, illustrate the mean COF observed for CCO with 15W40, CCO with nanoparticles and TiO_2/r-GO with 15W40 and CCO respectively. Samples S16, S17, S20, S24, S28, and S31 were selected as optimum concentrations to reduce friction. As a control experiment reference oil (Sample S1) was also

selected. The following are the sample descriptions with COF reduction percentage compared to S1 is given in brackets:

S1 – 15W40 (reference oil)

S3 – 15W40 + Al_2O_3 0.1 wt.% - (17%)

S7 – 15W40 + TiO_2 0.25 wt.% - (3%)

S9 – 15W40 + G 0.1 wt.% - (19%)

S16 – CCO + 15W40 10 v/v% - (32%)

S17 – CCO + Al_2O_3 0.1 wt.% - (27%)

S20 – CCO + TiO_2 0.1 wt.% - (17%)

S24 – CCO + G 0.25 wt.% - (21%)

S28 – 15W40 + TiO_2/r-GO 0.5 wt.% - (6%)

S31 – CCO + TiO_2/r-GO 0.5 wt.% - (17%)

Based on the test results samples S9, S16, and S17 had the highest COF reduction from the lubricant groups of 15W40 with nanoparticles, CCO with 15W40 and CCO with nanoparticles respectively (Fig. 5.2, a-d). Sample S16 had the highest COF reduction (32%, Fig. 5.2b) of all samples.

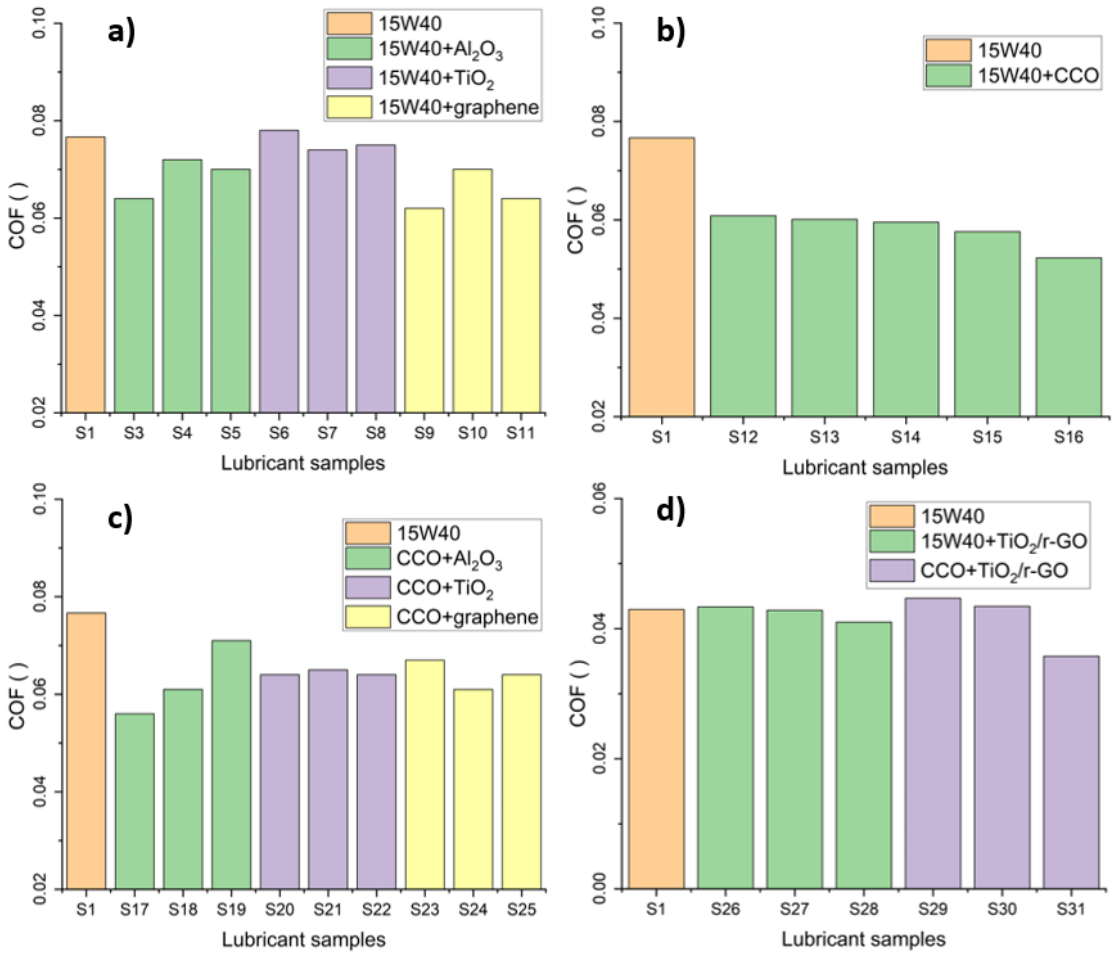

Figure 5.2, Mean COF observed from the Phase-I LRT test with the sliding frequency of 20 Hz (1200 rpm) under 120 N load at 100 °C for different sample lubricants; a) 15W40 with different nanoparticles, b) CCO with 15W40, c) CCO with nanoparticles, d) 15W40 and CCO with TiO2/r-GO, all in different concentrations. Sample S1 (15W40) is included in all four (a–d) plots as reference oil.

Phase-II, LRT test observations

Figures 5.3 and 5.4 demonstrate the tribological behavior of selected nine sample blends with reference oil for 16 different load/velocity combinations at 140 °C. Figure 5.3, shows the COF vs sliding frequency graphs, which reveals that the increment of sliding frequency reduces the COF value for all samples, which is directly correlated to the angular velocity (i.e., rpm) of the mechanism. This reduction is regardless of the load variation, indicating an increment of EHL, due to increase in fluid pressure with an increase in fluid entrain velocity. Fluid entrain velocity depends on the relative velocity of the surfaces in proximity, which agrees with Reynold's EHL film thickness equation (Eq. 2.7).[27, 35]

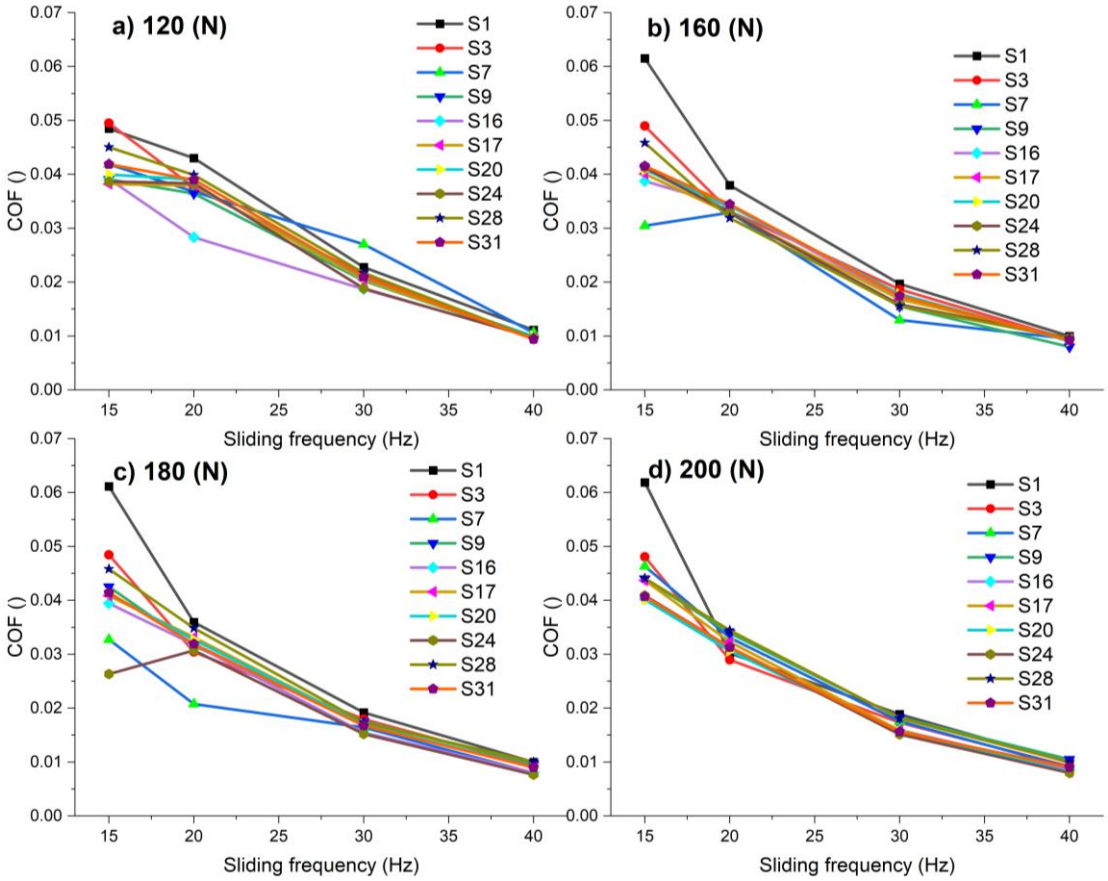

Figure 5.3, Tribometry curves of Phase-II LRT tests for COF vs sliding frequency analyses on selected sample blends with different loads; a) 120 N, b) 160 N, c) 180 N, d) 200 N at 140 °C.

Tribometry graphs for COF vs loads for all frequencies are shown in Figure 5.4. From these graphs it is evident that load has no effect on friction reduction when compared to the reductions observed with increasing velocity (Fig. 5.3). This agrees with Hammrock and Dowson's relationship for calculating film thickness (Eq. 2.8, 2.13), which indicates that the load parameter has the least impact when compared to the contributions of speed, material, and contact parameters.[35, 37]

Figures 5.3 and 5.4 show that all the sample blends reduce friction better than S1, except for sample S7, which is inconsistent under all load and velocity conditions. On the other hand, blends S24, S16, and S9 are screened for further investigation due to their consistency in reducing friction under any load/velocity combination, when compared to the other blends in the investigation. Summary of maximum and mean COF reduction by these samples after Phase-II LRT tests is shown in Table 5.1.

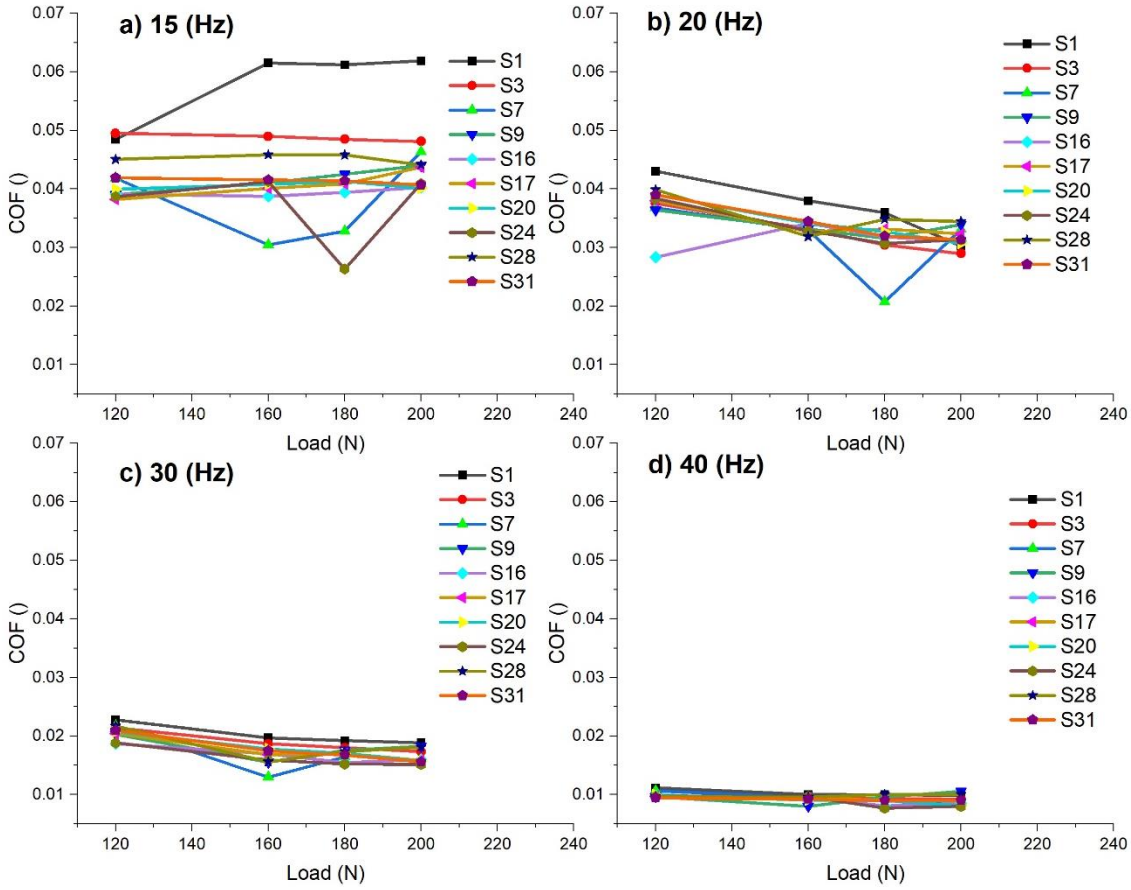

Figure 5.4, Phase-II LRT test results: tribometry graphs for COF vs load behavior of sample blends with different frequencies, a) 15 Hz, b) 20 Hz, c) 30 Hz, d) 40 Hz at 140 °C.

Table 5.1, Summary of mean and maximum COF reduction by selected samples for 16 load/velocity combinations after Phase-II LRT tests.

Sample	Composition	Mean COF reduction) (%)	Max. COF reduction) (%)	Test condition for Max. COF reduction Load/Frequency/Temp (N)	(Hz)	(°C)
S3	15W40 + Al_2O_3 0.1 wt.%	13	22	200	15	140
S7	15W40 + TiO_2 0.25 wt.%	-7	50	160	15	140
S9	15W40 + G 0.1 wt.%	18	33	160	15	140
S16	CCO + 15W40 10 v/v%	23	37	160	15	140
S17	CCO + Al_2O_3 0.1 wt.%	19	35	160	15	140
S20	CCO + TiO2 0.1 wt.%	19	35	200	15	140
S24	CCO + G 0.25 wt.%	24	57	180	15	140
S28	15W40 + TiO_2/r-GO 0.5 wt.%	14	29	200	15	140
S31	CCO + TiO_2/r-GO 0.5 wt.%	18	34	200	15	140

Phase-III, LRT test observations

Phase-III LRT tests were performed after improving sub standards of coconut oil and the dispersion stability of nano-lubricants. The aim was to study the effects of optimization in the tribological behavior of formulated samples. The test conditions were with 25 velocity/ load combinations at 140 °C to simulate the standard power band of a diesel engine.

Figure 5.5 shows the COF vs time analysis for FCO (S38) and reference oil (S1) under two different test conditions, a) 120 N load with 20 Hz of sliding frequency and b) 180 N load with 50 Hz of sliding frequency, both at 140 °C elevated temperature. The results indicate that the FCO is capable of reducing the COF by 7% (mean) for all 25 test conditions with maximum COF reduction of 53% under the test "b)" without adding any additives.

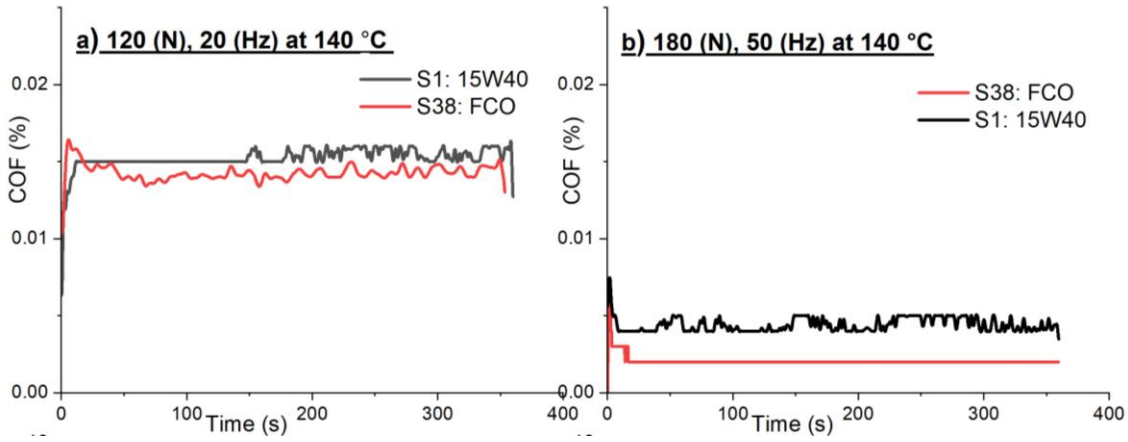

Figure 5.5, Tribometry graphs for Phase-III LRT tests; COF vs time analysis between samples S1 and S38 under two different test conditions, a) 120 N load with 20 Hz sliding frequency, b) 180 N load with 50 Hz sliding frequency, both at 140 °C.

From the test results (Figure 5.6) it is evident that the sample S9 is unstable at 15 Hz (Figure 5.6a), S1shows effective lubrication than S9 at 20 Hz (4.6b). Sample S9A is more effective than the S9 and S1 in reducing friction exhibiting a maximum of 72% COF reduction (for 50 Hz/200 N combination) with an average of 26% COF reduction for all 25 frequency/load combinations over reference oil (S1). In comparison sample S9 achieved a maximum of 42% and an average of 17% COF reduction over S1. Moreover, it is evident that the COF reading for S1 seems erotic under 40 Hz/200 N test condition (Figure 5.6d). Therefore, this reading is not considered for all maximum and average COF assessments.

Dispersion stability of GO was improved compared to G in the solution as observed during UV-vis analyses. It is hypothesized that the ability of GO nanoparticles to remain in the solution thus, interactions of carboxyl or carbonyl functional groups on the GO surface with sliding substrates reducing asperity contacts has generated this tribological enhancement.[104]

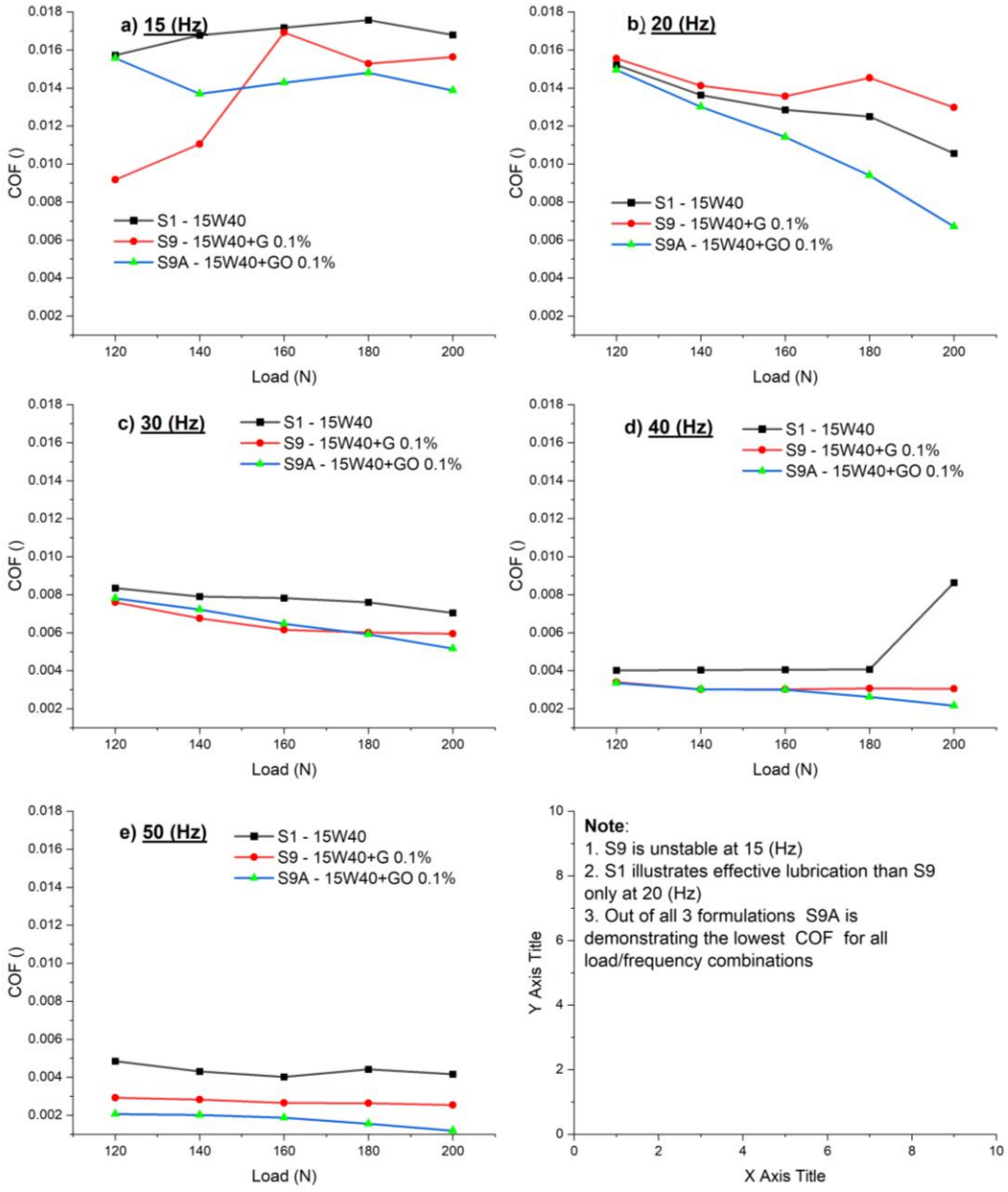

Figure 5.6, LRT tests Phase-III: tribological performance of graphene (G) over graphene oxide (GO) with mineral oil-based sample blends; COF vs load characteristics at different sliding frequencies, a) 15 Hz, b) 20 Hz, c) 30 Hz, d) 40 Hz, e) 50 Hz, at 140 °C.

Figures 5.7 – 5.9 present the tribological test results for the blends constitute with the combination of FCO and nanocomposites; TiO_2/r-GO, TiO_2/G and Al_2O_3/G respectively. S29 is lubricating more effectively at 20 Hz than both S1 and S30, however unstable at 180 N/20 Hz combination (Figure 5.7b). S1 and S29 show same COF for 40 Hz except for 200 N/40 Hz combination (Figure 5.7d). S30 is showing lowest COF of all 3 formulations other than 20 Hz (Figure 5.7).

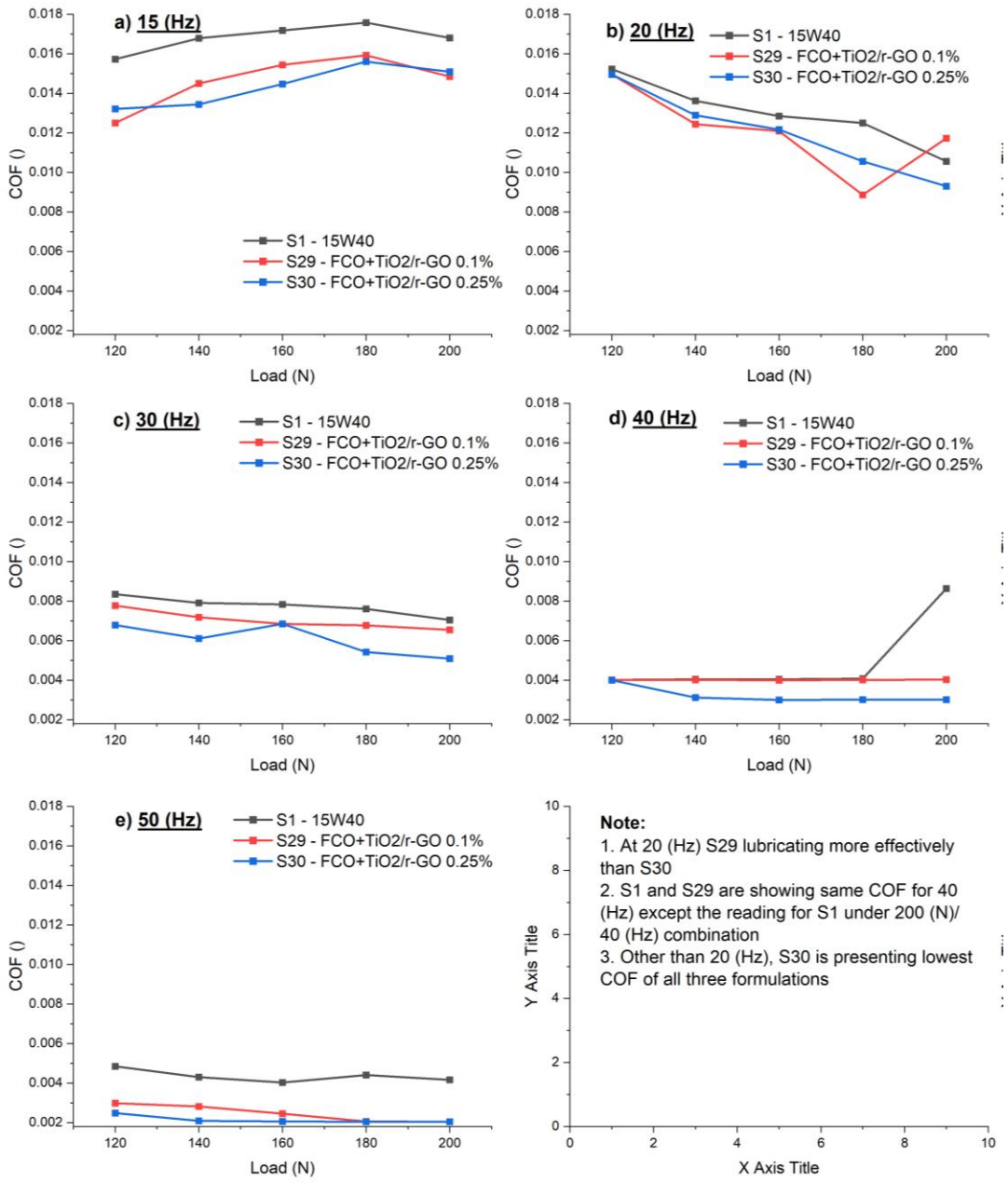

Figure 5.7, LRT Phase-III, tribological performance; COF vs load curves of FCO + TiO_2/r-GO blends having different nanoparticle (TiO_2/r-GO) concentrations with changing sliding frequencies; a) 15 Hz, b) 20 Hz, c) 30 Hz, d) 40 Hz, e) 50 Hz at 140 °C.

Figure 5.8 shows the tribometry test results for samples S32, S33, and S34. S32 shows slight instability at 140 N/15 Hz combination (Fig. 5.8a). S34 shows lowest COF at 15 Hz and 30 Hz sliding frequencies (Fig. 5.8a & c). S32 is indicating lowest COF at 30 Hz and sharing lowest COF with S33 and S34 at 50 Hz and 40 Hz respectively. Thus, S32 is selected for further investigations.

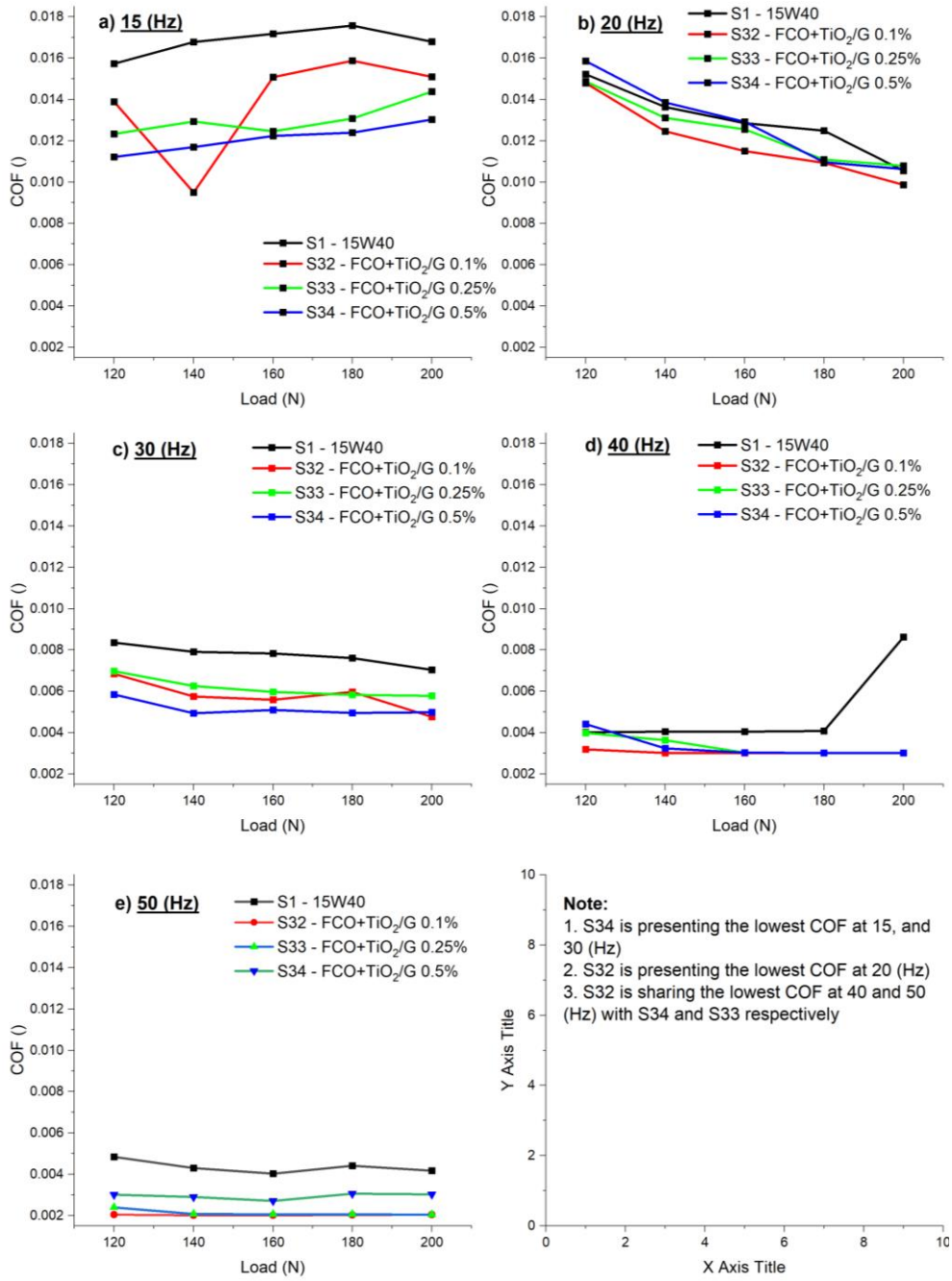

Figure 5.8, LRT Phase-III, tribological performance of FCO+TiO_2/G blends; COF vs load curves with varying sliding frequencies; a) 15 Hz, b) 20 Hz, c) 30 Hz, d) 40 Hz, e) 50 Hz, at 140 °C.

Figure 5.9 illustrates the LRT test results for sample S35, S36 and S37. Figure 5.9a shows a rapid increase of COF by S36 at 200 N and by S37 at 180 N under 15 Hz test conditions. Other than that, S35 is dominating throughout with effective lubrication to reduce friction under all 25 test conditions. Also, S1 seems more effective reducing friction than S36 and S37 at 15 Hz, 20 Hz, and 30 Hz test conditions.

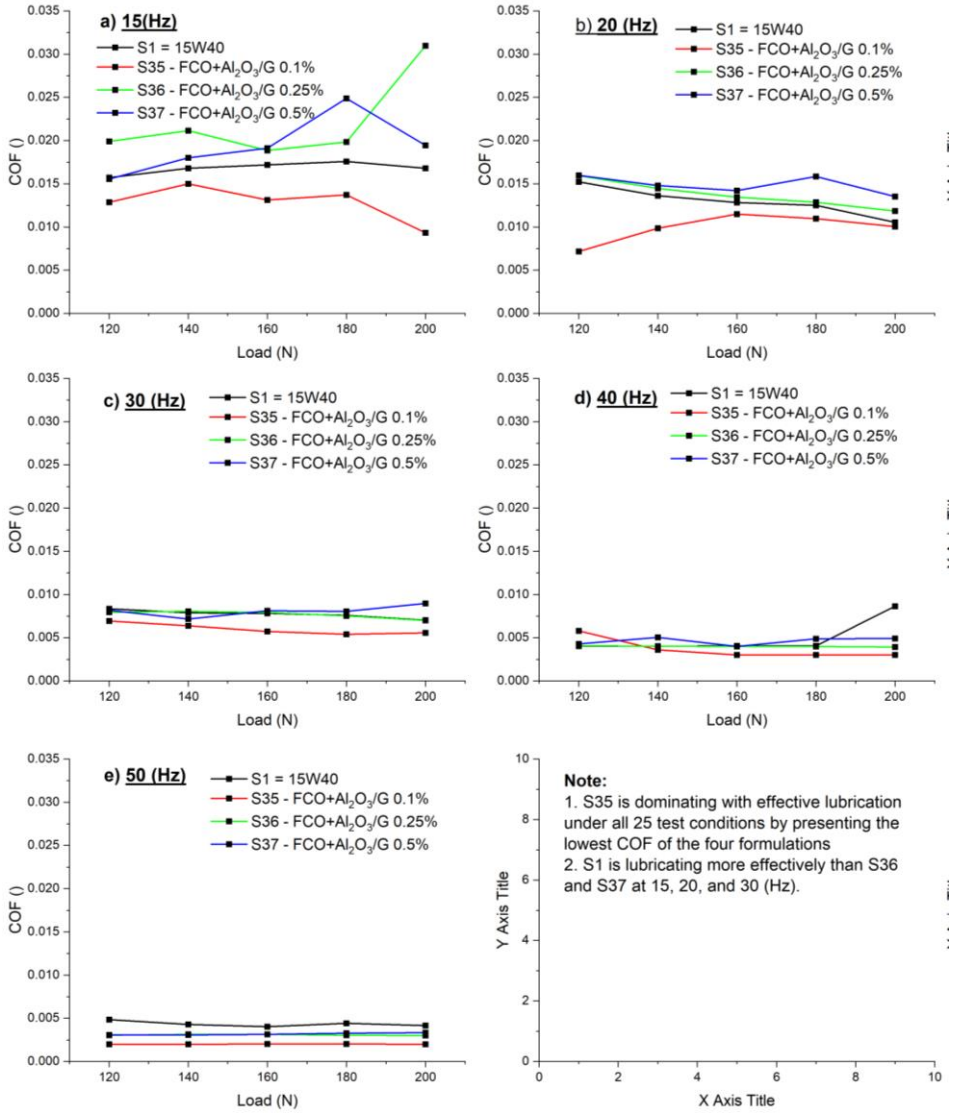

Figure 5.9, LRT Phase-III, tribological performance of FCO+Al_2O_3/G blends; COF vs load curves with varying sliding frequencies; a) 15 Hz, b) 20 Hz, c) 30 Hz, d) 40 Hz, e) 50 Hz, at 140 °C

Blends S30, S32, and S35 were selected as the optimum concentration to reduce friction under varying load and velocity conditions from each lubricant group (Fig. 5.7 – 5.9), thus comparisons were made for further evaluation and presented in Figure 5.10. From Figure 5.10b it is evident that the S35 is having the lowest COF among all 3 blends at 20 Hz. Samples S30, S32 and S 35 are jointly presenting the lowest COF at 40 Hz and 50 Hz, and all 3 blends are showing enhanced lubrication than S1 under all test conditions. Sample S35 emerged with the most promising performance among all (Figure 5.10) with a maximum of 59% COF reduction for the 200 N/50 Hz load/frequency combination, with an average of 28% COF reduction for all combinations compared to S1 (reference oil). Summary of COF

achievements for finalized formulations (S9, S9A, S30, S32, and S35 with S16 and S24) are presented in Table 5.2.

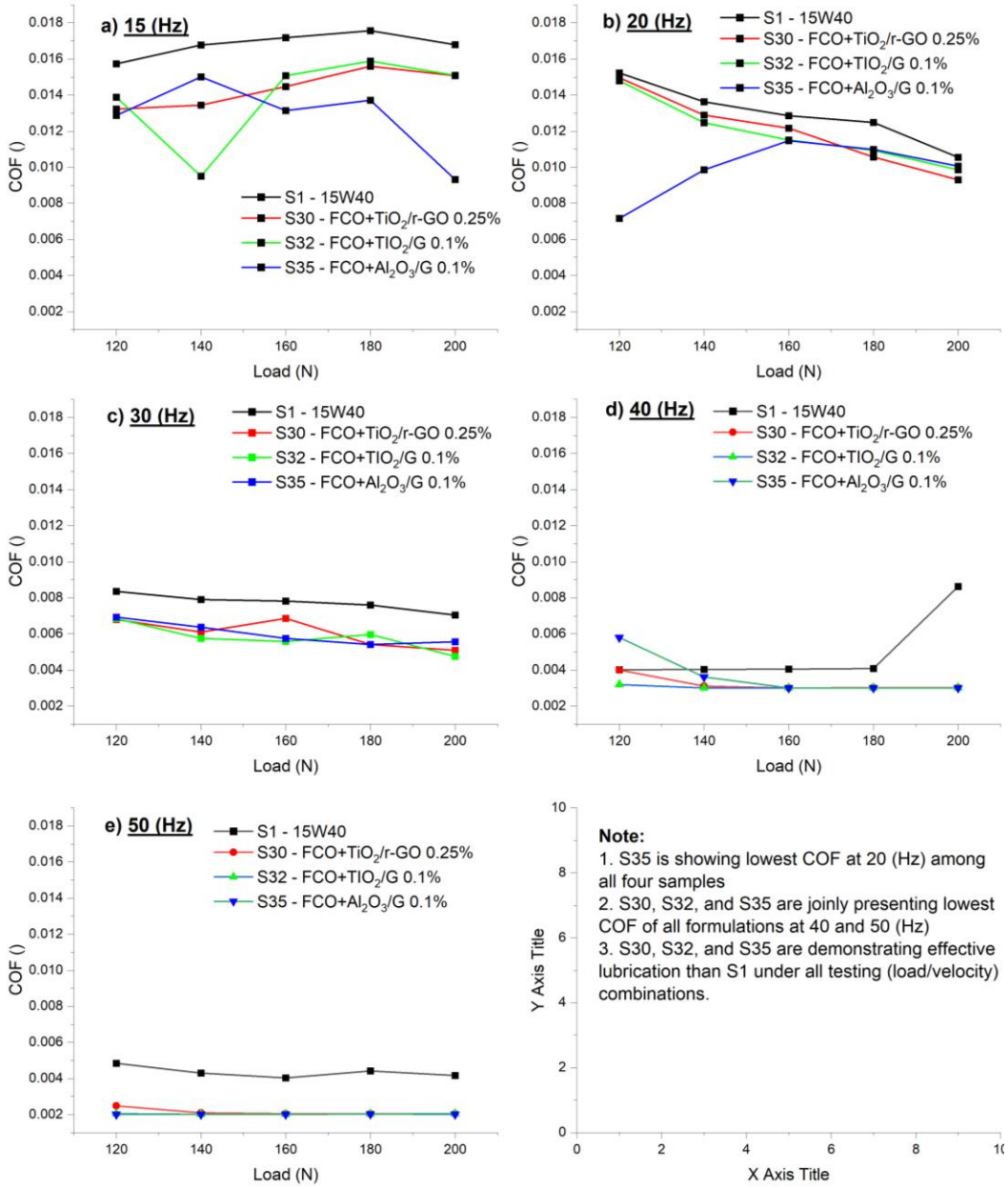

Figure 5.10, Comparison of LRT test results among lubricants constitute with FCO and TiO_2/r-GO, TiO_2/G, and Al_2O_3/G nanocomposites with optimum concentrations (S30, S32, and S35); COF vs load characteristics for different sliding frequencies, a) 15 Hz, b) 20 Hz, c) 30 Hz, d) 40 Hz, e) 50 Hz at 140 °C.

From Phase-III tests it is observed a few abnormal COF readings from tested samples. For example, S9 under 160 N/15 Hz, S1 under 22 N/40 Hz (Fig. 5.6a & d), S29 under 180 N/20 Hz (Fig. 5.7 b), and S32 under 140 N/15 Hz (Fig. 5.8a) test conditions with rapid increase or decrease of COF. In theory COF should be the same for a constant sliding velocity

with varying loads. Thus, this situation could be ascribed to rapid change of speed, material or contact parameters, perhaps entry of agglomerated nano-additive clusters or silicon particles to tribo-test interface when adding lubricant or adding excessive oil during load changing steps for increment or decrement of COF. This is one of the reasons to have 25 test conditions to minimize errors when selecting optimum formulation. All the samples were tested approximately one month after the blending was completed. Colloidal stability of nanoparticle dispersion is critical for any tribological application. This stability is achieved through thermal energy and Brownian motion of the molecules in the solution, which improves the tribological performance of any nanofluid. UV-vis analysis and visual observations revealed the stability of S35. During nanoparticle characterization (TEM, SAED, XRD) it is observed that Al_2O_3/G nanoparticles are having laminar/ spherical morphology with mean particle size of 10 ± 0.3 (nm) and are in amorphous nature. The properties which may have contributed to the colloidal stability of S35.

EDX analysis on the wear surface of piston ring segment of S35 after LRT test confirms the deposition of Al particles on the wear surface (Figure 5.14), which agrees with Ali, et al., (2016) observations.[9] Thus, the small particle size of approximately spherical alumina nanoparticles (10 ± 0.3 (nm)) combined with the laminar nature of the graphene, which also exhibits adhesion and cohesion qualities with the contacting substrate may have influenced the formation of a protecting layer supported by mending, and polishing effect with ball bearing mechanism, resulting in this tribological enhancement (Figure 5.11).[83, 92]

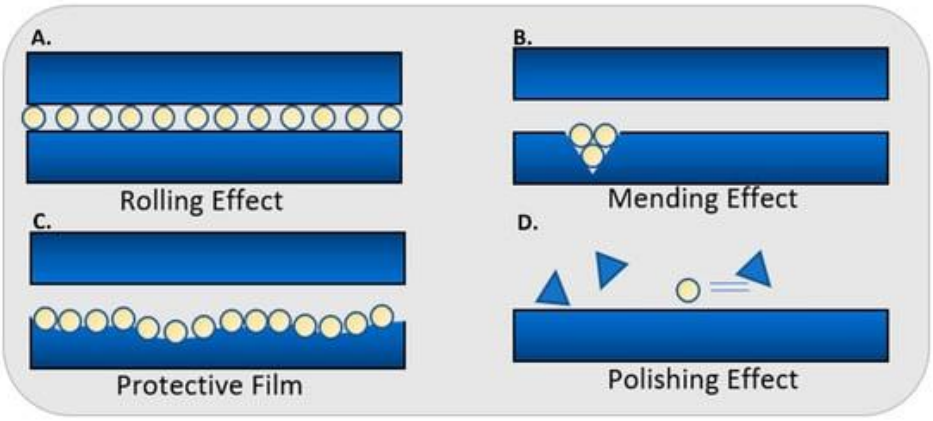

Figure 5.11, Suggested lubrication mechanisms associated with sample lubricants at piston ring cylinder liner interface of an ICE.[187]

Nevertheless, samples S16 (FCO + 15W40 10 v/v%) and S24 (FCO + G 0.25 wt.%), which have shown impressive performance during LRT Phase-II tests under all velocity/load variations (Table 5.1), did not perform well during Phase-III tests. Albeit, both S16 and S24 reduced COF by 11% on average across all conditions, it is hypothesized that FOC may have not been effective with these two combinations. As a result, S16 and S24 were not considered for further investigation beyond Phase-III tests.

Moreover, trimethylolpropane (TMP) esters of vegetable oils are reported to have increased COF compared to the mineral based conventional engine oils in use.[83] FCO exhibited 7% of mean COF reduction for all 25 load/velocity combinations during Phase-III LRT tests, without any additives. However, FOC lost its lubricity up to some extent compared to CCO. For example, CCO based S16 and S24 (S16-19 and S24-19) had a reported average of 23% and 24% COF reduction after Phase-II LRT tests (Table 5.1). However, FCO based S16 and S24 (after formulation of FCO with enhanced lubrication characteristics; S16-22 and S24-22) have reported 11% COF reduction after Phase-III LRT tests (with reference to S1: 15W40 for both cases) indicating a loss of lubricity by ~ 12% (Table 5.2). This observed phenomenon is further supported by the 3D optical profilometry test results, which show a higher S_a and S_q values for S16-22 and S24-22 than S16-19 and S24-19 (Figures 5.23 and 5.24). However, Phase II and III LRT experiments have dissimilar test protocols.

Table 5.2, Summary, LRT Phase-III test results: reduction of COF by formulations S9, S9A, S16, S24, S30, S32 and S35, comparison with reference oil S1 (15W40)

Sample	Composition	Mean COF reduction) (%)	Max. COF reduction) (%)	Test condition for Max. COF reduction Load/Frequency/Temp (N)	(Hz)	(°C)
S9	15W40 + G 0.1 wt.%	17	42	120	15	140
S9A	15W40 + GO 0.1 wt.%	26	72	200	50	140
S16	FCO + 15W40 10% v/v	11	71	120	15	140
S24	FCO + G 0.25 wt.%	11	37	120	50	140
S30	FCO + TiO_2/r-GO 0.25 wt.%	23	54	180	50	140
S32	FCO + TiO_2/G 0.1 wt.%	26	58	120	50	140
S35	FCO + Al_2O_3/G 0.1 wt.%	28	59	120	50	140

5.2. Wear scar analyses

Following Phase-III LRT tests, wear scars of test specimens; piston ring segments (PRS) and cylinder liner segments (CLS) were analyzed using SEM, EDX and 3D noncontact optical profilometry (Section 3.4.2) and the results are presented and discussed herein.

5.2.1. EDX observation

EDX analyses were performed along with SEM surface characterization on wear surfaces of test specimens (PRS and CLS) to evaluate elemental deposition on stroked surfaces. PRS and CLS have a surface area of ~ 29.45 mm^2 and ~ 400 mm^2 respectively (Table 3.4), thus EDX findings for PRSs are presented for better accuracy. Figure 5.12 shows the elemental spectra for unused PRS surface (without test), Figures 5.13 and 5.14 show the elemental spectra for PRS wear surfaces of samples S16, and S35 after Phase-III LRT tests respectively. This is to compare nanoparticle deposition and to assess a feasible lubrication mechanism. Tables 5.3 and 5.4 list the deposition of elements with atomic and weight percentages respectively for samples: S1, S9A, S16, S24, S30, S32 and S35. From these Figures and Tables, it is revealed that the used PRS surfaces are with additional elemental deposition than unused PRS surface (Fe, C, Si and P elements). Additional elements are Ni, Cr, Mo, O, K, and Al, perhaps Ni, Cr, and Mo are from the outer coating of the PRS, O from the atmospheric air as a result of combustion process. Element K is only with the formulations based with FCO, because of the usage of KOH during the formulation of FCO. Al is with the sample S35, which contains Al_2O_3/G as nano-additives.

Deposition of Al nanoparticles on PRS surface of S35 in addition to other elements (Figure 5.14) confirms the tribological enhancement of S35, suggesting protective layer formation assisted by secondary mending and polishing effect by Al_2O_3/G nanomaterials (Fig. 5.11). Furthermore, Figure 5.12 reveals that the 65% of Fe deposition on the surface of unused PRS specimen, whereas Figure 5.14 verifies that there are not any Fe elements on S35 wear surface, which confirms that the wear surface (PRS) of S35 was covered with the deposition of other elements leading to tribological enhancement.

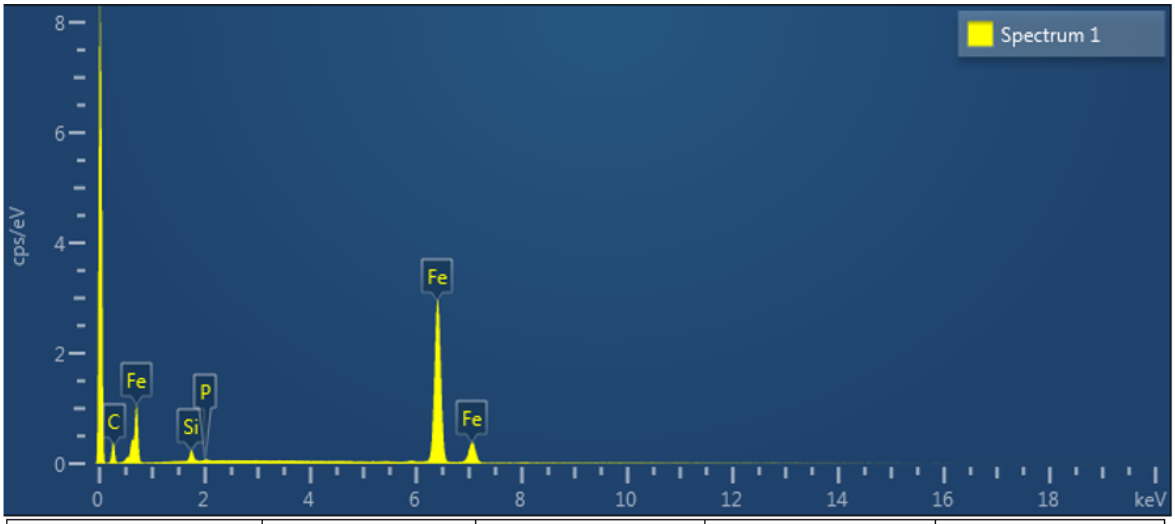

Spectrum 1				
Element	**Line Type**	**Weight %**	**Weight % Sigma**	**Atomic %**
C	K series	9.77	0.22	33.20
Fe	K series	89.09	0.22	65.15
Si	K series	1.00	0.03	1.46
P	K series	0.14	0.03	0.19
Total		100.00		100.00

Figure 5.12, EDX analysis on unused PRS surface (without LRT test)

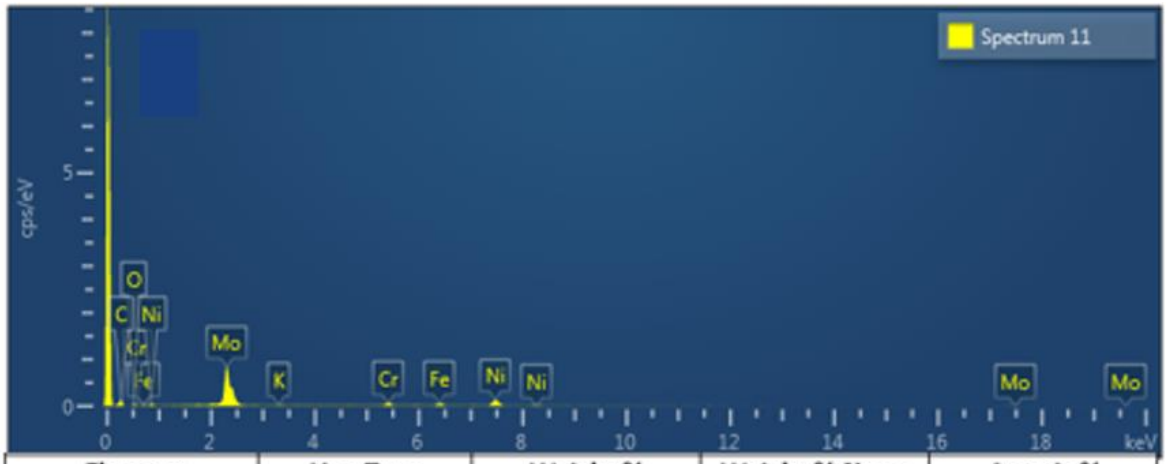

Element	**Line Type**	**Weight %**	**Weight % Sigma**	**Atomic %**
Ni	K series	27.16	0.66	17.11
Cr	K series	4.78	0.24	3.40
Fe	K series	6.53	0.32	4.32
Mo	L series	41.36	0.77	15.94
C	K series	16.89	1.09	52.01
O	K series	3.02	0.28	6.98
K	K series	0.26	0.08	0.25
Total		100.00		100.00

Figure 5.13, EDX analysis on the wear surface of the PRS used with sample S16 after LRT test.

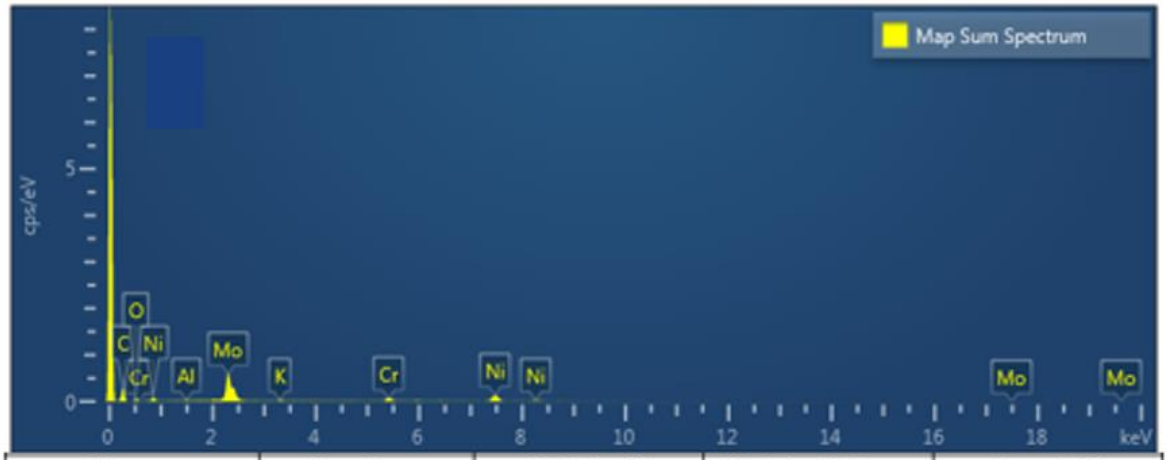

Element	Line Type	Weight %	Weight % Sigma	Atomic %
C	K series	29.20	1.61	66.74
Ni	K series	29.11	1.00	13.61
Cr	K series	6.21	0.36	3.28
O	K series	3.94	0.44	6.76
K	K series	0.86	0.12	0.60
Mo	L series	30.38	0.97	8.69
Al	K series	0.31	0.09	0.32
Total		100.00		100.00

Figure 5.14, EDX analysis on the wear surface of the PRS used with sample S35, after LRT tests.

Table 5.3, Summary of elemental depositions with atomic %, observed via EDX analyses of PRS surfaces without test (blank) and after LRT testing with different sample blends

	Sample (atomic %)							
Element	**Blank**	**S1**	**S9A**	**S16**	**S24**	**S30**	**S32**	**S35**
C	33.2	72.61	72.06	64.62	47.73	41.2	67.77	66.74
Ni	0	9.24	10.49	7.65	21.14	24.8	12.14	13.16
Cr	0	1.78	2.51	1.68	4.14	5.16	2.37	3.28
Mo	0	6.95	8.23	10.33	19.49	20.12	6.76	8.69
Fe	65.15	4.3	0	9.98	0	0.84	4.91	0
Si	1.46	0.18	0	0.19	0	0	0.18	0
O	0	4.93	6.71	5.1	7.18	7.78	5.19	6.76
K	0	0	0	0.44	0.32	0.3	0.46	0.6
P	0.19	0	0	0	0	0	0	0
Al	0	0	0	0	0	0	0	0.32

Table 5.4, Summary of elemental depositions with weight %, observed via EDX analyses of PRS surfaces without test (blank) and after LRT testing with different sample blends

	Sample (weight %)							
Element	**Blank**	**S1**	**S9A**	**S16**	**S24**	**S30**	**S32**	**S35**
C	9.77	34.9	34.5	26.17	14.24	11.45	30.19	29.2
Ni	0	21.71	24.56	15.14	30.83	33.69	26.44	29.11
Cr	0	3.71	5.2	2.95	5.34	6.21	4.57	6.21
Mo	0	26.69	31.46	33.41	46.43	44.66	24.04	30.38
Fe	89.09	9.62	0	18.8	0	0.65	10.16	0
Si	1	0.21	0	0.18	0	0	0.19	0
O	0	3.16	4.28	2.75	2.85	2.88	3.08	3.94
K	0	0	0	0.58	0.31	0.27	0.67	0.86
P	0.14	0	0	0	0	0	0	0
Al	0	0	0	0	0	0	0	0.31

5.2.2. Results of 3D noncontact optical profilometry

Apart from SEM and EDX evaluations, 3D noncontact optical profilometry tests were done to analyze changes to the surface texture of test specimens after tribometer tests to predict a feasible lubrication mechanism. Changes are quantified in terms of surface roughness, which is correlated with friction behavior of the utilized sample lubricant. Profilometry tests were done as explained in the methodology (Section 3.4.2) in two stages: a) after Phase-II, LRT tests, before formulating CCO, b) after Phase-III, LRT tests following formulating CCO with enhanced physicochemical properties. Some samples were tested on both occasions (S1, S9, S16, S24). Thus, all samples are labeled with the year of testing. For example, sample S1 was tested twice. Therefore, profilometry test results for 2019 LRT tests for the sample S1 is presented with the label S1-19 and S1-22 refers to the test performed in 2022 for the same.

Figure 5.15 shows the 2D and 3D optical profiles for unused CLS surface, having area surface roughness parameters as S_a = 1018 (nm) and S_q = 2270 (nm). 2D topography is confirming with SEM micrograph (Fig. 5.25) for having surface texture with cross-hatched

honing contours. Figure 5.16 illustrates the surface roughness evaluation of the sample S1-19 in the sequence of a) friction test analysis, b) wear scare on CLS, and c) and d) for 2D and 3D optical profiles correspondingly. Results of friction tests and wear scar micrographs were discussed in Sections 5.1, and 5.2.3), thus effects to the surface roughness of test specimens are compared with the roughness of an unused CLS and CLS used with reference oil (S1-19 and S1-22). This confirms that S1-19 is with smoother surface than unused CLS having S_a and S_q measurements as 786 nm and 1937 nm respectively.

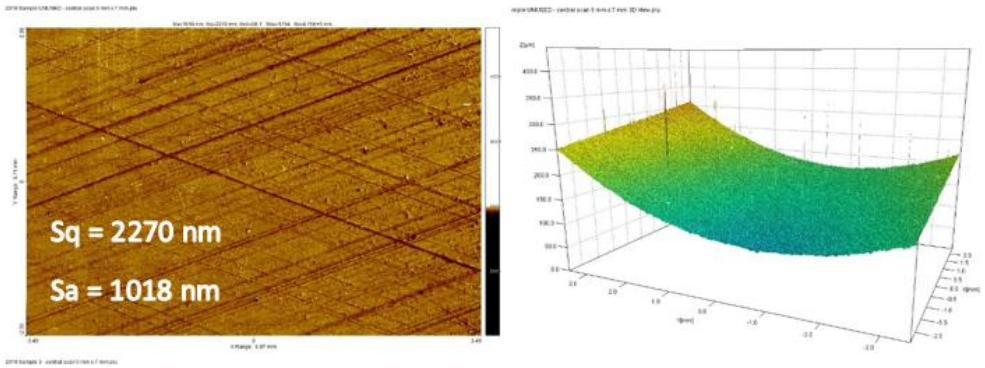

Figure 5.15, 2D and 3D noncontact optical profiles for unused CLS

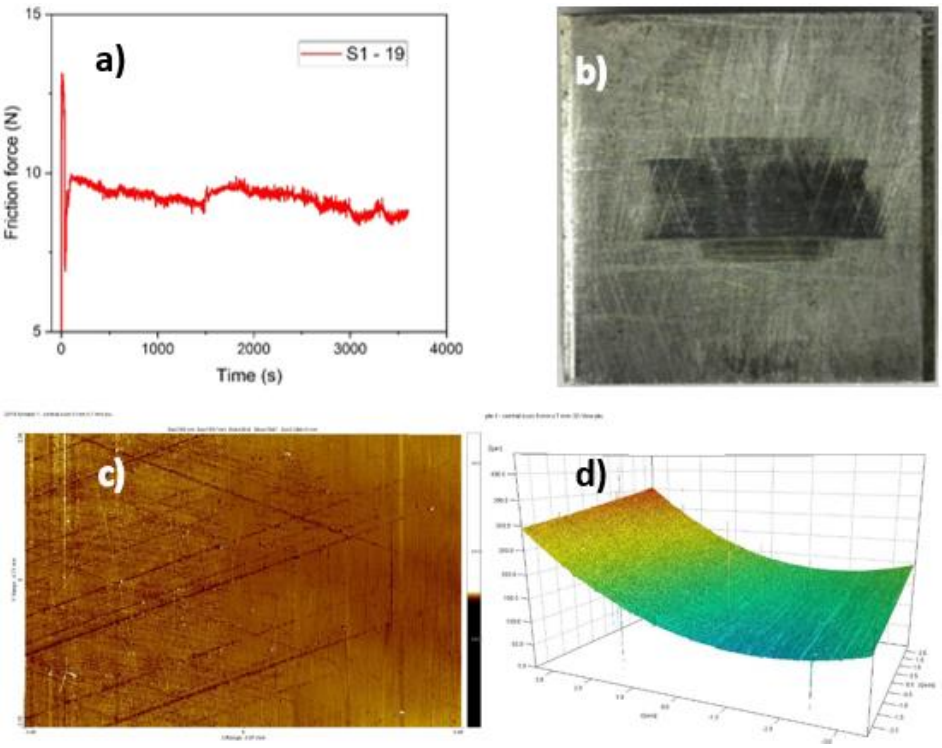

Figure 5.16, Friction behavior and effect to the surface roughness of sample S1-19; a) Friction force vs time analysis, b) wear scar as a result of friction test, and C) and d) for 2D and 3D optical profiles for wear surface of CLS after Phase-II, LRT test.

Stage-1 profilometry test results for 15W40 based nano-lubricants (S3-19, S7-19, and S28-19) are shown in Figure 5.17, which indicates that significant reduction of surface roughness compared to S1-19 (S_q = 1937 nm, S_a = 786 nm). Highest smoothening effect is shown by S3-19 (S_q = 987 nm, S_a = 649), the sample which established 17% of COF reduction after Phase-I, LRT test (Section 5.1). Samples S7-19 and S28-19 also show smoothened surface textures than S1-19 could be assigned to the ability of nano-additives to separate the asperities in motion, which are disperse within the solution during lubrication.

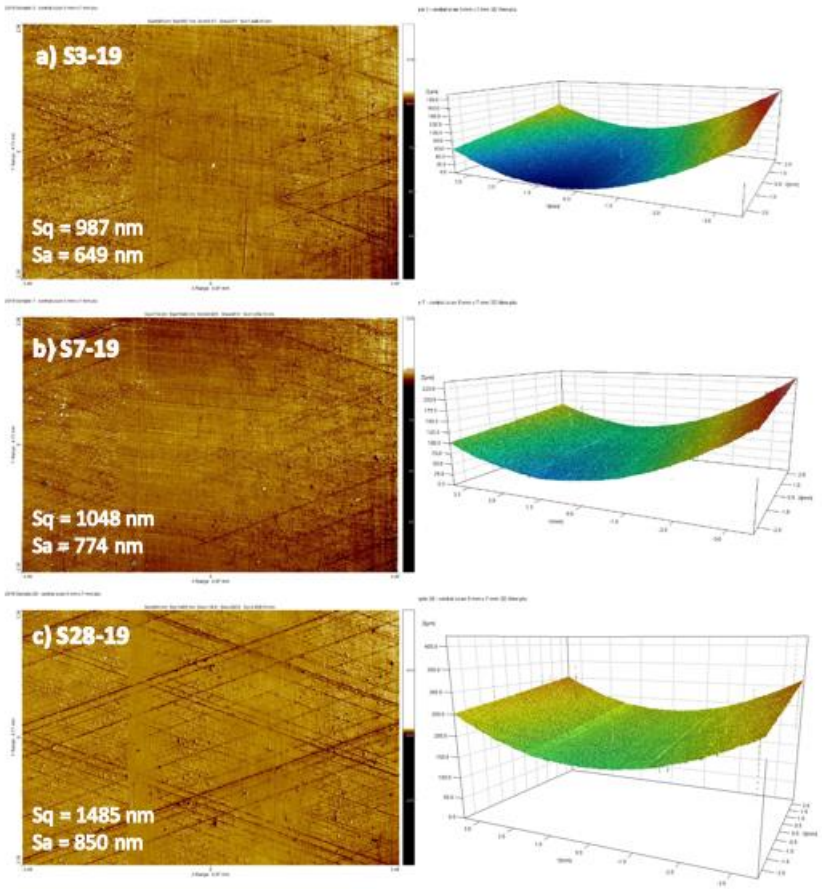

Figure 5.17, 2D and 3D optical profiles for the worn CLSs used with 15W40 based lubricants containing different nano additives; a) S3-19, b) S7-19, c) S28-19

Roughness profiles for samples containing CCO with different nano-additives are presented in Figure 5.18. Sample S17-19 indicates the best roughness reduction among the group with the measurements of S_q = 1726 nm and S_a = 644 nm, not better than any of 15W40 group blends, albeit better than S1-19. Sample S31-19 shows intermediate results among the group, still better than S1-19. However, S20-19 shows a sever distortion to the surface texture

of worn surface having S_q and S_a values as 3071 nm and 918 nm respectively, which are worse than the roughness values of unused CLS surface (Figure 5.15). Nevertheless, S17-19, S20-19, S31-19 are with impressive COF reduction rates of 27%, 17% and 17% respectively, which were recorded during Phase-I, LRT tests. Thus, it is hypothesized that the friction and wear behaviors are different parameters of a lubricant with complex relationship between each other, depending on the properties of the constituents of the formulation. Also, it is significant that, S3-19 and S17-19, which are having Al_2O_3 as nano-additive had shown best surface enhanced profiles from 15W40 and CCO groups. The blends from 15W40 group had shown better surface roughness profiles than CCO based blends. Therefore, this high surface roughness could be attributed to the agglomeration of nanoparticles and the properties of some constituents of CCO.

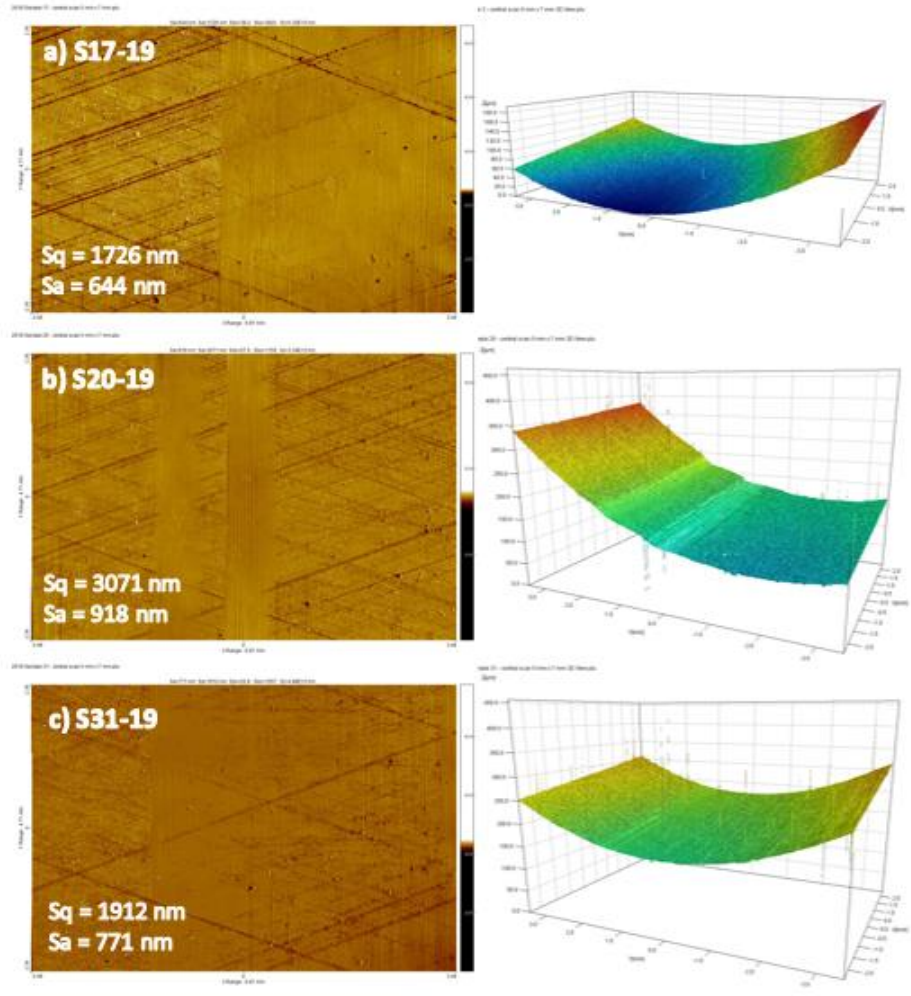

Figure 5.18, 2D and 3D optical profiles for the worn CLSs used with CCO based lubricants containing different nano additives; a) S17-19, b) S20-19, c) S31-19

Figures 5.19 and 5.20 are for both 19 and 22 series surface roughness profiles for samples S9, S16 and S24. Samples S16-19 and S24-19 are CCO based formulations and S16-22 and S24-22 are FCO based formulations. Surface roughness results for both series are not similar for the same sample formulation, which could be ascribed to differences in base stock and LRT test protocols on both occasions. For example, S9-19 presents surface topographies with roughness values of S_q = 1670 nm and S_a = 901 nm, compared to S_q = 1500 nm and S_a = 972 nm of S9-22 measurements. In-addition, S1-19 is with S_q = 1937 nm and S_a = 786 nm and S1-22 is with S_q = 2252 nm and S_a = 1309, albeit same oil (15W40) with different LRT test protocols.

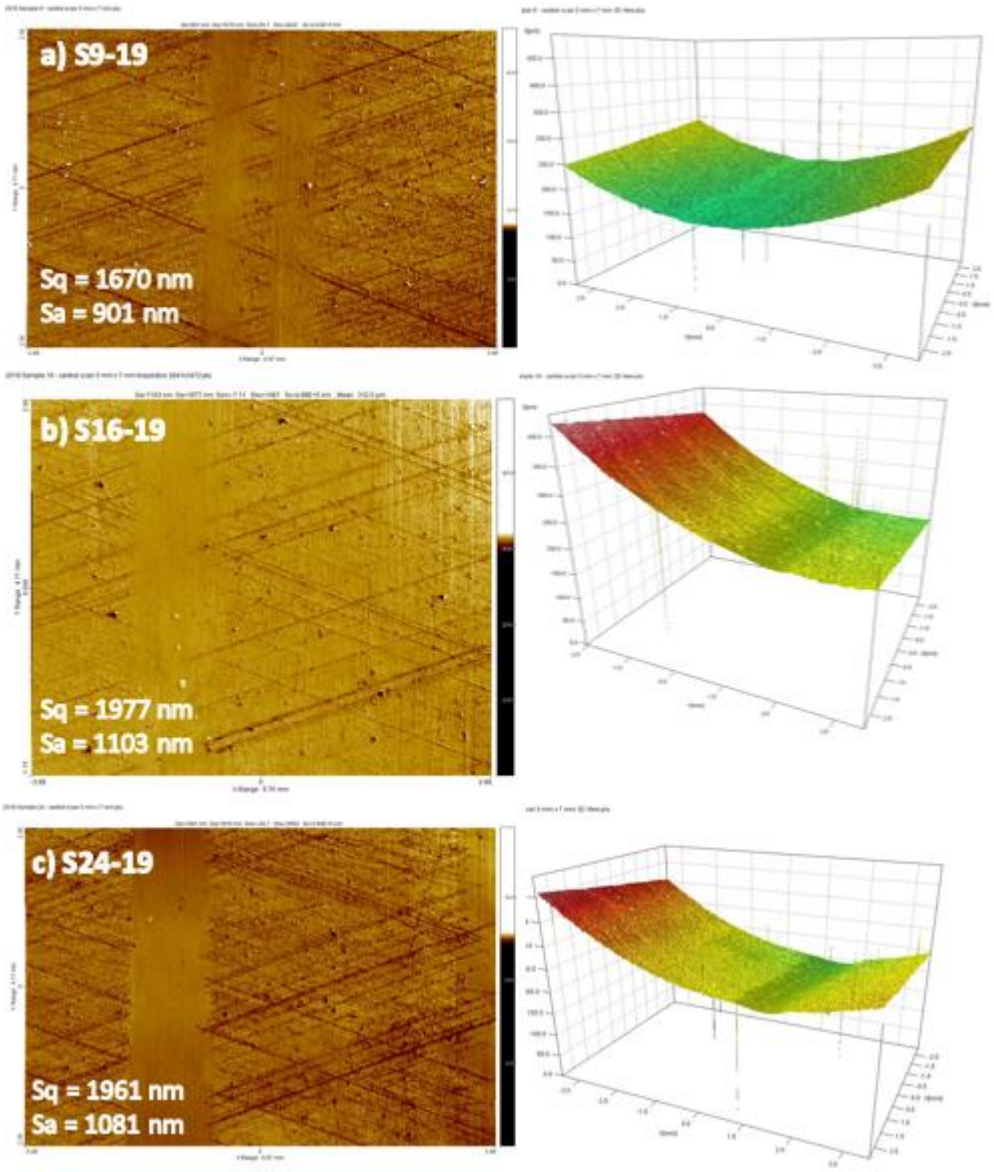

Figure 5.19, 2D and 3D surface roughness profiles for samples a) S9-19, b) S16-19 and c) S24-19

Samples S16-19 and S16-22 indicate an increase of surface roughness on both occasions (S_q = 1977 nm, S_a = 1103 nm for S16-19 and S_q = 2380 nm and S_a = 1479 nm for S16-22) above reference oil 15W40 (S1), albeit with 23% and 11% COF reduction for S16-19 and S16-22 respectively (Tables 5.1, and 5.2) over the reference oil (S1). Sample S24-22 is indicating adverse effects to the worn surface with S_q = 4405 nm and S_a = 1524 nm, in contrast to 11% of COF reduction compared to S1-22, which could be assigned to poor dispersion and agglomeration of nanoparticles and possible corrosive constituents of FCO than CCO. Otherwise, the situation could be assigned to the poorer lubricity of FCO than CCO (Fig. 5.19 – 5.20).

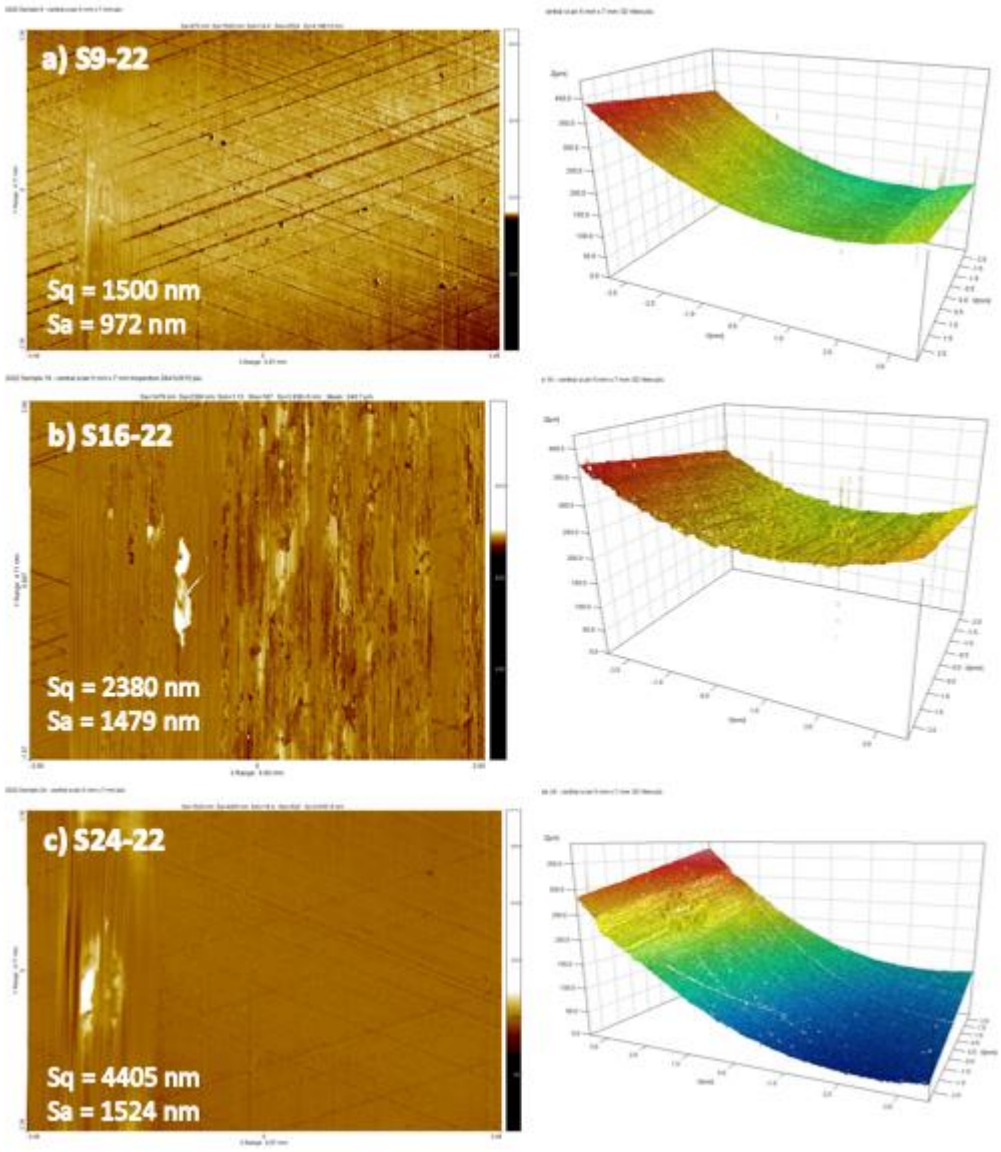

Figure 5.20, 2D and 3D surface roughness profiles for samples a) S9-22, b) S16-22 and c) S24-22

Optical morphologies for samples S30-22, S32-22 and S35-22 are presented in Figure 5.21. All are FCO based formulations with different nano-additives. Figure 5.22 illustrates 2D and 3D roughness profiles for the sample S1-22. Sample S30-22 is with roughness measurements of S_q = 3105 nm and S_a = 766 nm (Figure 5.21a). This confirms the increase of surface roughness by ~ 38% with reference to surface roughness values of S1-22. Both S32-22 and S35-22 have smoothened surface morphologies with ~ 54% and 25% roughness reduction compared to S1-22.

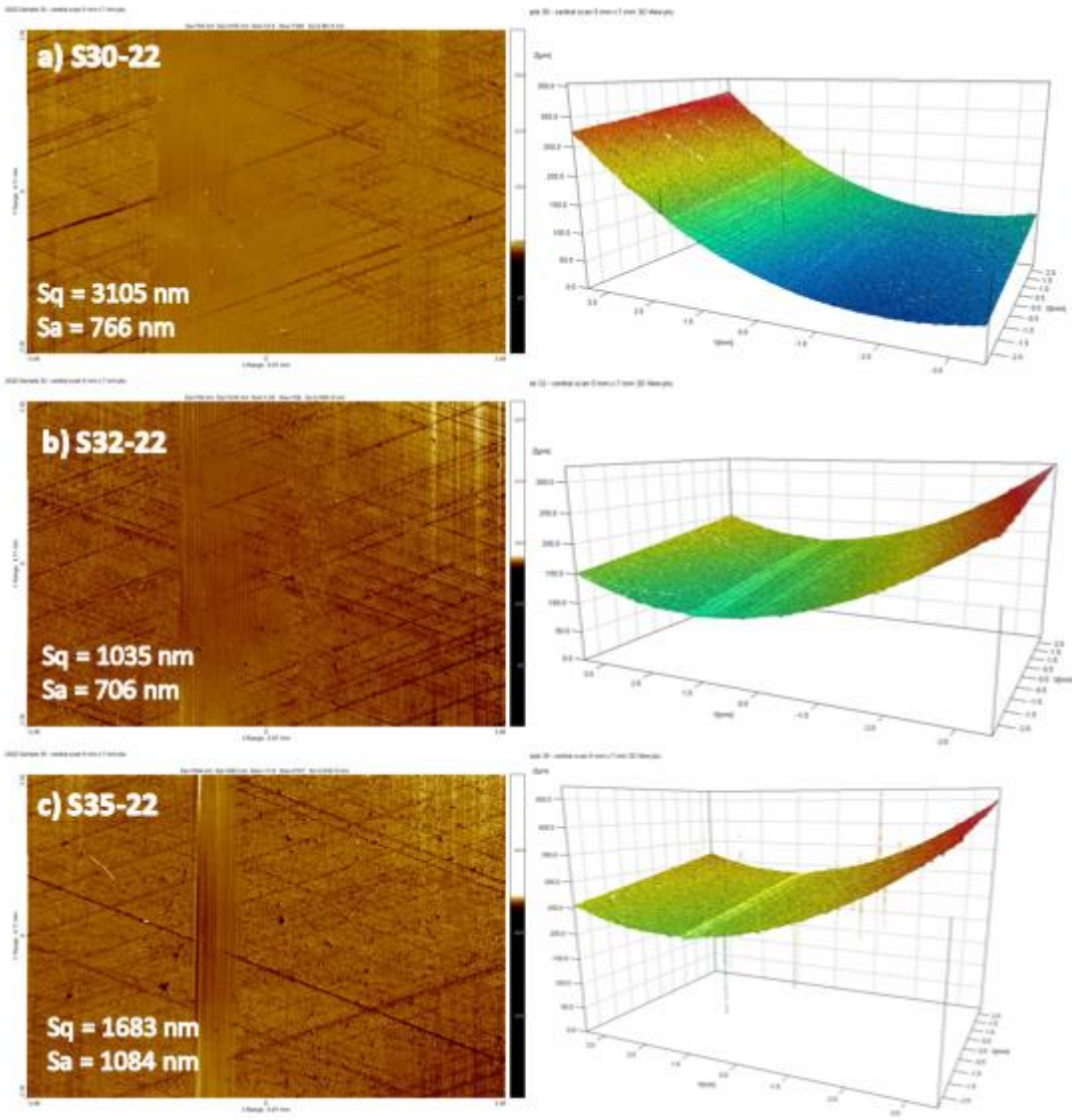

Figure 5.21, 2D and 3D optical profiles for FCO based formulations with different nano-additives; a) S30-22, b) S32-22, c) S35-22

All three samples (S30, S32, and S35) are with enhanced tribological performance to reduce friction (COF) by 23%, 26% and 28% correspondingly (Table 5.2) in comparison with reference oil S1-22. Earlier it was proved that S30-22 has better dispersion stability compared to other formulations. Base oil FCO and LRT test conditions are the same as for other blends. Nevertheless, with reference to the 3D linear measurements (S_a) of S30-22 it is indicating ~ 54% of surface smoothening compared to S1-22, which is complementing micrograph for the worn surface of S30-22 presented in Figure 5.28, situation which needs further investigation.

From the outcomes it is hypothesized that the enhancement of surface roughness is directly correlated with the reduction of friction by reducing shear stress between mating asperities in relative motion. The presence of nano-additives is affecting smoothen the surface texture. For example, S3-19, S7-19, S9-19 have enhanced surface roughness than base oil S1-19. This surface enhancement by the presence of nanoparticles could be attributed to the creation of ball bearing effect or protective layer assisted with mending and polishing or synergistic effect between sliding asperities by nano-additives with the aid of their laminar/spherical morphologies. Colloidal stability plays a major role in keeping nanoparticles disperse in the solution. Otherwise, agglomeration leading to large cluster formation will tend to deteriorate the surface texture affecting adversely to the tribological behavior of the lubricant. Nevertheless, reduction of surface roughness or smoothening of surface texture will not guarantee the reduction of wear. Because the surface smoothening could be either by mending and polishing effect with elastic deformation or by polishing with removal of nascent layer leading to material removal from the tribo-site. Also, wear would increase the gap between sliding asperities, which affect the pressure distribution in the fluid. Increasing asperity gap will certainly reduce the COF. From the other hand excessive gap between piston ring cylinder liner interface will lead to compression leak and entry of excessive lubricant to combustion chamber thus effect to reduce the mechanical/thermal efficiency of an ICE. Thus, investigation of wear metal particles from each lubricant after equal running time is the remedy suggested for a feasible prediction.

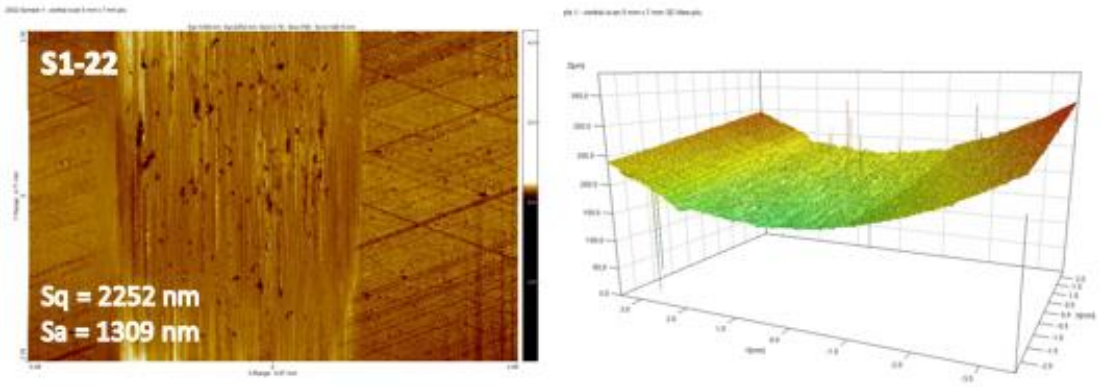

Figure 5.22, 2D and 3D optical profiles for the reference oil, S1-22

5.2.2.1. High-resolution measurement of S1-22, PRS and CLS

Bruker UK kindly granted free temporary access to a ContourX-500 Optical Profilometer, during which time high-resolution measurements of selected samples in the set S1-22, for the worn surfaces of PRS and CLS were obtained. This involved obtaining and stitching together a series of overlapping images, yielding a large area map of each specimen. Figures 5.23 and 5.24 illustrate the generated 3D optical profiles with material displacement measurements for the worn surfaces of CLS and PRS respectively. The PRS required 6 images whereas the CLS required 40 images. Post-processing to remove the curvature of the CLS permitted an estimate of the volume removed during the tribology testing. For S1-22 the volume is ~ 0.15 mm^3 for CLS (Figure 5.23) and ~ -0.01 mm^3 for PRS (Figure 5.24). Although stitched images were acquired for selected other samples, it was not possible to obtain an estimate of the volume removed, because the worn area was not fully separable from the native topography of the CLS surface. For example, S32-22 shows light grazing over an area of approximately 15 mm × 1.5 mm. However, the characteristic machining marks of the CLS are still discernible within the worn region. The wear scar on S1-22 suggests this sample is one which sustained perhaps the most damage with minor reduction of surface roughness (~ 0.01%) during the tribology testing. Therefore, the removed volume of approximately 0.15 mm^3 from CLS surface could be considered an upper limit for the volume removed from samples having smoothen surface textures than S1-22 (S9, S30, S32, and S35).

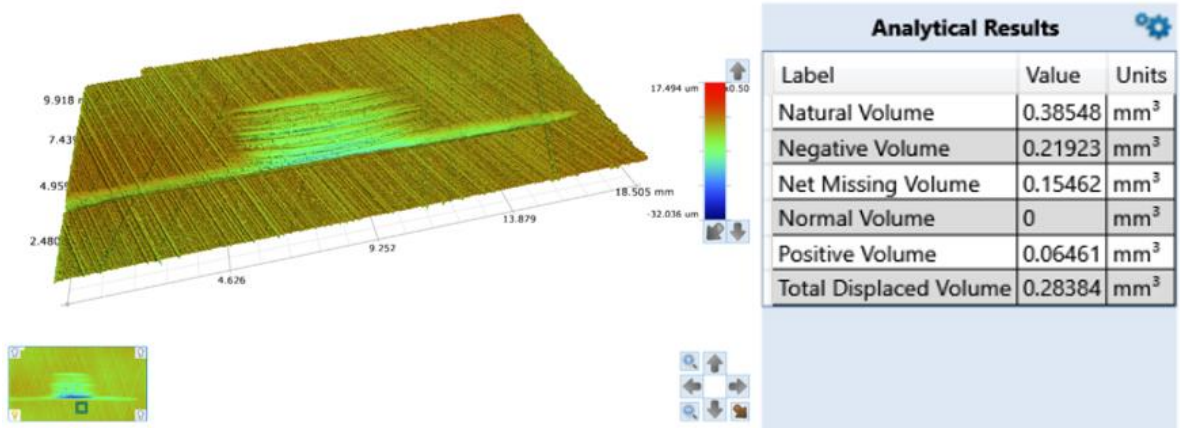

Figure 5.23, High-resolution 3D optical profile with material displacement measurements during LRT testing for the CLS of S1-22.

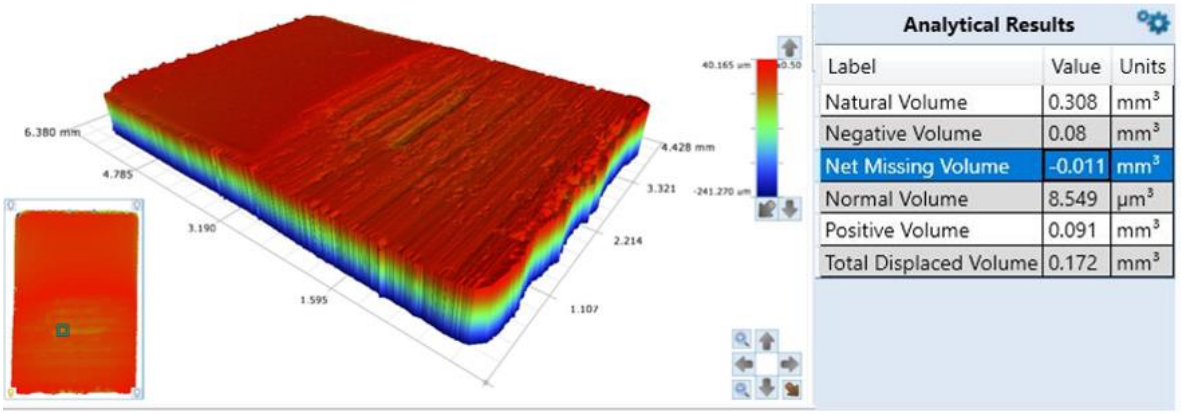

Figure 5.24, High-resolution 3D optical profile with material displacement measurements during LRT testing for the PRS of S1-22.

5.2.3. SEM characterization

SEM analysis was used to characterize the morphologies of wear surfaces, which were obtained after LRT tests with different lubricant samples. All the micrographs are presented with two magnifications. Thus, figures presented with low magnification are at left-side and right-side with higher magnification images. The focus is to study the wear patterns generated on test specimens (PRS and CLS) via LRT tests utilizing different sample lubricants to suggest a viable hypothesis for their tribological behavior.

Figure 5.25(a-b) presents the micrographs of unused CLS with 356× (low) and 2.5K× (high) magnifications respectively. The images precisely illustrate the cross-hatched honing contours of liner surface. The surface texture entrap lubricant to avoid oil starving condition. Specifically at boundary and mixed lubrication regimes as a remedy to minimize collision of rubbing asperities in case of failure to produce a lubricating film.

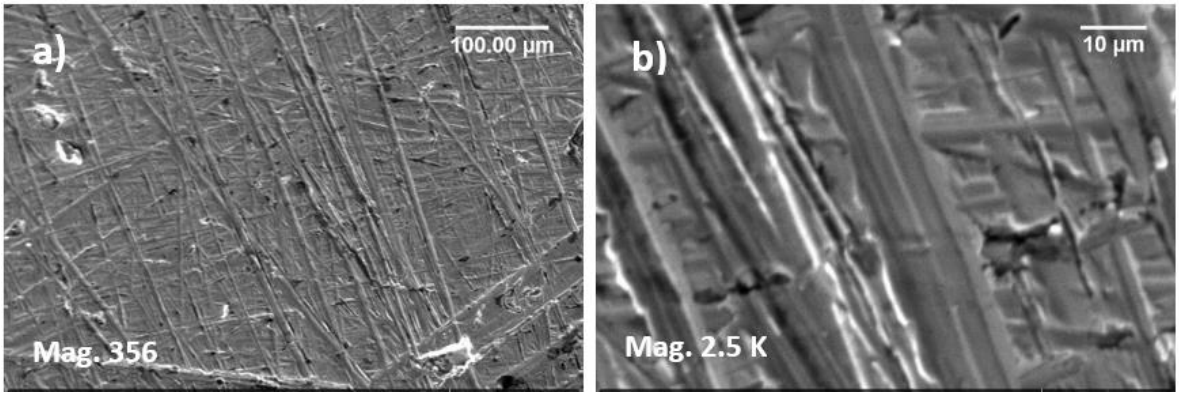

Figure 5.25, SEM micrographs of unused CLS with a) low (356×), b) high (2.5K×) magnifications, illustrating cross-hatched honing surface texture.

Figure 5.26 illustrates the micrographs of wear scars on CLSs used with mineral-based lubricant samples; S1, S9 and S9A. Low magnifications are presented in Figures 5.26a-c, while corresponding figures with higher magnifications are shown in Fig. 5.26a_1-c_1. Samples S1, S9 and S9A are with 15W40, 15W40 + G and 15W40 + GO respectively. Micrographs of S1 indicates shallow grooving, pitting and abrasive wear leading to material removal from tribo-interface.

Figures 5.26b, b_1, c, and c_1 indicate the improved morphologies for wear scars of S9 and S9A, because of addition of graphene (G) and graphene oxide (GO) as additives to 15W40 respectively. This agrees with the outcome of LRT test results i.e., average COF reduction for all load /velocity conditions by 17% and 26% by S9 and S9A respectively (Table 5.2).

Images of S9A (Fig. 5.26c, c_1) still with cross-hatched honing marks confirming the ability of GO to create a protective layer assisted by mending, and polishing effects at boundary and mixed lubrication to protect the surfaces in relative motion. Presumably, in-addition to laminar morphology (Fig. 4.1f), uniform, and stable dispersion of GO over G in the solution have affected this significant improvement.

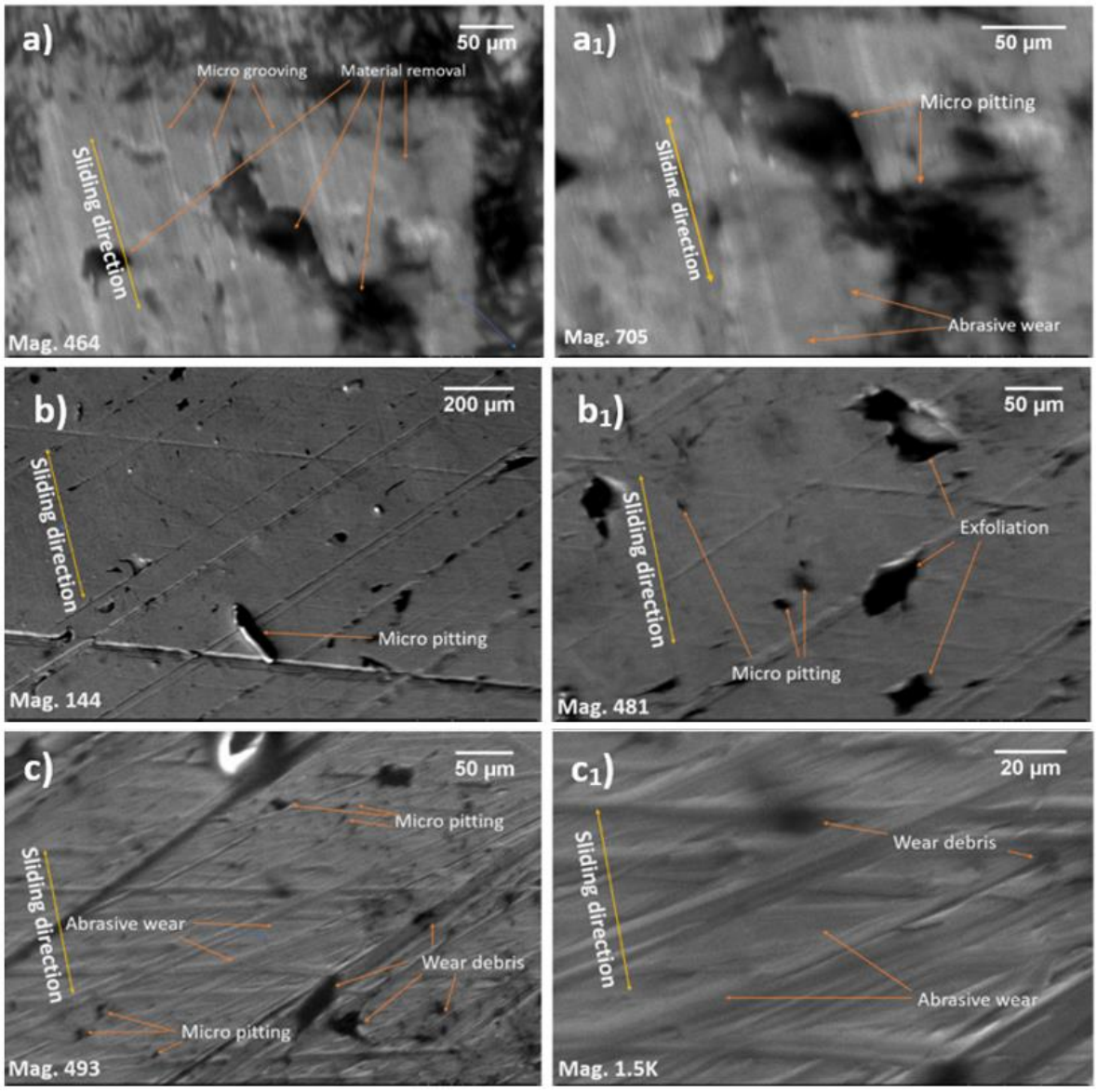

Figure 5.26, SEM micrographs for samples S1, S9 and S9A with a - c for low magnification and a_1 - c_1 for high magnification images; a) – a_1) S1, b) – b_1) S9, c) – c_1) S9A

SEM micrographs for samples S16 and S24 are presented in Figure 5.27. Images 5.27a and 5.27b for low magnification and 5.27a_1, and 5.27b_1 for high magnifications respectively. Both are formulated coconut oil (FCO) based lubricants with 15W40 and G, as additives in different concentrations. Images are with same wear patterns, albeit showing improved tribological performance compared to S1. Average COF reduction observed for all 25 load/frequency combinations is 11% over S1 for both (S16 and S24) formulations.

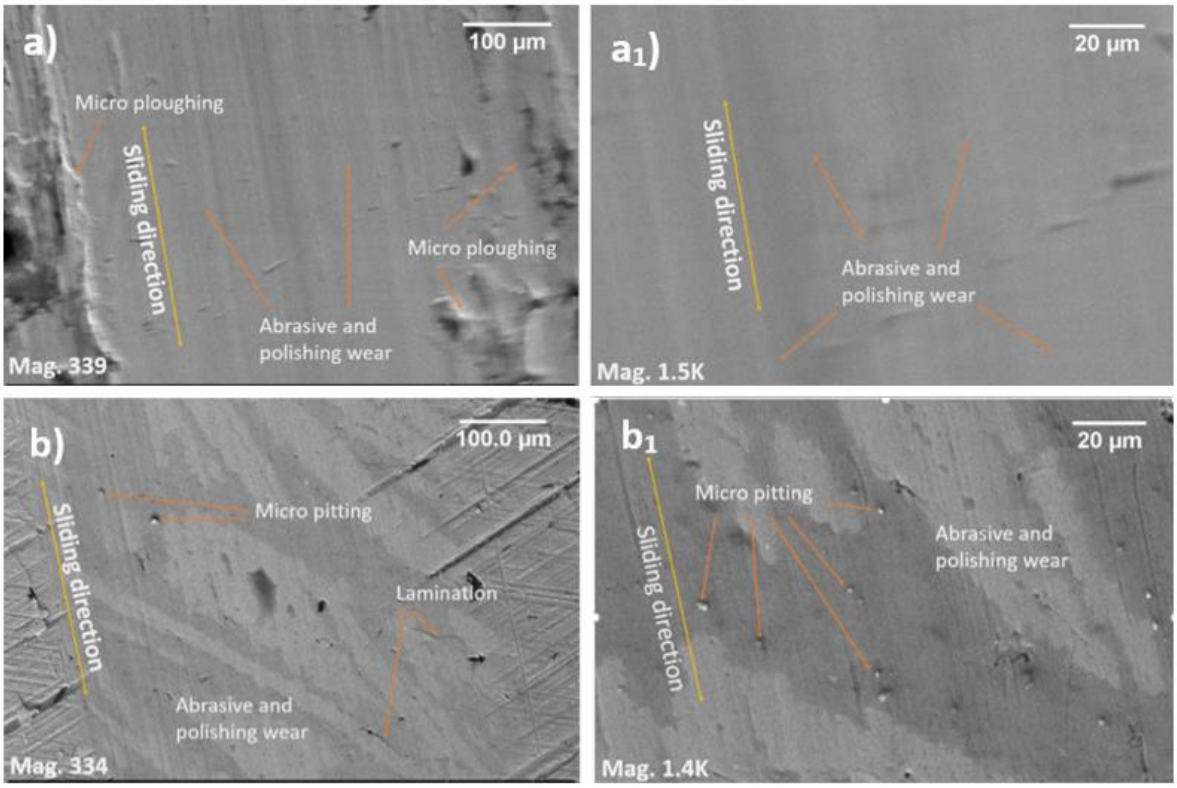

Figure 5.27, SEM images for samples S16 and S24 with a), and b), for low magnifications and a_1), and b_1), for high magnifications respectively; a) – a_1) S16, b) – b_1) S24

SEM micrographs of samples constituted with FCO and nanocomposites (S30, S32, and S35) are presented in Figure 5.28. From the morphologies presented in Figures 5.27 and 5.28, it is evident that, the abrasive and polishing effect illustrated on wear surfaces have affected to the enhancement of COF by all FCO based lubricants. From EDX analyses it is observed that all test specimens tested with FCO are with potassium (K) deposition on wear surface may have affected to this polishing behavior (Tables 5.3 and 5.4). However, Figures 5.28b and 5.28b_1 are perceiving heavy ploughing and pitting thus material removal, sign of excessive wear by sample S32. The situation suggests that instability of solution thus agglomeration and large size cluster formation or entry of silicon particles (dust) to the sliding interface. Albeit morphologies of S35 wear scars (Fig. 5.28c and 5.28c_1) demonstrate an enhanced tribological performance by mending and protective layer formation on friction surface. Average COF reductions by S30, S32, and S35 against S1 are 23%, 26% and 28% for all 25 Phase-III, LRT test conditions (Table 5.2).

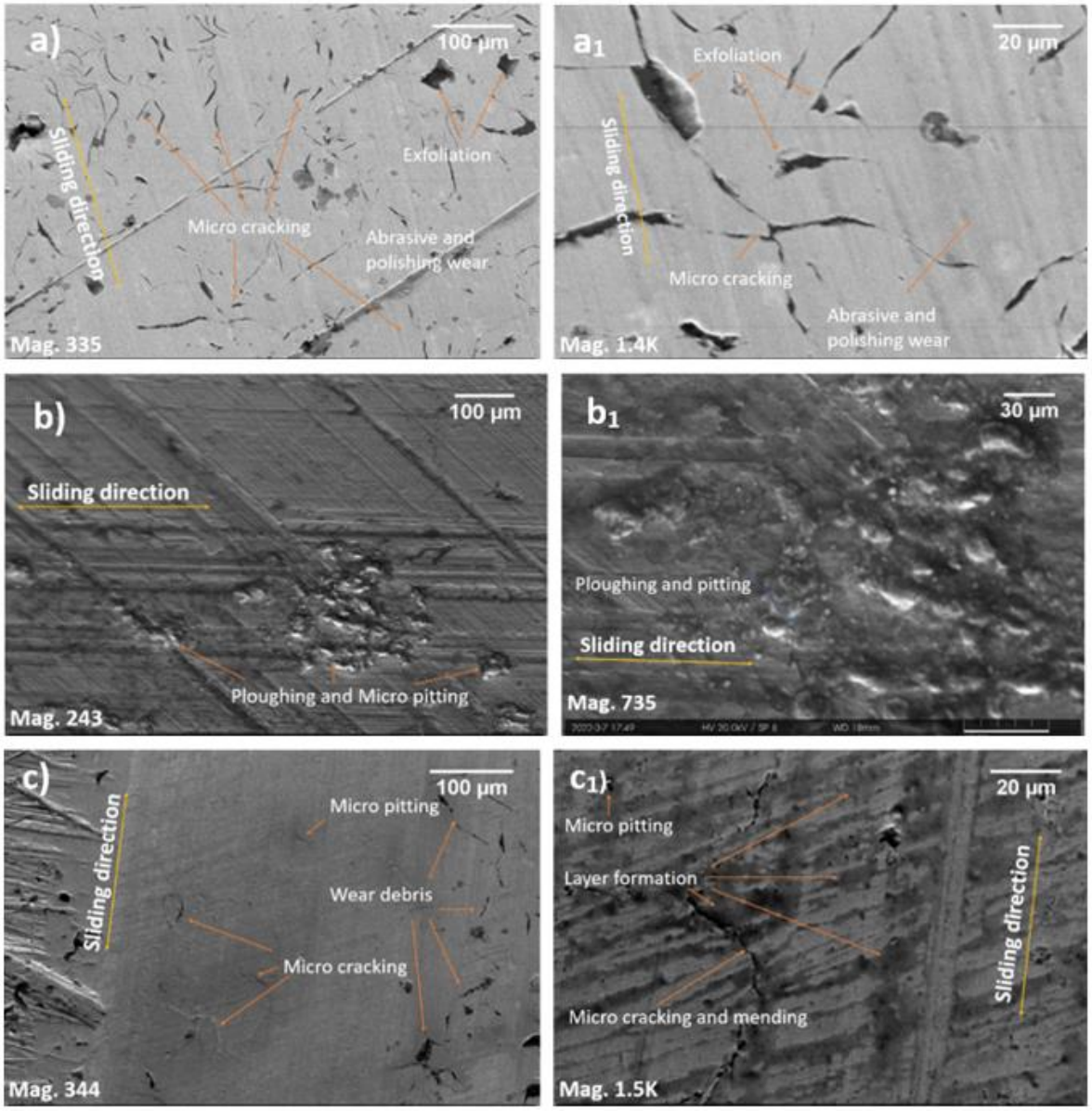

Figure 5.28, SEM micrographs for the wear scars of sample lubricants S30, S32 and S35 with a), b), c), and a_1), b_1), c_1) for low and high magnifications respectively; a) – a_1) S30, b) – b_1) S32, c) – c_1) S35.

6. Chapter 6: Results part III – Field performance tests

Field performance tests were done to examine the competence of formulated lubricants in accordance with contemporary industrial environment. This is to link laboratory testing with actual engine performance. Tests were done to study I) specific fuel consumption (SFC), II) exhaust emissions and III) contents and properties of used crankcase oil samples, following procedures outlined in section 3.4.

6.1. Specific Fuel consumption

Fuel consumptions (FC) were tested for samples S9, S16, S30, S32 and S35 along with S1 as reference oil. Tests were done with five load variations: 5, 10, 14, 17, and 20 kg at 1500 rpm with coolant temperature at ~ 80 °C – 100 °C. However, engine revolution slightly varied with changing loads. All the tests were done thrice to minimize the errors and results are presented in Table 6.1. With these results it is evident that, the sample S35 is having the best performance among all samples tested, showing reduction of specific fuel consumption (SFC) by 8% compared to S1 (Figure 6.1). The results, which could be assigned to the ability of S35 to reduce friction than S1 as explicated with Phase-III LRT test results (Figure 5.9), thus confirms the correlation between friction and fuel consumption of an ICE. The test rig is rated as 4.8 kW (Table 3.5), nevertheless, tests were extended to 25% overload condition (~ 6 kW) to study the lubricants characteristics under adverse conditions. Figure 6.1 indicates that S1 is failing under overload conditions with increasing SFC, where S35 is showing stable SFC confirming its shear stability, which shed light on the rheometric observations reported in Section 4.3 (Figure 4.30).

Table 6.1, Test results of SFC analysis using a dynamometer test rig for sample formulations, S9, S16, S30, S32, and S35 with S1 as the reference oil.

Sample no.		L	V	Time (s)				T_E	BP	FC	SFC
	(rpm)	(kg)	(ml)	T-1	T-2	T-3	Mean	(Nm)	(kW)	(kg h^{-1})	(kg kWh^{-1})
S1	1552	5	20	97.2	95.88	94.61	95.90	9.90	1.61	0.63	0.39
	1530	10	20	68.98	67.68	69.13	68.60	19.80	3.17	0.88	0.28
	1500	14	20	52.6	53.38	53.4	53.13	27.71	4.36	1.14	0.26
	1477	17	20	45.84	44.86	44.39	45.03	33.65	5.21	1.34	0.26
	1445	20	20	36.96	36.88	36.52	36.79	39.59	5.99	1.64	0.27
S9	1559	5	20	96.23	94.58	97.73	96.18	9.90	1.62	0.63	0.39
	1529	10	20	65.95	68.74	67.53	67.41	19.80	3.17	0.90	0.28
	1515	14	20	52.78	52.62	52.42	52.61	27.71	4.40	1.15	0.26
	1488	17	20	44.31	44.38	44.78	44.49	33.65	5.25	1.36	0.26
	1454	20	20	37.21	36.11	35.56	36.29	39.59	6.03	1.67	0.28
S16	1564	5	20	105.1	102.4	105	104.19	9.90	1.62	0.58	0.36
	1536	10	20	71.62	71.02	71.58	71.41	19.80	3.19	0.85	0.27
	1514	14	20	52.9	54.16	54.64	53.90	27.71	4.40	1.12	0.26
	1492	17	20	45.2	45.25	45.84	45.43	33.65	5.26	1.33	0.25
	1483	20	20	40.93	38.48	38.86	39.42	39.59	6.15	1.53	0.25
S30	1559	5	20	107.3	105.6	104.1	105.67	9.90	1.62	0.57	0.35
	1538	10	20	69.35	71	71.95	70.77	19.80	3.19	0.85	0.27
	1517	14	20	53.5	52.72	52.62	52.95	27.71	4.40	1.14	0.26
	1491	17	20	46.02	45.24	45.8	45.69	33.65	5.26	1.32	0.25
	1463	20	20	37.89	36.2	38.36	37.48	39.59	6.07	1.61	0.27
S32	1591	5	20	103.8	105.4	104.2	104.47	9.90	1.65	0.58	0.35
	1546	10	20	71.69	72.88	72.86	72.48	19.80	3.21	0.83	0.26
	1508	14	20	54.6	54.51	54.62	54.58	27.71	4.38	1.11	0.25
	1489	17	20	45.9	46.2	45.98	46.03	33.65	5.25	1.31	0.25
	1457	20	20	38.14	36.64	39.36	38.05	39.59	6.04	1.59	0.26
S35	1590	5	20	105.9	106.5	104.7	105.71	9.90	1.65	0.57	0.35
	1531	10	20	73.78	72.26	71.3	72.45	19.80	3.18	0.83	0.26
	1530	14	20	56.36	56.52	57.2	56.69	27.71	4.44	1.07	0.24
	1502	17	20	47.01	46.41	46.49	46.64	33.65	5.30	1.30	0.24
	1475	20	20	44.24	37.66	38.3	40.07	39.59	6.12	1.51	0.25

Key: L – load; V – volume of fuel; T-1, T-2, T-3, - test numbers; T_E – engine torque; BP – brake power; FC – fuel consumption, SFC – specific fuel consumption.

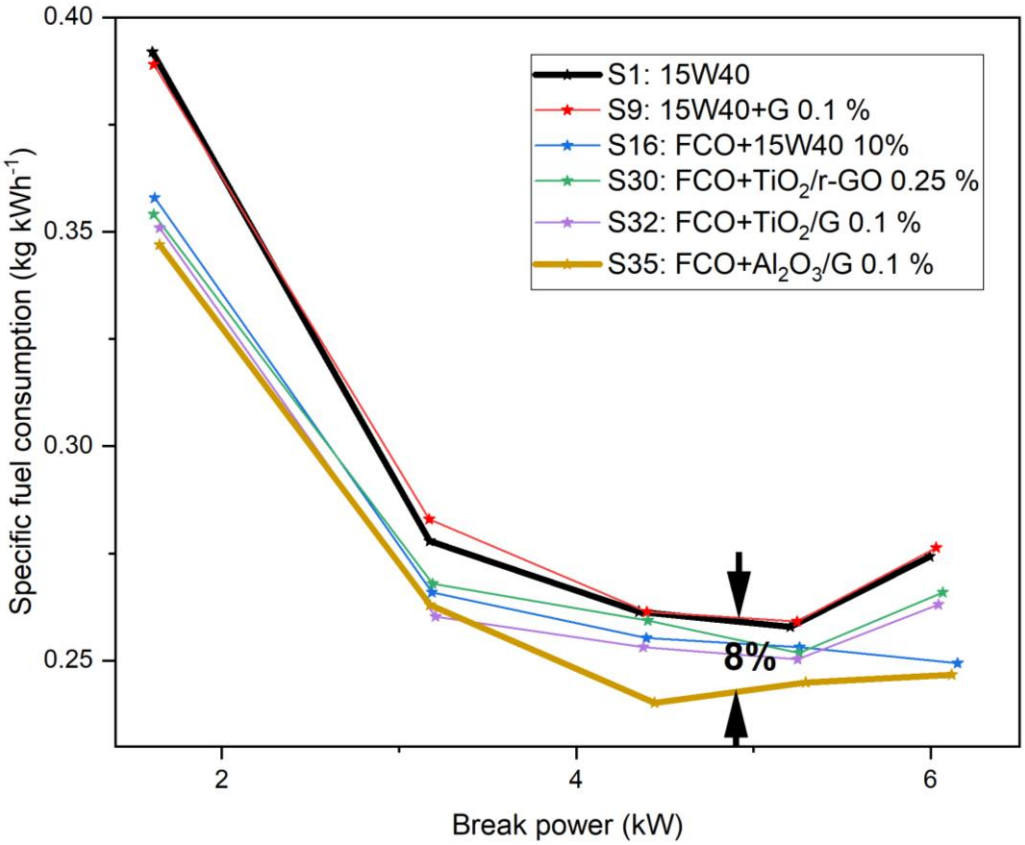

Figure 6.1, Break power vs specific fuel consumption analysis for selected sample lubricants (S9, S16, S30, S32, S35) including S1,

6.2. Analysis of exhaust emissions

After the SFC tests, exhaust emissions of the same test rig were analyzed using an exhaust gas analyzer (TECHNOVATION – FEM7) for same lubricant samples tested for SFC. Tests were done at constant engine revolution of 1500 rpm with approximately ≥ 65.0% of load. Test results are presented in Figure 6.2, which indicates the release of different concentrations of pollutants by different sample formulations. Among all S35 is showing better pollutant reduction than rest of the samples. Significant reduction of NO and NO_2 concentrations (ppm) by S35 could be attributed to the better heat transferring ability of S35 than other samples on test, which will affect to have lower combustion temperature causing less production of NO_x gases. In addition, all samples have reduced production of SO_2 led by S35. This suggests that the FCO-based formulations do not have any sulfur-containing constituents or thiol groups like S1 (15W40), which could react with oxygen (intake air) to produce sulfuric gases. Also, could be assigned to creation of sulphate salts by reaction

between metal oxides (nanocomposites) of sample formulations and S contents of diesel fuel during combustion. Besides, S30 is showing less ppm than S1, albeit higher than the rest of the samples in contest, which could be ascribed to the oxygen functional groups attached to r-GO segment of nanocomposite (TiO_2/r-GO) used in this formulation. In fact, showing SO_2 concentration could be from the constituents of diesel fuel used to run the test rig.

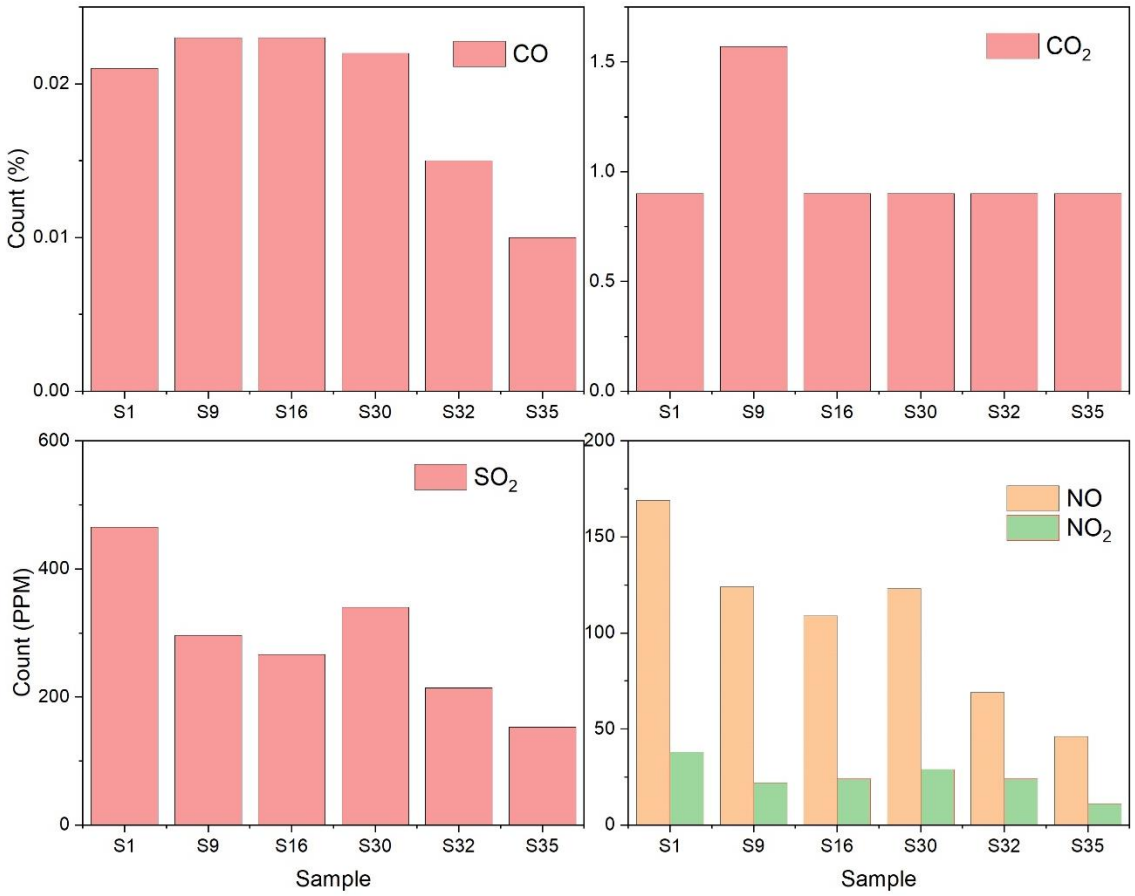

Figure 6.2, Results of exhaust gas analysis for the sample blends S1, S9, S16, S30, S32, and S35.

Samples S32 and S35 had shown their consistency to reduce exhaust pollutants except CO_2. From above annotations it is postulated that the ability of heat transfer of a lubricant is affecting not only to reduce friction, but also, to reduce production of NO_x emissions. For other assumptions, the lubricant has to be inside combustion chamber. Otherwise, there will be reactions between only the constituents of fuel with intake air, thus emissions should be equal for any lubricant. Nevertheless, it is the prime reliability of piston rings to seal combustion chamber to prevent leakage of air compression for enhanced thermal and mechanical efficiency of an ICE. Also, to restrict entry of excessive lubricant via this route to combustion chamber to deter production of hazardous emissions, [5, 23-25] which is entirely

dependent on the mechanical condition, thus maintenance of an engine. In section 5.2 it was revealed through SEM and 3D optical profiles, that the surface morphology of cylinder liner surface exhibits cross-hatched horned contours to entrap lubricant for lubrication at TDC. Therefore, it is presumed that the formation of protective layer or tribo-boundary film by specific nano/bio lubricants (for example: sample S35) according to their capabilities would have affected to prevent excessive lubricant entry to combustion chamber resulting reduction of exhaust pollutants.

6.3. Used crankcase oil sample analysis

Initially, the samples selected after Phase-I, LRT tests were examined for their physicochemical properties to understand the substandard of formulations (Table 6.2). From the results poor cold flow behavior, low TBN and viscosity at 100 °C of CCO were observed as substandard. Observed imperfect properties were improved as elaborated via Section 4.2.

Table 6.2, Physicochemical properties of selected samples after Phase-I, LRT tests

Sample	Viscosity at 40 °C (mm^2s^{-1})	Viscosity at 100 °C (mm^2s^{-1})	VI (-)	TBN (mg KOH g^{-1})	PP (°C)	COF reduction (%)
S1	109.0	14.1	130	9.8	-33	0
S3	108.7	14.3	133.82	6.2	-15	17
S7	111.2	13.7	121.91	4.1	-15	3
S9	110.3	14.4	133.03	6.9	-12	19
S16	28.2	6.3	184.34	1.5	21	32
S17	26.2	6.0	187.13	0.3	18	26
S20	26.1	6.0	188.24	0.2	18	17
S24	27.6	6.2	184.59	0.6	15	21
S28	109.4	14.0	128.6	4.7	-27	5
S31	27.6	6.1	178.56	0.5	18	17

Following the creation of FCO, Phase-III, LRT tests were performed. After Phase-III, LRT tests, selected samples (S1, S9, S30, S35) were used to run a generator (5 kW) for a

period of 100 h from each sample with reference to the manufacture's specifications. Used crankcase oil samples were tested for the degradation of formulations as mentioned in Section 3.4.4. Full spectrometric and property analyses were carried out, albeit only relevant findings are presented herein.

From the test results it is evident that the FCO based formulations (S30 and S35) have low TBN (2.4 mg KOH g^{-1}), which needs to be improved for an extended lubricant life (Figure 6.3 and Table 6.3). Sample S9, which is a combination of 15W40, and graphene shows the highest TBN (8.2 mg KOH g^{-1}) indicating extended lubrication life after 100 running hours.

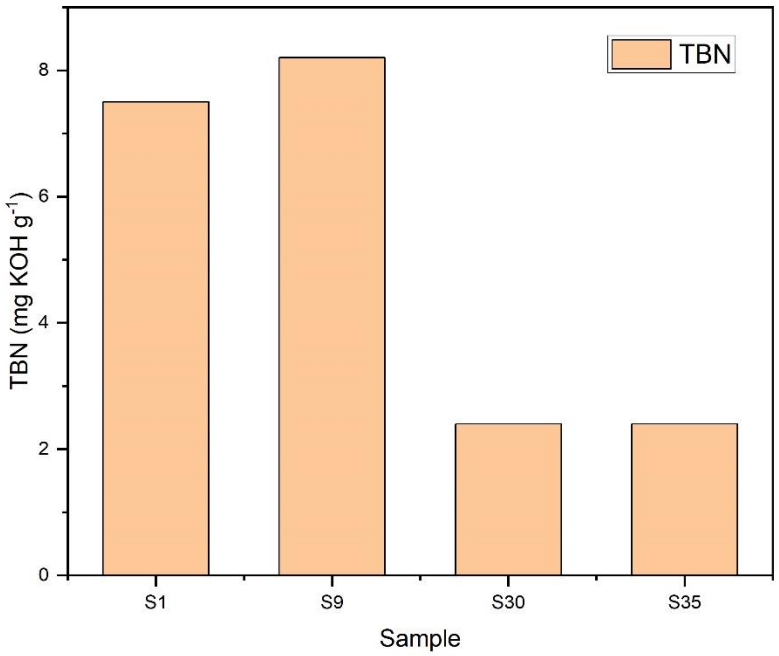

Figure 6.3, TBN comparison on formulations S9, S30 and S35 with S1 after 100 running hours

Figure 6.4 exemplifies the rheological behavior of above samples indicating almost same VI for all samples after equal running hours. Samples S30 (VI = 128) shows a slight advantage over S1 (VI = 125) confirming the shear stability of S30 under ramping temperatures, established via rheometric tests (Figure 4.30). Besides, S35 (VI = 121) is showing minor degradation over usage and thermal instability than S30 over the usage of 100 hours need to be investigated and improved. However, recorded kinematic viscosity of S35 at 100 °C (10.4 mm^2 s^{-1}) is still within the accepted range with reference to local and international standards.[137-139]

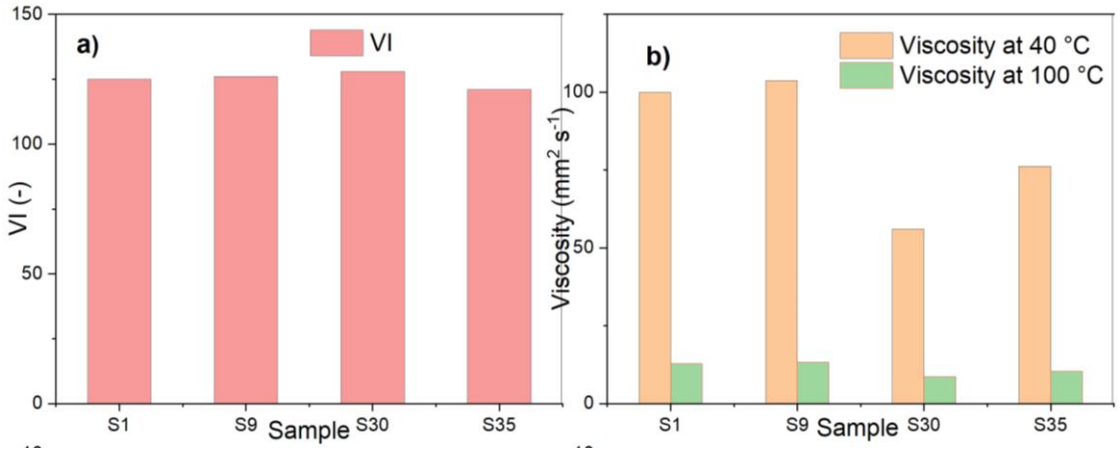

Figure 6.4, Rheological behavior of samples S1, S9, S32, and S35 after 100 hours usage; a) change of VI, b) change of kinematic viscosity at 40 °C and 100 °C.

Summary of used oil test results are presented in Table 6.3 which indicates the increase of particle quantifier (PQ) index with reduced Fe particle concentration for S35. Nevertheless, the results indicate significant reduction of hazardous contaminants (P, S, Zn, and Mo) by the samples S30 and S35. This is a positive sign by S30 and S35, which could be assigned to the nonuse of popular additive ZDDP during formation of FCO.

Table 6.3, Summary of used crankcase oil sample monitoring test results.

	Wear metal		contaminants					
Sample	Fe (ppm)	PQ ID	P	S (ppm)	Zn	Mo	TBN (mg KOH g^{-1})	Viscosity at 100 °C ($mm^2 s^{-1}$)
S1	28	18	864	3518	1026	43	7.5	12.9
S9	19	17	904	3490	1016	44	8.2	13.3
S30	11	21	159	438	142	2	2.4	8.6
S35	22	26	180	359	139	3	2.4	10.4

Key: PQ ID – particle quantifier index, TBN – total base number, ppm – parts per million

In view of the higher PQ index, the generator engine was dismantled to inspect any severe wear or damage to the internal components. After dismantling it is confirmed that there were not any visible damages to the engine components other than normal use as illustrated in Figure 6.5, thus reassembled the engine, recommissioned, and continued.

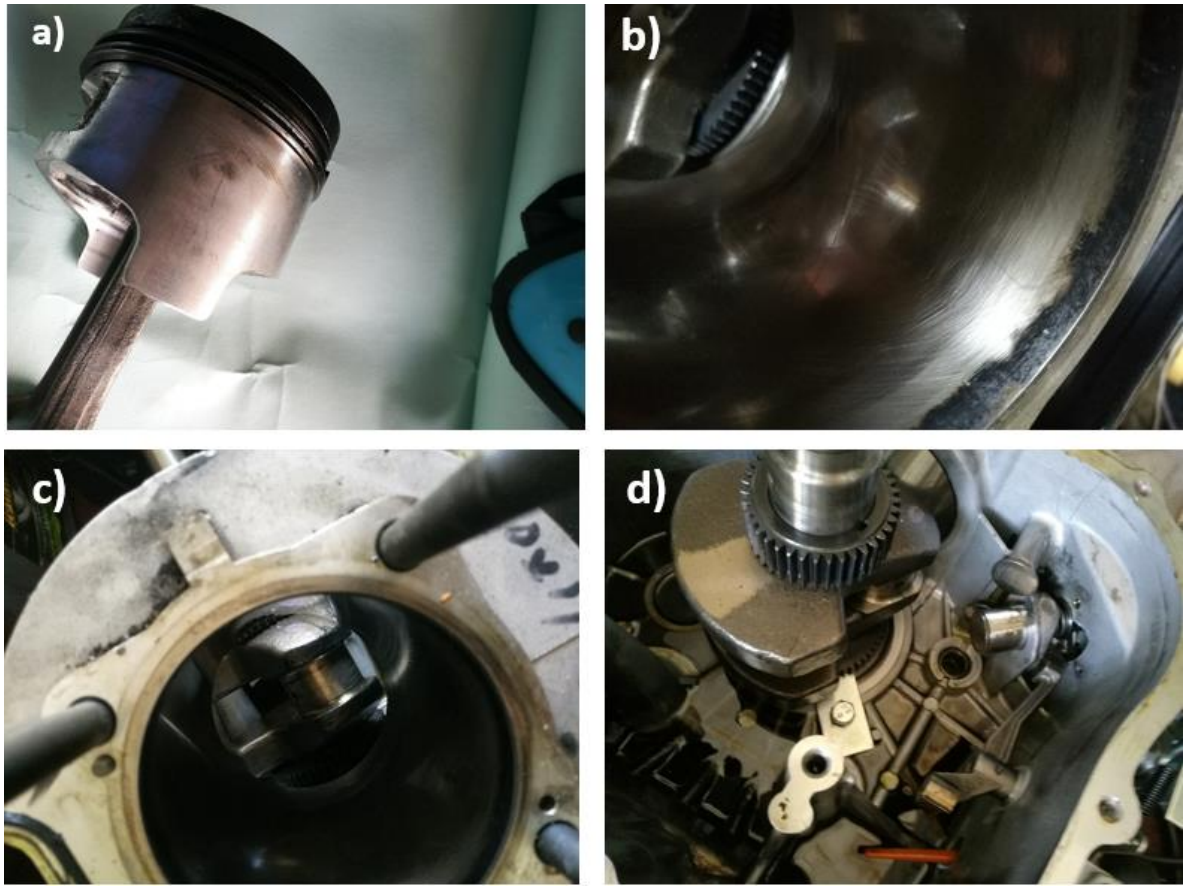

Figure 6.5, Images of the main components of generator engine after dismantling for visual inspection showing not any damages to the engine components; a) piston assembly, b) cylinder bore at TDC, c) crankshaft big-end bearing journal, d) crank shaft main bearing journal with front timing gear attachments.

6.4. Summary of the research test results

a) **Characterization of nanomaterials**: It was confirmed that the nanomaterials used in this research are Al_2O_3, TiO_2, graphene, Al_2O_3/G, TiO_2/G and TiO_2/r-GO. Measured particle sizes were: Al_2O_3, 7.0 ± 0.7 nm, TiO_2, 9.0 ± 0.2 nm, Al_2O_3/G, 10.0 ± 0.3 nm, TiO_2/G, 14.0 ± 0.3 nm, TiO_2/r-GO, 10.0 ± 0.3 nm, and graphene sheets with 319 ± 50 nm lateral dimensions. Also, approximately spherical surface morphologies of Al_2O_3, TiO_2, laminar layers of graphene and laminar/spherical surface morphologies of Al_2O_3/G, TiO_2/G and TiO_2/r-GO were identified. (Section 4.1)

b) **Enhancement of physicochemical properties of CCO:**

I. Reduction of PP – from 21 °C to 6 °C (Section 4.2.1)

II. Increase of VI – from 169 to 206 (unitless) (Section 4.2.2)

III. Increase of TBN – from 0 to 4.14 (mg KOH g^{-1}) (Section 4.2.3)

c) **Thermal and oxidative stability of formulated samples:** STA test results indicate that, the FCO has better thermal and oxidative stability than CCO. (Section 4.2.4)

d) **Shear stability:** From rheological analysis it was confirmed that at elevated temperatures FCO exhibits better shear stability than reference oil 15W40. Nanocomposites of r-GO (which contains oxygen functional groups) when used as additives in nano/bio lubricants exhibited improved shear stability compared to the other samples tested. (Section 4.3)

e) **Dispersion stability:** Dispersion stability of formulated samples were achieved by using a surfactant, using an ultrasonic mixer for blending an increasing the time of agitation. Higher stability was observed for nanomaterials which contained oxygen functional groups; for example, using graphene oxide or reduced graphene oxide in place of graphene, and their corresponding metal oxides nanocomposites. (Section 4.4)

f) **LRT test results:**

I. Phase-I (Constant load 120 N, frequency 20 Hz, at 100 °C): Following samples were selected as best nanoparticle concentration from each group to reduce COF compared to S1 (percentage of COF reduction is given in brackets), S3 (17), S7 (3), S9 (19), S16 (32), S17 (27), S20 (17), S24 (21), S28 (6), S31 (17) (Section 5.1).

II. Phase-II (16 load/velocity combinations (at 140 °C) were included in a test): Samples with best performance to reduce COF for all combinations (with mean COF reduction percentage within brackets) are S3 (13), S7 (-7), S9 (18), S16 (23), S17 (19), S20 (19), S24 (24), S28 (14) and S31 (18) (Table 5.1).

III. Phase-III (25 load velocity combinations at 140 °C): Samples with optimum (mean) COF reduction for all test combinations are S35 (28), S32 (26), S30

(23) and S9A (26), S9 (17), S24 and S16 (11) (Table 5.2). In-addition FCO had reported 7% COF reduction over S1(Fig. 5.5).

g) **EDX analysis:** EDX test results reveled the deposition of C, Ni, Cr, O, Mo, and K elements including Al elements on the wear scar of the test specimen used with S35. The phenomenon, which suggests a formation of protective layer on sliding tribo interface covering all Fe elements on wear surface during LRT tests. S35 was formulated using Al_2O_3/G as nano-additives with FCO as base-stock (Section 5.2.1, Table 5.3, Figs 5.12, 5.14).

h) **3D none contact optical profilometry:** Surface roughness test results confirmed the smoothen wear surfaces of the samples, S32 and S35 by, 54 and 25% respectively compared to S1. Sample S30 had shown increase of roughness by 37% compared to S1. (Section 5.2.2, Fig. 5.21, 5.22).

i) **SEM analysis:** Micrographs of S35 indicates the formation of protective layer on the wear scar of the test specimen of S35 (Section 5.2.3, Fig. 5.28).

j) **Performance test results:**

   i. Sample S35 had shown reduction of SFC by 8% compared to S1 (Section 6.1, Fig. 6.1).

   ii. Samples S30, S32, and S35 had shown their capabilities to reduce exhaust pollutants; CO, SO_2 and NO_x gases led by S35 as the top performer compared to S1 (Section 6.2, Fig. 6.2).

   iii. Sample S35 had shown a significant reduction S, P, and Zn particles in used crank case oil samples, which are labeled as hazardous elements, compared to S1(Section 6.3, Table 6.3).

7. Chapter 7: Conclusions and future works

This research reported here aimed to study the tribological behavior of lubricants formulated with nano/mineral, nano/bio and bio/mineral combinations for the purpose of enhancing internal combustion engine (ICE) performance by reducing friction and wear. With the above aim, factors affecting the dispersion stability of nano/mineral and nano/bio sample formulations were studied, implemented possible remedial processes to improve colloidal stability and results are presented and discussed in this thesis. In addition, possible improvements for physicochemical characteristics were achieved on identified sub standards of CCO. The entire project could be split into 2 segments; prior and posterior formulation of CCO with improved physicochemical properties.

7.1. Conclusions

With reference to the results discussed in Chapters 4, 5, and 6, significant achievements are summarized herein.

With the results of nanoparticle characterization, it was confirmed that the structure of nanoparticles used in this research are graphene (G), Al_2O_3, TiO_2, TiO_2/r-GO, TiO_2/G and Al_2O_3/G, which all have nano scale dimensions. All exhibit laminar or spherical morphology, or combinations of lamina/spherical surface morphologies, with fine particle size (ranging from 7.0 nm – 14.0 nm). The morphology attributes, which are in favor of enhancing tribological performances within an ICE lubrication.

From the dispersion stability test results, it was confirmed that the particle size, concentration, method and time of agitation, polarity of particle substrates, thus double layer potential, all are essential aspects affecting the homogeneity of a solution. Results of optical absorbance analyses for samples S28, S31, S9A, and S30 (Figures 4.28 – 4.30, and 4.34) reinforce the colloidal stability achieved because of oxygen functional groups attached to GO or r-GO elements, which could have been functionalized with molecular chains of base stock. This confirms the significance of surface functionalization to create repulsive or attractive forces between the molecular substrates within a solution for a lasting colloidal stability for that formulation. However, GO and r-GO groups seems to be more stable with the base stock

15W40 than FCO, which could be ascribed to long chain molecular structures of 15W40 compared to medium chain molecules of FCO. Also, it is evident that the samples mentioned above have different degrees of sedimentation within the initial 72 h period post-formulation (Figure, 4.32, 4.33, 4.35 and 4.36). Formulations became stable after sedimentation of surplus quantities than soluble, confirming the importance of particle concentration for the colloidal stability of a solution.

Improvement to poor cold flow behavior of CCO was accomplished without the popular transesterification reaction route. Avoiding time consuming transesterification route means a cost-effective short time blending process. Also, prevents usage of hazardous material, and eliminating hazard waste production is an added advantage. Moreover, TMP esters of vegetable oils are reported to have increased COF compared to the mineral based conventional engine oils in use.[83] Nevertheless, FCO had reported 7% COF reduction over S1 without any additives (Fig 5.5).

Adding PMMA or SP separately to CCO did not work well to improve poor cold flow behavior. Instead, adding both influenced significantly to improve cold flow characteristics in reducing pour point (PP) by 15 °C (from 21 °C to 6 °C; Section 4.2.1). Also, the addition of PMMA improved the VI of the CCO. Therefore, it is presumed that, both entangling and creating branches to the molecular structure would have inhibited macro crystallization causing micro crystallization impeding self-molecular stacking (Section 4.2.2, Fig 4.18). The hypothesis, which is appreciated by DSC test results, which showed the change of crystallization and de-crystallization patterns of FCO than CCO during endothermic and exothermic operations (Figure 4.16, 4.17).

Rheological analyses on the above samples further reinforce the importance of colloidal or dispersion stability for enhanced shear stability by retaining additive particles dispersed within the formulation. For example, sample S30, which is a combination of FCO and TiO_2/r-GO had shown the optimum shear stability among all the samples tested, which could be attributed to the dispersion stability achieved via surface functionalization by functional groups attached to r-GO segment; (Figures 4.27 and 4.34).

Tribological tests begin with Phase-I LRT tests with a test protocol of constant load, velocity, and temperature (120 N, 0.4 m s^{-1} [20 Hz], and 100 C°). This is to identify optimum nano-additive concentration to reduce friction from each nanoparticle category used in this

research. Phase-II, and III testing were performed with different load velocity combinations at elevated temperatures to study the tribological characteristics of sample formulations with simulated real ICE operational environment. This facilitates studying the lubricant's ability to generate lubricant film, thick enough to separate asperities at reciprocating piston ring cylinder wall interface with varying load and speed parameters.

With the Phase-III LRT test results it is evident that the Sample S9A (which is a combination of 15W40 and GO) has enhanced friction characteristics than S9 (which is composed of G in place of GO as nano-additive, Figure 5.6). The phenomenon, which could be attributed to the surface functionalization of rubbing asperities due to interaction of oxygen functional groups on the GO surface with the substrates of sliding asperities. From the UV-vis and stability observation analyses it is revealed that S9A has improved dispersion stability (Figure 4.30, 4.33). In-addition, SEM images for wear surface of S9A illustrates the cross-hatched honing texture still on the rubbed surface indicating less wear compared to worn surfaces of reference oil (S1). Therefore, it emphasizes the importance of surface fictionalization for augmented dispersion stability, which is directly correlated to the tribological characteristics of a lubricant.

From all the samples tested, sample S35, which is a combination of FCO, and Al_2O_3/G nanocomposite emerged with the best tribological performance after Phase-III LRT tests, followed by wear scar analyses and field performance tests. Dominance of tribological characteristics; reduction of friction and wear by S35 are demonstrated with tribometer test results (Figures 5.9 – 5.10), EDX surface analysis (Figure 5.14, Table 5.3), 3D optical profiles (Figure 5.21), SEM micrographs (Figure 5.28), performance tests (Figure 6.1) and used oil sample analysis (Figures 6.2 – 6.4). With these observations 28% of overall COF reduction, 8% of specific fuel consumption (SFC) reduction, reduction of CO, SO_2 and NO_x emissions, reduction of S, P, Mo, and Zn particles in used crankcase oil are revealed. Dispersion stability of S35 (Figures 4.35 and 4.36) particle size (10.0 ± 0.3 nm) laminar/spherical surface morphology, amorphous nature (Figures 4.1 – 4.4) all are contributing attributes for this tribological enhancement. Deposition of C, Ni, Cr, O, Mo, K with Al traces on wear surface covering all Fe elements shown with EDX results (Figure 5.12, 5.14) indicates the formation of protective tribo film on sliding interface. The phenomenon, which is reinforced further by SEM images indicating formation of protective layer on wear surface supported by secondary mending and polishing effects. Moreover,

above 50% of COF reduction at higher sliding velocities (50 Hz frequency; Figure 5.10), specifically during EHL could be assigned to rolling or ball bearing effect in-place of sliding lubrication at sliding interface because of the spherical nature of the morphology of Al_2O_3/G nano-additives (Figure 4.1).

Reduction of SFC by 8% and mean COF by 28% (for all 25 tests) are underpinning the enhanced tribological behavior of S35. The decrease of exhaust pollutants is a noteworthy achievement. Reduced NO_x emissions emphasize the comparatively low combustion temperature than S1, confirming the improved heat transfer attributes of sample S35.

7.2. Suggestions for future works

Based on the acquired results of this research, the following recommendations are made for related further studies.

1. Combination of nano metal oxide and r-GO group (for example, TiO_2/r-GO) had shown improved dispersion stability, shear stability with enhanced tribological performance. Also, the formulation containing Al_2O_3/G as nano-additives had surfaced with optimum tribological performance with reduced fuel consumption, hazardous exhaust emissions along with moderate dispersion and shear stabilities compared to TiO_2/r-GO. Therefore, suggesting synthesizing Al_2O_3/r-GO, blending with FCO in place of Al_2O_3/G and being examined for tribological and physicochemical property improvements.

2. Tribometer tests to be performed on S35 and other finalized formulations using different contact geometries, for example sphere on flat or sphere on sphere (4 ball test) to have diversity on contact parameter. This is including the evaluation of wear scar diameter (WSD), and specific wear volume (SWV) of test specimens after tribometer testing to investigate the tribological characteristics of selected formulations under complex operating environments.

3. FCO has reported total base number (TBN) as 4.1 (mg KOH g^{-1}) at 0 hours and FCO based formulations are showing TBN as 2.4 (mg KOH g^{-1}) after 100 h of operation (Tables 4.8 and 6.3), which needs to be improved for an extended lubricant life.

4. It is recommended to perform field tests with longer hours; 250 h or 500 h, using an industrial engine having higher capacity for finalized formulations including S35. The purpose is also to investigate the lubrication behavior including environmental impact of sample formulations under extended usage time.

5. During simultaneous thermal analysis (STA) on FCO for extended hours had shown average of 3.6% mass loss at 120 ° C. Mass loss had continued for first 30 hours under isothermal condition before the solution become stable (Figure 4.22). Therefore, further investigation is recommended to improve the thermal and oxidative stability of FCO.

7.3. Contribution to new knowledge; Coconut oil as bio-based lubricant

There are numerous on-going research on lubricant formulation using nano/bio combination, albeit not many for using coconut oil as base stock for bio-based engine lubricants. In-addition the following points are considered fresh contributions to the knowledge of nano/bio lubricant formulation.

1. Application of nanocomposites consist of metal oxides, graphene and reduced graphene oxide, for example: Al_2O_3/G, TiO_2/G and TiO_2/r-GO as nano-additives with FCO for sample formulation.

2. Improving dispersion stability of nano-additives in nonaqueous sample lubricants by using GO in place of graphene and nanocomposites consist of metal oxides with r-GO group in place of nanoscale metal oxides or graphene.

3. Minimizing particle content of S, P, and Zn elements compared to mineral engine oil 15W40 (which are labeled as hazardous substances by leading environmental legislations) in used crank case oil samples by not using popular lubricant additive ZDDP during sample lubricant formulation.

4. Test results and methodologies used in this research for achieving dispersion stability of nano-additives in nano/bio lubricants, improvements to physicochemical properties of CCO, field performance tests for tribological enhancements and other relevant tests could be applied to other similar investigations.

7.4. Publications

- Alli, U., Hettiarachchi, S. J., Kellici, S., (2020), Functionalization of advanced 2D materials via batch and continuous hydrothermal flow synthesis. *Chemistry a European Journal*, 26 (29), 6447 – 6460.

8. Chapter 8: References

1. Statista.com (2020), Worldwide automobile production through 2019. *Statista.com, Transport & Logistics – Vehicles & Road Traffic.* [Accessed: 06/06/2020]

2. Iea.org (2019), Tracking transport. *International Energy Agency.* [Accessed: 10/05/2020]

3. Iea.org (2020), Global CO2 emissions in 2019. *International Energy Agency.* [Accessed: 10/05/2020]

4. Europarl.europa.eu (2019), CO2 emission from cars: facts and figures (infographics). *European Parliament.* [Accessed: 10/05/2020]

5. Tung, S. C., McMillan, M. L., (2004), Automotive tribology overview of current advances and challenges for the future. *Tribology International*, Vol. 37, pp 517-536.

6. Li J., Jacobs T. J., Bera T., Parkes M.A., (2018), Comparison of diesel engine efficiency and combustion characteristics between different bore engines. *Journal of Engineering for Gas Turbine and Power, The American Society of Mechanical Engineering*, Vol. 140 (10)

7. Neculer-power.net (2020), *Thermal Efficiency for Diesel Cycle.* [Accessed: 07/05/2020]

8. Ali M. K. A., Xianjun, H., (2015). Improving the tribological behaviour of internal combustion engines via the addition of nanoparticles to engine oils. *Nanotechnology Reviews*, Vol. 4 (4), pp 347–358.

9. Ali, M.K. A., Xianjun, H., Mai, L., Quingping, C., Turkson, F. R., Bicheng, C., (2016). Improving the tribological characteristics of piston ring assembly in automotive engines using Al_2O_3 and TiO_2 nanomaterials as nano-lubricant additives. *Tribology International*, Vol. 103, pp 540–554.

10. Jia B., Mikalsen R., Smallbone A., Roskilly A. P., (2018), A study and comparison of frictional losses in free-piston and crankshaft engines. *Applied Thermal Engineering*, Vol. 140 (2018), pp 217-224.

11. atc–europe.org (2016), *Lubricant additives; Use and benefits.* [Accessed: 07/05/2019]

12. Statista.com (2020), Global demand for lubricants from 2000 to 2018. *Statista.com, Chemistry & Resources, Chemical Industry.* [Accessed: 06/06/2020]

13. Vazquez-Duhalt, R., (1989), Environmental impact of used motor oil. *Science of the total environment,* Vol. 79 (1), pp 1-23.

14. Ghaednia, H., Jackson, R.L., *(2015). The role of Nanoparticles in Lubricants; Performing Lubricated and Dry Friction tests. Tribology & Lubrication Technology,* Vol. 71 (7), pp 20-24.

15. Stachowiak, G. W., Batchelor, A. W., (2005), Chapter 8: Boundary and extreme pressure lubrication. *Engineering tribology, 3rd Ed.*, pp 363-417.

16. UKLA (2016) *Bio – lubricants; understanding the potential and impact of new renewable sources on lubricant technology and application.* [Accessed: 10/05/2019]

17. Syahir, A. Z., et al, (2017). A review on bio-based lubricants and their application. *Journal of cleaner production,* Vol. 168, pp 997-1016.

18. Ebtisam, K. H., Elmelawy, M. S., Salah, A. K., Elbasuny, M. M., (2016). Manufacturing of environment friendly bio-lubricant from vegetable oils. *Egyptian journal of petroleum,* Vol. 26, pp 53-59.

19. Murilo, F. T., Lunga, T., Cavalcante, J.B., Silva, F.O.N., Cavalcante Jr., C.L., (2019), Studies on biodegradability of bio-based lubricants, *Tribology International,* Vol. 92, pp 301–306.

20. Clark, N., (2020), The end of the internal combustion engines. *Kenya International.*

21. Quora.com (2019), *In motor mechanics what does the acronym "TDC" stands for?* [Accessed: 05/01/2020]

22. Britannica.com (2020), *Diesel engine.* [Accessed: 05/01/2020]

23. Morris, N., Mohammadpour, M., Rahmani, R., Rahnejat, H., (2017), Optimization of the piston compression ring for improved energy efficiency of high-performance race

engines. *Proceedings of IMechE, Part D: Journal of Automobile Engineering*, Vol. 23 (13), pp 1806-1817.

24. Kurbet, S. N., Kumar, R. K., (2004), A finite element study of piston tilt effects on piston ring dynamics in internal combustion engines. *Proceedings of the Institution of Mechanical Engineers Part K: Journal of Multi-body Dynamics,* Vol. 218 (2), pp 107–117.

25. Delprete, C., Razavykia, A., Baldissera, P., (2019), Detailed analysis of piston secondary motion and tribological performance. *International Journal of Engine Research – IMechE*, pp 1-15.

26. Mang, T., Bobzin, K., Bartels, T., (2011), History of tribology. *Industrial Tribology.*

27. Mate, C. M., (2008). Chapter 9: Lubrication, *Tribology on the small scale*. Oxford UK, Oxford university press, pp 207-245.

28. Stachowiak, G. W., Batchelor, A. W., (2005), Chapter 2: Physical properties of lubricants. *Engineering tribology, 3rd Ed.*, pp 41–50.

29. Engineering toolbox (2017), *Absolute, Dynamic, and Kinematic viscosity.* [Accessed: 09/09/2019]

30. Porter, R. S., Johnson, J. F., (1961), Viscosity performance of lubricating base oils at shears developed in machine elements. *Wear, California Research Corporation, Richmond, Calif. (U.S.A.),* Vol. 4 (1), pp 32–40.

31. Spikes, H. A., (1990). *Infrared study of a piston ring temperature in a fired engine*. Kensington, London, Imperial college of science, technology and medicine.

32. Mate, C. M., (2008). Chapter 2: Characterizing surface roughness. *Tribology on the small scale,* pp 24-37.

33. Dimitri, K., (2021), Lubrication regimes. *Substech.com,*

34. Stachowiak, G. W., Batchelor, A. W., (2005), Chapter 4: Hydrodynamic lubrication. *Engineering tribology, 3rd Ed.*, pp 103-204.

35. Stachowiak, G. W., Batchelor, A. W., (2005), Chapter 7: Elastohydrodynamic lubrication. *Engineering tribology, 3rd Ed.*, pp 287-362.

36. Leeuwen, H. V., (2009). The determination of the pressure – viscosity coefficient of a lubricant through an accurate film thickness formula and accurate film thickness measurements. *IMechE, Journal of Engineering tribology,* Vol. 223 (J), pp 1143-1163.

37. Stachowiak, G. W., Batchelor, A. W., (2005), Chapter 3 – Lubricants and their composition. *Engineering tribology, 3rd Ed.,* pp 51-99.

38. Chaomleffel, J. P., Dalmaz, G., Vergene, P., (2007), Experimental results and analytical predictions of EHL film thickness. *Tribology at the interface.*

39. Obert, P., Muller, T., Fuber, H., Bartel, D., (2016). The influence of oil supply and cylinder liner temperature on friction, wear and scuffing behaviour of piston ring cylinder liner contacts – A new model test. *Tribology International,* Vol. 94, pp 306-314.

40. Minami, I., (2017), Molecular science of lubricant additives. *Applied Sciences – MDPI Journals,* Vol. 7 (5) – 445, pp 1–33.

41. Dwyer-Joyce, R. S., Drinkwater, B. W., Donohoe, C. J., (2003), Measurement of lubricant film thickness using ultrasound. *Proceedings of Royal society A, Mathematical, Physical and Engineering science*, Vol. 459 (2032), pp 957–976.

42. Dwyer-Joyce, R. S., Harper, P., Pritchard, J., Drinkwater, B. W., (2006), Oil film measurement in polytetrafluoroethylene – faced thrust pad bearings for hydrogenerator application. *Proceedings of the Institution of Mechanical Engineers, Part A: Journal of power and energy,* Vol 220 (6), pp 619–628.

43. Dwyer-Joyce, R.S., Reddyhoff, T. and Zhu, J. (2011) Ultrasonic Measurement for Film Thickness and Solid Contact in Elastohydrodynamic Lubrication. *Journal of Tribology. White rose research online/ American society of mechanical engineers,* Vol. 133 (3). 031501.

44. Green, D., (2007). *The tribological effects of soot contaminated lubricants on engine components,* Sheffield, University of Sheffield.

45. Mills, R., Vail, J. R., & Dwyer-Joyce, R. (2015). Ultrasound for the non-invasive measurement of internal combustion engine piston ring oil films. *Proceedings of the*

Institution of Mechanical Engineers, Part J: Journal of Engineering Tribology, Vol. 229 (2), 207–215.

46. Ziqiang, C., et al., (2014), Liquid film thickness estimation using electrical capacitance tomography. *Measurement Science Review*, Vol 14 (1), pp 8–15.

47. Dhar, A., Agarwal, A. K., Saxena, V., (2008). Measurement of dynamic lubricating oil film thickness between piston ring and liner in a motored engine. *Sensors and actuators A: Physical*, Vol. 149 (1), pp 7–15.

48. Dellis, P. S., (2015), An attempt to calibrate the Laser Induced Fluorescence (LIF) signal used for Oil Film Thickness (OFT) measurement in simulating test rigs. *Tribology in industry*, Vol. 37 (4), pp 525–538.

49. Fowell, M. T., (2014) A study of lubricant film thickness in compliant contact of elastomeric seal materials using a laser induced fluorescence technique. *Tribology International*, Vol. 80, pp 76–89.

50. Obert, P., Fuber, H., Bartel, D., (2019). Oil distribution and oil film thickness within the piston ring-liner contact measured by laser-induced fluorescence in a reciprocating model test under starved lubrication conditions. *Tribology International*, Vol. 129, pp 191-201.

51. Lubrecht, A. A., Venner, C. H., Colin, F., (2009). Film thickness calculation in elasto-hydrodynamic lubricated line and elliptical contacts: The Dowson, Higginson, Hamrock contribution. *IMechE, part J: Journal of engineering tribology, 1994 - 1996*, Vol 223 (5), pp 511–515.

52. Masjedi, M., Khonsari, M. M., (2015), On the effect of surface roughness in point contact EHL: Formulas for film thickness and asperity load, *Tribology international*, Vol 82 – Part A, pp 228–244.

53. Vrcek, A., Hultqvist, T., Baubet, Y., Bjorling, M., Marklund, P, Larsson, R., (2019), Micro pitting and wear assessment of PAO vs mineral-based engine oil operating under mixed lubrication conditions: Effects of Lambda ratio, roughness lay and sliding direction. *MDPI – Lubricants.*

54. Kumar, J. V., Rao, R. R., (2015), Effects of surface roughness in squeeze film lubrication of two parallel plates, *Tribology in industry*, Vol. 37 (2), pp 161–169.

55. Zapletal, T., Sperka, P., Krupka, I., Hartl, M., (2018), The effect of surface roughness on friction and film thickness in transition from EHL to mixed lubrication. *Tribology International*, Vol 128, pp 356–364.

56. Cann, P., Ioannides, E., Jacobson, B., Lubrecht, A. A., (1994), The Lambda ratio – a critical re-examination, *Wear*, Vol. 175 (1 – 2), pp 177–188.

57. Poon., C. Y., Bhushan, B., (1995). Comparison of surface roughness measurement by stylus profiler, AFM and non-contact optical profiler, *Wear*, Vol. 190 (1), pp 76–88.

58. Demircioglu, P., Durakbasa, M.N., (2011). Investigation on machined metal surfaces through the stylus type and optical 3Dinstruments and their mathematical modelling with the help of statistical techniques, *Measurement*, Vol. 44 (4), pp 611–619.

59. Bruker nano surfaces (2019), *Performing 3D optical profiling surface measurements that correlated to traceable standards*, AZoM. [Accessed: 05/01/2020]

60. McCarthy, S. A., (2014), The future of heavy-duty diesel engine oils. *Tribology and Lubrication Technology, Oct 2014*, Vol. 70 (10), pp 38-50.

61. Mehic, S. H., (2016), *Additives in lubricants: types and chemical composition of lubricant additives*

62. Heinemann, H., Speight J. G., Rudnick, L. R., (eds.) (2008), *Lubricant additives chemistry and applications* 2nd ED. Chemical Industries/124.

63. Voong M., (2005), *Optimization of crankcase lubricant additive – material combination for reduced friction and wear in internal combustion engines*, Edinburgh, Harriet-Watt University.

64. Spikes, H., (2004), The history and mechanisms of ZDDP. *Tribology section, Department of Mechanical Engineering, Imperial College, London SW7 2AZ, UK*, Vol, 17(3), pp 469-489.

65. Anil, P. M., Gopal K. N., Ashok, B., (2017), Tribological characteristics of Zinc-dialkyldithiophosphate blended with pongamia biodiesel. *SAE Technical paper,* 2017-28-1975.

66. Johnson, D. W., (2016), The tribology and chemistry of phosphorous containing lubricant additives. *Intech – Chapter 8, Advances in tribology,* pp 175–195.

67. Xu, D., Zhang, Q., Wang, J., (2019), Boundary lubrication in transient elliptical contact: part 1 – Theoretical formulation and results, *International Journal of Precision Engineering and Manufacturing,* Vol 20 (4), pp 609–617.

68. Whittle, T. J., Leggett, (2009), Influence of molecular weight on friction force microscopy of polystyrene and poly (methyl methacrylate) films: Correlation between coefficient of friction and chain entanglement. *Langmuir,* Vol. 25, pp 2217–2224.

69. Covitch, M. J., Trickett, K. J., (2015), How polymers behave as viscosity index improvers in lubricating oils. *Advances in Chemical Engineering and Sciences, Scientific Research Publishing,* Vol. 5, pp 134–151.

70. Zhao, Y., Li, W., Wang, X., Wang, J., (2018), Tribological properties of trimellitates containing polymethacrylates viscosity modifiers. *Proc IMechE Part J: Engineering Tribology*, Vol. 232 (7), pp 882–889.

71. Yan, L., Zheng, Y. B., Zhao, F., Li, S., Gao, X., Xu, B., Weiss, P. S., Zhao, Y., (2012), Chemistry and physics of a single atomic layer: Strategies and challenges for functionalization of graphene and graphene-based materials. *Chemical Society Reviews,* Vol. 47, pp 97–114.

72. Singh, B., P., (2004), Top-down and Bottom-up approaches for synthesis of nanomaterials. *The Royal Society and The Royal Academic of Engineering – Nanoscience and Nanotechnologies*, Vol. 25.

73. Priyadarshana, G., Kottegoda, N., Senaratne, A., de Alwis, A., Karunaratne, V., (2015), Synthesis of Magnetite Nanoparticles by Top-Down Approach from a Highly Purity Ore. *Hindawi – Journal of Nanomaterials*

74. Singh., R. K., Kumar, R., Singh, D. P., (2016), Graphene oxide: strategies for synthesis, reduction and frontier application, *The Royal Society of Chemistry Advances,* Vol. 6, pp 64993–65011.

75. Alli, U., Hettiarachchi, S. J., Kellici, S., (2020), Functionalization of advanced 2D materials via batch and continuous hydrothermal flow synthesis. *Chemistry a European Journal,* Vol. 26 (29), pp 6447–6460.

76. Agnieszka, J., Joanna, J., Joanna, K., Antoni, K., Wanda, Z., Andrzej, O., (2016), Controlled synthesis of graphene oxide/ alumina nanocomposites using a new dry sol-gel method of synthesis. *Institution of Chemistry, Slovak Academy of Sciences,* Vol. 71, pp 579-595.

77. Kellici S., Patel D., Saha B., (2014). Green Process Engineering as the Key to Future Processes, *Design and Engineering of Microreactor and Smart-Scaled Flow Processes*

78. Zahi, W., Zhou, K., (2019), Nanomaterials in Super-lubricity, *Advance functional materials.* Weinheim – GmbH, Wiley–VCH,

79. Hsu, S. M., (2004), Nano – lubrication: concept and design. *Tribology International,* Vol. 37 (7), pp 537–545.

80. Xiao H., Liu S., (2017) 2D nanomaterials as lubricant additive: A review. *Materials and Design,* Vol. 135, pp 319–332.

81. Zhang, S., Ma, T., Erdemir, A., Li, Q., (2019), Tribology for two-dimensional materials: From mechanisms to modulating strategies, *Materials today,* Vol. 26, pp 67-86.

82. Singh, A., Chauhan, P., Mamatha, T. G., (2020), A review on tribological performance of lubricants with nanoparticles additive. *Materials Today: Proceedings,* Vol. 25, pp 586–591.

83. Gulzar, M., (2018), Tribological study of nanoparticle enriched bio-based lubricants for piston ring-cylinder interaction. *Springer Theses.*

84. Song, W., Yan, J., Ji, H., (2019), Fabrication of GNS/MoS_2 composite with different morphology and its tribological performance as a lubricant additive, *Applied surface science,* Vol. 469 (1), pp 226–235.

85. Song, H. J., Jia, X. H., Li, N., Yang, X. F., Tang, H., (2012) Synthesis of α-Fe2O3 nanorod/graphene oxide composites and their tribological properties. *Journal of materials chemistry,* Vol. 22, pp 895–902.

86. Laad, M., Jatti, V. K. S., (2016). Titanium oxide nanoparticles as additives in engine oil. *Journal of King Saud University – Engineering Science,* Vol. 30(2), pp 116 - 122. *Energy,* Vol. 124(1), pp 413-422.

87. Jaiswal, V., Kalyani, Umrao, S., Rastogi, R. B., Kumar, R., Srivastava, A., (2016) Synthesis, Characterization, and Tribological Evaluation of TiO2-Reinforced Boron and Nitrogen co-Doped Reduced Graphene Oxide Based Hybrid Nanomaterials as Efficient Antiwear Lubricant Additives. *ACS Applied materials & interfaces,* Vol. 8(18), pp 11698–11710.

88. Meng, Y. Su, F. Chen, Y. (2015) Au/Graphene Oxide Nanocomposite Synthesized in Supercritical CO2 Fluid as Energy Efficient Lubricant Additive. *ACS Applied materials & interfaces,* ACS, Vol. 9(45), pp 39549–39559.

89. Ali, M. K. A., Xianjun, H., Abdelkareem, M. A. A., Gulzar, M., Elsheikh, A. H., (2018). Novel approach of the graphene nano-lubricant for energy saving via anti-friction/wear in automobile engines. *Tribology International,* Vol. 124 (2018), pp 209–229.

90. Luo, T., Wei, X., Huang, L., Yang, F., (2014), Tribological properties of Al_2O_3 nanoparticles as lubricating oil additives. *Ceramics International,* Vol. 40 (5), pp 7143–7149.

91. Meng, Y. Su F. Chen Y. (2015) Synthesis of nano-Cu/graphene oxide composites by supercritical CO_2-assisted deposition as a novel material for reducing friction and wear. *Chemical engineering journal,* Vol. 281, pp 11-19.

92. Abere, J.O., (2017), *Improved performance of bio-lubricants by nanoparticles additives.* White rose e-theses, Sheffield, University of Sheffield.

93. Kumar, A., Mundal, A., Dixit, A. R., Das, A. K., (2018), Performance evaluation of Al_2O_3 nanopowder mixed dielectric for electric discharge machining (EDM) of Inconel 825. *Materials and manufacturing processes,* Vol. 33(9), pp 986 – 995.

94. Lukin, E. S., Anufrieva, E. V., Popova, N. A., Morozov, B. A., Preobrazhenskii, V. S., Bezlepkin, V. A., Ukhvatova, L. S., Brzhezinskii, G. V., (2011), Analysis of surface microstructure and quality and properties of Aluminum oxide substrates. *Glass & Ceramics,* Vol. 67(9/10), pp 271–276.

95. Hassanpour, P., (2018), Bio medical application of Aluminium oxide nanoparticles, *Micro & Nano letters,* Vol. 13(9), pp 1227–1231.

96. Liu, H., Hou, X., Li, X., Jiang, H., Tian, Z., Ali, M.K.A., (2020), Effect of mixing temperature, ultrasonication, duration and nanoparticle/surfactant concentration on the dispersion performance of Al_2O_3 nano-lubricants. *Research Square – Research gate.*

97. Chen, X., (2009), Titanium dioxide nanomaterials and their energy application, *Chinese journal of catalysis,* Vol. 30 (9), pp 839–851.

98. Zhang, Z., Brown, S., Goodall, J. B. M., Weng, X., Thompson, K., Gong, K., Kellic, S., Clark, R. J. H., Evans, J. R. G., Darr, A. J., (2009), Direct continuous hydrothermal synthesis of high surface area nanosized Titania, *Journal of alloys and compounds,* Vol. 476 (1- 2), pp 451–456.

99. Zhu, K., Hu, G., (2014), Supercritical hydrothermal synthesis of titanium dioxide nanostructures with controlled phase and morphology. *The Journal of Supercritical Fluids,* Vol 94, pp 165–173.

100. Wu, H., Zhao, J., Xia, W., Cheng, X., He, A., Yun, J., Wang, L., Huang, H., Jiao, S., Huang, L., Zhang, S. & Jiang, Z. (2017). A study of the tribological behaviour of TiO2 nano-additive water-based lubricants. *Tribology International*, Vol.109, pp 398-408.

101. Velram, B. M., Kin-tak, L., Hui, D., Battacharyya, D., (2018), Graphene-based materials and their composites: A review on production, application and product limitations. *Composites part B: Engineering,* Vol. 142, pp 200-220.

102. Bhuyan, M. S. A., Uddin, M. N., Bipasha, F. A., Islam, M. M., Hossain, S. S., (2015), A review of functionalized Graphene properties and its application. *International journal of innovation and scientific research*, Vol. 17 (2), pp 303 – 315.

103. Meng, Y., Su, F., Chen, Y., (2016) Supercritical Fluid Synthesis and Tribological Applications of Silver Nanoparticle-decorated Graphene in Engine Oil Nanofluid. *Scientific reports,* 6, 31246.

104. Gupta, B., Kumar, N., Kalpataru, P., Vigneshwaran, K., Shailesh, J., Visoly-Fisher, I., (2017). Role of oxygen functional groups in reduced graphene oxide for lubrication. *Scientific Reports 7.*

105. Arjmandi, R., Hussan, A., Othman, N., Mohomad, Z., (2018), Characterization of carbon-based polypropylene nanoparticles. *Universiti Teknologi Malaysia.*

106. Moon, I. K., Lee, J., Ruoff, R. S., Lee, H., (2010), Reduce graphene oxide by chemical graphitation. *Nature communications 1, Article no. 73.*

107. Zainal, N. A., Zulkifli, N. W. M., Gulzar, M., Masjuki, H. H., (2018), A review on the chemistry, production, and technical potential of bio-based lubricants. *Renewable and sustainable energy reviews,* Vol. 82(1), pp 80–102.

108. Boateng, L., Ansong, R., Owusu, W. B., & Steiner-Asiedu, M. (2016). Coconut oil and palm oil's role in nutrition, health and national development: A review. *Ghana Medical Journal,* Vol. 50 (3), pp 189–196.

109. Ajithkumar G., (2009). Analysis, modification and evaluation of the cold flow properties of vegetable oils for industrial lubricants. *The thesis submitted to the School of Engineering, The Cohin University of Science and Technology.*

110. Kumar, G., Kumar D., Singh, S., Kothari, S., Bhatt, S., Singh, C.P., (2010). Continuous low-cost transesterification process for the production of coconut biodiesel. *Energies,* Vol. 3, pp 43-56.

111. Babu K. J., Kynadi A. S., Joy M.L., Nair K. P., (2018), Enhancement of cold flow property of coconut oil by alkali esterification process and development of a bio

lubricant. *Proc IMechE Part J: Journal of Engineering Tribology,* Vol. 232 (3), pp 307–314.

112. Sharma, K. B., Adhvaryu, A., Erhan, S. Z., (2009), Friction and wear behaviour of thioether hydroxy vegetable oil. *Tribology International,* Vol 42 (2), pp 353-358.

113. Bahari A., (2017), *Investigation into tribological performance of vegetable oils as bio-lubricants at severe contact conditions,* University of Sheffield.

114. Valeru, S. B., Sirinivas Y., Suman K.N.S., (2018). An attempt to improve poor performance characteristics of coconut oil for industrial lubricants. *Journal of Mechanical Science and Technology,* Vol. 32 (4), pp 1733-1737.

115. Abdulrahiman, K. T. A., Sajeeb, A. M., (2019), Characteristical study of coconut oil-based nano-lubricant. *International Conference on System Energy and Environment*

116. Talib, N., Nasir, R.M., Rahim, E.A., (2017), Tribological behaviour of modified jatropha oil by mixing hexagonal boron nitride nanoparticles as a bio-based lubricant for machining purposes. *Journal of Cleaner Production*, Vol. 147, pp 360–378.

117. Jibin T. P., Koshy, C.P., Mathew, M.D., Kuriachen, B., (2019), Tribological characteristic evaluation of coconut oil dispersed with surfactant modified ceria-zirconia hybrid nanoparticles. *Tribology - Materials, Surfaces & Interfaces,* Vol. 13 (4), pp 197-214.

118. Alves, S. M., Barros, B. S., Trajano, M. F., Rebiro, K. S. B., Moura E., (2013). Tribological behaviour of vegetable oil-based lubricants with nanoparticles of oxides in boundary lubrication conditions. *Tribology International,* Vol. 65, pp 28-36.

119. Escalante, C. F., (2019), *Fundamentals of transmission electron microscopy, the technique with the best resolution in the world.* Central University of Colombia, Bogota.

120. Scintag.com (1999), Basics of X-ray Diffraction. *Chapter 7; X2_Tech_Manual* [Accessed: 26/06/2019]

121. Pdx.edu (1995), Topica 5a XRD Lectures, *Portland State University – USA.* [Accessed: 08/03/2021]

122. Dutrow, B.L., Clark, C.M., (2020), X-ray Powder Diffraction. *Geochemical Instrumentation and analysis – SERC, Carlton College – USA.*

123. Ahmad, M., Foroughi, M.R., Mohammad, R.M., (2012). Modified Scherrer equation to estimate more accurate nano-crystallite size using XRD, *World Journal of Nano Science and Engineering*, Vol. 2, pp 154-160.

124. Raja, P. M. V., Barron, A. V., (2021), Raman spectroscopy. *Chemistry – Libre-Texts*

125. horiba.com (2021), What is Raman spectroscopy. *Horiba* [Accessed: 14/06/2021]

126. microspectra.com (2021), Science of micro-Raman spectroscopy, *CRAIC Technologies* [Accessed: 14/06/2021]

127. Hung, P. S., Kuo, Y. C., Chen, H. G., Chiang, H. H. K., Lee, O. K. S., (2013) Detection of osteogenic differentiation by differential mineralized matrix production in mesenchymal stromal cells by Raman spectroscopy. *PLoS ONE*, Vol. 8(5): e65438.

128. Costa, S., Borowaik-Palen, E., Krusznska, M., Bachmatiuk, A., Kalenczuk, R. J., (2008). Characterization of carbon nanotubes by Raman spectroscopy. *Material Science – Poland*, Vol. 26 (2), pp 433-44.

129. Korin, E., Froumin, N., Cohen, S., (2017), Surface analysis of nanocomplexes by X-ray Photoelectron Spectroscopy (XPS). *ACS – Biomaterials, Science & Engineering*, Vol. 3 (6), pp 882–889.

130. Good, C., Facey, H., (2020), X-Ray Photoelectron Spectroscopy (XPS). *Chemistry – Libre-Texts.*

131. xpssimplified.com, (2021), What is X-Ray Photoelectron Spectroscopy (XPS) *Thermo Scientific – XPS* [Accessed: 18/06/2021]

132. chem.libretexts.org (2020), Photoelectron spectroscopy: Theory. *Chemistry – LibreTexts*, pp 1837. [Accessed: 19/06/2021]

133. chem.libretexts.org (2020), Photoelectron spectroscopy: Application. *Chemistry – LibreTexts* [Online], pp 1836. [Accessed: 20/06/2021]

134. chem.libretexts.org (2020), How an FTIR spectrometer operates. *Chemistry – LibreTexts*, pp 1844. [Accessed: 23/06/2021]

135. Titus, D., Samuel, E. J. J., Roopan, S. S., (2019), Chapter 12 – Nanoparticle characterization techniques. *Green synthesis, characterization and application of nanoparticles; micro and nano technologies*, pp 303–319.

136. Gandomi, Y. A., Aaron, D. S., Houser, J. R., Daugherty, M. C., Clement, J. T., Pezeshki, A. M., Ertugrul, T. Y., Moseley, D. P., Mench, M. M., (2018), Critical review – Experimental diagnostics and material characterization techniques used on redox flow batteries. *Journal of the Electrochemical Society*, Vol. 165 (5), pp 970–1010.

137. slsi.lk (2021), Specification for crankcase lubricating oils for internal combustion diesel engines. *Sri Lanka Standards 1373:2020.* [Accessed: 01/07/2021]

138. acea.auto (2016), ACEA 2016 European oil sequences for service-fill oils. *European Automobile Manufacturers Association.* [Accessed: 07/07/2021]

139. Dorr, N., Agocs, A., Besser, C., Ristic, A., Frauscher, M., (2019), Engine oils in the field: A comprehensive chemical assessment of engine oil degradation in a passenger car. *Tribology Letters*, 67 (68).

140. Zhmud, B., (2018), TBN, What's in it, *Lube Magazine – Bizol Lubrticants, GmbH.*

141. Hohne, G.W.H., Hemminger, W.F., Flammersheim, H.-J., (2013), *Differential Scanning Calorimetry* (2nd Edi.) Springer. LSBN 978-3-642-05593-5,

142. Aboul-Gheit, A.K., Abd-el-Moghny, T., Al-Eseimi, M.M., (1997), Characterization of oils by differential scanning calorimetry. *Thermochimica Acta*, Vol. 306, pp 127–130.

143. Outlaw, J., (2011), Differential Scanning Calorimetry. *Champion Technologies – Perkin Elmer.*

144. Andrey Tarasov (2012), Thermal analysis: methods, principles, application. *Lecture series 121026, FHI MPG*.

145. Dong, J., Van De Voort, F.R., Yaylayan, V., Ismail, A.A., Pinchuk, D., Taghizadeh, A., (2001), Determination of total base number (TBN) in lubricating oils by mid-FTIR spectroscopy. *Journal of the Society of Tribologists and Lubrication Engineers*, Vol. 57.

146. Spectrosci.com (2017), Guide to measure TAN and TBN in oil, *Spectro Scientific.* [Accessed: 12/02/2021].

147. mt.com (2016), Automated Acid Number Determination according to ASTM D664 – 11a, *Mettler Toledo – Application M726.* [Accessed: 16/03/2021]

148. Baig, A., Paszti, M., Flora, T.T. Ng, (2013), A simple and green analytical method for acid number analysis of biodiesel and biodiesel blends on potentiometric technique. *Fuel,* Vol. 104, pp 426–432.

149. Anton-paar.com (2021) SAE viscosity grades. *Anton Paar GmbH.* [Accessed: 01/07/2021]

150. Siburian, R., Sihotang, H., Raju, S. L., Supeno, M., Simanjuntak, C., (2018), New route to synthesize of graphene nano sheets. *Oriental Journal of Chemistry,* Vol. 34 (1), pp 182-187.

151. Hayes, W. I., Joseph, P., Mughal, M. Z., Papakonstantinou, P., (2014), Production of reduced graphene oxide via hydrothermal reduction in an aqueous sulphuric acid suspension and its electrochemical behaviour. *Journal of Electrochemistry,*

152. Fatijo, G. G., Smith E. H., Sherrington, I., (2016), Assessing lubricating film thickness between compression ring and engine cylinders: A comprehensive comparison of theoretical predictions and experimental measurements. *Jost Institute of Tribotechnology, Uclan, Preston, Lancashire UK.*

153. Nguyen, T. T. D., Nguyen De, Doan, H. N., Vo, P. P., Huynh, V. T., Hoang, V. H., Phan, T. B., Kinashi, K., Nguyen, P. T., (2022) In-depth understanding of the photoreduction of graphene oxide to reduce-graphene oxide in TiO_2 surface: statistical analysis of X-ray photoelectron and Raman spectroscopy data. *Applied Surface Science,* Vol. 581 (2022) 152325.

154. Maruthy, M., Tubaki, S., Lokesh, S. V., Rangappa, D., (2017), Co, N-doped TiO_2 coated r-GO as a photo catalyst for enhanced photo catalytic activity. *Materials Today: Proceedings*, Vol. 4 (11), pp 11873–11881.

155. Rozita, Y., Brydson, R., Scott, A. J., (2009), An investigation of commercial gamma-Al_2O_3 nanoparticles. *EMAG conference, Journal of Physics, conference series* Vol. 241(2010) 012096

156. Feret, F. R., Roy, D., Boulanger, C., (2000), Determination of alpha and beta alumina in ceramic alumina by X-ray diffraction. *Spectrochimica Acta Part B, Atomic Spectroscopy*

157. Aziz, M., Halim, F. S. A., Jaafar, J., (2014), preparation and characterization of graphene membrane electrode assembly. *Jurnal Teknologi (Sciences & Engineering)*, Vol. 69 (9), pp 11-14.

158. Baragau, I. A., Power, N. P., Morgan, D. J., Heil, T., Lobo, R. A., Roberts, C. A., Titirici, M. M., Dunn, S., Kellici, S., (2020), Continuous hydrothermal flow synthesis of blue-luminescent, excitation-independent N-doped CQDs as nano-sensors. *Journal of Materials Chemistry A, Open Research Online,* pp 1–21.

159. Saleem, H., Haneef, M., Abbasi, H. Y., (2018), Synthesis route of reduced graphene oxide via thermal reduction of chemically exfoliated graphene oxide (GO). *Journal of Materials Chemistry and physics,* Vol. 204, pp 1–7.

160. Ciplak, Z., Yildiz, N., Calimli, A., (2015), Investigation of graphene/Ag nanocomposites synthesis parameters for two different synthesis models. *Fullerenes, Nanotubes and Carbon Nanostructures, T & F Group,* Vol. 23 (4), pp 361-370.

161. Wu, J. B., Lin, M. L., Cong, X., Liu, H. N., Tan P. H., (2018), Raman spectroscopy of graphene-based materials and its application in related devices. *Journal of Chemical Society Reviews, (RSC),* Vol. 47, pp 1822-1873.

162. Flack, A., (2021), Raman microscopy of graphene. *Application Note, Edinburgh Instruments*

163. Challagulla, S., Tarafder, K., Ganesan R., Roy, S., (2017), Structure and Sensor photo catalytic reduction of nitroarenes over TiO_2. *Scientific reports,* Vol 7:8783.

164. Ohsaka, T., Izumi, F., Fujiki, Y., (1978), Raman spectrum of anatase, TiO_2. *Journal of Raman Spectroscopy,* Vol. 7 (6), pp 321–324.

165. Jbara, A. S., Othaman, Z., Saeed, M. A., (2017), Structural, morphological and optical investigations of θ-Al_2O_3 ultrafine powder. *Journal of Alloys and Compounds.*

166. Aminzadeh, A., Sarikhani-fard, H., (1999), Raman spectroscopic study of Ni/Al_2O_3 catalyst. *Spectrochimica Acta Part A: Molecular and Biomolecular Spectroscopy,* Vol. 55 (7), pp 1421–1425.

167. Tuschel, D., (2019), Stress, strain and Raman spectroscopy. *Journal of Spectroscopy,* Vol. 34 (9).

168. Ghos, B. C., Farhad, S. F. D., Pathwary, M. A. M., Majumder, S., Hossain, M. A., Tanvir, N. I., Rahman, M. A., Tanaka, T., Guo, Q., (2021), Influence of the substrate, process conditions, and post-annealing temperature on the properties of ZnO thin film grown by the successive ionic layer adsorption and reaction method. *Journal of ACS Omega,* Vol. 6, pp 2665–2674.

169. Baragau, I. A., Lu, Z., Power, N. P., Morgan, D. J., Bowen, J., Diaz, P., Kellici, S., (2021), Continuous hydrothermal flow synthesis of S-functionalized carbon quantum dots for enhanced oil recovery. *Chemical Engineering Journal,* Vol 405, 126631

170. Teodorescu, C. M., Esteva, J.M., Karnatak, R. C., Afif El A., (1994), An approximation of the Voigt I profile for the fitting of experimental X-ray absorption data. *Nuclear Instruments and Methods in Physics Research Section A: Accelerators, Spectrometers, Detectors and Associated Equipment,* Vol. 345 (1), pp 141–147.

171. Wagner, C. D., Davis, L. E., Zeller, M. V., Taylor, J. A., Raymond, H. A., Gale, L. H., (1981), Empirical atomic sensitivity factors for quantitative analysis by electron spectroscopy for chemical analysis. *Journal of Surface and Interface Analysis,* Vol.3 (5), pp 211–225.

172. Kellici, S., Acord, J., Ball, J., Reehal, H. S., Morgan, D., Saha, B., (2014), A single rapid route to synthesis of reduced graphene oxide with antibacterial activities. *RSC Adv.,* Vol. 4, pp 14858–14861.

173. Djebaili, K., Mekhalif, Z., Boumaza, A., Djelloul, A., (2015), XPS, FTIR, EDX and XRD analysis of Al_2O_3 scales grown on PM2000 alloy. *Journal of Spectroscopy*, Article ID. 868109.

174. Hao, J., Li, Y., Liao, R., Liu, G., Liao, Q., Tang, C., (2017), Fabrication of Al_2O_3 nano structure functional film on a cellulose insulation polymer surface and its space charge suppression effect. *Polymer,* Vol. 9 (10), 502.

175. Qu, D., Zheng, M., Zhang, L., Zhao, H., Xie, Z., Jing, X., Haddad, R. E., Fan, H., Sun, Z., (2014), Formation mechanism and optimization of highly luminescent N – doped graphene quantum dots. *Scientific Reports,* Vol. 4, 05294.

176. Hsu, S.M., Cummings, A.L., (1983), Thermogravimetric analysis of lubricants. *SAE: Lubricant and Additive Effects on Engine Wear – SP-558,*

177. Mosarof, M.H., Kalam, M.A., Masjuki, H.H., Arslan, A., Monirul, I.M., Ruhul, A.M., Shahir, S.A., Khuong, L.S., (2016), Analysis of thermal stability and lubrication characteristics of millettia pinnata oil. *Royal Society of Chemistry; Advances,* Vol. 6, pp 81414–81425.

178. Satheeshan, K. N., Seema, B. R., Meera, A. V. M., (2019), Quality analysis of virgin coconut oil processed through different methods. *Journal of Pharmacognosy and Phytochemistry,* Vol. 8 (3), pp 2119–2123.

179. Sergio, L. D. K., Soares, E. J., Thompson, R. L., Siqueira, R. N., (2017), Friction coefficient of Bingham and power-law fluids in abrupt contractions and expansions. *Journal of Fluid Engineering,* Vol. 139 (2), pp 21203–21211.

180. Azeez, S., Bertola, V., (2021), Lubrication of journal bearings by shear thinning lubricants using different constitutive models. *Proc. IMechE Part J: Journal of Engineering Tribology,* Vol. 235 (6), pp 1203–1210.

181. Imam, Z., (2020), Modelling non-Newtonian fluids, *Rheosence Inc*.

182. Agrawal, N., Sharma, S. C., (2022), Performance of textured spherical thrust hybrid bearing operating with shear thinning, piezo-viscous lubricants. *Proc. IMechE Part J: The Journal of Engineering Tribology,* Vol. 236(4), pp 607–633.

183. Kumar, P., Anuradha, P., (2014), Elasto-hydrodynamic lubrication model with limiting shear stress behaviour considering realistic shear-thinning and piezo-viscous response. *Journal of Tribology,* Vol. 136 (2), 021503 – 8.

184. Elimelech, M. Gregory, J. William, R. A., (1995), *Particle deposition and aggregation – Measurement, Modelling and Simulation*. Oxford, Butterworth-Heinemann.

185. Mejia, J., Valembois, V., Piret, Jean-P., Tichelaar, F., Huis, M. V., Masereel, B., Toussaint, O., Delhalle, J., Mekhalif, Z., Lucas, S., (2012), Are stirring and sonication pre-dispersion methods equivalent for in vitro toxicology evaluation of SiC and TiC?. *Journal of Nanoparticle Research,* Vol. 14 (815).

186. Hao, T., (2005), Chapter 6 - Physics of electrorheological fluids. *Studies in Interface Science, Elsevier,* Vol. 22, pp 235-340.

187. Cortes, V., Ortega, J. A., (2019), Evaluating the rheological and tribological behaviours of coconut oil modified with nanoparticles as lubricant additives. *Lubricants,* Vol. 7 (9), 76.

188. Owen, T., (1996), *Fundamentals of UV – Visible Spectroscopy,* Germany, Hewlett-Packard 09/96.

189. Gulzar, M., et al, (2017), Chemically Active Oil Filter to Develop Detergent Free Bio-based Lubrication for Diesel Engine

190. Tadmor, R., et al, (2000), Resolving the Puzzle of Ferrofluid Dispersants. *Langmuir – American Chemistry Society (ACS) publication,* Vol. 16 (24), pp 9117 – 9120.

191. Howell-Smith, S. J., (2011), *Tribological optimisation of the internal combustion engine piston to bore conjunction through surface modification,* Loughborough - UK, Loughborough University.

192. Mostofi, A., (1982), *Oil film thickness and pressure distribution in EHL elliptical contacts.* 283582

193. Zahi, W., Zhou, K., (2019), Nanomaterial in Superlubricity. *Advance functional materials,*

194. Ahmed, E., Ali, M.K.A., Hou, X., Mohamed A. A. Abdelkareem, (2019), Techniques used to improve the tribological performance 0f the piston ring-cylinder liner contact. *IOP conference series: Material Science and Engineering 563-022024.*

195. Ali, M.K.A., Hou, X., Mohamed A. A. Abdulkareem, Elsheikh, A., (2019). Role of nano-lubricants formulated in improving vehicle engine performance. *IOP Conference Series: Material Science and Engineering 563-022015.*

196. Ali, M.K.A., Hou, X., Turkson, R.F., Ezzat, M., (2016). An analytical study of tribological parameters between piston ring and cylinder liner in internal combustion engine. *Proc IMechE Part K; J Multi-Body Dynamics,* Vol 230 (4), pp329-349.

197. Lal, R., Singh R. C., Ranganath M. S., Maji S., (2014). Friction and wear of tribo-elements in power producing units for IC engines – A Review. *International Journal for Engineering Trends and Technology (IJETT), Vol. 4(5), pp 225-231*.

198. Bulsara, M. A., Bhatt, D. V., Mistry, K. N., (2009), Prediction of oil film thickness in piston ring – cylinder assembly in an IC engine: A review. *Proceedings of the World Congress in Engineering (WCE), Vol. II*.

199. Wool, R. P., (2008), Self-healing materials: a review. *Soft Matter,* Vol. 4, pp 400-418.

200. Spori, D. M., (2010), Structural influences on self-cleaning surfaces. *ETH Zurich Research Collection.*

201. Peng, J., Xue, B., Zhang, Y., Bai Kingpeng (2012), Directional crystallization kinetics of coconut oil under temperature gradient. *Global Journal of Science Frontier Research Chemistry,* Vol. 12 (4) – 1.

202. Rizza M. A., Wijayanti W., Hamidi N., Wardana I. N. G., (2018), Role of intermolecular forces on the contact angle of vegetable oil droplets during the cooling process. *The Scientific World Journal,* Vol. 2018, Article ID: 5283753.

203. Dolatabadi, N., Rahmani, R., Rahnejat, H., Garner, C. P., Brunton, C., (2020), Performance of poly alpha olefin nano-lubricants. *Lubricants, MDPI Journals.*

204. Bouassida, H., (2014), *Lubricated piston ring cylinder liner contact: Influence of the liner microgeometry*, Lyon, INSA de Lyon.

205. Chen, Y., Renner, P., Liang, H. (2019), Dispersion of nanoparticles in lubricating oil: A critical review. *Lubricants – MDPI,* Vol 7 (1) 7.

206. Denis, J., (1989), Pour point depressants in lubricating oils. *Lubrication Science,* vol. 1 (2), pp 103–120.

207. Sundararajan, P. R., Flory, P. J., (1974), Configurational characteristics of Poly (methyl methacrylate). *ACS Publications: Journal of the American Chemical Society*, Vol. 96 (16), pp 5025–5031.

208. Greenwood, J. A., Tripp, J. H., (1970), The contact of two nominally flat rough surfaces. *Proceedings of the Institution of Mechanical Engineers*, Vol. 185 (1), pp 625–633.

209. Ilie, F., Covaliu, C., (2016), Tribological properties of the lubricant containing titanium dioxide nanoparticles as an additive. *MDPI; Lubricants.*

210. Thanh, L. T., Okitsu, K., Boi, V. L., Maeda, Y., (2012), Catalytic technologies for biodiesel fuel production and utilization of glycerol: A review. *MDPI – Catalysts,* Vol. 2, pp 191-222,

211. Perez, J.M., (2000), Oxidative properties of lubricants using thermal analysis. *Thermochimica Acta,* Vol. 357–358, pp 47–56.

212. Tripathi, A.K., Vinu, R., (2015), Characterization of thermal stability of synthetic and semi-synthetic engine oils. *MDPI – Lubricants,* Vol. 3(1), pp 54–79.

213. Brooke, D., Burns, J., Cartwright, C., Person, A., (2009), Environmental risk evaluation report: Styrenated Phenol. *Evidence – Environment Agency.*

214. Ali, M. K. A., Xianjun, H., (2020), Improving the heat transfer capability and thermal stability of vehicle engine oils using Al_2O_3/TiO_2 nanomaterials. *Powder Technology*, Vol. 363, pp 48–58.

215. Yu, H., Zhang, B., Bulin, C., Li, R., Xing, R., (2016), High-efficient synthesis of graphene oxide based on improved Hummers method. *Scientific Reports – 16;36143.*